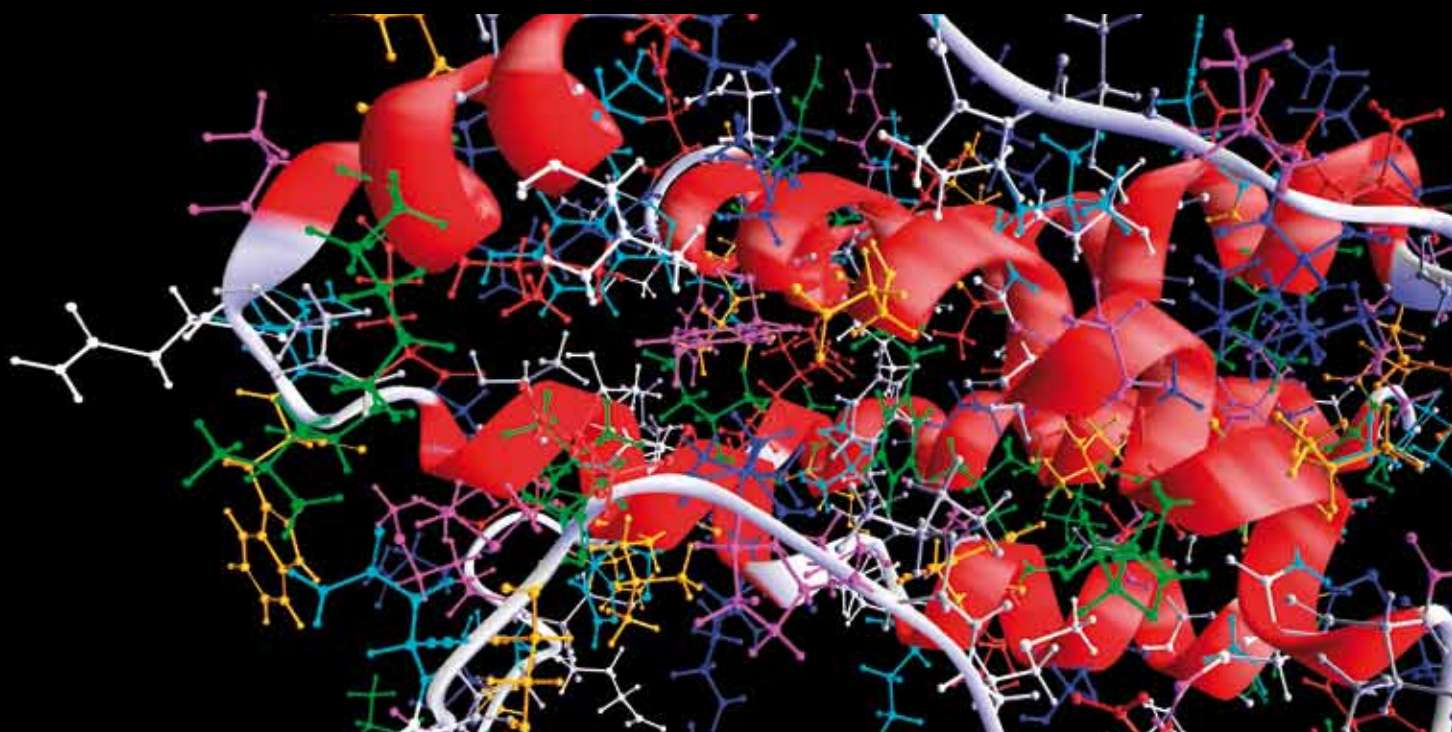


PREGNANCY MONITORING

GUEST EDITORS: M. MISCHI, B. KARLSSON, M. G. SIGNORINI, M. UNGUREANU,
AND C. MARQUE





Pregnancy Monitoring

Computational and Mathematical Methods in Medicine

Pregnancy Monitoring

Guest Editors: M. Mischi, B. Karlsson, M. G. Signorini,
M. Ungureanu, and C. Marque



Copyright © 2014 Hindawi Publishing Corporation. All rights reserved.

This is a special issue published in “Computational and Mathematical Methods in Medicine.” All articles are open access articles distributed under the Creative Commons Attribution License, which permits unrestricted use, distribution, and reproduction in any medium, provided the original work is properly cited.

Editorial Board

Emil Alexov, USA
Georgios Archontis, Cyprus
Dimos Baltas, Germany
Chris Bauch, Canada
Maxim Bazhenov, USA
Thierry Busso, France
Carlo Cattani, Italy
Shengyong Chen, China
William Crum, UK
Ricardo Femat, Mexico
Alfonso T. García-Sosa, Estonia

Damien Hall, Australia
Volkhard Helms, Germany
Seiya Imoto, Japan
Sebastien Incerti, France
Lev Klebanov, Czech Republic
Quan Long, UK
Changming Ma, USA
Reinoud Maex, France
Michele Migliore, Italy
Karol Miller, Australia
Ernst Niebur, USA

Kazuhisa Nishizawa, Japan
Hugo Palmans, UK
David J. Sherman, France
S. Sivaloganathan, Canada
Nestor V. Torres, Spain
N. J. Trujillo-Barreto, Cuba
Gabriel Turinici, France
Kutlu O. Ulgen, Turkey
Edelmira Valero, Spain
Guang Wu, China
Henggui Zhang, United Kingdom

Contents

Pregnancy Monitoring, M. Mischi, B. Karlsson, M. G. Signorini, M. Ungureanu, and C. Marque
Volume 2014, Article ID 507613, 2 pages

Fetal ECG Extraction from Abdominal Signals: A Review on Suppression of Fundamental Power Line Interference Component and Its Harmonics, Dragoş-Daniel Țarălungă, Georgeta-Mihaela Ungureanu, Ilinca Gussi, Rodica Strungaru, and Werner Wolf
Volume 2014, Article ID 239060, 15 pages

Monitoring Fetal Heart Rate during Pregnancy: Contributions from Advanced Signal Processing and Wearable Technology, Maria G. Signorini, Andrea Fanelli, and Giovanni Magenes
Volume 2014, Article ID 707581, 10 pages

New Estimators and Guidelines for Better Use of Fetal Heart Rate Estimators with Doppler Ultrasound Devices, Iulian Voicu, Sébastien Ménigot, Denis Kouamé, and Jean-Marc Girault
Volume 2014, Article ID 784862, 10 pages

Automatic Identification of Motion Artifacts in EHG Recording for Robust Analysis of Uterine Contractions, Yiyao Ye-Lin, Javier Garcia-Casado, Gema Prats-Boluda, José Alberola-Rubio, and Alfredo Perales
Volume 2014, Article ID 470786, 11 pages

Automated Conduction Velocity Analysis in the Electrohysterogram for Prediction of Imminent Delivery: A Preliminary Study, Hinke de Lau, Chiara Rabotti, Rianne Bijloo, Michael Johannes Rooijackers, Massimo Mischi, and S. Guid Oei
Volume 2013, Article ID 627976, 7 pages

Comparison of Different EHG Feature Selection Methods for the Detection of Preterm Labor, D. Alamedine, M. Khalil, and C. Marque
Volume 2013, Article ID 485684, 9 pages

Coarse-Grained Multifractality Analysis Based on Structure Function Measurements to Discriminate Healthy from Distressed Foetuses, Souad Oudjemia, Amira Zaylaa, Salah Haddab, and Jean-Marc Girault
Volume 2013, Article ID 152828, 9 pages

Probabilistic Source Separation for Robust Fetal Electrocardiography, Rik Vullings and Massimo Mischi
Volume 2013, Article ID 109756, 8 pages

Assessment of Parturition with Cervical Light-Induced Fluorescence and Uterine Electromyography, Miha Lucovnik, Ruben J. Kuon, and Robert E. Garfield
Volume 2013, Article ID 165913, 6 pages

Automatic Evaluation of Progression Angle and Fetal Head Station through Intrapartum Echographic Monitoring, Sergio Casciaro, Francesco Conversano, Ernesto Casciaro, Giulia Soloperto, Emanuele Perrone, Gian Carlo Di Renzo, and Antonio Perrone
Volume 2013, Article ID 278978, 8 pages

Editorial

Pregnancy Monitoring

M. Mischi,¹ B. Karlsson,² M. G. Signorini,³ M. Ungureanu,⁴ and C. Marque⁵

¹ Eindhoven University of Technology, Electrical Engineering Department, Signal Processing Systems, Biomedical Diagnostics Research laboratory, Den Dolech 2, 5612 AZ Eindhoven, The Netherlands

² Reykjavik University, School of Science and Engineering, Institute of Biomedical and Neural Engineering, Menntavegur 1, 101 Reykjavik, Iceland

³ Politecnico di Milano, Dipartimento di Elettronica, Informazione e Bioingegneria DEIB, Piazza Leonardo da Vinci 32, 20133 Milano, Italy

⁴ Politehnica University of Bucharest, Applied Electronics and Information Engineering Department, Iuliu Maniu 1-3, 060042 Bucharest, Romania

⁵ Université de Technologie de Compiègne, UMR CNRS 7338, Biomécanique et Bioingénierie, rue Roger Couffolenc, CS60319, 60203 Compiègne Cedex, France

Correspondence should be addressed to M. Mischi; m.mischi@tue.nl

Received 23 January 2014; Accepted 23 January 2014; Published 4 March 2014

Copyright © 2014 M. Mischi et al. This is an open access article distributed under the Creative Commons Attribution License, which permits unrestricted use, distribution, and reproduction in any medium, provided the original work is properly cited.

Pregnancy is a happy but also very risky time, especially for the fetus. Fetal distress and preterm birth make this the most dangerous period in a person's life. Indeed the risk of death for the fetus during the last third of pregnancy is similar to the accumulated risk of death in traffic during the rest of a person's life. Early assessment of these risks enables timely and effective intervention, which is essential to minimize perinatal mortality and long term morbidity. With this aim, this issue presents modeling and signal processing methods for reliable pregnancy monitoring, possibly overcoming current diagnostic limitations due to motion artifacts, low signal-to-noise ratio (SNR), and complex signal and image interpretation. In particular, the authors have focused on three main technologies, namely, ultrasound (imaging and Doppler), fetal electrocardiography (fECG), and uterine electromyography, referred to as electrohysterography (EHG). In fact, improved pregnancy monitoring for accurate assessment of both fetal condition and uterine activity requires advances in all of these technologies. In addition, specific methods for reduction of artifacts and interference in biopotential recordings are also presented and discussed aiming at producing data of better quality, which are suitable for reliable analysis.

In the area of ultrasound Doppler analysis of the heart rate, the paper "New estimators and guidelines for better use of fetal heart rate estimators with Doppler ultrasound

devices" investigates a number of heart rate estimators, with the aim of achieving an accuracy of 0.25 beats per minute, required for reliable analysis of heart rate parameters. Based on the comparison of several estimators with simulations and 580 min recordings, only those estimators based on directional envelopes (using quadrature and in-phase components) and autocorrelation delay estimation could achieve the target accuracy. Moreover, combination of directional signals provided 14% increase in sensitivity, suggesting the implementation of a multitransducer approach for parallel processing as a valid strategy to pursue. Moving to ultrasound imaging, the paper "Automatic evaluation of progression angle and fetal head station through intrapartum echographic monitoring" provides a new automatic and reliable option for assessment of labor progression, without the need for digital inspection of the cervix. Progression angle and fetal head station could successfully be assessed in 10 women during labor with accuracy superior to standard methods. Earlier identification of abnormal labor patterns could therefore be achieved, supporting clinical decision.

Analysis of the fECG is complicated by the mixture of signals originating from different sources that contribute to the recorded signals, resulting in low-SNR fECG. The paper "Probabilistic source separation for robust fetal electrocardiography" proposes a probabilistic framework where blind

source separation incorporates and exploits prior knowledge based on physiological modeling. The superiority of the approach as compared to standard blind separation methods is proven by simulation and multichannel fECG recordings. The fetal heart rate variability (FHRV) is among the most relevant features that can be extracted from the fECG. The paper “*Monitoring fetal heart rate during pregnancy: contributions from advanced signal processing and wearable technology*” proposes new diagnostic and classification indices based on advanced signal processing. Results on normal fetuses and intrauterine growth-restricted fetuses show that the estimation of different indices from FHRV signals, both linear and nonlinear, provides valuable indications to describe the pathophysiological mechanisms influencing the fetal heart rate. This paper also provides a perspective on wearable technology for fECG monitoring, focusing on the “Telefetal-care” system, using textile electrodes embedded in everyday garments. Still in relation to FHRV analysis for detection of fetal distress, nonlinear analysis tools are also proposed by the paper “*Coarse-grained multifractality analysis based on structure function measurements to discriminate healthy from distressed foetuses,*” where coarse-grained multifractal analysis of the fetal heart rate, using the Hurst exponent together with singularity and Holder spectra, shows promising results to discriminate healthy from distressed fetuses on 100 recordings.

EHG analysis is very promising and yet controversial. While evidence is being provided on the value of EHG analysis for detection of preterm labor, the complex mechanisms underlying the uterine activity are not fully understood yet. As a result, different groups are proposing different EHG parameters to characterize the uterine contractions. In the paper “*Comparison of different EHG feature selection methods for the detection of preterm labor,*” the best classification results (48 women) are obtained by nonlinear approaches, for either feature selection or classification, making also use of nonlinear features such as variance entropy. Different conclusions are somehow drawn in the paper “*Assessment of parturition with cervical light-induced fluorescence and uterine electromyography,*” where linear EHG features, such as propagation velocity and peak frequency, permitted prediction of the delivery time in a study with 88 patients. This paper also shows the value of light-induced fluorescence (LIF) of cervical collagen for monitoring labor progression, reflected in changes in the cervix compliance. Although with different velocity amplitudes, this result is in line with the paper “*Automated conduction velocity analysis in the electrohysterogram for prediction of imminent delivery: a preliminary study,*” where the amplitude of the EHG conduction velocity was found to be increased prior to (preterm) delivery based on the analysis of 22 patients. Moreover, the authors were able to automatically extract this feature from the EHG. In general, the controversial conclusions among the authors on the best EHG analysis may also be ascribed to the different geometry and configuration of the employed electrode grid, possibly sensitive to different EHG features evidenced at different spatial scales.

Dealing more specifically with artifacts and interference in biopotential recordings, accurate motion artifact detection

is proposed in the paper “*Automatic identification of motion artifacts in EHG recording for robust analysis of uterine contractions,*” where detection is obtained with a classifier based on a total of 11 spectral, temporal, and nonlinear features, although the results suggest possible reduction to 7 features. The results were obtained with a Laplacian electrode configuration in 12 women in their first stage of labor. Another relevant noise source in the recording may be represented by the powerline. The paper “*Fetal ECG extraction from abdominal signals: a review on suppression of fundamental power line interference component and its harmonics*” presents a state-of-the-art review comparing the performance of digital notch filters, adaptive filters, Hilbert Huang transform, Wavelet transform, blind source separation, and neural networks with the Hilbert Huang transform method showing the best results for the implemented scenarios.

M. Mischi
B. Karlsson
M. G. Signorini
M. Ungureanu
C. Marque

Research Article

Fetal ECG Extraction from Abdominal Signals: A Review on Suppression of Fundamental Power Line Interference Component and Its Harmonics

Dragoș-Daniel Țarălungă,¹ Georgeta-Mihaela Ungureanu,¹
Ilinca Gussi,² Rodica Strungaru,¹ and Werner Wolf³

¹ Applied Electronics and Information Engineering Department, Politehnica University of Bucharest, 061071 Bucharest, Romania

² University of Medicine and Pharmacy Carol Davila, 050474 Bucharest, Romania

³ Institut für Infomationstechnik, Universität der Bundeswehr München, 85577 Neubiberg, Germany

Correspondence should be addressed to Dragoș-Daniel Țarălungă; dragos.taralunga@upb.ro

Received 15 July 2013; Revised 11 November 2013; Accepted 20 December 2013; Published 9 February 2014

Academic Editor: Maria G. Signorini

Copyright © 2014 Dragoș-Daniel Țarălungă et al. This is an open access article distributed under the Creative Commons Attribution License, which permits unrestricted use, distribution, and reproduction in any medium, provided the original work is properly cited.

Interference of power line (PLI) (fundamental frequency and its harmonics) is usually present in biopotential measurements. Despite all countermeasures, the PLI still corrupts physiological signals, for example, electromyograms (EMG), electroencephalograms (EEG), and electrocardiograms (ECG). When analyzing the fetal ECG (fECG) recorded on the maternal abdomen, the PLI represents a particular strong noise component, being sometimes 10 times greater than the fECG signal, and thus impairing the extraction of any useful information regarding the fetal health state. Many signal processing methods for cancelling the PLI from biopotentials are available in the literature. In this review study, six different principles are analyzed and discussed, and their performance is evaluated on simulated data (three different scenarios), based on five quantitative performance indices.

1. Introduction

The fetal heart rate (fHR) and the morphological analysis of the fetal electrocardiogram (fECG) are two of the most important tools used nowadays in clinical investigations to examine the health state of the fetus during pregnancy. The fHR is the mostly used parameter in fetal monitoring, since 1818 [1]. While the fHR track shows a predictive value of almost 99% for the fetal well being investigation, an abnormal fHR has a predictive value of only 50%. Hence, it provides relatively poor specificity in detecting the fetal distress [2]. Additional information about the fetal well being can be obtained by analyzing the morphology of the fECG signal, which was recently introduced in clinical practice for fetal monitoring. Its clinical relevance was demonstrated by a series of clinical studies [3], randomized controlled trials [4–8] and prospective observational studies [9–18], which prove that clinical fetal monitoring based on both fHR and fECG morphology analysis, especially the ST waveform analysis,

leads to the reduction in the number of operative vaginal deliveries, smaller rate of metabolic acidosis at birth, less blood samples performed during labor, and fetal morbidity reduction.

The standard procedure to record the fHR is the cardiotocography (CTG), sometimes known as electronic fetal monitoring [19]. When necessary to investigate both the instantaneous fHR and the fECG morphology, an invasive fetal monitoring method that uses a wire electrode attached to the fetal scalp [20], after the membrane rupture, is preferred. However, both methods have important drawbacks: (i) the fHR obtained via CTG has the potential problems of reliability and accuracy [21, 22]; in addition, the beat-to-beat variability of fHR is not present in the CTG traces [23, 24]; hence, rapid variations of the fHR cannot be detected; (ii) the second recording technique is invasive [20]; thus, it can put the life of both the mother and the fetus in danger (e.g., possible infections can lead to different complications).

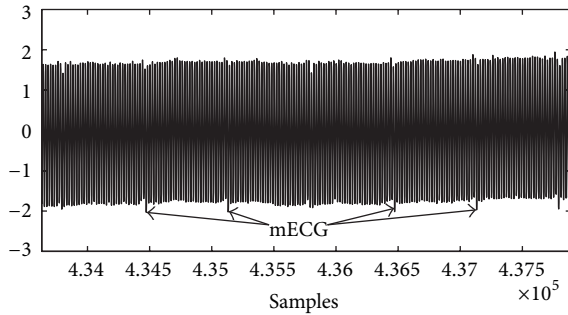


FIGURE 1: Abdominal signal affected by PLI including harmonics.

An alternative method to obtain the instantaneous fHR and the fECG morphology is the abdominal recording of the fECG which considers an array of electrodes placed on the maternal abdomen. This recording procedure overcomes the main drawbacks of the methods used in clinical routine for fetal monitoring. However, the limitation of this technique is the very low signal-to-noise-ratio (SNR) of the available recorded fECG. This is mainly due to the fact that the fECG signal is generated by a small source (fetus heart). In addition, it has to propagate through different attenuating media to reach the maternal belly surface. Hence, the fECG signals contained in abdominal signals (ADSs) provide an amplitude of about $10 \mu\text{V}$ [24] which becomes still smaller around 28th until 32nd weeks of gestational age due to the appearance of the insulating layer called *vernix caseosa*.

Furthermore, the signal of interest, that is, the fECG, is only one (weak) component of the ADS mixture; other (disturbing) signals with higher power that also exist are the electromyogram (EMG) of the abdominal muscles, the electrohysterogram (EHG), the maternal ECG (mECG), the baseline wander basically due to the maternal respiration, and the power line interference (PLI). Among them, the PLI, with the fundamental PLI component of 50 Hz/60 Hz, and its harmonics is one of the most disturbing noise sources, because it can reach amplitudes much greater than the abdominal fECG signal, making its analysis almost impossible (see Figure 1).

The PLI is determined by the power supply network, and its appearance in the abdominal recordings is explained by (i) the electrostatic induction and parasitic capacitance coupling between the body and the ground; and (ii) the electromagnetic induction through loops of the recording cables, where a time-varying magnetic field generates a voltage proportional to the loop area (depending on its orientation) and to the strength of the magnetic field [25]. If the cables are twisted, the induced voltage is reduced [25], but still significant for the fECG analysis.

The fundamental PLI is definitely a problem in fECG analysis, and its harmonics, usually present, make the PLI cancelling problem even more complex. The harmonics are usually generated by connected nonlinear loads: neon lamps, TVs, microwaves ovens, fridges, air conditioning devices, computers, and basically almost any power electronics device connected to a single-phase distribution system. The disturbing sources are in fact the rectifiers and semiconductor

switches present in almost all of these nonlinear loads which introduce distortions in the power supply waveforms [26, 27]. Surprisingly, the 3rd harmonic, that is, 150 Hz/180 Hz, is the most powerful PLI harmonic [28].

Although there are many practical solutions to reduce the PLI, for example, the cable twisting and shielding, the use of differential recording involving an instrumentation amplifier with high common mode rejection ratio (CMRR) at power line frequency, and the proper skin preparation to reduce the electrode imbalance, the PLI still affects the biopotential measurements. For example, the advantage of high CMRR instrumentation amplifiers is limited in real life applications, since a slight imbalance in the electrode-skin impedance leads to the divider effect [25]; thus, the PLI is partly transformed into a differential signal [25, 29, 30] which passes through the amplifier together with the signal of interest, when no notch filter is available in the amplifier circuit to suppress the PLI components. However, the spectrum of the ECG signal for neonates ranges between 0.01 Hz and 250 Hz [31], while the abdominal fECG frequencies are supposed to be up to 500 Hz; thus, such a notch filter affects also the signal of interest. Finally, any PLI disturbance, even if much attenuated, impairs the morphological analysis of the abdominal fECG due to its very low amplitude.

There are many processing methods available in the literature, addressing the PLI suppression in biopotential recordings. The main PLI cancelling techniques are (i) fixed-frequency digital notch filters [32–36], (ii) adaptive filters [37–42], (iii) time-frequency processing of nonstationary signals (wavelet transform) [43–45], (iv) time-frequency nonlinear analysis of nonstationary signals [46–48], (v) Kalman filters [49, 50], (vi) neural networks [51, 52], (vii) blind source separation [53–55], (viii) spectral Hampel filter [56], and (ix) subtraction procedure [57, 58]. These nine categories can be further grouped into nonmodel techniques (a) (iii, iv, vii, and viii) and model based techniques (b) (v, vi, and ix).

From this large variety of PLI suppression methods, six representative approaches are selected in this review study: digital notch filters (DNF), adaptive filters (AF), Hilbert Huang transform (HHT), wavelet transform (WT), blind source separation (BSS), and neural networks (NN); they are briefly described in the following sections which discuss their advantages and disadvantages. A recent and representative algorithm is implemented for each PLI cancelling approach and is evaluated using simulated data. The signal processing method with the best performance in PLI reduction, considering the minimal distortion of the original signal as the evaluation criterion, is identified.

2. Materials and Methods

2.1. PLI Cancellation Using Digital Fixed Notch Filters. Notch filters are used to cancel narrow band interferences, one common application being the PLI suppression in biopotential measurements. Digital fixed notch filters can be designed to remove multiple frequencies, having the advantage of being designed to remove the fundamental frequency and also its harmonics (multiple-notch filters or comb filters [34, 59]).

However, the main problem of multiple-notch filters, when used for cancelling the PLI signal from fECG signals, is the fECG and PLI spectral overlapping. Thus, the notch filter should have a very narrow bandwidth in order to suppress mainly the 50 Hz and its harmonic components, and not the useful information contained in the fECG spectrum. But this requirement comes into conflict with the fact that actually the real PLI signal does not have a fixed fundamental frequency, but rather a frequency that varies around the value of 50 Hz which requires a wide bandwidth of the multiple-notch filter. Moreover, the transient time introduced by the notch filter can be too long, in which case the fECG can be considerably distorted. Hamilton [60] has investigated the effect of the transient time of the notch filters, which increases much when the bandwidth is decreased. They observed the ringing effect appearing near the QRS complex and ST segment when narrow bandwidth notch filters are used. This distortion decreases when the transient time increases [60, 61]. However, in practice, a long transient time reduces the capacity of the filter to track the noise level changes [60]. The latest available international standards for ECG acquisition, American National Standard Association for the Advancement of Medical Instrumentation (AAMI) [62] and International Standard IEC 60601 [63], do not specify any requirements for the transition band of the notch filters. The only specification present in the IEC 60601 standard states that “notch filters for line frequency interference suppression shall not introduce on the ECG record more than 25 μ V peak ringing noise” [63]. Nevertheless, the notch filter should have a short transient time, minimal distortion, and very narrow bandwidth.

Pei and Tseng [64] propose a method to decrease the transient time of multiple IIR notch filters. This technique uses the vector projection in order to find better initial values for the IIR notch filter. A more recent paper [32] reports better results in suppressing the transient time than the ones obtained when applying the method introduced in [64]. Piskorowski proposes a time-variant multiple-notch IIR filter. The transient time is reduced by varying the pole radius with time and thus the filter is able to cancel the fixed frequencies PLI components as fast as possible, with no long-term selectivity impairment [32]. This type of filter should not be confused with adaptive filters, which are varying the notch central frequency, as is explained in the next section.

The *time-varying multiple-notch IIR filter (TVMNF)* proposed in [32] is chosen as representative for this category of power line PLI suppression methods. Thus, the general transfer function of the multiple-notch filter is

$$H(z) = \prod_{i=1}^K \frac{1 - 2 \cos(\Omega_{Ni}) z^{-1} + z^{-2}}{1 - 2r \cos(\Omega_{Ni}) z^{-1} + r^2 z^{-2}} = \frac{B(z)}{B(r^{-1}z)}, \quad (1)$$

$$B(z) = \sum_{i=0}^{2K} b_i z^{-i},$$

where K is the number of notches, Ω_{Ni} is the central frequency of the notch, N is the order of the harmonics, $B(z)$

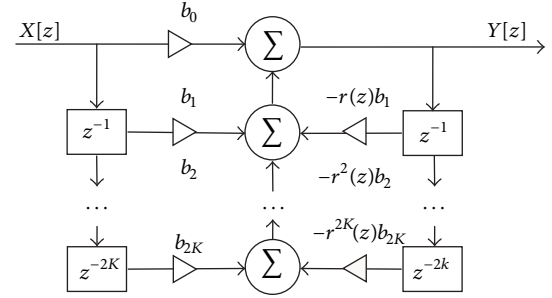


FIGURE 2: The block diagram of the TVMNF.

is a symmetrical polynomial, and r is the pole radius. The selectivity of the filter increases when r is increased, but this results also in a longer transition. Thus, the transition time is influenced by the radius r and in order to improve the time domain filter response, the r is varying in time. The difference equation of the IIR multiple-notch filter with a time-varying parameter r is

$$\begin{aligned}
 y(n) &= b_0 x(n) + b_1 x(n-1) + \dots + b_{2K} x(n-2K) \\
 &\quad - r(n) b_1 y(n-1) - \dots - r^{2K}(n) b_{2K} y(n-2K), \quad (2)
 \end{aligned}$$

where the variation of the pole radius varies is described by [65]

$$r(n) = \bar{r} \left(1 + (d_r - 1) e^{-n/\nu f_s} \right), \quad n \geq 0, \quad (3)$$

with variation range $d_r = r(0)/\bar{r}$ and $\bar{r} = \lim_{n \rightarrow \infty} r(n)$; ν includes the exponential variation of $r(n)$ in (3), and f_s is the sampling frequency [32]. The value chosen for r is critical; a very high value generates narrow notches, but their transition time is increased, while a small r value leads to a decreased transition time, but less selective notches are obtained, which results in filtering out important fECG frequency components. Thus, $r(n)$ has an exponential variation, from an initial value, $r(0)$, to the desired one, \bar{r} [32].

The filter is implemented with one notch frequency and three notch frequencies, respectively, choosing $d_r = 0.9$ and $\nu = 2$, as suggested in [32]. In Figure 2 a block diagram is used to describe the TVMNF algorithm.

2.2. Adaptive Filtering in PLI Cancellation. As previously described, fixed notch filters have the main drawback that the central frequency of the notch cannot be modified. This makes the PLI cancellation difficult when the PLI fundamental frequency has slight variations, which is often the case in real applications. To overcome this problem adaptive filters are introduced, which have the ability to adapt their notch frequency, tracking the changes in the PLI fundamental frequency. The first adaptive filter was introduced by Widrow et al., [41] and according to the review [60], this type of filters introduces less distortion than the fixed notch filters, having also a shorter transition time. The adaptive noise cancellers assume simultaneous recording of the noise source by an

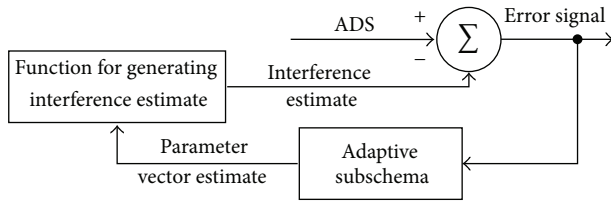


FIGURE 3: The block diagram of the general adaptive interference canceller [40].

additional channel, that is, the reference signal. The reference is supposed to be uncorrelated with the signal of interest, but correlated with the disturbing signal. The filter adapts its parameter in order to make the reference signal as close as possible to the noise that disturbs the signal of interest, by minimizing the output error, considering the least mean square (LMS) criterion.

Many adaptive filters that suppress the PLI in ECG recordings are available in the literature. Wan et al. [67] propose a LMS adaptive algorithm with variable step size and suggest that faster convergence rate and smaller mean square error are obtained, as compared to the traditional approach. Costa and Tavares [68] come with an improvement of the basic adaptive canceller by providing also harmonics' suppression, with a minimal increase in computational complexity. Thus, the algorithm is suitable for low cost acquisition systems. Liangling et al. [42] exploit the capability of the adaptive filters to cancel the PLI component and baseline wander from ECG tracings [67].

However, these adaptive filters have a practical drawback. They all need an additional recording of the disturbing signal, that is, the reference signal. That is not always possible (e.g., in abdominal fECG recording using portable devices). Thus, adaptive filters with no reference signal are more suitable for practical applications. Ziarani and Konrad [69] propose a filter which is able to estimate the amplitude, the phase, and the frequency of the PLI components. An improved version of these adaptive filters is presented by Martens et al. [39] (Improved Adaptive Cancellor—IAC), who developed an algorithm able to suppress both the PLI fundamental frequency and its harmonics. The algorithm considers the fact that large QRS amplitudes can distort the estimation of the PLI components and produce large transient segments and thus the adaptive process is blocked in such situations. The algorithm is compared with the classical adaptive filter and two notch filters with large and narrow bandwidth, respectively. The algorithm proposed by Martens et al. outperforms the other techniques, showing a stable behavior even in the worst conditions. This algorithm is chosen as representative for the adaptive filtering PLI cancellation approach and is implemented in the current study.

In Figure 3 a general scheme of the adaptive notch filter is presented.

2.3. Blind Source Separation Applied in PLI Suppression. This PLI cancelling method is based on a completely different concept than digital filters, considering the statistical properties

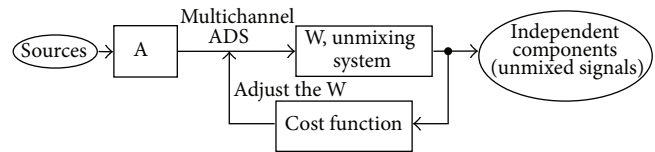


FIGURE 4: The general block diagram of the ICA algorithm.

of a mixture of signals. Each signal source is extracted from the mixture, as long as they satisfy some conditions.

Many approaches to estimate the ICA parameters exist: maximization of nongaussianity [65, 70], maximum likelihood estimation [71, 72], tensorial methods [73], and so forth. Different research groups use ICA algorithms to extract the fECG from abdominal recorded signals: Zarzoso and Nandi 2001 [74], Vrins et al. [75], Sameni et al. [76, 77], Lathauwer et al. [73], Camargo-Olivares et al. [78], Cardoso [79], and so forth. All ICA studies report that the used ICA methods perform reasonably well in extracting the fECG signals from ADS, that is, separating the abdominal fECG from other types of noise signals, including the PLI component, present in the ADSs. It should be noticed that the interpretation of the abdominal fECG obtained via BSS methods does not have a clear physical explanation, since ICA does not take into account the position of the electrodes and other physical parameters.

The algorithm proposed in [65], FastICA, is chosen as representative for this PLI cancelling approach and is considered in the current study. In Figure 4 the general block diagram of the ICA concept is depicted.

2.4. Hilbert Huang Transform Applied in PLI Reduction. The Hilbert Huang Transform (HHT) is a powerful method for analyzing nonlinear and nonstationary time series and it was introduced by Huang et al. [80]. The method overcomes the shortcomings of the Fourier transform which is valid just for stationary time series. It is proven that Fourier transform offers a wrong energy-frequency distribution with no physical meaning when applied on nonstationary time series [80]. Taking into account that most real signals, and especially the biopotentials, are nonstationary, the HHT is suitable for their analysis.

The method has two steps: (i) generation of Intrinsic Mode Functions (IMFs) through Empirical Mode Decomposition (EMD); (ii) Hilbert analysis [80]. IMFs are fully generated from the data set and must satisfy two conditions: (a) the number of zero crossing and the number of extrema have to be equal or to differ at maximum by one; (b) the mean value of the envelope including the local maxima and the envelope defined by the local minima is zero at any point.

The generation of IMFs is fully data driven and is obtained by decomposing the time series (the process is called “sifting”) using the EMD; high frequency components are decomposed into the first IMFs, while the low frequency components are found in the higher order IMFs.

This method is reported to cancel the PLI signal from the ECG [81–83]. The basic idea is to discard the IMFs which contain noise and to reconstruct the signal from the remaining

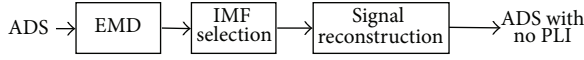


FIGURE 5: The block diagram of the HHT algorithm.

IMFs. The main problem is to identify which IMFs contain just the PLI signal. In conventional EMD the first IMF is considered to be related to the PLI signal since it contains the higher frequency and is therefore discarded, which is not necessarily true, since the sifting process is not perfect, allowing high frequency ECG components in the first IMF. Moreover, if the PLI contains harmonics, then the number of IMFs containing PLI components is higher, since the harmonics are decomposed into different IMFs.

Pal and Mitra [66] propose an algorithm that identifies the IMFs containing the PLI components. It computes the IMFs' cumulative mean and their powers, and using these parameters identifies which IMFs contain PLI components, on a threshold basis. However, the algorithm is not robust when the power of the PLI signal is high as compared to the signal of interest, the fECG. Therefore, the current study improves the original HHT based PLI cancelling method, by a more precise identification of the noise IMFs being obtained. The Hilbert transform is computed for each IMF and the instantaneous frequency is derived thereafter. The IMFs containing the PLI components are then discarded; as already mentioned, these IMFs can still contain information about the high frequency ECG components, that is, the QRS complex. In order to recover the QRS complex, the IMFs with QRS complex are firstly detected, based on the instantaneous frequency, and then the algorithm described by Kabir and Shahnaz [47] is applied as follows:

- (a) the QRS complex boundaries are identified:
 - (a.1) the R peak locations are detected;
 - (a.2) two nearest local minima, located on both sides of R peak are found;
 - (a.3) one zero-crossing point on the left-hand side of its left minimum and the other one on the right-hand side of the right minimum are detected. The boundaries of the QRS complex are assumed to be between these two points;
- (b) a Tukey window centered on the R peaks, which spans to cover the QRS complex, is applied, that is, multiplies the selected IMF. This window offers a flat gain at the R wave and decreases gradually to zero ensuring a smooth transition with minimal distortion. Thus, the information of the QRS complex is preserved, allowing the estimation of the fECG. In Figure 5 the block diagram of the algorithm is depicted.

2.5. PLI Cancellation by Applying Neural Networks. The classical application of NN in cardiac signals processing is the classification of ECG signals, pattern recognition [84, 85], and fECG extraction from ADS [86]. Methods for fECG SNR improvement are described in [87] where a Functional Link Artificial Neural Network (FLANN) is proposed to

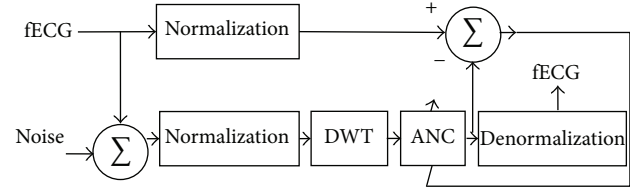


FIGURE 6: The block diagram of the WNN algorithm.

remove the Gaussian and baseline wander noise. Zhang and Benveniste [88] and Pongpon Sri and Yu [89] use NN combined with Wavelet transform for better results. However, in a recent article Pongpon Sri and Yu [51] come with an improvement of the method in [89] and the algorithm is tested also on PLI cancellation (Wavelet Neural Network—WNN). The NN based adaptive filtering approach proposed in [51] for ECG signal noise reduction removes the PLI signal by applying firstly the wavelet decomposition. The wavelet coefficients are further applied to a neural network trained to reconstruct the denoised ECG (see Figure 6). The algorithm was initially developed by the authors to cancel all the noise sources overlapping the ECG signal recorded at 360 Hz (the PLI fundamental frequency is 60 Hz).

The algorithm presented by Suranai et al. is chosen as representative for this category of methods and its steps are as follows:

- (a) A real signal, not affected by the PLI, is applied to a feed-forward NN with 64 inputs, 2 hidden layers, and 1 output corresponding to the denoised ECG signal. The inputs of the NN are obtained by applying the Wavelet Packet Decomposition (WPD) using the Daubechies 4 wavelet; the thresholding (soft threshold) is then applied to reduce the high frequency noise. The resulting 64 wavelet coefficients are the inputs of the NN having 56 hidden neurons on the first hidden layer and 12 neurons on the second one. The hyperbolic tangent activation function is used for all the neurons:

$$f(x) = \frac{1 - e^{-x}}{1 + e^x}. \quad (4)$$

The first 3350 samples of the “clean” selected signal resampled at 300 Hz (record 220 from the Massachusetts Institute of Technology (MIT-BIH) database [90]) are used for this training phase involving the back propagation algorithm (4000, for the raw signal, recorded at 360 Hz). In order to allow the NN to remove the PLI from signals recorded with different amplifier gains, the signals are initially normalized as follows:

$$s_{\text{norm}}(t) = \frac{2}{s_{\text{max}} - s_{\text{min}}} \cdot s(t) - \frac{s_{\text{max}} + s_{\text{min}}}{s_{\text{max}} - s_{\text{min}}}, \quad (5)$$

where s_{max} and s_{min} are the maximum, and, respectively, the minimum values of the signal.

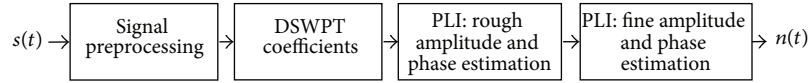


FIGURE 7: The block diagram of the DSWPT algorithm. $d(t)$ is the signal of interest contaminated with the PLI signal, and $n(t)$ represents the estimation of the PLI signal.

The training is then continued for the same segment, affected by the PLI, so that the NN learn to cancel the PLI noise.

- (b) The noisy signals are then applied to the network (i.e., their wavelet coefficients, after thresholding); the denoised signal is considered as the output of the network.

It should be noticed that the algorithm presented above is adapted in this study to remove the PLI signal with the fundamental frequency of 50 Hz and for a sampling frequency of 1000 Hz.

2.6. PLI Reduction by Applying the Wavelet Transform. In the recent years, discrete wavelet transforms and thresholding techniques have been used for ECG denoising [91]. Wavelet based noise cancelling techniques became very popular because they are able to decompose the signal into time-frequency domain which is appropriate for the analysis of nonstationary signals. It is reported in the literature that discrete wavelet transform does not introduce any artificial information to the original signals; the threshold is generated based on the attributes extracted from the signal [92, 93].

The main problem is the identification of the mother wavelet, the level of decomposition, and the optimal threshold. Garg et al. [94] compare different mother wavelet functions for ECG denoising and conclude that the recovery of the ECG with minimal artifacts is obtained when using Sym10 decomposition at level 5 and hard shrinkage function with either rigorous SURE or heuristic SURE threshold [94]. More recently, Galiana-Merino et al. [43] use the discrete stationary wavelet packet transform (DSWPT) to suppress the PLI signal and its harmonics from electromyographic (EMG) signals (the DSPT algorithm). Basically it is a shift invariant transform to isolate the 50 Hz and its harmonics, with the disturbing sine signals being reconstructed thereafter using the DSPT coefficients. In Figure 7 the steps of the DSPT algorithm are described as follows.

- (a) The linear trend is removed from the signal.
- (b) DSPT is applied to the detrended signal using the Meyer wavelet and considering the maximum decomposition level fixed to 3, to allow the identification of 50 Hz and of its harmonics.
- (c) The amplitude and the phase of the sine noise signals are roughly estimated by dividing the DSPT coefficients associated with the disturbing frequencies into segments of 20 samples which are then averaged to obtain templates for the sine wave disturbances. Based on this template some pure sine signals are generated

having the amplitudes equal to the maximum values of the sine templates. The correlation between these pure sine signals and the corresponding templates allow the roughly determination of the phase shift of the PLI.

- (d) The amplitude and the phase of the sine disturbances are further adjusted, for a better estimation of the PLI. Firstly, the best phase shift is computed by varying the phase shifts in the range $[-10, 10]$ samples around the roughly estimated phase shifts. Secondly, the computation of the correlation between the shifted pure sine and the signal is performed. Then, the amplitudes are refined by analyzing the correlation between the signal and the pure sine waves with the amplitudes varying in the range $[0.6, 1.4]$ around the roughly estimated amplitudes. The variation step is equal to 0.01% of the roughly estimated amplitude.
- (e) The refined sine disturbances are subtracted from the signal that has to be denoised.

The main results regarding the performance of the selected algorithms are summarized in Table 1.

2.7. Data Simulation and Performance Measurements. The simulated data, used to quantitatively estimate the performance of the proposed algorithms are generated in two steps. Firstly, the fECG is simulated using the dynamic model introduced in [95, 96]:

$$\begin{aligned} \dot{x} &= \alpha x - \omega y, \\ \dot{y} &= \alpha y - \omega x, \\ \dot{z} &= -\sum_i a_i \Delta \theta_i e^{-(\Delta \theta_i)^2 / 2(b_i)^2}, \end{aligned} \quad (6)$$

where ω is the angular velocity of the time vector as it moves around the limit circle (representing the period T), $\alpha = 1 - \sqrt{x^2 + y^2}$, $\theta = a \tan(y/x)$, $\Delta \theta_i = \theta - \theta_i$, a_i contains the amplitudes of the peaks, b_i contains the width of each peak, and θ_i are the angles which specify the P -, Q -, R -, S -, T -waves/peaks.

Secondly, the PLI components, simulated as sinusoids, are added. Usually the PLI fundamental component is supposed to be constant. However, there are some deviations from the fundamental frequency in real applications, mainly due to unstable power sources. Thus, the PLI components can exhibit significant frequency deviation, up to 3% [30, 97–100] (the deviation differs from country to country, depending on the available power supply technologies).

TABLE 1: Main characteristics and findings for the selected algorithms, representative for the PLI cancelling approaches available in the literature.

Authors/year	Title	Type of publication	Category/acronym of the algorithm	Main results
Piskorowski/2012 [32]	Suppressing harmonic powerline interference using multiple-notch filtering methods with improved transient behavior	Review article	Digital fixed notch filters/TVMNF	A new class of digital parameter varying IIR multiple-notch filters with reduced transient response is introduced. The simulations and the quantitative evaluation on suppressing the 60 Hz PLI show that the concept of the filter with time-varying pole radius may be used to improve the dynamic behavior of multiple-notch filter.
Martens et al./2006 [39]	An improved adaptive power line interference canceller for electrocardiography	Research article	Adaptive filters/IAC	An improved version of the adaptive canceller for the reduction of the PLI components is proposed. The algorithm is able to track the frequencies, the amplitudes, and the phases for PLI deviations up to about 4 Hz; it is also insensitive to baseline wander.
Hyvärinen et al./2001 [65]	Independent component analysis: algorithms and applications	Research article	Blind source separation/FastICA	A new ICA algorithm, based on a fixed-point iteration scheme when finding a maximum of the nongaussianity, is proposed. It has some advantages as compared to other existing ICA methods: it finds directly independent components (ICs), which can be estimated one by one; the algorithm is, in addition, parallelizable, computationally simple, and requires little memory space.
Pal and Mitra/2012 [66]	Empirical mode decomposition based ECG enhancement and QRS detection	Research article	EMD and HHT/HHT	A new algorithm is proposed based on EMD methods. The improved algorithm proposed in this article differs from the similar algorithms in the following: the baseline wander is corrected by selective reconstruction from IMFs, considering the slope minimization technique; the noise is removed by eliminating a noisy set of lower order IMFs, based on their power. A statistical peak correction is also performed since the noise cancellation affects the sharp morphology of the peaks. The results reveal that the proposed algorithm shows good detection sensitivity and specificity.
Poungponsri and Yu/2013 [51]	An adaptive filtering approach for electrocardiogram (ECG) signal noise reduction using neural networks	Research article	Neural networks/WNN	In this article the authors propose an adaptive filtering approach based on discrete wavelet transform and artificial neural network. The obtained results, considering simulated data, show that the algorithm can successfully remove various noise and artifacts, leading to a significant SNR improvement, as compared to other algorithms.
Galiana-Merino et al./2013 [43]	Power line interference filtering on surface electromyography based on the stationary wavelet packet transform	Research article	Wavelet transform/DSWPT	A new method is proposed to estimate and remove PLI components from EMG signals. The method is based on the stationary wavelet packet transform. The quantitative evaluation is performed using synthetic signals, with different SNR values, and the results are compared with the ones obtained when using an adaptive Laguerre filter and other digital filters. In all cases, the proposed algorithm shows an excellent performance, independent of the SNR value.

Three data sets are therefore constructed, considering three PLI scenarios (7): (i) the PLI contains just the fundamental power line interference component, of 50 Hz, (ii) the

PLI includes both the power line fundamental frequency and its 3rd harmonic (150 Hz), and (iii) the PLI is a sinusoid whose frequency slightly varies in time around 50 Hz. Consider

$$\begin{aligned} \text{PLI}(t) &= \begin{cases} A_1 \cdot \sin(2\pi f_1 \cdot t), & f_1 = 50 \text{ Hz, ideal case} \\ A_1 \cdot \sin(2\pi f_1 t) + A_3 \cdot \sin(2\pi f_3 \cdot t), & f_1 = 50 \text{ Hz, } f_3 = 150 \text{ Hz, } A_3 = kA_1, \\ A_1 \cdot \sin(2\pi f_1(t) \cdot t), & f_1(t) = 50 \text{ Hz} \pm \text{rand}(t), f_1(t) \text{ exhibits stepwise changes,} \end{cases} \end{aligned} \quad (7)$$

where $k = 20\%$.

It is clear that the worst scenario is the third one, assuming that the power line fundamental frequency is time-varying.

For each scenario, the SNR defined by (8) is varied; five noise levels are considered: -2 dB, 0 dB, 2 dB, 4 dB, and 5 dB:

$$\text{SNR} = 10 \log_{10} \left(\frac{P_{\text{fECG}}}{P_{\text{PLI}}} \right) = 10 \log_{10} \left(\frac{\sum_{i=1}^n \text{fECG}(i)}{\sum_{i=1}^n \text{PLI}(i)} \right). \quad (8)$$

For the qualitative evaluation of the implemented algorithms, the following performance indices are considered as follows.

- (a) Normalized root mean square error, expressed in percentage:

$$\text{RMSD} = \sqrt{\frac{\sum_{i=1}^N (\text{orig_fECG}(i) - \text{est_fECG}(i))^2}{\sum_{i=1}^N \text{orig_fECG}(i)^2}} * 100. \quad (9)$$

- (b) Noise retention, expressed in percentage:

$$\text{NR} = \frac{P_{\text{orig_fECG}} - P_{\text{est_fECG}}}{P_{\text{orig_fECG}}} * 100, \quad (10)$$

where P is the power of the signal computed with

$$P_{\text{orig_fECG}} = 10 * \log_{10} \sum_{i=1}^N \text{orig_fECG}(i)^2. \quad (11)$$

- (c) SNR improvement [47]:

$$\begin{aligned} \text{SNR}_{\text{imp}} &= 10 * \log_{10} \left\{ \frac{\sum_{i=1}^N [\text{signal}(i) - \text{orig_fECG}(i)]^2}{\sum_{i=1}^N [\text{est_fECG}(i) - \text{orig_fECG}(i)]^2} \right\}, \end{aligned} \quad (12)$$

where signal is the input signal containing both the fECG and the PLI.

- (d) Cross-correlation coefficient, considering the original and the denoised fECG signal:

$$p = \frac{\sum_{i=1}^N (\text{est_fECG}(i) * \text{orig_fECG}(i))}{\sqrt{\sum_{i=1}^N \text{est_fECG}(i)^2 * \sum_{i=1}^N \text{orig_fECG}(i)^2}}. \quad (13)$$

3. Results

The results obtained when applying the five selected algorithms are organized as follows. (i) For each performance index a table is constructed. The columns correspond to the evaluated algorithms and the rows to the scenarios, assuming that the SNR is -2 , 0 , 2 , 4 , and 5 dB. The best result obtained for the performance index is emphasized in bold for each case and for each scenario. The scenarios for which some algorithms are not working by principle are represented by empty gray cells. (ii) The performance indices for scenario 2, when the SNR is -2 dB, are illustrated for each algorithm (see Figures 8, 9, 10, and 11). The second scenario is chosen instead of the worst case scenario (scenario 3) because two algorithms are not working by principle in this case. Furthermore, if the algorithms with worst performance have the performance indices very far from the other values (i.e., are outliers), they are excluded from the graphical representation, in order to offer a meaningful comparison of the algorithms. (iii) The results obtained for the selected BSS method (FastICA) are considered apart from the others, because this method has a totally different working principle, assuming that more recorded channels are available. Thus, for each scenario, the FastICA algorithm is evaluated by considering that the available ICA inputs are the five simulated signals, with different SNRs.

4. Discussion

In Tables 2, 3, 4, and 5, it can be observed that the worst overall performance is obtained when the WNN is applied. The algorithm is able to reduce the noise if its level is very low, but the QRS complex, containing high frequencies, is disturbed, impairing the fECG morphology analysis. When the signal is hidden by the noise, that is, low level of SNR, the method fails to extract the denoised signal, which can be explained by the thresholding step. The main advantage of the algorithm is the computation time of the testing (denoising) phase, assuming that the neural network is already trained. Because of the overall bad performance the algorithm is excluded from the following discussion.

The TVMNF method proposed by [32] shows good results for scenarios 1 and 2 having a RMSD of 2.11%, Figure 8, and a SNR improvement, $\text{SRN}_{\text{imp}} = 76$ dB for the scenario 2 (see Figure 11), $\text{SNR} = -2$ dB (worst scenario). No ringing effect is observed near the QRS complexes. However, despite

TABLE 2: The RMSD (%) obtained for each algorithm and for each data set.

Data set	SNR (dB)	Algorithm					
		TVMNF	HHT	DSWPT	WNN	IAC	FastICA
1	-2	2.003515	0.292652	0.195444	77.31631	1.77611	0,073811
	0	2.003515	1.740565	0.018847	70.02215	0.667624	
	2	2.003515	1.197345	0.001283	33.19379	0.666902	
	4	2.003515	1.624253	0.000778	5.631514	0.666882	
	5	2.003515	2.09266	0.000883	3.244183	0.666879	
2	-2	2.112907	0.292852	0.60503	72.03313	3.822223	0,001657
	0	2.112907	1.743529	0.059846	68.07016	0.669611	
	2	2.112907	1.205285	0.005355	33.1956	0.666898	
	4	2.112907	1.603147	0.000589	5.626975	0.666882	
	5	2.112907	2.109169	0.00079	3.230891	0.666879	
3	-2		38.81253		64.46775	655.1273	1,269908
	0		1.884043		49.6627	396.5219	
	2		1.185072		47.70798	394.4479	
	4		1.62743		38.65239	393.3756	
	5		1.221664		43.60649	393.305	

TABLE 3: The NR (%) obtained for each algorithm and for each data set.

Data set	SNR (dB)	Algorithm					
		TVMNF	HHT	DSWPT	WNN	IAC	FastICA
1	-2	0.03426	0.038749	0.023308	6.295244	1.628744	0,010982
	0	0.03426	1.022943	0.000225	4.176215	1.705774	
	2	0.03426	0.333364	6.54E - 06	10.28646	1.711423	
	4	0.03426	0.033125	8.93E - 06	3.873963	1.711467	
	5	0.03426	0.435546	8.96E - 06	2.62773	1.711466	
2	-2	0.098402	0.038435	0.040232	4.781289	1.577947	0,000112
	0	0.098402	1.006355	0.000395	3.559141	1.699513	
	2	0.098402	0.338354	4.81E - 06	10.28173	1.71136	
	4	0.098402	0.032068	8.91E - 06	3.874016	1.711466	
	5	0.098402	0.529579	8.95E - 06	2.628339	1.711466	
3	-2		38.94626		3.701535	95.16797	0,024024
	0		0.926928		0.853499	42.01306	
	2		0.320873		1.394364	38.06225	
	4		0.032029		7.147367	37.07462	
	5		0.228292		5.364868	37.0534	

TABLE 4: The SRN_{imp} obtained for each algorithm and for each data set.

Data set	SNR (dB)	Algorithm					
		TVMNF	HHT	DSWPT	WNN	IAC	FastICA
1	-2	66.88941	83.59046	87.09688	0.995959	67.90879	89,90204
	0	46.88941	48.10367	87.41253	0.457028	56.40755	
	2	26.88941	31.35309	90.75301	-0.97771	36.41695	
	4	6.889411	8.704401	75.09279	-2.46131	16.41721	
	5	-3.11059	-3.4965	63.99507	-7.4033	6.417252	
2	-2	76.16926	93.32959	87.0233	7.64809	70.99347	132,618
	0	56.16926	57.83398	87.11819	7.199378	66.12334	
	2	36.16926	41.04077	88.08339	7.304312	46.15861	
	4	16.16926	18.5631	87.25321	7.064304	26.15881	
	5	6.169261	6.180338	74.70329	2.304354	16.15886	
3	-2		41.20189		2.384226	16.90442	65,2529
	0		47.44316		3.811226	4.910191	
	2		31.48669		5.564842	0.575438	
	4		8.713179		7.955288	0.242613	
	5		1.236451		7.002494	0.220137	

TABLE 5: Cross-correlation coefficient, p , obtained for each algorithm and for each data set.

Data set	SNR (dB)	Algorithm					
		TVMNF	HHT	DSWPT	WNN	IAC	FastICA
1	-2	0.997565	0.999947	0.999343	0.000708	0.607869	
	0	0.997565	0.994679	0.999996	0.002489	0.992365	
	2	0.997565	0.99794	1	0.348027	0.987873	0,999997
	4	0.997565	0.996368	1	0.976249	0.999875	
	5	0.997565	0.990019	1	0.987159	0.999987	
2	-2	0.997018	0.999947	0.998855	0.000667	0.464252	
	0	0.997018	0.992789	0.999991	0.002342	0.984898	
	2	0.997018	0.997911	1	0.347902	0.999995	1
	4	0.997018	0.996415	1	0.976263	0.999999	
	5	0.997018	0.989539	1	0.987179	1	
3	-2		0.313497		-0.00072	0.00938	
	0		0.992068		-0.00131	0.073122	
	2		0.997936		0.005998	0.187229	0,999191
	4		0.996377		0.004007	0.205138	
	5		0.997482		0.010274	0.237579	

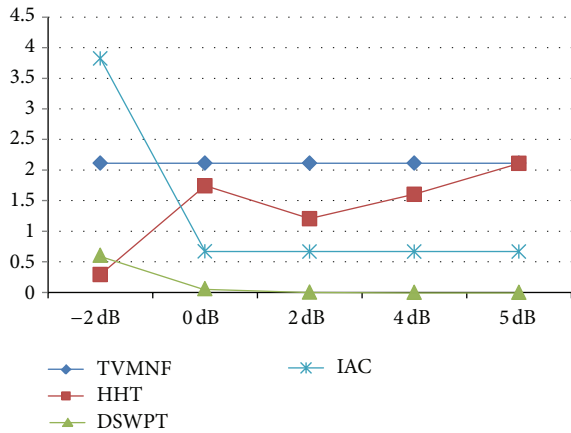


FIGURE 8: The RMSD (%) for scenario 2 (WNN is excluded).

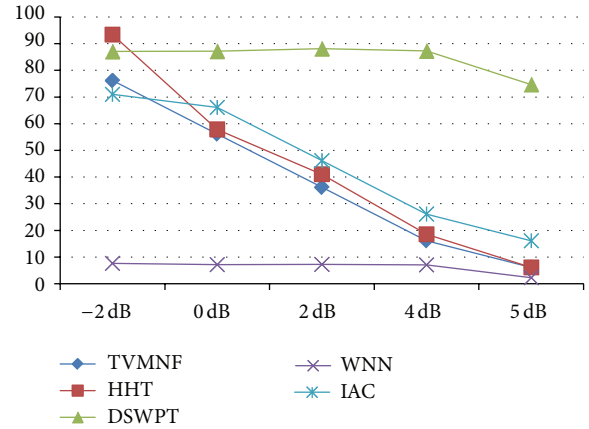


FIGURE 10: The SRN_{imp} for scenario 2.

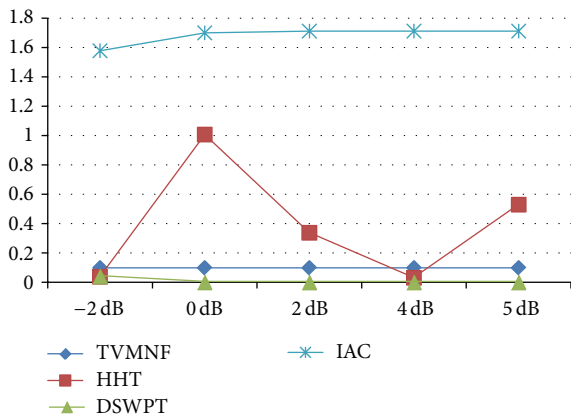


FIGURE 9: The NR (%) for scenario 2 (WNN is excluded).

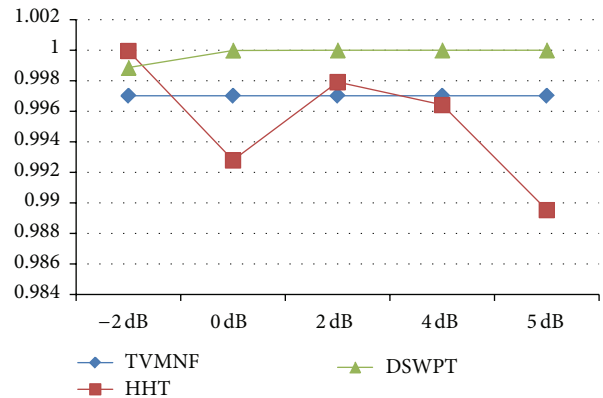


FIGURE 11: The cross-correlation coefficient for scenario 2 (WNN and IAC are excluded).

the good results, the main drawback is that the filter cannot be applied when the fundamental frequency is varying, as expected in real applications. Thus, this type of filter is of limited usage.

As expected, the adaptive methods are able to follow the changes in the frequencies of the PLI components; hence, they can be successfully applied in scenario 3. According to the computed performance indices, the IAC is able to obtain good estimates of the fECG signal when the fundamental frequency is fixed, even when the harmonics are present. However, for the worst SNR, that is, -2 dB, the obtained performance is slightly worse as compared to the performance of the other algorithms (see Figures 8–11). For scenario 3 the algorithm has the worst performance (RMSD = 655% and a noise retention factor of NR = 95%). This is due to the fact that the algorithm needs very long adaptation time (approximately 10 s) when step variations in the PLI fundamental frequency appear. Thus, IAC is of limited use in real applications.

The HHT method implemented in this study shows also good results. However, at small SNR values, small oscillations appear near the QRS complex, suggesting that some very low PLI components can be found in the low order IMFs. Moreover, when the method is applied in scenario 3, outliers appear when the PLI fundamental frequency is changing. The main advantage of this method is that it is suitable for nonstationary signals like the biopotentials and that it is fully data driven; that is, no *a priori* knowledge is necessary. The main disadvantage is that the decomposition does not fully separate the oscillations; thus, some useful information can be found in the IMFs containing the PLI components; in addition, it does not have, by now, a complete mathematical evaluation. However, recent papers present some improvements to the basic method claiming a better decomposition (e.g., Ensemble Empirical Mode Decomposition (EEMD) [101] and Complete Ensemble Empirical Mode Decomposition [102]).

The BSS algorithm is able to separate the fECG from the PLI showing the same performance no matter how the SNR is varying, because by principle it exploits the independence between any two signal sources. However, it should be noted that the comparison with the other method is not quite fair in the current study; in order to have the same simulations, the same signals used for the other algorithms were fed to the FastICA. In real application, the input of ICA algorithm is signals obtained from different channels, meaning different fECG waveforms, which can lower the performance of ICA in fECG extraction. Moreover, the physical relevance of the fECG independent components obtained when applying ICA is still a subject of discussion among researchers. Thus, the method has limited usage in real application, but it can be successfully combined with the adaptive filtering techniques, improving the estimation provided by the PLI reference block.

As theoretically expected, the best performance is obtained when using the DSWPT, if the PLI is stationary and includes exactly the 50 Hz and its harmonics. However, the method does not work in the worst scenario. Since the algorithm estimates the PLI interference assuming that the power line frequency is 50 Hz (in step 2, templates of the sine disturbances are constructed, averaging the segmented signal, using

a window of 20 samples), it is expected that the algorithms fail in cancelling the PLI when the frequency is more or less different from 50 Hz, or even worse, when the power line frequency is varying, which is supported by the obtained results.

5. Conclusions

In this paper a review of PLI cancelling methods applied in fECG signal processing is proposed, revealing the main concepts provided in the literature for suppressing the 50 Hz/60 Hz component and its harmonics from biosignals. The selected algorithms are quantitatively analyzed, using different performance criteria and practical considerations are provided when discussing the PLI cancelling from abdominal fECGs. Three sets of simulated data are constructed and used in the quantitative evaluation of the algorithms, considering the 50 Hz PLI fundamental frequency, the 50 Hz combined with the 150 Hz PLI component, and a varying PLI fundamental frequency. The quantitative performance is monitored using five different indices, corresponding to different SNRs.

While some methods, like WNN, show very bad performances, most of the algorithms have good results, especially in scenarios 1 and 2. The DSWPT has the best performance in scenarios 1 and 2, as depicted in the Figures 8–11, but its main drawback is that it is not suitable for the most realistic scenario, scenario 3. The HHT based algorithm shows the best performance overall, considering the implemented scenarios. Thus, further studies should concentrate on exploiting the capabilities of the HHT method.

Conflict of Interests

The authors declare that there is no conflict of interests in the publication of the paper.

Authors' Contribution

Dragoş-Daniel Țarălungă and Georgeta-Mihaela Ungureanu contributed equally to the paper and, therefore, both are considered as first authors.

References

- [1] J. R. Woods, "Case #680 Topic: Fetal Heart Rate Monitoring," 2013, http://www.perifacts.eu/cases/Case_680.Fetal_Heart_Rate_Interpretation.php.
- [2] K. Hinshaw and A. Ullal, "Peripartum and intrapartum assessment of the fetus," *Anaesthesia and Intensive Care Medicine*, vol. 8, no. 8, pp. 331–336, 2007.
- [3] M. G. Ross, L. D. Devoe, and K. G. Rosen, "ST-segment analysis of the fetal electrocardiogram improve fetal heart rate tracing interpretation and clinical decision making," *Journal of Maternal-Fetal and Neonatal Medicine*, vol. 15, no. 3, pp. 181–185, 2004.
- [4] J. Westgate, M. Harris, J. S. H. Curnow, and K. R. Greene, "Plymouth randomized trial of cardiotocogram only versus ST waveform plus cardiotocogram for intrapartum monitoring in 2400 cases," *American Journal of Obstetrics and Gynecology*, vol. 169, no. 5, pp. 1151–1160, 1993.

- [5] I. Amer-Wählin, C. Hellsten, H. Norén et al., “Cardiotocography only versus cardiotocography plus ST analysis of fetal electrocardiogram for intrapartum fetal monitoring: A Swedish randomised controlled trial,” *Lancet*, vol. 358, no. 9281, pp. 534–538, 2001.
- [6] K. Ojala, M. Väärasmäki, K. Mäkikallio, M. Valkama, and A. Tekay, “A comparison of intrapartum automated fetal electrocardiography and conventional cardiotocography—A Randomised Controlled Study,” *International Journal of Obstetrics and Gynaecology*, vol. 113, no. 4, pp. 419–423, 2006.
- [7] C. Vayssiere, E. David, N. Meyer et al., “A French randomized controlled trial of ST segment analysis in a population with abnormal cardiotocograms during labor,” *American Journal of Obstetrics & Gynecology*, vol. 197, pp. 299.e1–299.e6, 2007.
- [8] M. E. Westerhuis, G. H. Visser, K. G. Moons et al., “Cardiotocography plus ST analysis of fetal electrocardiogram compared with cardiotocography only for intrapartum monitoring: a randomized controlled trial,” *Obstetrics & Gynecology*, vol. 115, pp. 1173–1180, 2010.
- [9] H. Norén, S. Blad, A. Carlsson et al., “STAN in clinical practice—The outcome of 2 years of regular use in the city of Gothenburg,” *American Journal of Obstetrics and Gynecology*, vol. 195, no. 1, pp. 7–15, 2006.
- [10] H. Norén, A. K. Luttkus, J. H. Stupin et al., “Fetal scalp pH and ST analysis of the fetal ECG as an adjunct to cardiotocography to predict fetal acidosis in labor: A multi-center, case controlled study,” *Journal of Perinatal Medicine*, vol. 35, no. 5, pp. 408–414, 2007.
- [11] M. Massoud, A. Giannesi, N. Amabile, M. Manevy, G. Geron, and P. Gaucherand, “Fetal electrocardiography in labor and neonatal outcome: An observational study in 1889 patients in the French center of Edouard Herriot, Lyon,” *Journal of Maternal-Fetal and Neonatal Medicine*, vol. 20, no. 11, pp. 819–824, 2007.
- [12] N. S. Palmgren Colov, “Need for extensive education when implementing new foetal monitoring technology,” *Ugeskrift for Laeger*, vol. 169, no. 39, pp. 3294–3297, 2007.
- [13] M. Melin, A. Bonnevier, M. Cardell, L. Hogan, and A. Herbst, “Changes in the ST-interval segment of the fetal electrocardiogram in relation to acid-base status at birth,” *International Journal of Obstetrics and Gynaecology*, vol. 115, no. 13, pp. 1669–1675, 2008.
- [14] A.-K. Welin, H. Norén, A. Odeback, M. Andersson, G. Andersson, and K. G. Rosén, “STAN, a clinical audit: The outcome of 2 years of regular use in the city of Varberg, Sweden,” *Acta Obstetrica et Gynecologica Scandinavica*, vol. 86, no. 7, pp. 827–832, 2007.
- [15] A. Kale, Y.-S. Chong, and A. Biswas, “Effect of availability of fetal ECG monitoring on operative deliveries,” *Acta Obstetrica et Gynecologica Scandinavica*, vol. 87, no. 11, pp. 1189–1193, 2008.
- [16] H. Norén and A. Carlsson, “Reduced prevalence of metabolic acidosis at birth: an analysis of established STAN usage in the total population of deliveries in a Swedish district hospital,” *American Journal of Obstetrics and Gynecology*, vol. 202, no. 6, pp. 546.e1–546.e7, 2010.
- [17] R. Rzepka, A. Torbé, S. Kwiatkowski, W. Blogowski, and R. Czajka, “Clinical outcomes of high-risk labours monitored using fetal electrocardiography,” *Annals of the Academy of Medicine Singapore*, vol. 39, no. 1, pp. 27–32, 2010.
- [18] K. Ragupathy, F. Ismail, and A. E. Nicoll, “The use of STAN monitoring in the labour ward,” *Journal of Obstetrics and Gynaecology*, vol. 30, no. 5, pp. 465–469, 2010.
- [19] M. G. Signorini, G. Magenes, S. Cerutti, and D. Arduini, “Linear and nonlinear parameters for the analysis of fetal heart rate signal from cardiotocographic recordings,” *IEEE Transactions on Biomedical Engineering*, vol. 50, no. 3, pp. 365–374, 2003.
- [20] J. P. Neilson, “Fetal electrocardiogram (ECG) for fetal monitoring during labour,” *Cochrane Database of Systematic Reviews*, no. 4, Article ID CD000116, 2012.
- [21] W. R. Cohen, S. Ommani, S. Hassan et al., “Accuracy and reliability of fetal heart rate monitoring using maternal abdominal surface electrodes,” *Acta Obstetrica et Gynecologica Scandinavica*, vol. 91, no. 11, pp. 1306–1313, 2012.
- [22] J. Jezewski, J. Wrobel, and K. Horoba, “Comparison of Doppler ultrasound and direct electrocardiography acquisition techniques for quantification of fetal heart rate variability,” *IEEE Transactions on Biomedical Engineering*, vol. 53, no. 5, pp. 855–864, 2006.
- [23] M. A. Hasan, M. B. I. Reaz, M. I. Ibrahimy, M. S. Hussain, and J. Uddin, “Detection and processing techniques of FECG signal for fetal monitoring,” *Biological Procedures Online*, vol. 11, no. 1, pp. 263–295, 2009.
- [24] M. Peters, J. Crowe, J.-F. Piéri et al., “Monitoring the fetal heart non-invasively: a review of methods,” *Journal of Perinatal Medicine*, vol. 29, no. 5, pp. 408–416, 2001.
- [25] J. C. Huhta and J. G. Webster, “60-Hz interference in electrocardiography,” *IEEE Transactions on Biomedical Engineering*, vol. 20, no. 2, pp. 91–101, 1973.
- [26] M. E. Villablanca, “Harmonic-free line-commutated ac/dc rectifiers,” *Electric Power Systems Research*, vol. 79, no. 11, pp. 1531–1537, 2009.
- [27] S. K. Jain and S. N. Singh, “Harmonics estimation in emerging power system: key issues and challenges,” *Electric Power Systems Research*, vol. 81, no. 9, pp. 1754–1766, 2011.
- [28] K. Wada and T. Shimizu, “Mitigation method of 3rd-harmonic voltage for a three-phase four-wire distribution system based on a series active filter for the neutral conductor,” in *Proceedings of the 37th IAS Annual Meeting and World Conference on Industrial Applications of Electrical Energy*, vol. 1, pp. 64–69, October 2002.
- [29] A. C. Metting van Rijn, A. Peper, and C. A. Grimbergen, “High-quality recording of bioelectric events. Part 1. Interference reduction, theory and practice,” *Medical and Biological Engineering and Computing*, vol. 28, no. 5, pp. 389–397, 1990.
- [30] C. Levkov, G. Mihov, R. Ivanov, I. Daskalov, I. Christov, and I. Dotsinsky, “Removal of power-line interference from the ECG: a review of the subtraction procedure,” *BioMedical Engineering Online*, vol. 4, article 50, 2005.
- [31] P. Kligfield, L. S. Gettes, J. J. Bailey et al., “Recommendations for the Standardization and Interpretation of the Electrocardiogram: Part I: The Electrocardiogram and Its Technology A Scientific Statement From the American Heart Association Electrocardiography and Arrhythmias Committee, Council on Clinical Cardiology; the American College of Cardiology Foundation; and the Heart Rhythm Society Endorsed by the International Society for Computerized Electrocardiology,” *Journal of the American College of Cardiology*, vol. 49, no. 10, pp. 1109–1127, 2007.
- [32] J. Piskorski, “Suppressing harmonic powerline interference using multiple-notch filtering methods with improved transient behavior,” *Measurement*, vol. 45, no. 6, pp. 1350–1361, 2012.
- [33] Y. V. Joshi and S. C. Dutta Roy, “Design of IIR multiple notch filters,” *International Journal of Circuit Theory and Applications*, vol. 26, no. 5, pp. 499–507, 1998.

- [34] R. Deshpande, B. Kumar, and S. B. Jain, "On the design of multi notch filters," *International Journal of Circuit Theory and Applications*, vol. 40, no. 4, pp. 313–327, 2012.
- [35] R. Deshpande, B. Kumar, and S. B. Jain, "Highly narrow rejection bandwidth finite impulse response notch filters for communication," *IET Communications*, vol. 4, no. 18, pp. 2208–2216, 2010.
- [36] J. Piskorowski, "Digital Q-varying notch IIR filter with transient suppression," *IEEE Transactions on Instrumentation and Measurement*, vol. 59, no. 4, pp. 866–872, 2010.
- [37] I. S. Badreldin, D. S. El-Kholy, and A. A. El-Wakil, "A modified adaptive noise canceler for electrocardiography with no power-line reference," in *Proceedings of the 5th Cairo International Biomedical Engineering Conference (CIBEC '10)*, pp. 13–16, December 2010.
- [38] I. S. Badreldin, D. S. El-Kholy, and A. A. Elwakil, "Harmonic adaptive noise canceler for electrocardiography with no power-line reference," in *Proceedings of the 16th IEEE Mediterranean Electrotechnical Conference (MELECON '12)*, pp. 1017–1020, March 2012.
- [39] S. M. M. Martens, M. Mischi, S. G. Oei, and J. W. M. Bergmans, "An improved adaptive power line interference canceller for electrocardiography," *IEEE Transactions on Biomedical Engineering*, vol. 53, no. 11, pp. 2220–2231, 2006.
- [40] M. Maniruzzaman, K. M. S. Billah, U. Biswas, and B. Gain, "Least-Mean-Square algorithm based adaptive filters for removing power line interference from ECG signal," in *Proceedings of the International Conference on Informatics, Electronics & Vision (ICIEV '12)*, pp. 737–740, May 2012.
- [41] B. Widrow, J. R. Glover Jr., and J. M. McCool, "Adaptive noise cancelling: principles and applications," *Proceedings of the IEEE*, vol. 63, no. 12, pp. 1692–1716, 1975.
- [42] G. Liangling, Z. Nanquan, and W. Haotian, "Application of interference canceller in bioelectricity signal disposing," *Procedia Environmental Sciences*, vol. 10, part A, pp. 814–819, 2011.
- [43] J. J. Galiana-Merino, D. Ruiz-Fernandez, and J. J. Martinez-Espla, "Power line interference filtering on surface electromyography based on the stationary wavelet packet transform," *Computer Methods and Programs in Biomedicine*, vol. 111, no. 2, pp. 338–346, 2013.
- [44] P. Karthikeyan, M. Murugappan, and S. Yaacob, "ECG signal denoising using wavelet thresholding techniques in Human Stress Assessment," *International Journal on Electrical Engineering and Informatics*, vol. 4, no. 2, 2012.
- [45] M. Alfaouri and K. Daqrouq, "ECG signal denoising by wavelet transform thresholding," *American Journal of Applied Sciences*, vol. 5, no. 3, pp. 276–281, 2008.
- [46] S. Pal and M. Mitra, "Empirical mode decomposition based ECG enhancement and QRS detection," *Computers in Biology and Medicine*, vol. 42, no. 1, pp. 83–92, 2012.
- [47] M. A. Kabir and C. Shahnaz, "Denoising of ECG signals based on noise reduction algorithms in EMD and wavelet domains," *Biomedical Signal Processing and Control*, vol. 7, no. 5, pp. 481–489, 2012.
- [48] J. Artūras, M. Vaidotas, and L. Arūnas, "Ensemble empirical mode decomposition based feature enhancement of cardio signals," *Medical Engineering & Physics*, vol. 35, no. 8, pp. 1059–1069, 2012.
- [49] G. Li, X. Zeng, X. Zhou, Y. Zhou, G. Liu, and X. Zhou, "Robust suppression of nonstationary power-line interference in electrocardiogram signals," *Physiological Measurement*, vol. 33, no. 7, pp. 1151–1169, 2012.
- [50] H. Hajimolahoseini, M. R. Taban, and H. Soltanian-Zadeh, "Extended Kalman Filter frequency tracker for nonstationary harmonic signals," *Measurement*, vol. 45, no. 1, pp. 126–132, 2012.
- [51] S. Pongpornsri and X.-H. Yu, "An adaptive filtering approach for electrocardiogram (ECG) signal noise reduction using neural networks," *Neurocomputing*, vol. 117, pp. 206–213, 2013.
- [52] J. Mateo, C. Sánchez, A. Torres, R. Cervigon, and J. J. Rieta, "Neural network based canceller for powerline interference in ECG signals," in *Proceedings of the Annual International Conference on Computers in Cardiology (CAR '08)*, pp. 1073–1076, September 2008.
- [53] Y.-D. Lin, C.-Y. Hsu, H.-Y. Chen, and K.-K. Tseng, "Efficient block-wise independent component analysis with optimal learning rate," *Neurocomputing*, vol. 117, pp. 22–32, 2013.
- [54] M. P. S. Chawla, "PCA and ICA processing methods for removal of artifacts and noise in electrocardiograms: a survey and comparison," *Applied Soft Computing Journal*, vol. 11, no. 2, pp. 2216–2226, 2011.
- [55] A. Hyvärinen, "Fast and robust fixed-point algorithms for independent component analysis," *IEEE Transactions on Neural Networks*, vol. 10, no. 3, pp. 626–634, 1999.
- [56] D. P. Allen, "A frequency domain Hampel filter for blind rejection of sinusoidal interference from electromyograms," *Journal of Neuroscience Methods*, vol. 177, no. 2, pp. 303–310, 2009.
- [57] C. Levkov, G. Mihov, R. Ivanov, I. Daskalov, I. Christov, and I. Dotsinsky, "Removal of power-line interference from the ECG: a review of the subtraction procedure," *BioMedical Engineering Online*, vol. 4, article 50, 2005.
- [58] G. Mihov, I. Dotsinsky, and T. Georgieva, "Subtraction procedure for powerline interference removing from ECG: improvement for non-multiple sampling," *Journal of Medical Engineering and Technology*, vol. 29, no. 5, pp. 238–243, 2005.
- [59] Y. V. Joshi and S. C. Dutta Roy, "Design of IIR multiple notch filters," *International Journal of Circuit Theory and Applications*, vol. 26, no. 5, pp. 499–507, 1998.
- [60] P. S. Hamilton, "A comparison of adaptive and nonadaptive filters for reduction of power line interference in the ECG," *IEEE Transactions on Biomedical Engineering*, vol. 43, no. 1, pp. 105–109, 1996.
- [61] S. Luo and P. Johnston, "A review of electrocardiogram filtering," *Journal of Electrocardiology*, vol. 43, no. 6, pp. 486–496, 2010.
- [62] American National Standard ANSI/AAMI EC11, *Diagnostic Electrocardiographic Devices*, Association for the Advancement of Medical Instrumentation, Arlington, Va, USA, 2007.
- [63] International Standard IEC 60601-1, *Medical Electrical Equipment—Part 1: General Requirements for Basic Safety and Essential Performance*, 2005.
- [64] S.-C. Pei and C.-C. Tseng, "Elimination of AC interference in electrocardiogram using IIR notch filter with transient suppression," *IEEE Transactions on Biomedical Engineering*, vol. 42, no. 11, pp. 1128–1132, 1995.
- [65] A. Hyvärinen, J. Karhunen, and E. Oja, *Independent Component Analysis*, John Wiley & Sons, 2001.
- [66] S. Pal and M. Mitra, "Empirical mode decomposition based ECG enhancement and QRS detection," *Computers in Biology and Medicine*, vol. 42, no. 1, pp. 83–92, 2012.
- [67] H. Wan, R. Fu, and L. Shi, "The Elimination of 50 Hz power line interference from ECG using a variable step size LMS adaptive filtering algorithm," *Life Science Journal*, vol. 3, no. 4, 2006.

- [68] M. H. Costa and M. C. Tavares, "Removing harmonic power line interference from biopotential signals in low cost acquisition systems," *Computers in Biology and Medicine*, vol. 39, no. 6, pp. 519–526, 2009.
- [69] A. K. Ziarani and A. Konrad, "A nonlinear adaptive method of elimination of power line interference in ECG signals," *IEEE Transactions on Biomedical Engineering*, vol. 49, no. 6, pp. 540–547, 2002.
- [70] A. Hyvärinen and E. Oja, "A fast fixed-point algorithm for independent component analysis," *Neural Computation*, vol. 9, no. 7, pp. 1483–1492, 1997.
- [71] J.-F. Cardoso, "Infomax and maximum likelihood for blind source separation," *IEEE Signal Processing Letters*, vol. 4, no. 4, pp. 112–114, 1997.
- [72] B. A. Pearlmutter and L. C. Parra, "Maximum likelihood blind source separation: a context-sensitive generalization of ICA," *Advances in Neural Information Processing Systems*, vol. 9, pp. 613–619, 1997.
- [73] L. De Lathauwer, B. De Moor, and J. Vandewalle, "Fetal electrocardiogram extraction by blind source subspace separation," *IEEE Transactions on Biomedical Engineering*, vol. 47, no. 5, pp. 567–572, 2000.
- [74] V. Zarzoso and A. K. Nandi, "Noninvasive fetal electrocardiogram extraction: blind separation versus adaptive noise cancellation," *IEEE Transactions on Biomedical Engineering*, vol. 48, no. 1, pp. 12–18, 2001.
- [75] F. Vrins, C. Jutten, and M. Verleysen, "Sensor array and electrode selection for non-invasive fetal electrocardiogram extraction by independent component analysis," in *Independent Component Analysis and Blind Signal Separation*, vol. 3195 of *Lecture Notes in Computer Science*, pp. 1017–1024, 2004.
- [76] R. Sameni, *Extraction of fetal cardiac signals from an array of maternal abdominal recordings [Ph.D. dissertation]*, Sharif University of Technology—Institut National Polytechnique de Grenoble, July 2008.
- [77] R. Sameni and G. D. Clifford, "A review of fetal ECG signal processing, No.s and promising directions," *The Open Pacing, Electrophysiology & Therapy Journal*, vol. 3, pp. 4–20, 2010.
- [78] J. L. Camargo-Olivares, R. Martín-Clemente, S. Hornillo-Mellado, M. M. Elena, and I. Román, "The maternal abdominal ECG as input to MICA in the fetal ECG extraction problem," *IEEE Signal Processing Letters*, vol. 18, no. 3, pp. 161–164, 2011.
- [79] J.-F. Cardoso, "Multidimensional independent component analysis," in *Proceedings of the IEEE International Conference on Acoustics, Speech and Signal Processing (ICASSP '98)*, vol. 4, pp. 1941–1944, May 1998.
- [80] N. E. Huang, Z. Shen, S. R. Long et al., "The empirical mode decomposition and the Hubert spectrum for nonlinear and non-stationary time series analysis," *Proceedings of the Royal Society A*, vol. 454, no. 1971, pp. 903–995, 1998.
- [81] N. E. Huang, M. L. Wu, S. R. Long et al., "A confidence limit for the empirical mode decomposition and the Hilbertspectral analysis," *Proceedings of the Royal Society A*, vol. 459, pp. 2317–2345, 2003.
- [82] M. Blanco-Velasco, B. Weng, and K. E. Barner, "ECG signal denoising and baseline wander correction based on the empirical mode decomposition," *Computers in Biology and Medicine*, vol. 38, no. 1, pp. 1–13, 2008.
- [83] C. Zhang, X. Li, and M. Zhang, "A novel ECG signal denoising method based on Hilbert-Huang Transform," in *Proceedings of the International Conference on Computer and Communication Technologies in Agriculture Engineering (CCTAE '10)*, vol. 2, pp. 284–287, June 2010.
- [84] W. Jiang, S. G. Kong, and G. D. Peterson, "ECG signal classification using block-based neural networks," in *Proceedings of the International Joint Conference on Neural Networks (IJCNN '05)*, pp. 326–331, August 2005.
- [85] M. Jezewski, J. Wrobel, P. Labaj et al., "Some practical remarks on neural networks approach to fetal cardiocograms classification," in *Proceedings of the 29th Annual International Conference of IEEE-EMBS, Engineering in Medicine and Biology Society (EMBC '07)*, pp. 5170–5173, August 2007.
- [86] M. A. Hassan, M. I. Ibrahimy, and M. B. I. Reaz, "An efficient method for fetal electrocardiogram extraction from the abdominal electrocardiogram signal," *Journal of Computer Science*, vol. 5, no. 9, pp. 619–623, 2009.
- [87] N. Dey, T. P. Dash, and S. Dash, "ECG signal denoising by Functional Link Artificial Neural Network (FLANN)," *International Journal of Biomedical Engineering and Technology*, vol. 7, no. 4, pp. 377–389, 2011.
- [88] Q. Zhang and A. Benveniste, "Wavelet networks," *IEEE Transactions on Neural Networks*, vol. 3, no. 6, pp. 889–898, 1992.
- [89] S. Pongponsoi and X.-H. Yu, "Electrocardiogram (ECG) signal modeling and noise reduction using wavelet neural networks," in *Proceedings of the IEEE International Conference on Automation and Logistics (ICAL '09)*, pp. 394–398, August 2009.
- [90] G. B. Moody and R. G. Mark, "The impact of the MIT-BIH arrhythmia database," *IEEE Engineering in Medicine and Biology Magazine*, vol. 20, no. 3, pp. 45–50, 2001.
- [91] E.-S. A. El-Dahshan, "Genetic algorithm and wavelet hybrid scheme for ECG signal denoising," *Telecommunication Systems*, vol. 46, no. 3, pp. 209–215, 2011.
- [92] C. Kezi Selva Vijila and C. Ebbie Selva Kumar, "Interference cancellation in EMG signal Using ANFIS," *International Journal of Recent Trends in Engineering*, vol. 2, no. 5, 2009.
- [93] P. Karthikeyan, M. Murugappan, and S. Yaacob, "ECG signal denoising using wavelet thresholding techniques in human stress assessment," *International Journal on Electrical Engineering and Informatics*, vol. 4, no. 2, 2012.
- [94] G. Garg, S. Gupta, V. Singh, J. R. P. Gupta, and A. P. Mittal, "Identification of optimal wavelet-based algorithm for removal of power line interferences in ECG signals," in *Proceedings of the India International Conference on Power Electronics (IICPE '10)*, January 2011.
- [95] P. E. McSharry, G. D. Clifford, L. Tarassenko, and L. A. Smith, "A dynamical model for generating synthetic electrocardiogram signals," *IEEE Transactions on Biomedical Engineering*, vol. 50, no. 3, pp. 289–294, 2003.
- [96] P. E. McSharry and G. D. Clifford, "ECGSYN—a realistic ECG waveform generator," <http://www.physionet.org/physiotools/ecgsyn/>.
- [97] K.-M. Chang, "Arrhythmia ECG noise reduction by ensemble empirical mode decomposition," *Sensors*, vol. 10, no. 6, pp. 6063–6080, 2010.
- [98] S. Tabakov, I. Iliev, and V. Krasteva, "Online digital filter and QRS detector applicable in low resource ECG monitoring systems," *Annals of Biomedical Engineering*, vol. 36, no. 11, pp. 1805–1815, 2008.
- [99] C. D. McManus, K.-D. Neubert, and E. Cramer, "Characterization and elimination of AC noise in electrocardiograms: a comparison of digital filtering methods," *Computers and Biomedical Research*, vol. 26, no. 1, pp. 48–67, 1993.

- [100] N. Kumaravel, A. Senthil, K. S. Sridhar, and N. Nithiyanandam, "Integrating the ECG power-line interference removal methods with rule-based system," *Biomedical Sciences Instrumentation*, vol. 31, pp. 115–120, 1995.
- [101] Z. Wu and N. E. Huang, "Ensemble empirical mode decomposition: a noise-assisted data analysis method," *Advances in Adaptive Data Analysis*, vol. 1, no. 1, pp. 1–41, 2009.
- [102] J. Lin, "Improved ensemble empirical mode decomposition and its applications to gearbox fault signal processing," *International Journal of Computer Science*, vol. 9, no. 6, pp. 194–199, 2012.

Research Article

Monitoring Fetal Heart Rate during Pregnancy: Contributions from Advanced Signal Processing and Wearable Technology

Maria G. Signorini,¹ Andrea Fanelli,² and Giovanni Magenes³

¹ *Dipartimento di Elettronica, Informazione e Bioingegneria (DEIB), Politecnico di Milano, piazza Leonardo da Vinci 32, 20133 Milano, Italy*

² *Computational Physiological and Clinical Inference Group, 143 3rd Street, Apt. 1, Cambridge, MA 02141, USA*

³ *Dipartimento di Ingegneria Industriale e dell'Informazione, University of Pavia, Via A. Ferrata 1, 27100 Pavia, Italy*

Correspondence should be addressed to Maria G. Signorini; mariagabriella.signorini@polimi.it

Received 15 July 2013; Revised 29 October 2013; Accepted 10 November 2013; Published 30 January 2014

Academic Editor: Mihaela Ungureanu

Copyright © 2014 Maria G. Signorini et al. This is an open access article distributed under the Creative Commons Attribution License, which permits unrestricted use, distribution, and reproduction in any medium, provided the original work is properly cited.

Monitoring procedures are the basis to evaluate the clinical state of patients and to assess changes in their conditions, thus providing necessary interventions in time. Both these two objectives can be achieved by integrating technological development with methodological tools, thus allowing accurate classification and extraction of useful diagnostic information. The paper is focused on monitoring procedures applied to fetal heart rate variability (FHRV) signals, collected during pregnancy, in order to assess fetal well-being. The use of linear time and frequency techniques as well as the computation of non linear indices can contribute to enhancing the diagnostic power and reliability of fetal monitoring. The paper shows how advanced signal processing approaches can contribute to developing new diagnostic and classification indices. Their usefulness is evaluated by comparing two selected populations: normal fetuses and intra uterine growth restricted (IUGR) fetuses. Results show that the computation of different indices on FHRV signals, either linear and nonlinear, gives helpful indications to describe pathophysiological mechanisms involved in the cardiovascular and neural system controlling the fetal heart. As a further contribution, the paper briefly describes how the introduction of wearable systems for fetal ECG recording could provide new technological solutions improving the quality and usability of prenatal monitoring.

1. Introduction

Monitoring biomedical signals, through measurement, quantification, evaluation, and classification of signal properties, is one of the primary tools for investigating the evolution of disease states. The overall architecture of a monitoring system has to combine technological tools with signal analysis methods in order to extract useful information to identify patient's condition.

Inside these procedures, it is very important to select processing methods that can enhance pathophysiological signal properties, thus linking parameters to physiological events (and maybe to physical quantities).

Traditional monitoring systems received a fundamental improvement by new technological devices allowing longer

and deeper data collection as well as by advanced clinical tools for data interpretation.

In recent years, the development of dynamical system analysis has led to the introduction of a large amount of signal processing techniques aimed at the extraction of parameters from experimental time series, thus enhancing new information about the characteristics of the system generating the time series. In most cases, however, an accurate model of the generating system is unknown or too complex and the output signal is the main available information about the system itself.

A typical example is the cardiovascular system, where the main way to investigate heart function consists of the analysis of heart rate variability signal (HRV). It has been shown that HRV signal can be related to the activity of several

physiological control mechanisms of different nature. Their interaction produces changes in the beat rate assuring the system controlling heartbeats reacts efficiently to different incoming stimuli. HRV variance is related to changed conditions of heart activity. Frequency domain analysis of the HRV signal provides quantitative and noninvasive measures of the activity of the autonomic nervous system (ANS) [1]. A linear modeling approach is adopted to quantify both the sympathetic and parasympathetic control mechanisms and their balance through the measure of spectral low and high frequency components (LF and HF). The same approach can extract parameters related to the heart and to the cardiovascular control even from systolic and diastolic values in arterial blood pressure (ABP), on a beat-to-beat basis [2].

Nevertheless, even if the HRV analysis through classical linear methods provides the quantification the ANS regulating action in the short period [1], the linear approach cannot explain the whole information carried by beat-to-beat variability [3]. Results on HRV signal analysis show that its dynamic behavior also involves nonlinear components that contribute to the signal generation and control [3, 4]. Signal structure appears erratic but it presents abrupt changes and patterns in which a more regular behavior appears. To investigate the erratic components of the cardiac rhythms and to assess nonlinear deterministic phenomena affecting HRV signal, both in short and long temporal windows, nonlinear signal analysis has demonstrated its usefulness [5].

In the field of fetal heart rate monitoring during pregnancy, linear time and frequency techniques were traditionally adopted. Fetal HR monitoring is a challenging procedure for people working in the obstetric field, in order to check if the fetus is and remains in a wellbeing state as the pregnancy develops.

The most employed diagnostic examination in the clinical practice is cardiotocography (CTG). CTG combines fetal heart rate (FHR) measurement, obtained by means of a Doppler ultrasound probe and uterine contraction, recorded through an abdominal pressure transducer. During pregnancy, each woman undergoes one or more ambulatory monitoring tests and, in the last pregnancy trimester and/or in case of suspect that risky condition can take place, monitoring frequency can increase to weekly or even daily. We can certainly state that the total CTG recording amount, in our country, is about 1 million per year and reaches several million exams in EU countries.

CTG is universally accepted in the clinical practice and it is recognized as one of the most information rich among noninvasive diagnostic tests for prenatal monitoring. Nevertheless, the FHR signal is usually analysed by detecting and measuring morphological characteristics whose clinical relevance is established mainly by eye inspection. This represents a strong limitation because the application of subjective and qualitative methods lacks reliability and depends on the physician experience.

Moreover, the CTG exam needs a hospital context to be performed both as an expert clinician only can produce the clinical report and the technology the system requires for signal recording.

One can state with some confidence that the techniques used in the prenatal diagnosis for FHR analysis did not experience a growth rate as the knowledge did, concerning physiological mechanisms and the availability of methodological tools with clearly demonstrated investigation abilities.

The introduction of quantitative evaluation of both linear and nonlinear indices increases the diagnostic power and reliability of antepartum monitoring.

The paper presents results obtained by applying both linear and nonlinear quantitative analysis to fetal heart rate (FHR) signals collected in normal and intrauterine growth restricted (IUGR) fetuses (61 + 61 subjects).

Finally, as a further contribution, the paper briefly describes the simultaneous development of a new wearable monitoring system allowing comfortable collection of fetal ECG and HRV signals in long periods. This new device named *Telefetalcare* is equipped with the analysis tools developed for the fetal HR analysis and described in this paper, and can provide further improvements to pre-natal diagnostic system tools.

2. Materials and Methods

2.1. FHRV Recording. FHRV recordings were collected at the Azienda Ospedaliera Universitaria Federico II, Napoli, Italy. Signals were recorded by means of a Hewlett Packard CTG fetal monitor, linked with a PC computer through a USB port.

The HP fetal monitors use an autocorrelation technique to compare the demodulated Doppler signal of a heartbeat with the next one. Each Doppler signal is sampled at 200 Hz (5 ms). The time window over which the autocorrelation function is computed is 1.2 sec, corresponding to a FHR lower bound of 50 bpm. A peak detection software then determines the heart period (the equivalent of RR period) from the autocorrelation function. With a peak position interpolation algorithm, the effective resolution is better than 2 ms.

Due to historical reasons, almost all commercially available fetal CTG monitors display only the fetal heart rate expressed in number of beats per minute (bpm) and do not offer the series of interbeat intervals, usually employed in HRV analysis.

The HP monitor produces a FHR value in bpm every 250 msec. In the commercially available system, the PC reads 10 consecutive values from the monitor every 2.5 sec and determines the actual FHR as the average of the 10 values (corresponding to an equivalent sampling frequency of 0.4 Hz). We modified the software in order to read the FHR at 2 Hz (every 0.5 sec). The choice of reading the FHR values each 0.5 sec represents a reasonable compromise to achieve an enough large bandwidth (Nyquist Frequency 1 Hz) and an acceptable accuracy of the FHR signal. An example of CTG recording is shown in Figure 1, where both the FHR and the uterine contractions are plotted as functions of time.

The whole set of recordings was composed of 122 subjects (61 healthy and 61 IUGR). Both groups were defined “a posteriori,” after delivery, on the basis of standard parameters (Apgar scores, weight, abdominal circumference): IUGR

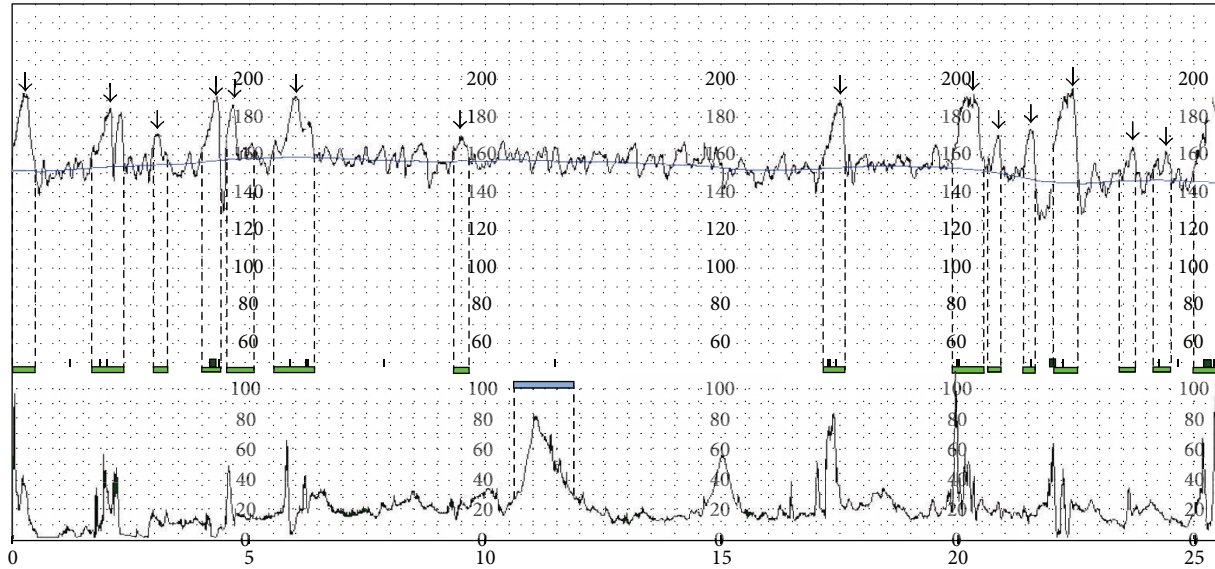


FIGURE 1: Example of CTG graph. The upper trace is fetal heart rate signal obtained by a Doppler ultrasound probe; the baseline is drawn and the arrows represent the detected accelerations. The lower tracing is the toco signal (uterine contractions). Time units are in minutes.

TABLE 1: Detailed summary of the two groups of fetuses.

Population details	Healthy	IUGR
Number	61	61
Mother age (years)	32.34 ± 5.64	29.68 ± 6.21
Gestational age at CTG recording (days)	34.78 ± 0.53	32.27 ± 2.79
Gestation age at delivery (days)	39.74 ± 1.15	34.15 ± 2.99
Weight of the baby after delivery	$3275 \text{ g} \pm 518 \text{ g}$	$1479 \text{ g} \pm 608 \text{ g}$
Delivery mode	58% spontaneous 42% caesarean	14.8% spontaneous 85.2% caesarean

fetuses were selected by weight below the 10th percentile for their gestational age and abdominal circumference below the 10th percentile.

Table 1 summarizes population details. All recordings were made in a controlled clinical environment, with the pregnant woman lying on a bed. The average length of the recordings was 2450 ± 724 sec for healthy and 3418 ± 1033 sec for IUGR group.

2.2. Time and Frequency Domain FHR Analysis

2.2.1. Baseline, Accelerations, and Decelerations. Interpretation of the heart rate pattern is usually performed by the physician who analyses the deviations of the signal from an imaginary line, the baseline. He/she hypothetically constructs it as a running average of the heart rate. Accelerations and decelerations are defined as deviations from the baseline, and more than one quantitative definition is available. In the construction of an automated system for the evaluation of the CTG recordings, a reproducible determination of the baseline

is a fundamental starting point. Several attempts in this direction have been made starting from the work of Dawes et al. [6]; the approach we followed was that suggested by Mantel et al. [7] (an example of baseline is shown in Figure 1). The algorithm is very complex, and a full description can be found in the cited reference.

Accelerations and decelerations are deviations of the fetal heart rate from the baseline lasting a sufficient amount of time (accelerations are positive deviations, decelerations negative). They are correlated with the normal activities of the fetus, who “trains,” moves, and exercises to breathe. Decelerations are usually correlated with uterine contraction. Unfortunately, different quantifications of the words “deviations” and “sufficient” led each medical school to develop its own method to evaluate, by means of a ruler, these quantities on the monitoring strip. We applied a quantitative procedure not only fully consistent with the definition of Mantel et al. [8], but also holding the suggestions of Arduini et al. [9].

Classical FHR linear indices are truly time domain measures. In the following, interbeat sequences $T(i)$, $i = 1, \dots, N$, will be used instead of heart rate sequences $S(i)$ in beats per minute, usually employed in cardiotocography: they are computed as $T(i) = 60000/S(i)$ ms. Moreover, in order to be compatible with previous works (Arduini et al. [9]) we also computed some indices on the basis of the undersampled time series $T_{24}(i) = 60000/S_{24}(i)$ ms, $i = 1, \dots, N/5$ obtained by taking $S_{24}(i)$ as the average of five consecutive FHR values of $S(i)$.

2.2.2. Long Term Irregularity. Long Term irregularity (LTI) was the first index ever introduced; it was proposed by De Haan et al. [10]. It is usually computed on a three-minute segment of interbeat sequence in milliseconds. We excluded from the computation large accelerations and decelerations, as suggested by Arduini et al. [9], to avoid deviations caused

by spurious measures of variability. The three minutes, after the removal of the undesired parts, must contain, at least, a continuous segment of 30 seconds.

Given a signal $T_{24}(i)$ with $i \in [a; b]$, LTI is defined as the interquartile range $[1/4; 3/4]$ of the distribution $m_{24}(j)$ with $j \in [a; b - 1]$ and $m_{24}(j) = \sqrt{T_{24}^2(j) + T_{24}^2(j + 1)}$.

2.2.3. Short Term Variability. Short term variability (STV) quantifies FHR variability over a very short time scale, usually on a beat-to-beat basis. We refer to the definitions provided by Dalton et al. [11] (even if we used a scale factor of 12) and by Arduini et al. [9]. By considering one minute of interbeat sequence, $T_{24}(i)$ in ms, $i = 1, \dots, 24$, we defined STV as

$$\begin{aligned} \text{STV} &= \text{mean}[|T_{24}(i + 1) - T_{24}(i)|]_i \\ &= \frac{\sum_{i=1}^{23} |T_{24}(i + 1) - T_{24}(i)|}{23}, \end{aligned} \quad (1)$$

where $T_{24}(i)$ is the value of the signal $T(i)$ taken each 2.5 sec (i.e., once each five samples).

2.2.4. Interval Index. Historically, Interval Index (II) was introduced just after LTI and it is certainly one of the most used variability indices. It was proposed by Yeh et al. [12] as a long term variability statistic; we adopted the formulation used by Arduini et al. [9],

$$\text{II} = \frac{\text{std}[T_{24}(i + 1) - T_{24}(i)]}{\text{STV}}, \quad i = 1, \dots, 23. \quad (2)$$

2.2.5. Power Spectral Analysis of Fetal HRV. Considering the FHRV signal as controlled by the ANS, as it happens in adult subjects, it could be of primary importance to own a tool quantifying its development during pregnancy. Literature reports several examples on this subject. The ANS is still developing, if not as the anatomic growth as in the regulatory activity which increases in time with the system maturation.

Estimation of the power spectral density (PSD) in the FHR signal provides parameters related to the ANS activity. Frequency domain FHR analysis adopt both the direct estimation of the periodogram and the autoregressive power spectrum estimation.

In fetal HR analysis it is customary to consider three frequency bands, Low Frequency (LF), Movement Frequency (MF), and High Frequency (HF) power components as well as the ratio LF/(MF + HF) [13], instead of the bands usually adopted for standard HRV analysis [1].

Low Frequency contributions (LF: 0.03–0.15 Hz) can be associated with the sympathetic control and vasomotor activity. HF is basically driven by respiration mediated by vagal activity (HF: 0.5–1 Hz). A third component needs to be considered: we called it Movement Frequency (MF: 0.15–0.5 Hz). MF should quantify the activity of the fetus and the mechanical influences of the maternal breathing.

This approach works well on a short time scale (3–5 min, 300 points about) as the stationarity of the fetal HRV signal is an essential requirement. We adopted the autoregressive

power spectrum estimation method as described in Signorini et al. [13].

LF/HF + MF ratio could represent a synthetic index of the balance between physiological control components and fetus activity level, representing the equivalent of the so-called sympathovagal balance in standard HRV analysis.

2.3. Nonstandard Parameters for FHR Analysis. The introduction of nonlinear approaches to signal processing led to considering a set of methods investigating geometric and dynamic properties of time series.

Differently from the approach usually adopted to study a well-known deterministic system, when we deal with complex nonlinear systems, very often we can only analyze experimental time series. Nevertheless important indications can be extracted from the parameters estimating nonlinear characteristics. Their statistical use can be of great importance, even in diagnostic field and in clinical knowledge related to different cardiovascular pathologies [5].

Various techniques exist aimed at quantifying the degree of similarity and/or complexity in time series which can be computed directly on the sequence of interbeat intervals [14, 15].

2.3.1. Regularity Properties: Entropy Estimators (ApEn, SampEn). ApEn index quantifies regularity and complexity of a time series. The index was proposed in [16] and further improvements and corrections were proposed by the introduction of the SampEn index.

The idea is to quantify the degree of regularity or loss of regularity in a time series without a priori information on its structure. ApEn works on short (<100 samples) and noisy time series.

ApEn estimator depends on a parameter m (length of runs compared in the time series) and on a parameter r (percentage of signal std., working as a filter). The ApEn(m, r, N) evaluates, within a tolerance r , the signal regularity, by assessing the frequency of patterns similar to a given pattern of window length m ($m = 1, 2, r : 0.1 - 0.25$ std of the input data [16]).

Once values of the two parameters m and r are fixed and given N data points, the procedure constructs sequences $x_m(i)$ and computes, for each $i \leq N - m + 1$,

$$\begin{aligned} C_i^m(r) &= (N - m + 1)^{-1} \{ \text{number of } j \leq N - m + 1 \\ &\quad \text{such that } d[x_m(i), x_m(j)] \leq r \}. \end{aligned} \quad (3)$$

Regularity parameter is defined as

$$\text{ApEn}(m, r, N) = \lim_{N \rightarrow \infty} [\Phi_m - \Phi_{m+1}], \text{ where } \Phi^m(r) = (N - m + 1)^{-1} \sum_{i=1}^{N-m+1} \ln C_i^m(r).$$

The estimator of this parameter for an experimental time series of a fixed length N is given by ApEn(m, r, N) = $[\Phi_m - \Phi_{m+1}]$.

Other methods estimate entropy-like indexes in time series. Among them, *Sample Entropy* (SampEn) has been largely employed in biomedical signal processing over time, as it improves the estimation performed by ApEn (i.e.,

removes the bias introduced by self-counts). SampEn is also the basis for a multiscale approach: entropy parameters are calculated at different scales in coarse-grained time series [17, 18].

ApEn and SampEn were estimated in the same time series by using the same parameter set: $m = 1$ and $r = 0.1$, $m = 2$ and $r = 0.15$ and 0.2 .

2.3.2. Lempel Ziv Complexity. Lempel Ziv complexity (LZC) was originally proposed in the information field to assess the complexity of data series [19]. Its measure is associated with the number of different substrings and to the rate of their recurrence. Namely, LZC reflects the gradual increase of new patterns along the given sequence. The measure of complexity introduced by Lempel and Ziv assesses the so-called algorithmic complexity, which is defined according to Information Theory as the minimum quantity of information needed to define a binary string. In case of random strings, the algorithmic complexity is the length of the string itself. In fact any compression effort will produce an information loss. In order to estimate the LZC in a time series, it is necessary to transform the signal (the FHR in our case) into symbolic sequences.

Calculation of the Lempel Ziv complexity $c(n)$ needs to define an alphabet A , that is, the set of symbols which compose the sequence S (for a binary string, A is simply $\{0, 1\}$).

Suppose the number of symbols in the alphabet A is α and the length of sequence is $l(S) = n$. The upper bound of $c(n)$ is given by:

$$c(n) < \frac{n}{(1 - \varepsilon_n) \log(n)}, \quad (4)$$

where $\varepsilon_n = 2(1 + \log \log(\alpha n)) / \log(n)$ [6]. When n is large enough ($n \rightarrow \infty$), $\varepsilon_n \rightarrow 0$ and we have that

$$\lim_{n \rightarrow \infty} c(n) = b(n) = \frac{n}{\log_{\alpha}(n)}. \quad (5)$$

The quantity $b(n)$ is the asymptotic behaviour of $c(n)$ for a random string. The normalized complexity is thus defined as $C(n) = c(n)/b(n)$.

In order to estimate the complexity measure for the HRV time series, we have transformed the signals in symbolic sequences. As a coding procedure we adopted both a binary and a ternary code. From an HRV series $\{x_n\}$, we construct a new sequence by mapping the original one through a binary alphabet. We symbolize with 1 a signal increase ($x_{n+1} > x_n$), and with 0 a decrease ($x_{n+1} \leq x_n$). In case of ternary alphabet, 1 denotes the signal increase ($x_{n+1} > x_n$), 0 the decrease ($x_{n+1} < x_n$) and 2 the signal invariance ($x_{n+1} = x_n$). To avoid the possible dependence of the encoded string on quantization procedure adopted to record the signal, a p factor is introduced representing the minimum quantization level for a symbol change in the coded string. We considered the encoding parameter $p = 0, 0.005, 0.01, 0.02\%$. The LZC index was computed 360 point-long FHR sequences (3 min).

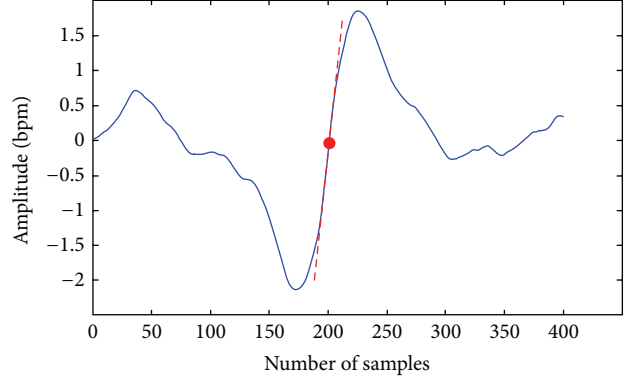


FIGURE 2: Phase Rectified Signal Average (PRSA) curve computed on a FHR recording. The computation of the Acceleration Phase Rectified Slope is shown: APRS is defined as the slope of the PRSA curve in the anchor point (red dot).

2.3.3. Phase Rectified Signal Average (PRSA). Phase rectified signal average (PRSA) is a technique introduced by Bauer et al. in 2006 [20]. It allows the detection and quantification of quasiperiodic oscillations in nonstationary signals affected by noise and artifacts, by synchronizing the phase of all periodic components. This method demonstrated its usefulness in FHR signal analysis, when episodes of increasing and/or decreasing FHR appear [21]. In fact, occurrence or absence of such periods can be related to the healthy status of the fetus. For this reason, we introduced the PRSA method to quantify fetal well-being states.

The PRSA curve is obtained from the HRV series. The procedure that can be followed to construct the curve is detailed and described in [20]. The great advantage given by the PRSA curve is the fact that a 30–40-minute HRV signal can be condensed in a single waveform, showing the average dynamic pattern of the recording under analysis. An example of PRSA curve is shown in Figure 2, where the red dot represents the anchor point and the dashed red line is the slope of the curve in the anchor point.

In order to construct the curve, we employed 200 sec windows (total number of 400 samples) obtained from the FHR signal, which were selected if the right average of the window was bigger than the left average. Then, the windows were synchronized in their anchor point (the middle point of the curve) and averaged.

Starting from the PRSA curve, it is possible to compute several parameters that describe its shape and, indirectly, quantify the overall dynamics in the HRV series. Thus, those parameters can be employed to provide a clue about fetal behavior and well-being.

In [22], we proposed the Acceleration Phase Rectified Slope (APRS) and the Deceleration Phase Rectified Slope (DPRS), as useful indices computed on the PRSA curve in order to verify fetal well-being. For a detailed description of how these parameters are computed, please refer to [22].

Table 2 summarizes all the parameters we have considered in fetal HR analysis. Parameters have been grouped as *Frequency domain* (autoregressive power spectrum

TABLE 2: Methods, extracted parameters, sequence lengths, and hypotheses for using the relevant parameter.

Method	Parameters	Sequence length	Hypothesis
Frequency domain analysis: periodogram and autoregressive model Measurement of spectral components in defined frequency bands	% of spectral power (msec^2) in frequency bands: Low frequency 0.03–0.15 Hz Movement (activity) frequency 0.15–0.5 Hz High frequency 0.5–1 Hz LF/(MF + HF)	3 min 360 values	Quantification of the activity of the autonomic nervous system
Time domain analysis: morphological HR modification and variability	STV (msec) II FHR avg (msec) LTI (msec)	1 min 120 values 3 min 360 values	Variability in the short period Variability in the long period
Approximate entropy	ApEn(m, r) $m = 1, 2; r = 0.1, 0.15, 0.2$	3 min $N = 360$ values	Recurrent patterns
Sample entropy	SampEn(m, r) $m = 1, 2; r = 0.1, 0.15, 0.2$	3 min $N = 360$ values	Recurrent patterns Basis for investigating repetitive patterns at different time scales
Lempel Ziv complexity (LZC)	LZC binary or ternary coding LZC (2 or 3, $P = 0, 0.005, 0, 01, 0.2$)	Whole recording	Rate of new patterns arising with signal evolution in time
PRSA	Acceleration/Deceleration Phase Rectified Slope	Whole recording	Quasiperiodic oscillations

estimation—LF-power, MF-power, HF power, and LF/(MF + HF)); *time domain* (short term variability (STV), long term irregularity (LTI), Interval Index (II)); and *regularity and complexity* parameters (*approximate entropy* (ApEn), *sample entropy* (SampEn), *Lempel Ziv complexity* (LZC), and finally *PRSA* parameters). All parameters are listed in Table 2 according to the time windows, which are suggested on the basis of our results.

For each group of them the pathophysiological meaning or the most reliable hypothesis is presented.

By this approach to the study of FHR we performed classification of different fetal states and we obtained diagnostic indications in pathologies such as intrauterine growth restriction (IUGR) and fetal distress [23, 24].

3. Results

Results are reported for the two groups of fetuses concerning the parameters illustrated in Sections: among the time parameters, STV, II, and LTI were selected; all frequency domains indices were computed by using the autoregressive power estimation (LF, MF, HF, and the ratio LF/(HF + MF)); among non-linear parameters, ApEn and SampEn were selected and compared to quantify non-linear complexity characteristics of FHR series; LZC parameters add information about complexity and predictability of FHR time series; finally, for the PRSA based parameters, APRS and DPRS were considered.

The target of the study was to identify which parameter or parameter set is most efficient in the discrimination between healthy and IUGR fetuses. Analysis of the FHR that consider more than one parameter at time has the objective to early identify signs of fetal distress that could bring interventions against possible life-threatening events.

In order to verify the ability of the selected parameters to discriminate between healthy and IUGR fetuses, we first verified that the two populations showed Gaussian distributions for all parameters using the Kolmogorov-Smirnov test, in order to further apply the t -test for the discrimination.

Table 3 summarizes the results concerning the healthy and IUGR groups of fetuses. Among the time parameters, both STV and LTI show great performance in the discrimination task (STV: P -value = $1.22e-9$; LTI: value = $1.5e-11$), while Interval Index does not.

Results in frequency domain parameters show a weak capability to differentiate normal versus IUGR fetuses. Nevertheless, many results reported in the literature demonstrate their ability in assessing the cardiovascular well-being in adults. So they still remain important candidates to monitor cardiovascular regulation dynamics in FHR time series, although in this case they do not seem able to discriminate IUGR fetuses. As a matter of fact, the frequency parameters are related to physiological mechanisms acting on the heart control. So, measuring the HF component of the PSD is a way to measure respiratory fetal activity providing a parameter directly related to hypoxia or to a respiratory stress state.

The analysis of non-linear parameters shows that all considered parameters allow the rejection of the null hypothesis: ApEn(1, 0.1) with P -value $5.14e-07$, confirming to be highly sensitive to the IUGR condition, LZC(2, 0) with P -value $7.8e-4$, and SampEn(1, 0.1) with P -value $2.08e-7$, demonstrating a very high discriminant ability between the two groups.

Moreover, even similar analysis we did in a different population of normal and IUGR fetuses by using multiscale entropy approach [23] also provided satisfying levels of discrimination power of the entropy indices, thus confirming

TABLE 3: Results of fetal HRV analysis by parameters in time domain, in frequency domain, by nonlinear indices and PRSA derived indices. Usefulness in separating populations is confirmed by t -test results.

Parameter	Healthy (mean \pm std)	IUGR (mean \pm std)	t -test	P value
Time parameters				
STV (ms)	6.7 \pm 2.24	4.29 \pm 1.62	* * *	1.22e - 09
Interval index	0.87 \pm 0.07	0.86 \pm 0.06		0.37
LTI (ms)	21.46 \pm 6.53	17.17 \pm 5.37	* * *	1.5e - 11
Frequency domain				
LF (Low Frequency power)	82.92 \pm 5.29	81.39 \pm 6.13		0.17
MF (Movement Frequency power)	6.7 \pm 2.24	11.61 \pm 3.50		0.63
HF (High Frequency power)	5.45 \pm 3.18	6.65 \pm 3.97		0.08
LF/HF + MF	5.36 \pm 1.78	4.89 \pm 1.76		0.16
Nonlinear parameters				
ApEn(1, 0.1)	1.33 \pm 0.13	1.21 \pm 0.11	**	5.14e - 7
Lempel Ziv complexity(2, 0)	1.00 \pm 0.08	0.94 \pm 0.09	*	0.00078
SampEn(1, 0.1)	1.3 \pm 0.19	1.13 \pm 0.15	**	2.08e - 7
PRSA parameters				
APRS	0.17 \pm 0.041	0.12 \pm 0.042	* * *	7.76e - 12
DPRS	-0.18 \pm 0.046	-0.12 \pm 0.042	* * *	1.08e - 13

the diagnostic and clinical usefulness of this family of parameters.

Among PRSA parameters, both APRS and DPRS, were demonstrated to be highly selective for the separation of the two groups. The APRS allows the rejection of the null hypothesis with a P -value of $7.76e - 12$. The DPRS behaves even better, with a P -value of $1.08e - 13$. The DPRS is the parameter in the analyses which exhibits the smallest P -value in the discrimination between healthy and IUGR patients. On the contrary other PRSA parameters reported in the literature by Huhn et al. [21], when applied to our population of fetuses, are not efficient in the discrimination as already reported in [22].

Figure 3 shows the boxplots of the subset of parameters which show significant P -values ($P < 0.05$) computed in the analysis of the two groups of fetuses.

A further improvement of the diagnostic ability of our set of parameters could be obtained by a multivariate analysis, in which two or more parameters are considered together for the discrimination task. We did not perform a multiparametric analysis in depth for the many combinations of indices we computed, but we can support the previous claim by some preliminary results. Figure 4 shows as an example of what can be obtained by combining the discrimination power of two parameters: plot of ApEn(1, 0.1) versus LTI values shows how healthy and IUGR populations can be separated, with very few errors, in different subspaces.

4. The Future: Wearable Technology for Fetal Monitoring

Monitoring fetal states can also be performed by measuring fetal ECG through electrodes placed over the maternal abdomen after the 26th week of pregnancy [25], which

directly provide a measure of the FECG. Unfortunately, it is very difficult to reliably reveal this FECG both for the low SNR, due to noise superimposed and maternal ECG interference, and for the position of the fetus that almost continuously changes his position inside the uterus. The recording can be made only at the hospital and requires the presence of expert personnel. Even in that case, measurement of FECG remains a difficult task.

Nevertheless, recording the FECG could provide information on the beat structure (long QT, T wave morphology and slope), which is related to heart diseases and to hypoxic fetal states. Moreover, FECG recordings allow longer periods of HRV measurements with respect to CTG which employs ultrasounds (being the ECG completely noninvasive). The idea is to design a "Fetal Holter" for very long FHRV signal acquisitions.

With this focus, recent evolution in wearable technology has started to produce effects even in the biomedical devices field. As a matter of fact, these new wearable devices allow measuring several physiological parameters continuously in normal life conditions for long periods. Thus, interesting perspectives are now open toward the development of new systems, even in the field of fetal monitoring. With this focus, our research group has designed a new monitoring system, namely, the Telefetalcare system, that makes use of wearable technologies to measure FECG [26] through textile electrodes embedded in everyday garments.

A first example of what we can obtain by a wearable prenatal garment sensorized with 8 ECG textile electrodes and a miniaturized acquisition system is illustrated in Figure 5, where one lead of the fetal-maternal ECG is reported together with the QRS detection. Till now, the Telefetalcare has been used on a limited number of patients, showing good performances in both terms of quality of the acquired signals

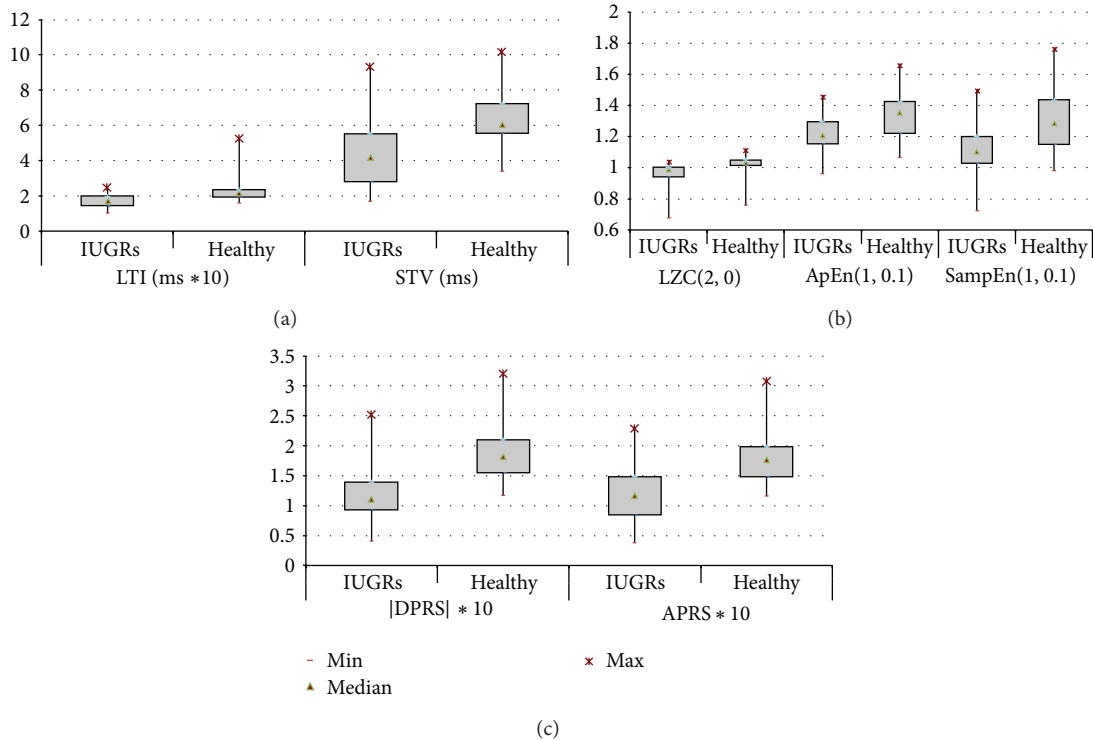


FIGURE 3: Boxplots of the significant parameters (the height of each box represents the distance between quartile 1 (25%) and quartile 3 (75%)); the triangular marker is the median; x denotes the maximum; and - marker is the minimum. (a) Diagram contains time domain indices, (b) diagram non linear indices and (c) diagram PRSA indices.

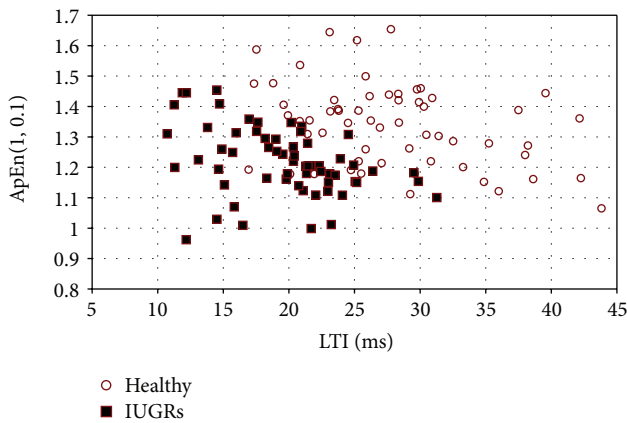


FIGURE 4: Individual data of ApEn(1, 0.1) versus LTI. The two groups of IUGRs and healthy fetuses occupy different subspaces in the diagram and can be separated quite easily with very few errors.

and in terms of fetal QRSs detection. At the moment both the separation of fetal-maternal ECGs and the digital processing are performed offline on a notebook computer, using a graphical user interface implemented in Matlab environment.

The final goal of this novel approach is to produce a system that every pregnant woman can use at home, able to collect FECG signal, for long periods, in a comfortable way, and to send data to the hospital for evaluation, through a wireless link.

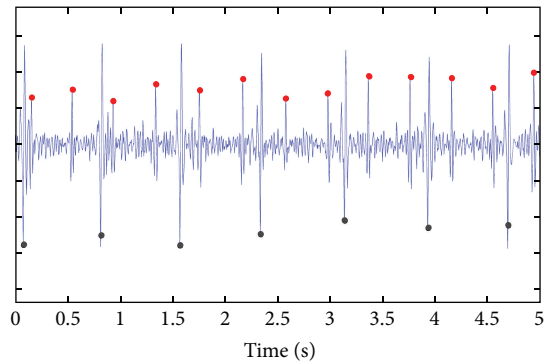


FIGURE 5: Example of ECG recording taken from the Telefetalcare system. The identification of maternal (gray dots, down) and fetal (red dots, up) heartbeats is computed off-line by a novel algorithm implemented in Matlab.

Figure 6 illustrates the functional architecture of the whole system. Acquisition of the cardiac electric signals takes place through a dedicated hardware device which is wireless connected to the patient through the sensorized garment. To reduce the costs connected with the hardware manufacturing, the device has no display for user interface and only consists of an 8-channel differential amplifier, paired with a Bluetooth™ wireless communication module. Smartphones or tablets available nowadays are endowed with high resolution color screens whose capabilities outpace

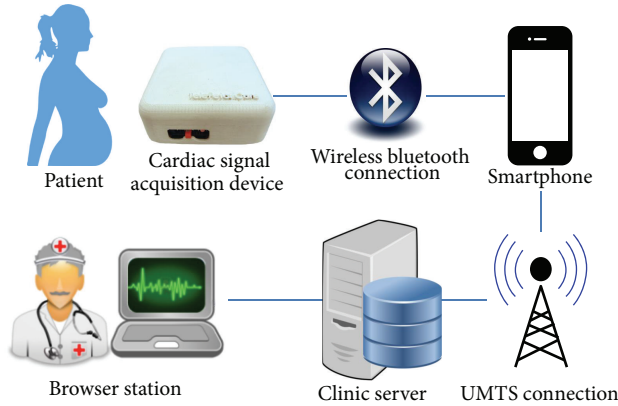


FIGURE 6: Actual architecture of the *Telefetalcare* system.

those of any other rendering device and computers available in the past decade.

Our objective is to obtain a high quality fetal ECG signal, for long periods, in an unsupervised environment (mother normal life) to extract fetal HRV in order to use it as an indicator of fetal well-being and/or stress conditions.

Of course, the analysis methods, previously presented and adopted for the fetal HRV signal from CTG recordings, will be used in the system postprocessing step. As a matter of fact, a significant improvement in the quality of fetal well-being assessment could be obtained by more frequent and accurate signal measurements and analysis, as costs in fetal monitoring will be drastically reduced.

5. Discussion

The paper presents results obtained from the application of several analysis tools to fetal heart rate variability signals. FHR signals were recorded through CTG in normal and IUGR fetuses, with the goal of demonstrating that fetal monitoring can be strongly improved by new analysis techniques and parameters related to pathophysiological fetal states.

The work evidenced some important points.

First, FHRV signal carries a lot of information about fetal condition during pregnancy and CTG, being the most employed technique supporting the diagnostic process along the final part of the pregnancy, and allows extracting this information through an accurate analysis. We considered a population including 61 normal and 61 IUGR subjects and we checked different approaches to find out reliable indices for separating the two groups. We tested time domain, frequency domain, and nonlinear approaches and results showed that time domain and nonlinear indices significantly separate the two groups allowing a clear classification. This is very important as early identification of IUGR condition allows proper intervention reducing life-threatening events.

However, not all parameters are equally sensitive to evolving fetal conditions. Entropy parameters, Lempel Ziv complexity indices, variability parameters in time domain, and PRSA derived indices exhibit excellent performance in classification of normal and IUGR population. Nevertheless

it is necessary to stress the importance of considering a quite large set of parameters to investigate the complex regulation of the fetal cardiovascular system. The interaction with the placenta, thus with the mother circulation, and the development of the controlling systems in the fetus are all factors influencing and acting on the fetal state.

Results and examples shown in the paper clearly suggest that monitoring systems could be improved by adding diagnostic and classification power through advanced signal processing techniques.

In particular, we want to stress the importance of adopting a multiparameter analysis to better identify fetal states for the sake of preventing disease insurgence. Our preliminary analysis (ApEn/LTI in Figure 4) shows how the simple combination of two parameters can improve the identification of IUGR subjects from healthy ones. These aspects deserve future investigations through a multivariate analysis.

Another important point relies on the general use the proposed approach could have in the fetal HR analysis as CTG data are routinely measured during pregnancy. As a matter of fact, analysis tools can complement the clinical routine steps, providing further indications to physicians and nurses.

Our experience has shown that implementing advanced signal processing techniques can provide better classification results of the fetal states either in a normal development of the pregnancy (activity-quiet) [13] (vibroacoustic stimulation) [23] or in pathological conditions (distressed fetuses) [24] (IUGRs) [27, 28].

Moreover, the intrinsic complexity which characterizes fetal life and the possible associated diseases complicates the prediction and control of fetal development. To face this problem we need to develop more personalized monitoring system allowing an almost continuous noninvasive evaluation of the fetal state and in which knowledge based systems contribute to the care improvement.

As a further contribution to a knowledge based fetal monitoring approach, supported by an advanced technology, we have briefly presented a fetal ECG monitoring system, *Telefetalcare*, based on wearable technology and designed to permit an accurate and continuing assessment of fetal well-being. Advantages are in the signal quality with the direct measurement of fetal HRV and the long-term monitoring that can be easily performed. A wearable garment equipped with textile electrodes will allow pregnant women to monitor fetus health state without moving to the hospital, always having the clinician remote support.

The system can contribute to reducing costs of fetal monitoring still maintaining a significant quality or even improving the fetal wellbeing assessment.

These novel approaches can open a new window on the continuous monitoring of fetal development: further information can be extracted by introducing novel analysis tools, more sensitive to fetal states both in healthy and stress conditions, by increasing length, frequency, and quality of monitoring session. Methods and technological advancements both have a key role contributing to reaching this important scientific and social objective.

Conflict of Interests

The authors declare that there is no conflict of interests regarding the publication of this paper.

References

- [1] Task Force of the European Society of Cardiology and the North American Society of Pacing and Electrophysiology, "Heart rate variability: standards of measurement, physiological interpretation, and clinical use," *Circulation*, vol. 93, no. 5, pp. 1043–1065, 1996.
- [2] G. Baselli, A. Porta, and S. Cerutti, "Spectral decomposition in multichannel recordings based on multivariate parametric identification," *IEEE Transactions on Biomedical Engineering*, vol. 44, no. 11, pp. 1092–1101, 1997.
- [3] H. Kantz, J. Kurths, and G. Mayer-Kress, Eds., *Nonlinear Analysis of Physiological Data*, Springer, Berlin, Germany, 1998.
- [4] D. Kaplan and L. Glass, *Understanding Nonlinear Dynamics*, Springer, New York, NY, USA, 1995.
- [5] T. H. Mäkikallio, T. Seppänen, K. E. Airaksinen et al., "Dynamic analysis of heart rate may predict subsequent ventricular tachycardia after myocardial infarction," *American Journal of Cardiology*, vol. 80, no. 6, pp. 779–783, 1997.
- [6] G. S. Dawes, C. R. S. Houghton, and C. W. G. Redman, "Baseline in human fetal heart-rate records," *British Journal of Obstetrics and Gynaecology*, vol. 89, no. 4, pp. 270–275, 1982.
- [7] R. Mantel, H. P. Van Geijn, F. J. M. Caron, J. M. Swartjes, E. E. Van Woerden, and H. W. Jongsma, "Computer analysis of antepartum fetal heart rate: 1. Baseline determination," *International Journal of Bio-Medical Computing*, vol. 25, no. 4, pp. 261–272, 1990.
- [8] R. Mantel, H. P. Van Geijn, F. J. M. Caron, J. M. Swartjes, E. E. Van Woerden, and H. W. Jongsma, "Computer analysis of antepartum fetal heart rate: 2. Detection of accelerations and decelerations," *International Journal of Bio-Medical Computing*, vol. 25, no. 4, pp. 273–286, 1990.
- [9] D. Arduini, G. Rizzo, G. Piana, A. Bonalumi, P. Brambilla, and C. Romanini, "Computerized analysis of fetal heart rate: I. description of the system (2CTG)," *Matern. Fetal. Invest.*, vol. 3, article 159, 1993.
- [10] J. De Haan, J. H. Van Bommel, B. Versteeg et al., "Quantitative evaluation of fetal heart rate patterns. I. Processing methods," *European Journal of Obstetrics and Gynecology and Reproductive Biology*, vol. 1, no. 3, pp. 95–102, 1971.
- [11] K. J. Dalton, G. S. Dawes, and J. E. Patrick, "Diurnal, respiratory, and other rhythms of fetal heart rate in lambs," *American Journal of Obstetrics and Gynecology*, vol. 127, no. 4, pp. 414–424, 1977.
- [12] S. Y. Yeh, A. Forsythe, and E. H. Hon, "Quantification of fetal heart beat-to-beat interval differences," *Obstetrics and Gynecology*, vol. 41, no. 3, pp. 355–363, 1973.
- [13] M. G. Signorini, G. Magenes, S. Cerutti, and D. Arduini, "Linear and nonlinear parameters for the analysis of fetal heart rate signal from cardiotocographic recordings," *IEEE Transactions on Biomedical Engineering*, vol. 50, no. 3, pp. 365–374, 2003.
- [14] J. M. Hausdorff and C.-K. Peng, "Multiscaled randomness: a possible source of 1/f noise in biology," *Physical Review E*, vol. 54, no. 2, pp. 2154–2157, 1996.
- [15] J. Beran, *Statistics for Long-Memory Processes*, Chapman v Hall, New York, NY, USA, 1994.
- [16] S. M. Pincus, "Approximate entropy (ApEn) as a complexity measure," *Chaos*, vol. 5, no. 1, pp. 110–117, 1995.
- [17] J. S. Richman and J. R. Moorman, "Physiological time-series analysis using approximate and sample entropy," *American Journal of Physiology: Heart and Circulatory Physiology*, vol. 278, no. 6, pp. H2039–H2049, 2000.
- [18] M. Costa, A. L. Goldberger, and C.-K. Peng, "Multiscale entropy analysis of complex physiologic time series," *Physical Review Letters*, vol. 89, no. 6, Article ID 068102, 2002.
- [19] A. Lempel and J. Ziv, "Multiscale entropy analysis of complex physiologic time series," *IEEE Transactions on Information Theory*, vol. 22, no. 1, pp. 75–81, 1976.
- [20] A. Bauer, J. W. Kantelhardt, A. Bunde et al., "Phase-rectified signal averaging detects quasi-periodicities in non-stationary data," *Physica A*, vol. 364, pp. 423–434, 2006.
- [21] E. A. Huhn, S. Lobmaier, T. Fischer et al., "New computerized fetal heart rate analysis for surveillance of intrauterine growth restriction," *Prenatal Diagnosis*, vol. 31, no. 5, pp. 509–514, 2011.
- [22] A. Fanelli, G. Magenes, M. Campanile, and M. G. Signorini, "Quantitative assessment of fetal well-being through CTG recordings: a new parameter based on Phase Rectified Signal Average," *IEEE Journal of Biomedical and Health Informatics*, vol. 17, no. 5, pp. 959–966, 2013.
- [23] G. Magenes, M. G. Signorini, D. Arduini, and S. Cerutti, "Fetal heart rate variability due to vibroacoustic stimulation: linear and nonlinear contribution," *Methods of Information in Medicine*, vol. 43, no. 1, pp. 47–51, 2004.
- [24] M. Ferrario, M. G. Signorini, G. Magenes, and S. Cerutti, "Comparison of entropy-based regularity estimators: application to the fetal heart rate signal for the identification of fetal distress," *IEEE Transactions on Biomedical Engineering*, vol. 53, no. 1, pp. 119–125, 2006.
- [25] S. Cerutti, G. Baselli, and S. Civardi, "Variability analysis of fetal heart rate signals as obtained from abdominal electrocardiographic recordings," *Journal of Perinatal Medicine*, vol. 14, no. 6, pp. 445–452, 1981.
- [26] A. Fanelli, M. Ferrario, L. Piccini et al., "Prototype of a wearable system for remote fetal monitoring during pregnancy," in *Proceedings of the 32nd Annual International Conference of the IEEE Engineering in Medicine and Biology Society (EMBC '10)*, pp. 5815–5818, September 2010.
- [27] M. Ferrario, M. G. Signorini, and G. Magenes, "Comparison between fetal heart rate standard parameters and complexity indexes for the identification of severe intrauterine growth restriction," *Methods of Information in Medicine*, vol. 46, no. 2, pp. 186–190, 2007.
- [28] M. Ferrario, M. G. Signorini, and G. Magenes, "Complexity analysis of the fetal heart rate variability: early identification of severe intrauterine growth-restricted fetuses," *Medical and Biological Engineering and Computing*, vol. 47, no. 9, pp. 911–919, 2009.

Research Article

New Estimators and Guidelines for Better Use of Fetal Heart Rate Estimators with Doppler Ultrasound Devices

Iulian Voicu,^{1,2} Sébastien Ménigot,^{1,2} Denis Kouamé,³ and Jean-Marc Girault^{1,2}

¹ Signal & Imaging Group, University François Rabelais of Tours, PRES Loire Valley University, UMR INSERM U930, 7 Avenue Marcel Dassault, 37200 Tours Cedex, France

² Inserm, U930, 10 Boulevard Tonnellé, BP 3223, 37032 Tours Cedex, France

³ IRIT UMR 5505, Université Paul Sabatier Toulouse 3, 118 Route de Narbonne, 31062 Toulouse Cedex 9, France

Correspondence should be addressed to Jean-Marc Girault; jean-marc.girault@univ-tours.fr

Received 28 May 2013; Revised 25 October 2013; Accepted 4 November 2013; Published 29 January 2014

Academic Editor: Brynjar Karlsson

Copyright © 2014 Iulian Voicu et al. This is an open access article distributed under the Creative Commons Attribution License, which permits unrestricted use, distribution, and reproduction in any medium, provided the original work is properly cited.

Characterizing fetal wellbeing with a Doppler ultrasound device requires computation of a score based on fetal parameters. In order to analyze the parameters derived from the fetal heart rate correctly, an accuracy of 0.25 beats per minute is needed. Simultaneously with the lowest false negative rate and the highest sensitivity, we investigated whether various Doppler techniques ensure this accuracy. We found that the accuracy was ensured if directional Doppler signals and autocorrelation estimation were used. Our best estimator provided sensitivity of 95.5%, corresponding to an improvement of 14% compared to the standard estimator.

1. Introduction

Continuous monitoring of fetal parameters has shown their advantages in estimating fetal wellbeing [1]. According to the report of the Society for Maternal-Fetal Medicine [2], continuous fetal heart rate monitoring has reduced infant mortality. The development or the improvement of noninvasive methods dedicated to continuous fetal monitoring is therefore of major interest.

One important parameter in assessing fetal wellbeing is the variability of the fetal heart rate. This parameter, which corresponds to the variation between intervals of two consecutive heart beats, is an indicator of central nervous system development [3–5]. It characterizes fetal behavior states [6–8] and can be an indicator of further neurological evolution [9]. Variability analysis provides a good indication of fetal distress [10] and identifies fetuses with intrauterine growth retardation [11]. According to Dawes criteria [12], variability of 4 ms is a predictor of the lack of acidosis, while a value of 2.6 ms is critical for the fetus. In the normal fetal heart rate range (110–160 bpm), a time variability of 4 ms corresponds to a cardiac frequency variability of 0.81 bpm, while a time variability of 2.6 ms corresponds to a cardiac

frequency variability of 0.53 bpm (the values of 0.53 bpm and 0.81 bpm are obtained as follows: $60/(60/110 - 2.6 \text{ ms}) - 110 = 0.56 \text{ bpm}$ and $60/(60/110 - 4.0 \text{ ms}) - 110 = 0.81 \text{ bpm}$, resp.). Other authors [13] suggest that it is necessary to estimate the heart rate with an accuracy of 0.25 bpm in order to analyze fetal heart rate variability correctly. Reliable estimation of fetal heart rate and hence of heart rate variability is therefore essential.

Several methods are available to assess the fetal heart rate. These methods differ both at the Doppler signal level (directional or nondirectional) and at the level of the algorithm that estimates the heart rate. For example, existing devices on the market such as Sonicaid Oxford (Oxford Sonicaid Instruments, Abington, UK) [14], Hewlett-Packard 8030A (Hewlett-Packard, Palo Alto, CA, USA) [15], and Philips Avalon F40 (Philips, Amsterdam, Netherlands) use the envelope of the nondirectional Doppler signal. Other authors [16, 17] have used the envelope of the directional Doppler signal. Several algorithms based on autocorrelation are commonly used to estimate the heart rate (Oxford Sonicaid, Hewlett-Packard 8030A, and Philips Avalon F40). These algorithms have been applied either directly to the Doppler signal envelope (directional or nondirectional) or to

the signals resulting from discrete wavelet decomposition of the envelope. In the latter case, the final estimated heart rate involves the combination of different estimates [16].

In this study, we first verified whether the pulsed Doppler techniques currently used in commercial devices ensure such an accuracy of 0.25 bpm, and we propose here some recommendations regarding parameter settings. We also compared the techniques used in commercial devices with other pulsed Doppler techniques that use directional Doppler signals. We evaluated the efficacy of all these techniques empirically (error of estimation of the fetal heart rate, sensitivity, and false negative rate).

The originality of this study lies in the recommendations on the parameter settings of the system and in the description of the individual limitations of each technique. Finally, to improve detection probability, a new method based on the combination of heart rates obtained from directional signals is proposed.

2. Materials and Methods

In this section, we describe the Doppler system we developed, the patients, and the synthetic signals used for the comparison of each estimator. The synthetic signals were inferred from real signals. Finally, we present the various existing techniques for estimation of fetal heart rate and we present a new technique based on a combined procedure.

2.1. The Doppler System. In order to evaluate fetal wellbeing objectively and to classify the fetus, we codeveloped the pulsed, multitransducer, multichannel Doppler Actifoetus unit with Althais Technologies (Tours, France).

Our system comprised a personal computer (PC) and our Actifoetus unit. The Actifoetus unit contained three groups of four transducers and a Doppler acquisition board. The detailed operating functions of the acquisition board were presented in [18].

The transducers exploring the fetal heart were non-focused and monoelement. They were circular in shape, with a diameter of 13.5 mm and an acoustic power of 1 mW/cm². Geometrically, the transducers were located at the center of gravity and at the top of an equilateral triangle with sides measuring 40.7 mm.

The transducers were placed on the mother's abdomen. They transmitted a sinusoidal pulse at 2.25 MHz with a pulse repetition frequency (PRF) of 1 kHz. Note that a theoretical accuracy of $60/2/1000 = 0.03$ bpm can be achieved with this value of 1 kHz and accuracy can be still further improved by performing interpolation of the correlation function. The wave was propagated through the mother's abdomen towards the fetal heart. The backscattered signal was recorded from five different depths, annotated D_1, \dots, D_5 . Note that only one channel was considered in the present study.

The ultrasound signal received was converted into an electrical signal and amplified to compensate for the attenuation of 1 dB/cm/MHz. The signal was then demodulated in phase (I) and quadrature (Q) [19]. After demodulation,

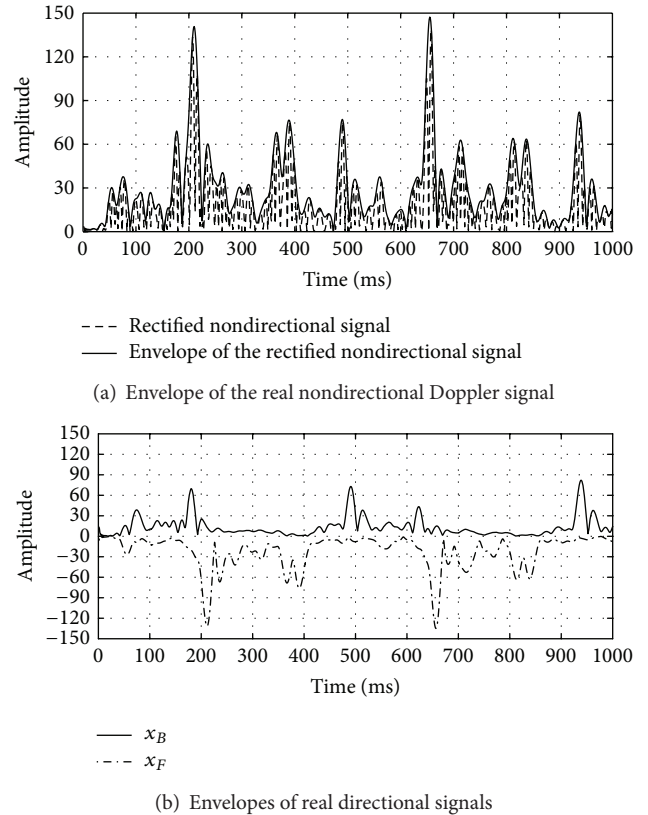


FIGURE 1: A real Doppler signal (PRF = 1 kHz) of 1000 ms, recorded with the second transducer in the fourth-channel: (a) Doppler signal (dashed line) and its envelope (solid line); (b) the envelopes of directional signals corresponding to ultrasound scatters approaching to the transducer (solid line) and moving away from the transducer (dash-dot line), respectively.

the signals were digitized. The digital outputs of the converters represented the digital Doppler signal.

2.2. Patients. The Doppler signals were acquired at the CHRU “Bretonneau” Tours, France. The consent of each patient was obtained and the study was approved by the Ethics Committee of the Clinical Investigation Centre for Innovative Technology of Tours (CIC-IT 806 CHRU of Tours). Patients were older than eighteen years and all pregnancies were single. The recordings were made during the twenty-fifth and fortieth gestational weeks. Evolution during pregnancy was normal for all fetuses.

2.3. Simulation. Because it was difficult to quantify the effectiveness of the estimation techniques directly on real signals and because there was no suitable model, we generated synthetic signals. These synthetic signals were used as a ground-truth to evaluate the effectiveness of each estimator. To make these signals as realistic as possible, we proceeded in two stages: an analyzing stage deducing the characteristics of the real Doppler signal envelope and a synthetic phase providing realistic simulated signals. Figures 1(a) and 1(b) show 1000 ms of the envelope of a real nondirectional Doppler signal

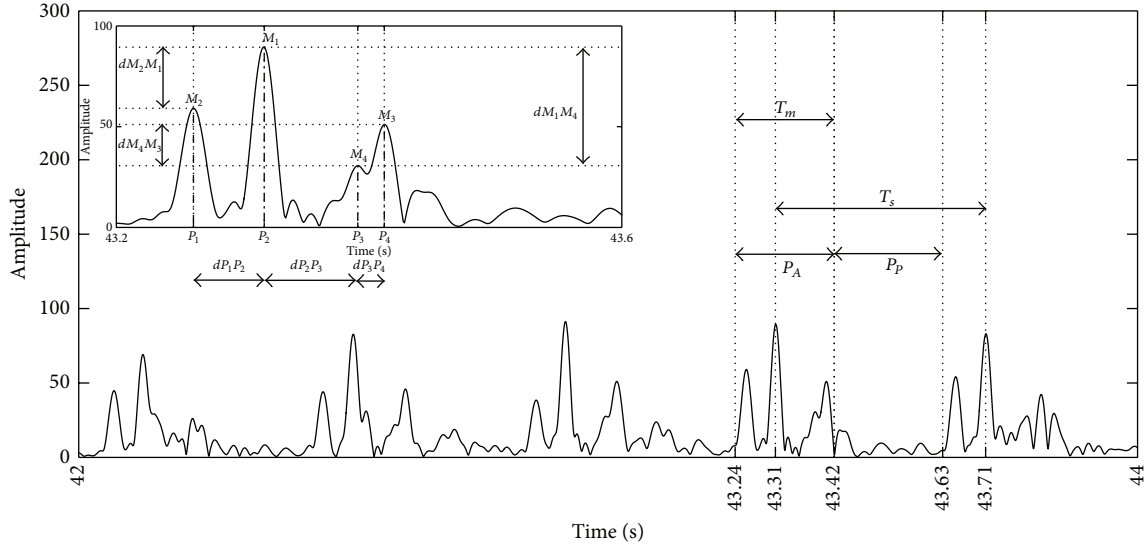


FIGURE 2: Envelope of a real directional Doppler signal of 2000 ms. The parameters defining the synthetic signal are the amplitudes and durations of peaks, the lag, and the differences in amplitude of two consecutive peaks over time.

and the two envelopes of corresponding directional signals obtained from the I and Q signals [19, 20]. The synthetic envelope signal was calculated as follows:

$$x_e(t) = x_B(t) + x_F(t), \quad (1)$$

where $x_B(t)$ and $x_F(t)$ are the envelopes of directional Doppler signals produced by the scatters that approach and move away from the transducer, respectively.

We verified (Figures 1(a) and 1(b)) that the envelope of the real nondirectional Doppler signal had the signatures of both envelopes of the directional signals. For example, at around 500 ms, the envelope of the nondirectional signal was mainly influenced by scatters that approached the transducer, while at around 400 ms, we observed the influence of movements away from the transducer. The alternating influence of these two movements determined the envelope of the nondirectional signal.

2.3.1. Analysis of Real Directional Signals. Figure 2 shows 2000 ms of the envelope of a real directional Doppler signal. In order to find the important parameters required for the synthesis of this signal, we extracted its intrinsic features (the number and amplitudes of the peaks, the lags between the peaks, and the differences in amplitude between the peaks). The values of these parameters were evaluated by considering a quasiconstant fetal heart rate.

Figure 2 represents a sequence of several patterns. These patterns were made up of peaks that corresponded to cardiac wall and valve movements of the fetal heart. As suggested by Shakespeare et al. [21], although six peaks (atrial contraction, ventricular contraction, opening and closing of the mitral valves, and opening and closing of the aortic valves) could be detected theoretically, only a few peaks were in practice detected in the nondirectional Doppler signal. From our

analysis, it appeared that the most likely pattern was that with four peaks. Note that this signature composed of four peaks could vary considerably from one beat to another, and it was similar to that identified by Jezewski et al. [13]. Among all these patterns, the most likely was the pattern with peaks in the order 2143; that is, the highest peak M_1 was in second position, the second highest peak M_2 was in first position, and so forth. For the 2143-pattern, we evaluated the amplitudes of each peak (M_1 , M_2 , M_3 , and M_4), the peak durations (T_1 , T_2 , T_3 , and T_4), the lags between two consecutive peaks (dP_1P_2 , dP_2P_3 , and dP_3P_4), and the differences in amplitude between two consecutive peaks (dM_2M_1 , dM_1M_4 , and dM_4M_3). The results of this statistical analysis are reported in Table 1.

As the patterns observed in Figure 2 were noisy, we decided to assess the noise level in order to simulate noisy synthetic Doppler signals. We assessed the signal to noise ratio (SNR) as follows:

$$\text{SNR} = 10 \cdot \log_{10} \left(\frac{P_A}{P_P} \right), \quad (2)$$

where P_A and P_P are the powers of the active and passive regions, respectively. We considered the active region as the area containing the pattern peaks, whereas there were none in the passive region. Using (2), we found that the SNR calculated on our real signals corresponded to a Gaussian law: $\text{SNR} \sim N(11, (\sqrt{2.5})^2(\text{dB}))$.

2.3.2. Synthesis of Synthetic Directional Signals. Analysis of the envelope of directional signals showed the presence of four peaks, which appeared in order 2143 inside the periodic patterns. The synthesis of such a signal must account for

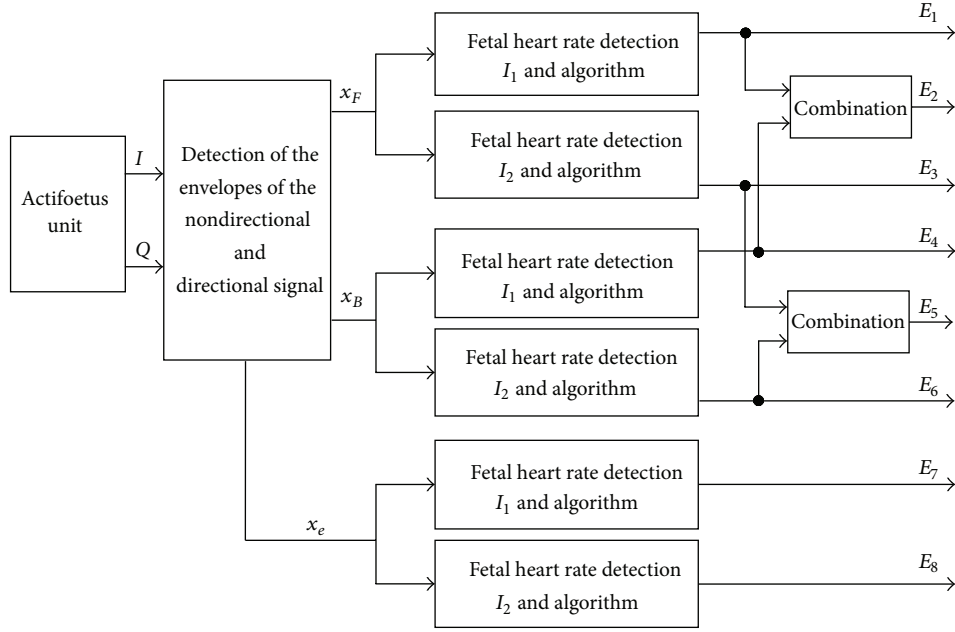


FIGURE 3: General diagram of the Doppler data processing acquired using one transducer and one channel. x_F and x_B represent the envelopes of the directional signals, and x_e represents the envelope of the nondirectional signal. I_1, I_2 are the two autocorrelation estimators.

TABLE 1: Statistics evaluated using (2143) patterns: M_i represents the statistics of the maxima, where $i = 1, \dots, 4$, $dP_1P_2, dP_2P_3, dP_3P_4$ represent the differences between the positions of two adjacent maxima over time; $dM_2M_1, dM_1M_4, dM_4M_3$ represent statistical differences between two adjacent maxima over time, and T represents the statistics of the peak durations. We found that the statistics of the four peaks of $T_i, i = 1, \dots, 4$, were identical.

	Law	
	Gaussian	Uniform
M_1	89.06 ± 31.48	
M_2	69.70 ± 21.84	
M_3	54.80 ± 19.21	
M_4	36.28 ± 18.28	
dM_2M_1		(5-50)
dM_1M_3		(5-50)
dM_3M_4		(5-40)
dP_1P_2	41.50 ± 18.18	
dP_2P_3	92.92 ± 27.76	
dP_3P_4	47.81 ± 30.09	
T (ms)		(25-45)

these characteristics. Equation (3) shows the two possible components of such a signal:

$$x_B(t) = \begin{cases} b(t) + \sum_{i=1}^4 M_i \sin\left(2\pi f_i \left(\theta + \frac{T_i}{2}\right)\right) \text{Rect}_{T_i}(\theta), & \forall t \in [0, T_m], \\ b(t), & \forall t \in (T_m, T_s], \end{cases} \quad (3)$$

where $b(t)$ is the noise, M_i is the peak amplitude, $f_i = 1/(2T_i)$ is the peak frequency, $\text{Rect}_{T_i}(\theta)$ is the unit rectangular function centered on T_i with width T_i and $\theta = t - T_i$, T_m is the pattern duration, and T_s is the synthetic signal period. We set a constant interval T_s between the highest peaks of two consecutive patterns of the synthetic signal, as illustrated in Figure 2. We also chose the T_m pattern period as 50% of the synthetic cardiac cycle period T_s , since this period can vary between 40 and 60% [22].

Using (3), we generated two synthetic noisy envelopes corresponding to the envelopes of the directional signals. The envelope of the nondirectional synthetic signal was modeled using (1), being the sum of the envelopes of the both directional synthetic signals. In order to simplify our study, only $x_B(t)$ was calculated, $x_F(t)$ being a delayed and amplified version of $x_B(t)$. To simulate realistic signals, we introduced a lag τ between the directional components:

$$x_F(t) = \alpha x_B(t - \tau), \quad (4)$$

where $x_F(t)$ and $x_B(t)$ are the envelopes of directional signals and τ is the lag between the two envelopes. α is a factor that represents the amplitude ratio between the two types of envelope. From Figure 1, $\tau \approx 40$ ms and $\alpha \approx 2$.

2.4. Estimators. In this section, we describe the different estimators used in our study. Each estimator that was based on the autocorrelation function was denoted by $E_i, i = 1, \dots, 8$, as illustrated in Figure 3. Each estimator operated on different signals: $x_F(t)$, $x_B(t)$, and $x_e(t)$.

Devices existing on the market currently use the $x_e(t)$ envelope and autocorrelation. The estimators that used these configurations were E_7 and E_8 . The mathematical expression

of the two autocorrelation estimators is given in [23] and is represented thereafter by

$$I_1(t, k) = \frac{1}{W} \sum_{n=0}^{W-|k|-1} x(t, n) \cdot x(t, n+k); \quad (5)$$

$$I_2(t, k) = \frac{1}{W} \sum_{n=0}^{W-1} x(t, n) \cdot x(t, n+k),$$

where W is the size of the analyzing window, t is the time for which the estimator is computed, and k is the lag. $x(t)$ represents one of the signals analyzed ($x_F(t)$, $x_B(t)$, or $x_e(t)$).

We tested other estimators (E_1, \dots, E_6) which used directional signals $x_F(t)$ and $x_B(t)$, together with I_1 and I_2 .

2.4.1. Algorithm. The algorithm to estimate the fetal heart rate was the same for all three signals ($x_e(t)$, $x_F(t)$, and $x_B(t)$). The steps of the algorithm were as follows.

- (1) Extract from each signal under consideration ($x_e(t)$, $x_F(t)$, or $x_B(t)$) a limited number W of samples, W being the window size.
- (2) Compute $I_1(W)$ and $I_2(W)$.
- (3) Using an empirical threshold, detect the position of N peaks in $I_1(W)$ and $I_2(W)$.
- (4) From the position of N peaks of $I_1(W)$ and $I_2(W)$, determine the durations D_i between consecutive peaks with $i = 1, 2, \dots, N - 1$.
- (5) Calculate the $N - 1$ cardiac frequencies with $CF_i = 60/D_i$, $i = 1, 2, \dots, N - 1$. This conditional test limits the number of cardiac frequencies CF_i estimated from I_1 or I_2 in the average computation. This conditional test also permits removal of cardiac frequency estimates that are half the expected value, as are sometimes observed (Shakespeare et al. [21]).
- (6) Calculate the average cardiac frequency (FHR) from CF_i not exceeding 35 bpm [13]:

$$\text{FHR} = \frac{1}{N-1} \sum_i^{N-1} CF_i. \quad (6)$$

As an illustration, consider a window of 4.096 s. Whenever the cardiac frequency was 240 bpm, 16 peaks were observed in the autocorrelation function. Using an empirically set threshold, the duration between each peak was measured ($D_1 = 0.250$ s, \dots , $D_{15} = 0.250$ s) and cardiac frequencies of $CF_1 = 60/0.250$ bpm, \dots , $CF_{15} = 60/0.250$ bpm were estimated. The average cardiac frequency was obtained by $\text{FHR} = (1/15) \sum_i^{15} CF_i = 240$ bpm. Note that 4 peaks were observed with 60 bpm and $D_1 = 60/1.0 = 1.0$ s, \dots , $D_3 = 60/1.0 = 1.0$ s were estimated. The average cardiac frequency was obtained by $\text{FHR} = (1/3) \sum_i^3 CF_i = 60$ bpm.

Thus the proposed algorithm correctly worked in the range of 60–240 bpm. However, the standard deviation of the FHR estimation was not the same for its extreme values since in one case the average was obtained with three values

whereas the average was obtained with fifteen values in the other.

Note that such an algorithm is not perfect since it is hypothesised that the FHR is constant during the process. Sometimes the second peak of the autocorrelation can be lower than the third and the FHR estimate is incorrect. A process must be performed to remove outliers.

2.4.2. Elimination of Outliers. In order to eliminate outlier estimates associated with estimator dysfunction, we introduced a postprocessing step. This postprocessing step was applied only in the case of real signals. An estimate was considered to be an outlier if it laid outside the statistic computed from 40 previous estimates, or if it differed between two consecutive analysis windows by 35 bpm.

2.4.3. Combination. In order to improve the effectiveness of the FHR estimation, we combined estimations. For E_2 and E_5 , the two values of the fetal heart rate estimated on signals $x_F(t)$ and $x_B(t)$ were combined. The estimate on the two signals was achieved using I_1 or I_2 . The combination rule we used was as follows:

- (i) if the heart rate was detected on a single signal, the combined value took this value;
- (ii) if the heart rate was detected on both signals, the combined value was the average of the two values.

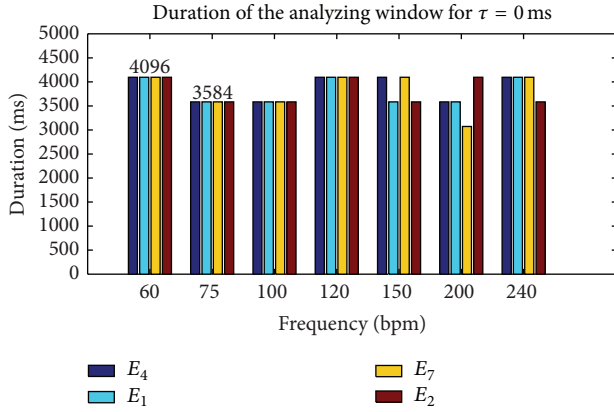
Note that, in contrast to Kret's study [16], we combined the fetal heart rates estimated on both directional Doppler signals, while Kret's technique was based on combination of fetal heart rate estimations computed after discrete wavelet decomposition of the envelope of the directional Doppler signal. Since Kret's technique was applied only for continuous Doppler signals, it was not taken into consideration in our study.

3. Results

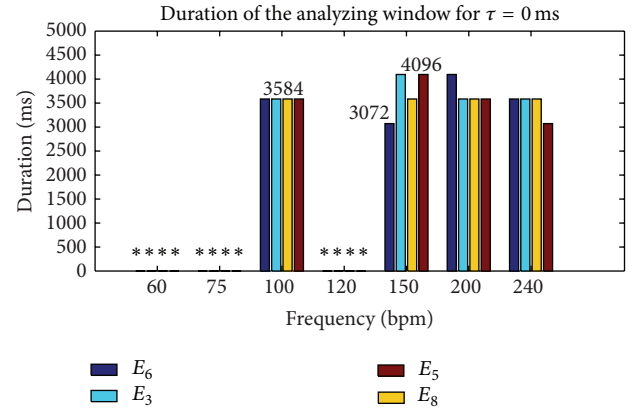
To find the best estimators and the conditions in which they could be used, we performed a series of simulations and experiments. Using simulations, we sought configurations that ensured an error of estimation, that is, the expected accuracy below 0.25 bpm, the highest sensitivity, and the lowest false negative rate. Experimentally, we sought the best configuration for optimal use of the estimator.

3.1. Simulated Signals. We present the results from two types of simulation. In the first series of simulations, we sought parameter settings that ensured the desired accuracy of 0.25 bpm. In the second series of simulations, we evaluated the effectiveness of each estimator in terms of true positive rate and false negative rate.

3.1.1. Optimal Parameter Settings. The results presented in Figures 4 and 5 were obtained for synthetic signals of 30 s. The parameters that varied in our analysis were the periodicity of the signal T_s , the SNR, the window size W , and the lag

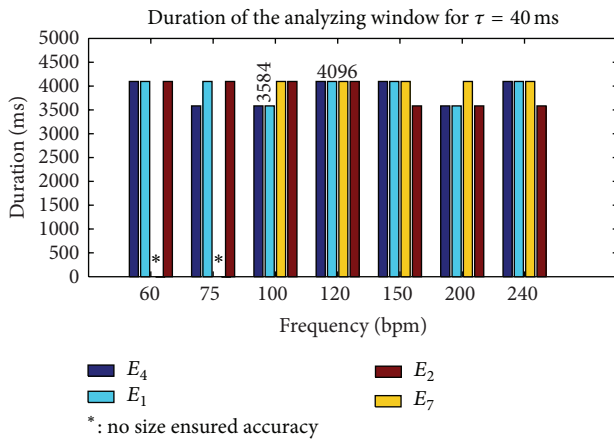


(a)

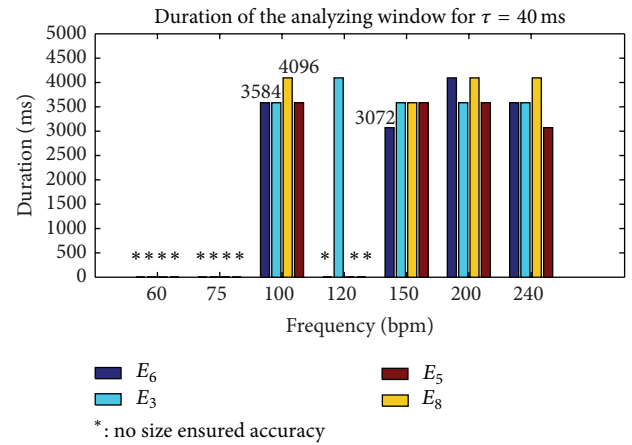


*: no size ensured accuracy

(a)



(b)



*: no size ensured accuracy

(b)

FIGURE 4: Duration of the analyzing window W required to reach an error of at least 0.25 bpm with the autocorrelation estimator (I_1) and a SNR > 0.6 dB.

τ . We varied the signal periodicity T_s between 1000 and 250 ms, as these values corresponded to the standard range of exploration (60–240 bpm) of different fetal monitors. The SNR range varied between 0 and 14 dB, in order to include our measured SNR values on the real signals and in order to take into account the worst cases. The range of W size varied between 512 and 4096 ms. The highest fetal heart rate could be obtained with a window size of 512 ms, although we limited the maximum window to 4096 ms to reduce computation time.

Figures 4 and 5 show the smallest window size analyzed ($W = 4096$ ms) of all estimators tested that ensured the expected accuracy of 0.25 bpm in the range of 60–240 bpm and that ensured a SNR at least greater than 0.6 dB. Note that for estimator I_2 reported in Figure 5, we showed that there was no size which ensured the desired accuracy, whatever the SNR or the frequency. To test estimator robustness in relation to the increasing complexity of the simulated signals, the lag τ varied between 0 and 40 ms, this value of 40 ms being taken from Figure 1.

The results derived from Figure 4 showed that accuracy for the envelope signal (estimator E_7) was no longer achieved

FIGURE 5: Duration of the analyzing window W required to reach an error of at least 0.25 bpm with the autocorrelation estimator (I_2) and with a SNR > 0.6 dB.

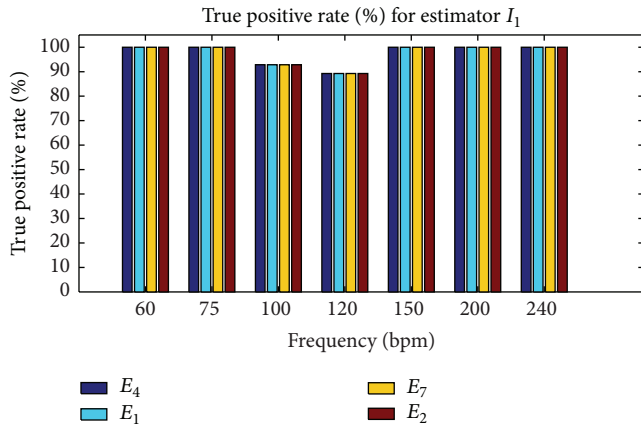
for certain frequencies, but it still was for directional signals. Finally, Figure 5, shows the best estimators (E_1, E_2, E_4) and their respective best parameter settings ($W = 4096$) that ensured an accuracy of 0.25 bpm with a SNR > 0.6 dB in the 60–240 bpm range.

To summarize, these first results showed the superiority of I_1 compared to I_2 and the superiority of the envelope of directional signals compared to that of nondirectional signals. We therefore recommend the use of I_1 and the estimators (E_1, E_2 , and E_4) based on the envelope of directional signals.

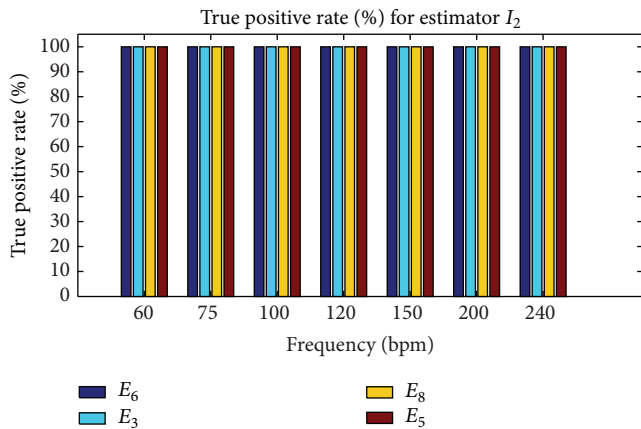
3.1.2. Performance Levels of Estimators. In this study, the performance levels of estimators we wanted to compute were sensitivity and the false negative rate. Fetal heart rates were evaluated every 250 ms from noisy signals with $W = 4096$ ms. Sensitivity was computed with the equation: $S = TP/(TP + FN)$, where TP was the true positive rate and FN was the false negative rate. Estimates of simulated heart rate were considered to be false negative if they did not ensure the expected accuracy; otherwise, they were true positive. Sensitivity and the false positive rate were evaluated as the

TABLE 2: FHR error of estimation (bpm) obtained by all estimators tested for different configurations of SNR, false negative rate (FNR), and $W = 4096$ ms.

Estimators	FHR error of estimation (bpm)		
	E_1, E_2, E_4, E_7	E_3, E_5, E_6	E_8
FNR = 0%, 6 dB > SNR > 2 dB	0.8	4	6
FNR = 1.5%, SNR > 6 dB	0.25	—	—



(a)



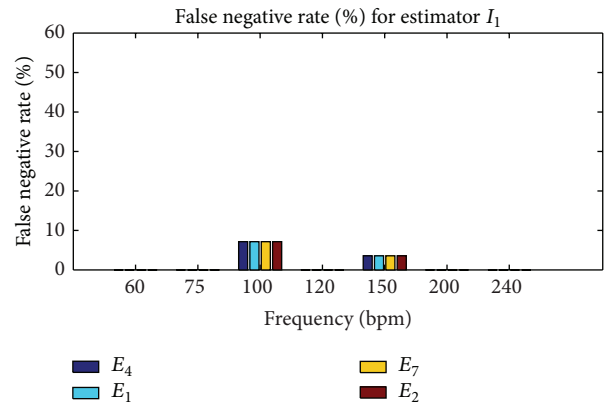
(b)

FIGURE 6: True positive rates for I_1 and I_2 with SNR > 0.6 dB, $W = 4096$, and an error of estimation of 0.25 bpm. (a) True positive rate for I_1 . (b) True positive rate for I_2 .

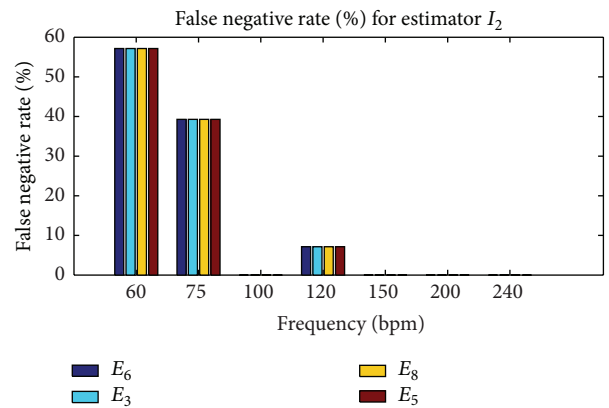
average of 30 values. Each value was determined after analysis of a noisy signal of 30 s where sensitivity and the false positive rate had converged to the highest value and to the lowest value, respectively. Convergence was reached for a minimum SNR of 6 dB.

The results of this second series of simulations are presented in Figures 6 and 7 for $W = 4096$ ms and SNR ≥ 6 dB. Note that the estimation of error of 25 bpm was obtained only for I_1 whatever the frequency, whereas accuracy for I_2 was obtained only for 100, 150, 200, 220, and 240 bpm.

The results set out in Figure 7 show that estimators based on I_1 ($E_1, E_2, E_4,$ and E_7) had an average (average obtained from the cardiac frequency) false negative rate of 1.5%, while those based on I_2 ($E_3, E_5, E_6,$ and E_8) presented a higher



(a)



(b)

FIGURE 7: False negative rates for I_1 and I_2 with SNR > 0.6 dB, $W = 4096$. Accuracy of 25 bpm was obtained only for I_1 whatever the frequency, whereas for I_2 accuracy was obtained for only 100, 150, 200, 220, and 240 bpm. (a) False negative rate for I_1 . (b) False negative rate for I_2 .

average false negative rate of approximately 14.8%. The 97.5% average true positive rate of I_1 was slightly lower than that of estimators based on I_2 , which was 100%. Finally, when the accuracy of 0.25 bpm was reached, we observed that the estimators based on I_1 were generally more accurate than those based on I_2 , although the average false negative rate was not zero.

Figure 8 shows the error of estimation corresponding to different values of SNR when a zero false negative rate was imposed. This zero false negative rate was obtained by modifying the detection threshold, and a direct consequence was an increase in the estimation. The results derived from Figure 8 showed that the zero false negative rate for I_1 was

TABLE 3: Sensitivity (%) of estimators for $W = 4096$ ms. I_1 and I_2 are the two autocorrelation estimators, respectively. x_B , x_F are the envelopes of directional signals, and x_e is the envelope of the nondirectional signal. Fus indicates the combined estimator.

Sensitivity (S)	Estimators	
	I_1	I_2
$S(x_B)$	88.50% (E_4)	88.43% (E_6)
$S(x_F)$	86.63% (E_1)	84.79% (E_3)
$S(x_e)$	81.79% (E_7)	75.05% (E_8)
$S(Fus)$	95.48% (E_2)	94.93% (E_5)

ensured for a SNR ≥ 2 dB (below the SNR measured on real signals) and for an error of estimation of 0.8 bpm. In the case of I_2 and directional signals, we obtained an error of estimation of 4 bpm, whereas for a nondirectional signal it was 6 bpm.

Table 2 summarizes the effectiveness of each estimator in terms of FHR error of estimation, SNR, and average false negative rate. To reach an error of estimation, that is, the expected accuracy of 0.25 bpm, we recommend I_1 , that is, autocorrelation-based estimators (E_1 , E_2 , E_4 , and E_7), the price to be paid being an average false negative rate of 1.5%. To reach an average false negative rate of 0%, we recommend I_1 autocorrelation-based estimators (E_1 , E_2 , E_4 , and E_7), where the price to be paid is an error of estimation of 0.8 bpm far from the expected accuracy of 0.25 bpm.

3.2. Results Obtained on Real Signals. We recorded 580 minutes for the analysis of real Doppler signals. We selected areas where signals had the cardiac activity signature. The performance levels on these signals were evaluated on the envelopes of both the nondirectional and the directional signals. The FHR estimation obtained with a commercial device (Oxford Sonicaid) was used as a reference to evaluate sensitivity which was evaluated for each estimator. All estimators were evaluated using a size of $W = 4096$ ms.

The results obtained for all the signals are presented in Table 3. The estimators based on directional signals (E_1 , E_4 , E_3 , and E_6) provided a higher level of sensitivity compared to those which used nondirectional signals (E_7 , E_8). In the case of directional signals, the results of I_1 and I_2 were close but slightly better for I_1 . This result confirmed the results obtained by simulations. We therefore recommend the use of estimators based on I_1 calculated on the directional signals (E_1 , E_4).

Sensitivity was improved using the combination method. The sensitivity of estimator E_2 was 95.5% (see Table 3). Using the combination method, the sensitivity increased to about $(95.5\% - 88.5\%) \approx 7\%$ compared to directional signals E_4 and to about $(95.5\% - 81.8\%) \approx 14\%$ compared to nondirectional signals E_7 .

4. Discussion and Conclusion

In this study, we focused on different settings of the estimators (window size, lag) that ensured a fetal heart rate estimation

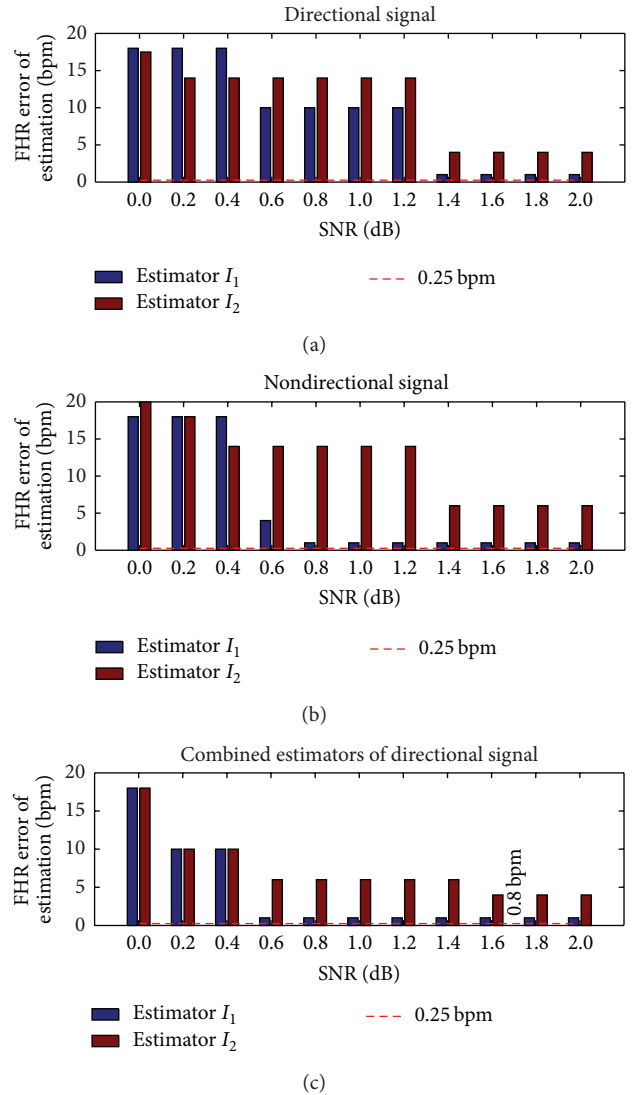


FIGURE 8: FHR error of estimation (bpm) when the false negative rate was zero, when the SNR $\in (0 \text{ dB}, 2 \text{ dB})$, and when the signals tested were x_F , x_B , and x_e .

with a maximum authorized error of 0.25 bpm. We found in simulation that only estimators based on I_1 and directional signals could ensure such an accuracy of 0.25 bpm. The size necessary in this case was $W = 4096$ ms.

Note that, although we proposed synthetic signals that were as realistic as possible, we are aware that the plotted performance levels are representative only of our simulations and not of all cases encountered in practice. It is likely that the performance levels of the algorithms tested can be reduced in the presence of artefacts. However, the 95% sensitivity obtained from real signals suggests that our proposed estimators may be trusted.

In the case of real signals, the sensitivity was quantified. Since in our study the estimated SNR on the real signals was greater than the threshold of 6 dB (deduced on simulated signals) required to reach the desired accuracy of 0.25 bpm, a denoising filter was not necessary. However, in cases of a

SNR lower than 6 dB, a denoising process (Wiener, wavelet) could be introduced.

Sensitivity was quantified using a W size of 4096 ms. We found that the estimators E_1 , E_2 , and E_4 based on I_1 had slightly greater sensitivity than those based on I_2 . We therefore recommend the use of I_1 .

Various cases were considered on the basis of this study, that is, those that do not require a precise estimate of the fetal heart rate and those for which accuracy is critical. The accuracy of fetal heart rate estimation in the first case is not important but the false negative rate should be as low as possible. For example, if the goal of a monitoring system is simply to verify that the fetal heart rate is in the normal range (110–160 bpm), very high accuracy is not needed. In this case, an error of estimation of 0.8 bpm is sufficient. Our computations showed that for an error of estimation of 0.8 bpm, a zero false negative rate in the zones when the rhythm is quasi-constant could be ensured. In the second case, an error of estimation of 0.25 bpm is required for a system in which the goal is not only to estimate the heart rate, but also to evaluate fetal wellbeing. Our study showed that for this type of system, the false negative rate may be slightly higher than zero. It is important to note that this error of estimation was guaranteed for a quasi-constant heart rate. This is not a constraint for such a system, since the variability of fetal heart rate must be evaluated in these ranges to predict fetal distress.

Applied to real signals, the estimators based on I_1 provided sensitivity close to those of I_2 , and the most efficient of these estimators were those that used directional signals (E_1 , E_2 , and E_4).

A 7% increase in sensitivity compared to estimators based on individual directional signals was possible when we combined the two heart rates calculated on the directional signals. A 14% increase in sensitivity compared to estimators based on individual nondirectional signals was possible when we combined the two heart rates calculated on the directional signals. When a combination was used, both signals were processed in parallel, thus doubling the number of operations.

The good levels of performance of our estimator based on this combination suggest first that it can be adapted to multitransducer, multichannel configurations and second that such an estimator will improve fetal diagnosis.

Conflict of Interests

The authors declare that there is no conflict of interests regarding the publication of this paper.

Acknowledgments

This study was supported by the Agence Nationale de la Recherche (Project ANR-07-TECSAN-023, Surfoetus). The authors would like to thank the Clinical Investigation Centre for Innovative Technology of Tours (CIC-IT 806 CHRU of Tours) and Professor F. Perrotin's Obstetric Department Team for their support in recording the signals. The authors

would like to thank the anonymous referees for their valuable comments.

References

- [1] F. Manning, I. Morrison, I. Lange, C. Harman, and P. Chamberlain, "Fetal assessment based on fetal biophysical profile scoring: experience in 12,620 referred high-risk pregnancies. I. Perinatal mortality by frequency and etiology," *The American Journal of Obstetrics and Gynecology*, vol. 151, no. 3, pp. 343–350, 1985.
- [2] H.-Y. Chen, S. P. Chauhan, C. V. Ananth, A. M. Vintzileos, and A. Z. Abuhamad, "Electronic fetal heart rate monitoring and infant mortality: a population-based study in the United States," *The American Journal of Obstetrics and Gynecology*, vol. 204, no. 6, pp. S43–S44, 2011.
- [3] G. G. Berntson, J. Thomas Bigger Jr., D. L. Eckberg et al., "Heart rate variability: origins methods, and interpretive caveats," *Psychophysiology*, vol. 34, no. 6, pp. 623–648, 1997.
- [4] M. Malik and A. J. Camm, "Heart rate variability," *Clinical Cardiology*, vol. 13, no. 8, pp. 570–576, 1990.
- [5] M. David, M. Hirsch, J. Karin, E. Toledo, and S. Akselrod, "An estimate of fetal autonomic state by time-frequency analysis of fetal heart rate variability," *Journal of Applied Physiology*, vol. 102, no. 3, pp. 1057–1064, 2007.
- [6] B. Arabin and S. Riedewald, "An attempt to quantify characteristics of behavioral states," *The American Journal of Perinatology*, vol. 9, no. 2, pp. 115–119, 1992.
- [7] B. Frank, B. Pompe, U. Schneider, and D. Hoyer, "Permutation entropy improves fetal behavioural state classification based on heart rate analysis from biomagnetic recordings in near term fetuses," *Medical and Biological Engineering and Computing*, vol. 44, no. 3, pp. 179–187, 2006.
- [8] S. Lange, P. Van Leeuwen, U. Schneider et al., "Heart rate features in fetal behavioural states," *Early Human Development*, vol. 85, no. 2, pp. 131–135, 2009.
- [9] J. A. DiPietro, D. M. Hodgson, K. A. Costigan, S. C. Hilton, and T. R. B. Johnson, "Fetal neurobehavioral development," *Child Development*, vol. 67, no. 5, pp. 2553–2567, 1996.
- [10] M. Ferrario, M. G. Signorini, G. Magenes, and S. Cerutti, "Comparison of entropy-based regularity estimators: application to the fetal heart rate signal for the identification of fetal distress," *IEEE Transactions on Biomedical Engineering*, vol. 53, no. 1, pp. 119–125, 2006.
- [11] A. Kikuchi, T. Shimizu, A. Hayashi et al., "Nonlinear analyses of heart rate variability in normal and growth-restricted fetuses," *Early Human Development*, vol. 82, no. 4, pp. 217–226, 2006.
- [12] G. S. Dawes, M. O. Lobbs, G. Mandruzzato, M. Moulden, C. W. G. Redman, and T. Wheeler, "Large fetal heart rate decelerations at term associated with changes in fetal heart rate variation," *The American Journal of Obstetrics and Gynecology*, vol. 188, no. 1, pp. 105–111, 1993.
- [13] J. Jezewski, J. Wrobel, and K. Horoba, "Comparison of Doppler ultrasound and direct electrocardiography acquisition techniques for quantification of fetal heart rate variability," *IEEE Transactions on Biomedical Engineering*, vol. 53, no. 5, pp. 855–864, 2006.
- [14] J. Pardey, M. Moulden, and C. W. G. Redman, "A computer system for the numerical analysis of nonstress tests," *The American Journal of Obstetrics and Gynecology*, vol. 186, no. 5, pp. 1095–1103, 2002.

- [15] E. Courtin, W. Ruchay, P. Salfeld, H. Sommer, and A. Versatile, "Semiautomatic fetal monitor for non-technical users," *Hewlett-Packard Journal*, vol. 28, no. 5, pp. 16–23, 1977.
- [16] T. Kret and K. Kaluzynski, "The fetal heart rate estimation based on continuous ultrasonic Doppler data," *Biocybernetics and Biomedical Engineering*, vol. 26, no. 3, pp. 49–56, 2006.
- [17] I. Voicu, D. Kouame, M. Fournier-Massignan, and J.-M. Girault, "Estimating fetal heart rate from multiple ultrasound signals," in *Proceedings of the International Conference on Advancements of Medicine and Health Care through Technology*, pp. 185–190, Berlin, Germany, September 2009.
- [18] A. Kribèche, F. Tranquart, D. Kouame, and L. Pourcelot, "The Actifetus system: a multidoppler sensor system for monitoring fetal movements," *Ultrasound in Medicine and Biology*, vol. 33, no. 3, pp. 430–438, 2007.
- [19] J. A. Jensen, *Estimation of Blood Velocities Using Ultrasound*, Cambridge University Press, Cambridge, UK, 1996.
- [20] N. Aydin, L. Fan, and D. H. Evans, "Quadrature-to-directional format conversion of Doppler signals using digital methods," *Physiological Measurement*, vol. 15, no. 2, article 007, pp. 181–199, 1994.
- [21] S. A. Shakespeare, J. A. Crowe, B. R. Hayes-Gill, K. Bhogal, and D. K. James, "The information content of Doppler ultrasound signals from the fetal heart," *Medical and Biological Engineering and Computing*, vol. 39, no. 6, pp. 619–626, 2001.
- [22] E. Hernandez-Andrade, H. Figueroa-Diesel, C. Kottman et al., "Gestational-age-adjusted reference values for the modified myocardial performance index for evaluation of fetal left cardiac function," *Ultrasound in Obstetrics and Gynecology*, vol. 29, no. 3, pp. 321–325, 2007.
- [23] A. V. Oppenheim and R. W. Schaffer, *Discrete-Time Signal Processing*, Prentice-Hall Signal Processing, Prentice-Hall International, Englewood Cliffs, NJ, USA, 1989.

Research Article

Automatic Identification of Motion Artifacts in EHG Recording for Robust Analysis of Uterine Contractions

Yiyao Ye-Lin,¹ Javier Garcia-Casado,¹ Gema Prats-Boluda,¹
José Alberola-Rubio,¹ and Alfredo Perales²

¹ Grupo de Bioelectrónica (I3BH), Universitat Politècnica de València, Camino de Vera s/n Ed.8B, 46022 Valencia, Spain

² Servicio de Obstetricia, H. U. La Fe, Valencia, Spain

Correspondence should be addressed to Javier Garcia-Casado; jgarcia@gbio.i3bh.es

Received 31 May 2013; Accepted 14 October 2013; Published 9 January 2014

Academic Editor: Catherine Marque

Copyright © 2014 Yiyao Ye-Lin et al. This is an open access article distributed under the Creative Commons Attribution License, which permits unrestricted use, distribution, and reproduction in any medium, provided the original work is properly cited.

Electrohysterography (EHG) is a noninvasive technique for monitoring uterine electrical activity. However, the presence of artifacts in the EHG signal may give rise to erroneous interpretations and make it difficult to extract useful information from these recordings. The aim of this work was to develop an automatic system of segmenting EHG recordings that distinguishes between uterine contractions and artifacts. Firstly, the segmentation is performed using an algorithm that generates the TOCO-like signal derived from the EHG and detects windows with significant changes in amplitude. After that, these segments are classified in two groups: artifacted and nonartifacted signals. To develop a classifier, a total of eleven spectral, temporal, and nonlinear features were calculated from EHG signal windows from 12 women in the first stage of labor that had previously been classified by experts. The combination of characteristics that led to the highest degree of accuracy in detecting artifacts was then determined. The results showed that it is possible to obtain automatic detection of motion artifacts in segmented EHG recordings with a precision of 92.2% using only seven features. The proposed algorithm and classifier together compose a useful tool for analyzing EHG signals and would help to promote clinical applications of this technique.

1. Introduction

Monitoring uterine contractions is commonly used to estimate the time of an approaching labour. In spite of the fact that intrauterine pressure (IUP) is regarded as the *gold standard* in monitoring these contractions, its use in clinical practice is limited since it requires rupturing the membranes to place a catheter inside the uterus. This not only leads to delivery but may also increase the risk of intrapartum infection [1]. Hospitals often use a pressure transducer (TOCOdynamometer or TOCO) placed on the mother's abdomen for basic noninvasive monitoring of uterine activity, thus obtaining the frequency and duration of contractions. However, the TOCO is not a reliable technique, as the measurements obtained are by no means precise and depend to a large extent on the subjective criteria of the operator

[2–4]. Neither do they provide much additional information on the efficiency of contractions in order to decide whether parturition is near. However, in spite of these disadvantages, the technique is widely used in maternity clinics due to its non-invasive nature.

The electrohysterogram (EHG) is the recording of uterine electrical activity from the abdominal surface. Earlier studies have shown that the EHG signal is synchronized in time with the electrical signal generated by the myometrial smooth muscle, which is also related in time with uterine contractions in all animal species, including humans [2, 5, 6]. In addition, the EHG also provides relevant information for assessing the efficiency of contractions, due to the fact that as pregnancy advances and the time of birth approaches uterine electrical activity undergoes changes which are reflected in EHG signals temporal and spectral characteristics [2, 3, 5, 7, 8].

Moreover, recent studies have shown that conduction velocity and direction are associated with the contractions efficiency [8–11].

However, due to the difficulties involved in interpreting the information contained in EHG recordings, this non-invasive technique is still not used in clinical practice. In order to promote its clinical application different methods have been applied to extract from EHG record a signal which is similar to pressure recordings (TOCO-like signal), with which clinical staff are familiar [3, 12–16], and algorithms have been developed to allow contractions to be detected automatically in the TOCO-like signals [12, 14, 16]. The main problem associated with the extensive application of these algorithms lies in the fact that EHG recordings contain not only uterine electrical activity but also a series of physiological interference elements (maternal and fetal ECG, abdominal muscle activity, and baseline fluctuations) and motion artifacts [3, 12, 17]. The presence of the latter phenomena can completely distort the spectral power density [18–21] which could lead to misinterpretation of the results. In addition, the presence of such artifacts makes the automatic identification of contractions based on TOCO-like signals generated from the EHG signal extremely difficult [12]. This is the reason why so many authors consider it necessary to have the recordings segmented manually prior to data analysis by experts in identifying signal windows containing contractions [7, 22–24]. This is a crucial task as it has repercussions on the information that may subsequently be extracted. However, it is also laborious and costly, not to mention the fact that the results are partially dependent on the subjective criteria of the operator. The aim of this work was therefore to develop a tool that would provide automatic segmentation of EHG recordings while distinguishing between uterine contractions and artifacts, to promote the future clinical use of this non-invasive technique for dynamic uterine monitoring and predicting premature births.

2. Materials and Methods

2.1. Data Acquisition. Twelve recording sessions were carried out at the *Hospital Universitario y Politécnico la Fe* in Valencia (Spain) on twelve healthy women in the first stages of labor having uneventful singleton pregnancies. Estimated gestational period was 37–41 weeks. The study adheres to the Declaration of Helsinki and was approved by the Ethical Committee of the hospital. All the volunteers were informed of the nature of the study, briefed on the recording protocol, and signed the consent form. The duration of the sessions was between 30 minutes and two hours. Patients were asked to report about fetal movements they could identify. Maternal movements were written down by the examiner.

The subjects were prepared by applying abrasive paste to the skin surface to reduce electrode contact impedance. In each session, 5 monopolar EHG signals were acquired through 5 unshielded Ag/AgCl electrodes with 8 mm in recording diameter placed in the form of a cross in the subumbilical zone, as shown in Figure 1. This arrangement was chosen since the best EHG signal/noise ratio is obtained

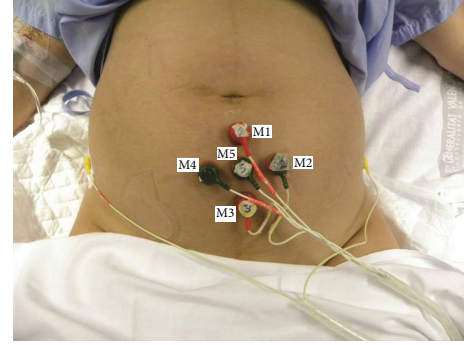


FIGURE 1: Configuration of contact electrodes for EHG recording.

close to the abdominal vertical midline, especially in the region immediately below the umbilicus [15]. Similar to other studies interelectrode distance was 25 mm [7, 8, 25] and the reference electrode was placed on the subjects' right hip [15, 24]. A third electrode was placed on the subjects' left hip and it was connected to the commercial bioamplifiers' ground terminal. All the monopolar EHG signals were amplified, analog bandpass filtered between 0.05 and 35 Hz (Biopac ECG100C), and acquired at a sampling frequency of 500 Hz.

At the same time a TOCOdynamometer was positioned on the abdominal surface together with an intrauterine pressure catheter (ACCU-Trace) to obtain the TOCO and IUP readings, respectively. The signals were conditioned in a commercial maternal/fetal monitor (Corometrics 170 Series, GE Medical Systems) and acquired at a sampling frequency of 4 Hz. All data were simultaneously stored in a PC for subsequent analysis.

2.2. Signal Preprocessing. Since EHG signal energy basically ranges from 0.1 to 3–5 Hz [5, 15, 26], a 5th order Butterworth bandpass digital filter between 0.1 and 4 Hz was used to eliminate undesirable components. Then monopolar EHG signals were downsampled at 20 Hz to reduce the computational cost of the data analysis. This sampling frequency is enough to compute the spectral parameters later described and showed no significant effects in the distribution of the nonlinear parameters studied in the next section. In this study, only the 4 bipolar EHG signals obtained from monopolar recordings were analyzed, since this configuration largely reduces the amount of interference present in monopolar EHG recordings [5, 15, 24, 27]:

$$\begin{aligned} B_1 &= M_1 - M_5; & B_2 &= M_5 - M_3; \\ B_3 &= M_4 - M_5; & B_4 &= M_5 - M_2, \end{aligned} \quad (1)$$

where M_i are the preprocessed EHG signals acquired by electrode i ($i = 1, \dots, 5$) and B_j ($j = 1, \dots, 4$) are the estimated bipolar signals.

As has been mentioned above, identifying uterine contractions in EHG recordings is usually performed by means of the TOCO-like signals derived from them [12, 14]. In the present study, in order to exclude from the analysis most of the artifact components due to motion, respiration, and

cardiac electrical signals, only frequency components in the 0.34–1 Hz (“uterine specific” range) [3, 22, 28] were used for generating the TOCO-like signal of the four bipolar signals. Concretely, two TOCO-like signals from bandpass filtered EHG bipolar signal were obtained by calculating the RMS value [12, 29] and the unnormalized first statistical moment of the frequency spectrum [15] of 30 s moving windows displaced every 0.25 s.

The TOCO-like signal segments with an amplitude significantly different to that of the baseline were then identified following a criteria similar to other authors’ proposals for automatic detection of contractions [12, 22]. The baseline activity of each TOCO-like signal was obtained with a 4-minute moving window displaced every 0.25 s, ordering the TOCO-like signal from highest to lowest values and calculating the average of the lowest 10% of values. The signal segments with an amplitude significantly different to that of the baseline were then identified when the TOCO-like signal amplitude remained at $> 2x$, the mean baseline activity, and at $> 25\%$, signal amplitude of each window for more than 30 s. A rise in amplitude in these segments could possibly have uterine origin, and would thus be due to a contraction, or could alternatively be caused by artifacts.

The corresponding segments in the EHG signal were classified as artifacted or non-artifacted signals by two experts (1 bioengineer and 1 clinician) with the help of the simultaneous TOCO and IUP recordings and the previously annotated events. Segments classified as artifacted signals should correspond in time to annotated events of mother or fetal movements, except for visually identifiable abrupt variations of the biosignals which were also considered artifacted signals since this behavior does not have an uterine physiological origin, and these episodes could have been missed in the annotated events. The segments classified as contractions (non-artifacted signals) had to correspond in time to uterine pressure events as measured by IUP and TOCO. In this study a segment of signals with both contraction and artifacts is considered to be an artifacted signal. We decided to work in this manner since when an artifact is present during a contraction it affects the signal parameters which could lead to misinterpretation of the EHG characteristics associated to that contraction. Only the segments in which the classification of both experts agreed were included in the design and test of the automatic classifier. A total of 277 EHG artifacted and 422 non-artifacted signal windows were used.

2.3. Feature Analysis. Motion artifacts in surface myoelectric recordings come in a wide range of waveforms according to the type of motion and the subject characteristics. Besides their presence is intermittent and unpredictable [18, 19]. For example, pulse-type motion artifacts often cause abrupt variations in the potential measured on the abdominal surface, while others are associated with a considerable rise in the potential amplitude. The presence of motion artifacts also affects the power spectral density (PSD) of the signal, distributing its energy in the high frequency range [18, 20]. In

this study, the following EHG signal features were proposed to detect their presence.

Spectral Parameters. To determine the energy distribution within the signal spectrum, the energy was calculated in certain frequency ranges [23]. Given the amplitude variations in the EHG signals obtained from the different channels and subjects during the sessions, this energy was normalized in relation to total energy. Three frequency ranges were defined to characterize energy distribution in the signal spectral domain (E_1 : 0.1–0.3 Hz; E_2 : 0.3–1 Hz; E_3 : 1–4 Hz):

$$E_j = \frac{\sum_{f_k=f_{0j}}^{f_{1j}} \text{PSD} [f_k]}{\sum_{f_k=0.1}^4 \text{PSD} [f_k]}, \quad (2)$$

where $\text{PSD} [f_k]$ is the bipolar signal PSD obtained from the periodogram with a Hamming window and f_{0j} and f_{1j} are the abovementioned lower and upper limits of the frequency band considered ($j = 1, 2, 3$).

Temporal Parameters. As previously mentioned, EHG signals containing artifacts often present sudden large amplitude variations. This can be characterized by means of parameters such as standard deviation (σ_x); relative amplitude (RA); kurtosis (κ); normalized maximum derivative in relation to standard deviation of the baseline (MD_{bs}); normalized maximum derivative in relation to standard deviation of the signal under study (MD_x); and the ratio between the RMS value of the segment of the signal under study and the RMS of the baseline extracted from the same channel and the same recording (R_{RMS}):

$$\begin{aligned} \text{RA} &= \frac{\max \{x_i\} - \min \{x_i\}}{\sigma_x}, \quad i = 1, \dots, N, \\ \text{MD}_{bs} &= \frac{\max \{|x_i - x_{i-1}|\}}{\sigma_{bs}}, \quad i = 2, \dots, N, \\ \text{MD}_x &= \frac{\max \{|x_i - x_{i-1}|\}}{\sigma_x}, \quad i = 2, \dots, N, \end{aligned} \quad (3)$$

where x_i is the i th sample of the bipolar EHG signal, N is the number of samples in the window length, σ_x is the standard deviation of the signal under study, and σ_{bs} is the standard deviation of the baseline extracted from the same channel of the same recording session.

Nonlinear Parameters. The presence of artifacts in an EHG signal may affect the signal non-linearity properties, such as regularity or complexity of finite length time series which can be measured by the sample entropy (E_n). This nonlinear technique seems to be an appropriate quantitative tool to measure the variability of underlying physiological mechanisms. It has been shown to discriminate between EHG signals of term and preterm deliveries [30], and it has been used for detection of eye blink artifact in multichannel EEG data [31]. We established a signal pattern dimension $m = 3$ and a pattern matches margin $r = 0.15$ to obtain the parameter

sample entropy. In addition time reversibility of the surrogate time series (T_r) was calculated. Probabilistic properties of artifacted signals are expected to be more susceptible with respect to time reversal than non-artifacted signals. The difference between the time reversibility of the original data and the surrogates was quantified as the measurement of signal non-linearity. For this the z score value was computed:

$$z = \frac{|T_{r\text{orig}} - \langle T_{r\text{surr}} \rangle|}{\sigma_{T_{r\text{surr}}}}, \quad (4)$$

where $T_{r\text{orig}}$ is the time reversibility of the original data, $T_{r\text{surr}}$ denotes the time reversibility for the 100 computations of the surrogate time series, and $\sigma_{T_{r\text{surr}}}$ is the standard deviation. The definition of the signal time reversibility and the method for generating surrogate time series is described in previous works [32].

2.4. Feature Selection. An important aspect in the design of a classifier is the selection of the features involved in it. The use of a single or a limited number of these could adversely affect the classifier accuracy due to lack of information. On the other hand, too many features could also give rise to an excess of information and over-training of data, which would also affect the classifier performance [33]. We opted for first determining which features contained the best information for distinguishing between EHG signals with and without artifacts and thus implemented a single-feature classifier in order to determine its individual discriminatory capacity [18]. Then the combination of features that gave maximum classifier accuracy in detecting artifacts by means of the sequential forward feature selection algorithm was found. The latter consists of an iterative process that checks whether or not the addition of a new feature will reduce classification errors and then selects the one with the least errors.

2.5. Design of the Classifier. In the present study, linear (LDA) and quadratic discriminant analysis (QDA); and support vector machine (SVM) classifier using RBF kernel was implemented. In order to determine the generalization capacity of the new data classifiers, in a first stage signals from ten patients were used (392 nonartifacted contractions and 253 artifacted segments). Specifically, two-fold cross-validation was used, with 50% of the data being used for training and 50% for validation [22]. In the second stage, classifiers were tested using signals from 2 additional patients (30 non artifacted contractions and 24 artifacted segments). Due to the random nature of the set of data used for training and validating, the cross-validation process was carried out 50 times to minimize bias. For each set of training data, various classifiers based on LDA and QDA and SVM (RBF kernel with optimized parameters) were implemented to distinguish between signals with and without artifacts. For each set of training data, optimal parameters for SVM classifier were carried out using the simplex method. All sets of data were then examined using these classifiers. Finally, classifier accuracy, sensitivity, specificity, positive predictive value (PPV), and negative predictive value (NPV) were analyzed and compared while using the best combination of features.

3. Results

Figure 2 shows a box and whisker plot of the 11 features of the EHG signals corresponding to Group 1 (no artifacts) and Group 2 (with artifacts). It can be seen that the presence of artifacts in the signal significantly raises the spectral content in the high frequency range (1–4 Hz, E_3). By contrast, even though differences were found in the spectral content in the 0.1–0.3 Hz (E_1) and 0.3–1 Hz (E_2) frequency ranges in both groups, the distribution of these two features is completely overlapping. In the temporal parameters, the presence of artifacts is also associated with a significant rise in the values of parameters RA, κ , MD_{bs} , and MD_x . On the other hand, even though the standard deviation of the signal (σ_x) and the R_{RMS} feature in EHG signals with artifacts tends to be higher than in signals with no artifacts, the distribution of these parameters shows considerable overlapping between both groups. As expected, the signals containing artifacts present a higher degree of nonlinear behavior as evidenced by the higher time reversibility z -score value, although the sample entropy in both groups is completely overlapping.

Table 1 shows the average accuracy of the single-feature classifier of the three classifiers obtained from the training and validation set of data. In general, SVM provided slightly better results than QDA, and this latter permits to achieve better accuracy than LDA. It can be seen that an accuracy higher than 75% can be obtained with the E_3 , RA, κ , MD_{bs} , and MD_x features for the three classifiers. The sequential forward feature selection algorithm provided a set of 7 features as the best combination of features for both QDA and SVM, 5 of them being common for both classifiers which provide complementary information among them. Table 2 gives the classifiers' accuracy for artifact detection in EHG signal using the best combination of features for QDA classifier, which are: E_3 , RA, κ , MD_{bs} , MD_x , E_n , and T_r . The optimal combination of specific features for LDA and SVM provided similar results to those shown in Table 2, with a difference less than 1%. It can be seen that LDA classifier presents the lowest accuracy values whereas similar results were obtained for QDA and SVM mean accuracy for the training and validation data set (92.1% and 93.3%, resp.). Nevertheless, for the test data set QDA clearly provided the highest accuracy values. Tables 3 and 4 show the values of additional prediction parameters for the training and validation and for the test data sets, respectively. Again it can be observed that LDA provides the worst results and that SVM and QDA present similar performance for the training and validation data set. In general it can be observed that the classifiers obtained higher PPV and specificity than NPV and sensitivity. This is probably due to the unbalanced database which contains a higher number of non-artifacted windows than of artifacted windows. Finally, it should be pointed out that the poorer performance of SVM in the test data set in comparison to QDA is also manifested in Table 4. This will be discussed in the next section.

Figure 3(a) shows a bipolar signal from an EHG register taken during the early stages of labor; the other three bipolar signals are not shown due to space issues. Figure 3(b) shows the corresponding TOCO-like signals using the RMS-based algorithm (grey line) and the unnormalized first statistical

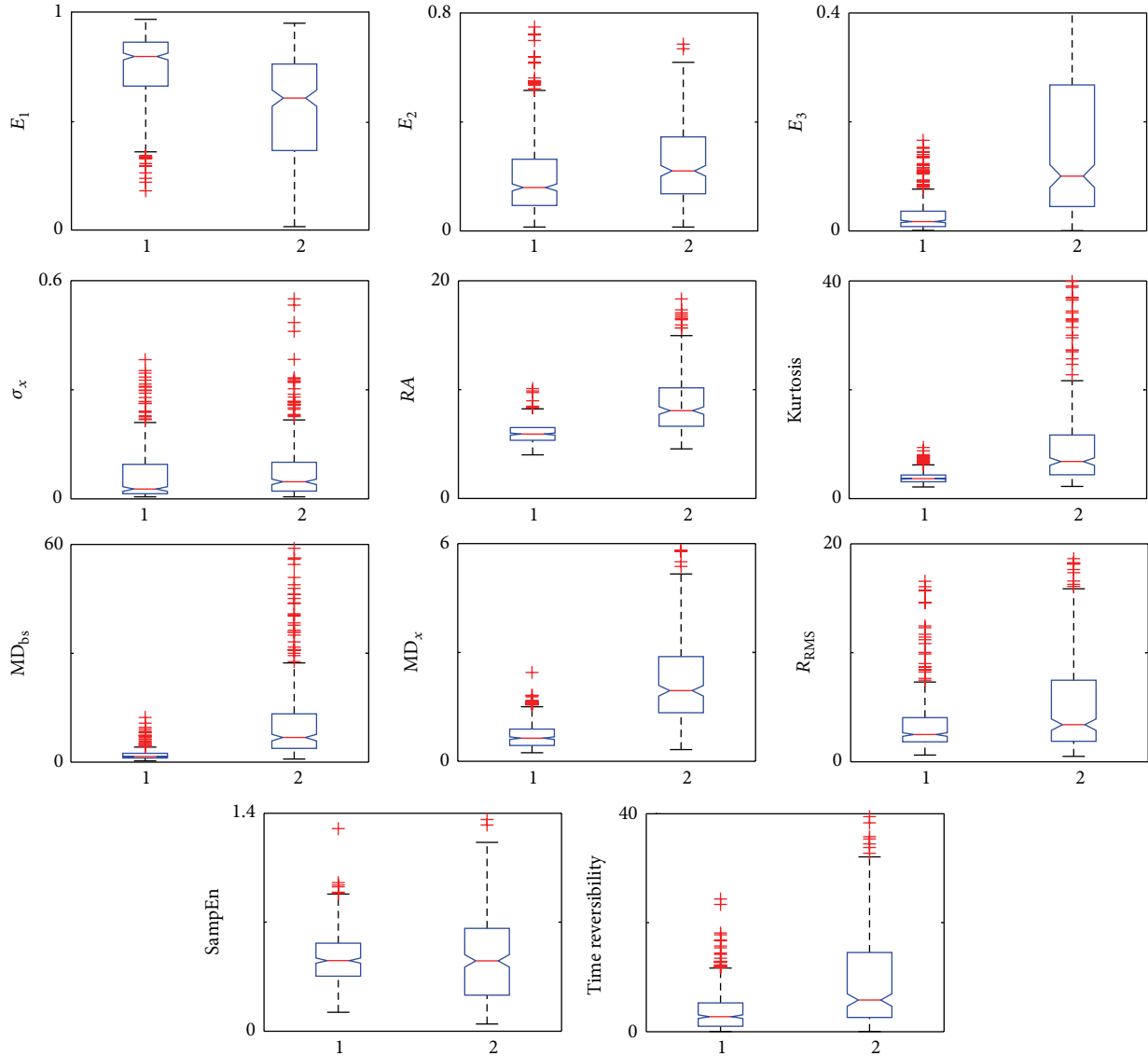


FIGURE 2: Influence of motion artifacts on EHG features. 1: non-artifacted EHG signal windows. 2: artifacted EHG signal windows. The feature E_3 upper quartile value for artifacted EHG signals (Group 2) is out of scale.

TABLE 1: Mean accuracy (%) of classifiers using a single feature for detecting motion artifacts (training and validation data set, 392 nonartifacted contractions versus 253 artifacted segments).

	E_1	E_2	E_3	σ_x	RA	κ	MD_{bs}	MD_x	R_{rms}	E_n	T_r
LDA	70.6	61.2	78.5	55.7	80.9	76.9	76.0	85.3	66.2	54.6	67.4
QDA	71.4	61.6	78.8	59.0	80.8	78.7	78.1	86.2	65.5	69.6	69.5
SVM	70.9	62.6	82.1	63.6	80.9	79.9	83.4	87.6	66.0	70.9	69.3

moment of the frequency spectrum (black line). The automatic detector of possible contractions identified 9 signal segments with a significant rise in amplitude in relation to baseline in both TOCO-like signals. Slight differences in the onset and the end of these segments can be observed. The waveforms in these 9 signal segments are given in greater detail in Figure 4. They were later evaluated by the classifiers designed to determine whether they were associated with

uterine contractions or were simply due to the presence of motion artifacts. The results suggest that the signal windows (6) and (8) identified in the two TOCO-like signals contained artifacts, while the remainder could be considered as artifact-free uterine contractions. These conclusions coincide with visual observations and the previous classification carried out by the experts. Moreover the simultaneously recorded IUP and TOCO recording corroborate this finding. In this case,

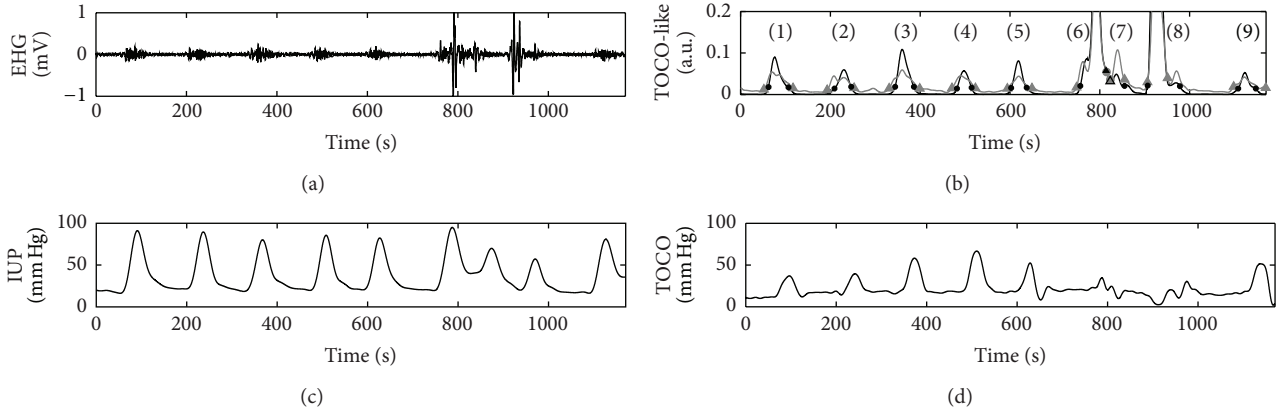


FIGURE 3: (a) EHG signal. (b) TOCO-like signal generated from EHG signal using RMS-based algorithm (grey line) and the unnormalized first statistical moment of the frequency spectrum algorithm (black line). The signal windows with amplitude significantly different from the baseline identified by the automatic contraction detector are marked by grey triangle and black point, respectively. (c)-(d) IUP and TOCO were acquired simultaneously.

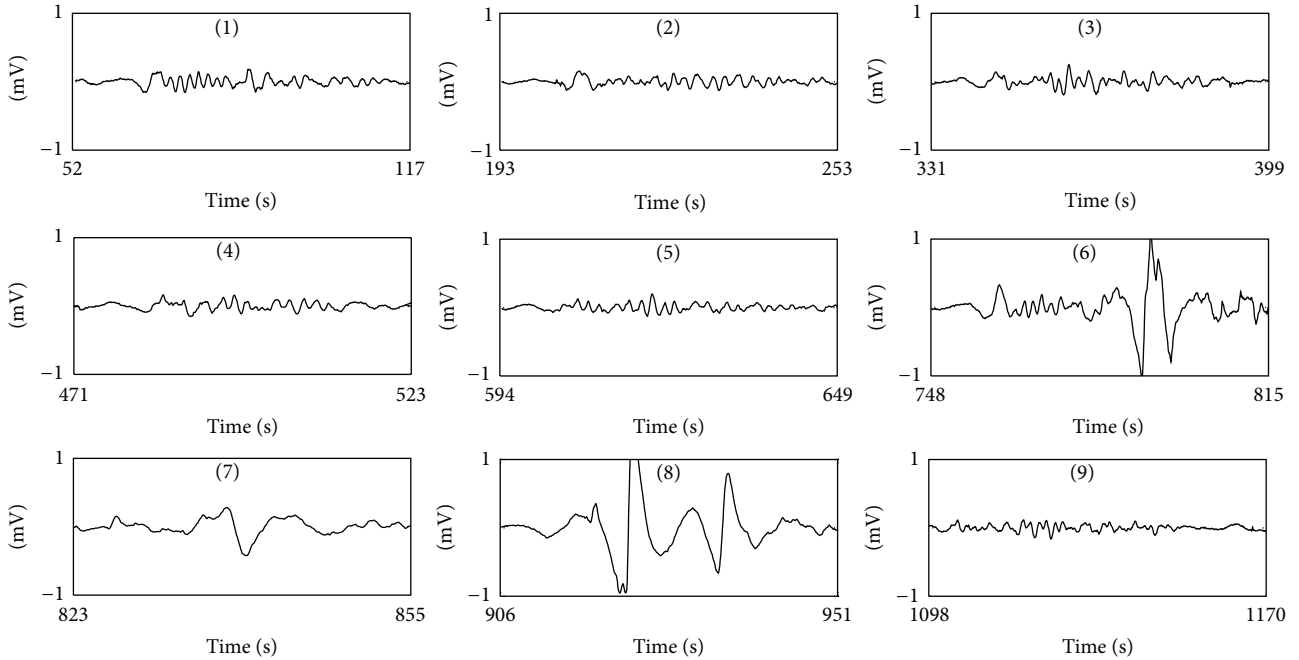


FIGURE 4: Waveform of 9 EHG signal windows identified by automatic contraction detector extracted from the recording session shown in Figure 3 using RMS-based algorithm.

TABLE 2: Comparison of the classifiers' accuracy using the best combination of features for motion artifact detection in EHG signals.

	LDA	QDA	SVM
Training + validation	$86.1 \pm 0.8\%$	$92.1 \pm 0.3\%$	$93.3 \pm 0.6\%$
Test	$79.4 \pm 3.5\%$	$92.2 \pm 1.8\%$	$83.6 \pm 3.5\%$

TABLE 3: Comparison of the classifiers' performance for the training and validation set of data (392 nonartifactual contractions versus 253 artifactual segments).

$N = 645$	Sensitivity	Specificity	PPV	NPV
LDA	69.4%	97.0%	93.7%	83.1%
QDA	84.3%	97.0%	94.8%	90.6%
SVM	87.1%	97.3%	95.5%	92.1%

contractions situated around 800 and 930 s (which coincide with windows (6) and (8), classified as containing artifacts) can be identified in the IUP. Nevertheless, these contractions

cannot be correctly identified in the TOCO recording. This was possibly due to movements made by the patient at this

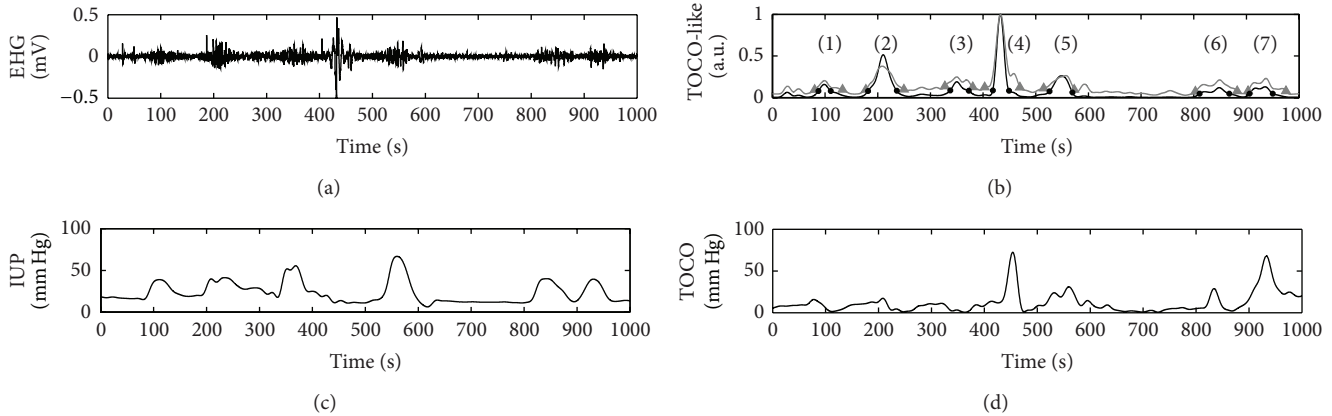


FIGURE 5: (a) EHG signal. (b) TOCO-like signal generated from EHG signal using RMS-based algorithm (grey line) and the unnormalized first statistical moment of the frequency spectrum algorithm (black line). The signal windows with amplitude significantly different from the baseline identified by the automatic contraction detector are marked by grey triangle and black point, respectively. (c)-(d) IUP and TOCO were acquired simultaneously.

TABLE 4: Comparison of the classifiers' performance for the test data set (30 nonartifacted contractions versus 24 artifacted segments).

$N = 54$	Sensitivity	Specificity	PPV	NPV
LDA	58.0%	96.5%	92.9%	74.2%
QDA	90.7%	93.5%	91.7%	92.6%
SVM	77.7%	88.4%	84.3%	83.2%

time, which would have given rise to incorrect readings not only in the EHG recording but also in the TOCO. In such cases, even though simultaneous contractions have occurred, no robust information about the characteristics of these contractions can be obtained from either noninvasive recording.

Another example of the application of the algorithm designed to automatically segment and classify EHG recordings is shown in Figure 5. A total of 7 signal windows were identified with a significant increase in amplitude in both the TOCO-like signal generated using the RMS-based algorithm and that obtained from time-frequency-based algorithm, showing again some minor difference in the onset and the end of these segments. Subsequent analysis of the corresponding EHG signal segments with the classifiers showed that only the signal window (4) was associated with artifacts, while the other 6 signals windows would be of artifact-free uterine contractions. In contrast to the previous example, in this case the artifacted window does not coincide with a simultaneous uterine contraction. The comparison of the TOCO-like signal with the IUP and TOCO recordings acquired simultaneously corroborates this result. The sudden amplitude rise that occurs around the second 450 was observed in both non-invasive TOCO recording and EHG recording, but no uterine contraction was recorded by IUP recording.

4. Discussion

Motion artifacts detection is a common problem in bioelectrical signal analysis and is extremely challenging as their characteristics show an extremely large variability depending on the specific source, making it hard to distinguish between target signal and artifacts. Although previous works have been made in this respect [18, 20, 21, 34–36], to our knowledge this is the first one in EHG recordings. In this paper, a method for the automatic detection of motion artifacts in EHG has been proposed without the need of additional accelerometers. This method was implemented in two steps: firstly a TOCO-like signal from the EHG recording was derived and the segments with amplitude significantly different to that of the baseline were identified. Subsequently a classifier for discriminating whether this signal segment is artifacted or not was implemented.

Concerning the TOCO-like generation from EHG recording, various methods that have been proposed in the literature were implemented and compared: RMS-based approach [12, 29] and the unnormalized first statistical moment of the frequency spectrum derived from time frequency analysis [15]. It was observed that similar TOCO-like signals can be obtained from these two methods. The latter method may give a better estimation of IUP from EHG recording [15], nevertheless both methods showed similar behavior in identifying signal segments with a significant increase in TOCO-like amplitude. Only, small differences in the width of the segment were found. In this sense, if the goal is to quickly identify those signal segments with an amplitude significantly higher than that of the baseline, the RMS-based method would be preferred due to its smaller computational cost.

Moreover, in this work it has been shown that the signal features of artifacted-EHG segments differ significantly from the non-artifacted ones. Artifacted EHG segments are associated with a rise in relative amplitude, maximum derivative,

and kurtosis value. These observations agree with other authors that analyzed noninvasive recordings of other myoelectric signals [18, 37]. Motion artifacts in EHG recording are also associated with a rise in relative energy between 1 Hz and 4 Hz. This is mainly due to the fact that the signal-noise ratio of EHG component decreases greatly over 1 Hz. This is the reason why several authors reduce the upper limit of signal bandwidth to 1 Hz for EHG signal feature extraction [9, 22, 28]. In addition, nonlinear parameters such as surrogate time reversibility were also tested, and clear differences were found between artifacted and non-artifacted EHG segments. Although it has been shown that the signal length has high effect on generating the surrogate data [38], we can discard this fact as the main responsible for the differences that were found since the average difference in signal length between artifacted and non-artifacted EHG signal windows was only about 6 s. Also, we tested (not shown) enlarging and reducing such difference with additional ± 10 s, and the much greater values of time-reversibility parameter for the artifacted EHG segments remained; suggesting their higher nonlinearity character in comparison to non-artifacted EHG segments. It should also be noted that only monovariate features were analyzed in this work. The use of bivariate parameters associated to the correlation or synchronization between signals could also provide valuable information for describing and discriminating artifacted and non-artifacted EHG segments. This would be further studied in future work.

In the present work, the ability of the different single features for discriminating the target signal and motion artifacted signal was further analyzed. Our experimental results are in partial agreement with another study on the analysis of parameters for detecting artifacts in surface electrogastrogram recordings [18]. In this latter work, neuronal network-based classifiers were obtained with an accuracy of 94.9%, 96.2%, and 97.4% for standard deviation, high frequency energy, and maximum derivative of signals, respectively. In the present study, the accuracy obtained in nonnormalized parameters, such as the standard deviation, is about 60%, which indicates that this type of parameters has a relatively low capacity to discriminate between artifacted and non-artifacted signals. This could possibly be due to the wide variation in EHG signal amplitude between the different channels and recording sessions. By contrast, the accuracy achieved by normalized features such as E_3 , MD_{bs} , and MD_x ranged from 76.0% to 87.6%.

On the other hand, various classifying techniques (LDA, QDA, and SVM) to distinguish the EHG signal segments with and without artifacts were compared. As it could be expected, the two nonlinear methods provided superior classifier accuracy than LDA which may be due to the fact that the features' distribution for artifacted signal and non-artifacted signal was highly overlapped. Regarding SVM and QDA, they yielded similar results for the training and validation data set. Theoretically, the SVM should provide lower generalization error [39]; however, SVM obtained significant lower accuracy values in the test data set than in the training and validation data set. Although the data set used for the design of the classifier contained more than six hundred signal windows, the data from the two additional subjects of the test set seems

to have compromised the values of the support vectors of the designed SVM classifier. A database with a higher number of subjects would help to enhance the generalization capability of this classifier. Nonetheless, the results suggest that the classifier based on QDA using the best 7 features possesses a high degree of generalization for detecting artifacts in EHG signals (extendable to signals not initially included in the data base), which can therefore be considered suitable for automatic artifact detection in these signals. Furthermore, from the computational point of view, discriminant analysis is much more effective than SVM and it does not need the optimization of the classifier's configuration parameters, which is a crucial part of advanced techniques. Nevertheless, it should be highlighted that the proposed method has been tested on measurements performed during the first stage of term labor, and its feasibility for preterm/non in labor measurements should be checked in future studies. On one hand, the interpretation of the EHG signal of pregnant patients at earlier gestational ages is more challenging due to its poorer signal-to-noise ratio, also making the detection of uterine contractions harder. On the other hand, as pregnancy progresses the uterine myoelectrical activity shifts towards higher frequencies and becomes more organized [3, 32]; therefore pregnancy contractions would also present some differences in the characteristic parameters used in this study; still they would be expected to remain different enough from those of artifacted signal windows. The inclusion of other features such as the conduction velocity [8] or the nonlinear correlation coefficient h_2 [24] that have been shown to provide additional information in EHG interpretation could help to improve the system's performance under these circumstances.

With respect to the motion artifacts detection in bioelectrical recording, manual identification by experts based on previous knowledge about both the target signal and motion artifacts has been often used [18, 34]. Other authors consider that annotations or accelerometers [36, 40] are more objective for the detection of motion artifacts. Nevertheless the automatic identification of motion artifacts in accelerometers signal is still problematic due to its high variability, and on the other hand annotations are not absolved of the subjectivity of each patient or observer. In this work, a method based on the features of the target signal and motion artifacts was proposed and checked with annotation method. This method could be of special interest as an incentive for the use of non-invasive myoelectric techniques in clinical environments since no additional accelerometers are needed for motion artifacts detection. On the other hand, a large percentage of motion artifacted segments in EHG recording were obtained in this work. Although the subject was asked to be as quite as possible during the recording session, motion artifacts in EHG recordings are unavoidable. Moreover the occurrence of a uterine contraction may also induce movement artifacts due to abdominal deformation, due to forced respiration patterns, or due to pain. In fact, a large percentage of artifacted segments occurred during a uterine contraction that could be simultaneously identified in the IUP and TOCO recordings. This phenomenon can be observed in the segments $n^{\circ}6$ and $n^{\circ}8$ in Figure 3 which were associated with an amplitude

rise in IUP recording. The presence of motion artifact may impair greatly in temporal and spectral parameters, and also on the measurement of conduction velocity and direction. Thus misinterpretation of the results may occur. For this reason, in this work it was preferred to classify such cases as artifacted signals not suitable for the characterization of uterine contractile behaviour.

Finally it should be noticeable that EHG recording is not only contaminated by motion artifacts but also by a set of physiological interferences, such as fetal and maternal ECG activity and respiration. Regarding the possible effects of such interferences in the proposed algorithm, ECG interference is partially cancelled in bipolar EHG recording, its energy content is mostly distributed over 1 Hz, and it is almost constant throughout the recording sessions. Therefore the proposed algorithm would not be very sensitive to this interference. Nevertheless, several techniques have been proposed for removing ECG from EHG recordings and could be used prior to applying the presented method [17, 41–43]. The respiration interference is mainly distributed within 0.20 and 0.34 Hz, which is partially overlapped with uterine electrical activity. For this reason, many authors prefer to analyze the EHG signal over 0.34 Hz [3, 22, 23, 28], although it has been shown that EHG component distributes its energy from 0.1 Hz [17, 26]. This respiration interference usually happens during a large period of time and does not suffer large variations in amplitude by contrast to uterine electrical activity, and therefore it would not be detected as possible contraction segments in our algorithm.

With respect to the potential use of EHG recordings and the proposed method in everyday clinical practice, although clinical staff is not accustomed to EHG recordings for monitoring uterine contraction, they are familiar to other bioelectrical recordings such as electrocardiogram or electroencephalogram. Therefore we consider that the progressive implementation of these methods would not be distressing. It would undoubtedly require a training period for the clinical staff to adapt to and learn about the electrode arrangement for the recording and electrode and bioamplifier wiring and handling. In this context, the TOCO-like signal generation with which clinicians are accustomed will also facilitate the introduction of this technique in clinical practice. Moreover the proposed algorithms do not require a high computational cost, and, from the user point of view, the application could be considered to work on real-time. The proposed method would greatly facilitate the task of segmenting recording sessions and evaluating uterine contractions based on the EHG recording. After having correctly identified the contractions, delivery room staff could be provided with relevant information on their efficiency, such as duration, frequency, signal amplitude, dominant frequency of the EHG signal, and the energy distribution in the spectral domain, among others [2, 5, 7–9, 22, 30].

5. Conclusion

The experimental results show that the most important features for detecting artifacts in EHG signals are E_3 , RA, κ ,

MD_{bs} , MD_x , sample entropy, and surrogate time reversibility. The proposed classifier, based on QDA with these features, can be used for the automatic detection of artifacts in the EHG recording, reaching a classification accuracy of 92.2%. This classifier, jointly with the proposed TOCO-like signal generation and analysis algorithms, provide a tool for the automatic detection and segmentation of uterine contractions, distinguishing them from possible artifacts. This technique could therefore be a valuable aid to the analysis of surface EHG recordings and could be used by clinical staff to extract additional information from the habitually used TOCO recordings.

Conflict of Interests

The authors declare that there is no conflict of interests regarding the publication of the paper.

Acknowledgments

The authors are grateful to the R + D + I Linguistic Assistance Office at the UPV for their help in proofreading this paper. The work was supported by the Ministerio de Ciencia e Innovación de España (TEC2010-16945).

References

- [1] F. A. Wilmlink, F. F. Wilms, R. Heydanus, B. W. J. Mol, and D. N. M. Papatsonis, "Fetal complications after placement of an intrauterine pressure catheter: a report of two cases and review of the literature," *Journal of Maternal-Fetal and Neonatal Medicine*, vol. 21, no. 12, pp. 880–883, 2008.
- [2] M. P. Vinken, C. Rabotti, M. Mischi, and S. G. Oei, "Accuracy of frequency-related parameters of the electrohysterogram for predicting preterm delivery: a review of the literature," *Obstetrical and Gynecological Survey*, vol. 64, no. 8, pp. 529–541, 2009.
- [3] D. Schlembach, W. L. Maner, R. E. Garfield, and H. Maul, "Monitoring the progress of pregnancy and labor using electromyography," *European Journal of Obstetrics Gynecology and Reproductive Biology*, vol. 144, supplement 1, pp. S33–S39, 2009.
- [4] A. M. Miles, M. Monga, and K. S. Richeson, "Correlation of external and internal monitoring of uterine activity in a cohort of term patients," *American Journal of Perinatology*, vol. 18, no. 3, pp. 137–140, 2001.
- [5] D. Devedeux, C. Marque, S. Mansour, G. Germain, and J. Duchene, "Uterine electromyography: a critical review," *American Journal of Obstetrics and Gynecology*, vol. 169, no. 6, pp. 1636–1653, 1993.
- [6] R. E. Garfield and W. L. Maner, "Physiology and electrical activity of uterine contractions," *Seminars in Cell and Developmental Biology*, vol. 18, no. 3, pp. 289–295, 2007.
- [7] C. K. Marque, J. Terrien, S. Rihana, and G. Germain, "Preterm labour detection by use of a biophysical marker: the uterine electrical activity," *BMC Pregnancy and Childbirth*, vol. 7, supplement 1, article S5, 2007.
- [8] M. Lucovnik, W. L. Maner, L. R. Chambliss et al., "Noninvasive uterine electromyography for prediction of preterm delivery," *American Journal of Obstetrics and Gynecology*, vol. 204, no. 3, pp. 228.e1–228.e10, 2011.

- [9] T. Y. Euliano, D. Marossero, M. T. Nguyen, N. R. Euliano, J. Principe, and R. K. Edwards, "Spatiotemporal electrohysterography patterns in normal and arrested labor," *American Journal of Obstetrics and Gynecology*, vol. 200, no. 1, pp. 54–57, 2009.
- [10] C. Rabotti, M. Mischi, J. O. E. H. van Laar, G. S. Oei, and J. W. M. Bergmans, "Inter-electrode delay estimators for electrohysterographic propagation analysis," *Physiological Measurement*, vol. 30, no. 8, pp. 745–761, 2009.
- [11] C. Rabotti and M. Mischi, "Two-dimensional estimation of the electrohysterographic conduction velocity," in *Proceedings of the 32nd Annual International Conference of the IEEE Engineering in Medicine and Biology Society (EMBC '10)*, pp. 4262–4265, September 2010.
- [12] J. Jezewski, K. Horoba, A. Matonia, and J. Wrobel, "Quantitative analysis of contraction patterns in electrical activity signal of pregnant uterus as an alternative to mechanical approach," *Physiological Measurement*, vol. 26, no. 5, pp. 753–767, 2005.
- [13] T. Euliano, M. Skowronski, D. Marossero, J. Shuster, and R. Edwards, "Prediction of intrauterine pressure waveform from transabdominal electrohysterography," *Journal of Maternal-Fetal and Neonatal Medicine*, vol. 19, no. 12, pp. 803–808, 2006.
- [14] T. Y. Euliano, M. T. Nguyen, D. Marossero, and R. K. Edwards, "Monitoring contractions in obese parturients: electrohysterography compared with traditional monitoring," *Obstetrics and Gynecology*, vol. 109, no. 5, pp. 1136–1140, 2007.
- [15] C. Rabotti, M. Mischi, J. O. E. H. van Laar, G. S. Oei, and J. W. M. Bergmans, "Estimation of internal uterine pressure by joint amplitude and frequency analysis of electrohysterographic signals," *Physiological Measurement*, vol. 29, no. 7, pp. 829–841, 2008.
- [16] T. Y. Euliano, M. T. Nguyen, S. Darmanjian et al., "Monitoring uterine activity during labor: a comparison of 3 methods," *American Journal of Obstetrics and Gynecology*, vol. 208, pp. 66.e1–66.e6, 2013.
- [17] M. Hassan, S. Boudaoud, J. Terrien, B. Karlsson, and C. Marque, "Combination of canonical correlation analysis and empirical mode decomposition applied to denoising the labor electrohysterogram," *IEEE Transactions on Biomedical Engineering*, vol. 58, no. 9, pp. 2441–2447, 2011.
- [18] J. Liang, J. Y. Cheung, and J. D. Z. Chen, "Detection and deletion of motion artifacts in electrogastrogram using feature analysis and neural networks," *Annals of Biomedical Engineering*, vol. 25, no. 5, pp. 850–857, 1997.
- [19] M. A. M. T. Verhagen, L. J. van Schelven, M. Samsom, and A. J. P. M. Smout, "Pitfalls in the analysis of electrogastrographic recordings," *Gastroenterology*, vol. 117, no. 2, pp. 453–460, 1999.
- [20] S. Conforto, T. D'Alessio, and S. Pignatelli, "Optimal rejection of movement artefacts from myoelectric signals by means of a wavelet filtering procedure," *Journal of Electromyography and Kinesiology*, vol. 9, no. 1, pp. 47–57, 1999.
- [21] H. Liang, Z. Lin, and R. W. McCallum, "Artifact reduction in electrogastrogram based on empirical mode decomposition method," *Medical and Biological Engineering and Computing*, vol. 38, no. 1, pp. 35–41, 2000.
- [22] W. L. Maner and R. E. Garfield, "Identification of human term and preterm labor using artificial neural networks on uterine electromyography data," *Annals of Biomedical Engineering*, vol. 35, no. 3, pp. 465–473, 2007.
- [23] B. Moslem, M. Khalil, C. Marque, and M. O. Diab, "Energy distribution analysis of uterine electromyography signals," *Journal of Medical and Biological Engineering*, vol. 30, no. 6, pp. 361–366, 2010.
- [24] M. Hassan, J. Terrien, C. Muszynski, A. Alexandersson, C. Marque, and B. Karlsson, "Better pregnancy monitoring using nonlinear correlation analysis of external uterine electromyography," *IEEE Transactions on Biomedical Engineering*, vol. 60, pp. 1160–1166, 2013.
- [25] H. Léman, C. Marque, and J. Gondry, "Use of the electrohysterogram signal for characterization of contractions during pregnancy," *IEEE Transactions on Biomedical Engineering*, vol. 46, no. 10, pp. 1222–1229, 1999.
- [26] H. Maul, W. L. Maner, G. Olson, G. R. Saade, and R. E. Garfield, "Non-invasive transabdominal uterine electromyography correlates with the strength of intrauterine pressure and is predictive of labor and delivery," *Journal of Maternal-Fetal and Neonatal Medicine*, vol. 15, no. 5, pp. 297–301, 2004.
- [27] J. Terrien, T. Steingrimsdottir, C. Marque, and B. Karlsson, "Synchronization between EMG at different uterine locations investigated using time-frequency ridge reconstruction: comparison of pregnancy and labor contractions," *Eurasip Journal on Advances in Signal Processing*, vol. 2010, Article ID 242493, 10 pages, 2010.
- [28] M. Lucovnik, R. J. Kuon, L. R. Chambliss et al., "Use of uterine electromyography to diagnose term and preterm labor," *Acta Obstetrica et Gynecologica Scandinavica*, vol. 90, no. 2, pp. 150–157, 2011.
- [29] I. Verdenik, M. Pajntar, and B. Leskošek, "Uterine electrical activity as predictor of preterm birth in women with preterm contractions," *European Journal of Obstetrics Gynecology and Reproductive Biology*, vol. 95, no. 2, pp. 149–153, 2001.
- [30] G. Fele-Žorž, G. Kavšek, Ž. Novak-Antolič, and F. Jager, "A comparison of various linear and non-linear signal processing techniques to separate uterine EMG records of term and preterm delivery groups," *Medical and Biological Engineering and Computing*, vol. 46, no. 9, pp. 911–922, 2008.
- [31] D. Zhu, J. Tong, and Y. Chen, "An ICA-based method for automatic eye blink artifact correction in multi-channel EEG," in *Proceedings of the 5th International Conference on Information Technology and Application in Biomedicine, in Conjunction with the 2nd International Symposium & Summer School on Biomedical and Health Engineering*, pp. 338–341, May 2008.
- [32] M. Hassan, J. Terrien, C. Marque, and B. Karlsson, "Comparison between approximate entropy, correntropy and time reversibility: application to uterine electromyogram signals," *Medical Engineering and Physics*, vol. 33, no. 8, pp. 980–986, 2011.
- [33] I. Guyon and A. Elisseeff, "An introduction to variable variable and feature selection," *Journal of Machine Learning Research*, vol. 46, pp. 1157–1182, 2003.
- [34] A. Irimia and L. A. Bradshaw, "Artifact reduction in magnetogastrography using fast independent component analysis," *Physiological Measurement*, vol. 26, no. 6, pp. 1059–1073, 2005.
- [35] M. Milanesi, N. Martini, N. Vanello, V. Positano, M. F. Santarelli, and L. Landini, "Independent component analysis applied to the removal of motion artifacts from electrocardiographic signals," *Medical and Biological Engineering and Computing*, vol. 46, no. 3, pp. 251–261, 2008.
- [36] I. Daly, M. Billinger, R. Scherer, and G. Muller-Putz, "On the automated removal of artifacts related to head movement from the EEG," *IEEE Transactions on Neural Systems and Rehabilitation Engineering*, vol. 21, pp. 427–434, 2013.
- [37] Y. Ye-Lin, J. Garcia-Casado, G. Prats-Boluda, and J. L. Martinez-De-Juan, "Combined method for reduction of high frequency interferences in surface electroenterogram (EEnG)," *Annals of Biomedical Engineering*, vol. 38, no. 7, pp. 2358–2370, 2010.

- [38] T. Schreiber and A. Schmitz, "Surrogate time series," *Physica D*, vol. 142, no. 3-4, pp. 346-382, 2000.
- [39] T. van Gestel, J. A. K. Suykens, B. Baesens et al., "Benchmarking least squares support vector machine classifiers," *Machine Learning*, vol. 54, no. 1, pp. 5-32, 2004.
- [40] C. Rabotti, *Characterization of Uterine Activity by Electrohysterography*, Eindhoven University of Technology, Eindhoven, The Netherlands, 2010.
- [41] H. Leman and C. Marque, "Rejection of the maternal electrocardiogram in the electrohysterogram signal," *IEEE Transactions on Biomedical Engineering*, vol. 47, no. 8, pp. 1010-1017, 2000.
- [42] C. Marque, C. Bisch, R. Dantas, S. Elayoubi, V. Brosse, and C. Pérot, "Adaptive filtering for ECG rejection from surface EMG recordings," *Journal of Electromyography and Kinesiology*, vol. 15, no. 3, pp. 310-315, 2005.
- [43] A. Matonia, J. Jezewski, K. Horoba, A. Gacek, and P. Labaj, "The maternal ECG suppression algorithm for efficient extraction of the fetal ECG from abdominal signal," in *Proceedings of the 28th Annual International Conference of the IEEE Engineering in Medicine and Biology Society (EMBS '06)*, vol. 1-15, pp. 296-299, September 2006.

Research Article

Automated Conduction Velocity Analysis in the Electrohysterogram for Prediction of Imminent Delivery: A Preliminary Study

Hinke de Lau,¹ Chiara Rabotti,² Rianne Bijloo,¹ Michael Johannes Rooijackers,² Massimo Mishi,² and S. Guid Oei¹

¹ Maxima Medical Center, P.O. Box 7777, 5500 MB Veldhoven, The Netherlands

² Department of Electrical Engineering, University of Technology Eindhoven, Eindhoven, The Netherlands

Correspondence should be addressed to Hinke de Lau; h.delau@gmail.com

Received 29 May 2013; Accepted 1 October 2013

Academic Editor: Mihaela Ungureanu

Copyright © 2013 Hinke de Lau et al. This is an open access article distributed under the Creative Commons Attribution License, which permits unrestricted use, distribution, and reproduction in any medium, provided the original work is properly cited.

Background. Analysis of the electrohysterogram (EHG) is a promising diagnostic tool for preterm delivery. For the introduction in the clinical practice, analysis of the EHG should be reliable and automated to guarantee reproducibility. **Study Goal.** Investigating the feasibility of automated analysis of the EHG conduction velocity (CV) for detecting imminent delivery. **Materials and Methods.** Twenty-two patients presenting with uterine contractions (7 preterm) were included. An EHG was obtained noninvasively using a 64-channel high-density electrode grid. Contractions were selected based on the estimated intrauterine pressure derived from the EHG, the tocodynamometer, and maternal perception. Within the selected contractions, the CV vector was identified in two dimensions. **Results.** Nine patients delivered within 24 hours and were classified as a labor group. 64 contractions were analyzed; the average amplitude of the CV vector was significantly higher for the labor group, $8.65 \text{ cm/s} \pm 1.90$, compared to the nonlabor group, $5.30 \text{ cm/s} \pm 1.47$ ($P < 0.01$). **Conclusion.** The amplitude of the CV is a promising parameter for predicting imminent (preterm) delivery. Automated estimation of this parameter from the EHG signal is feasible and should be regarded as an important prerequisite for future clinical studies and applications.

1. Introduction

Preterm delivery, defined as delivery before 37 weeks of gestation, constitutes a major problem in terms of neonatal mortality, morbidity, and healthcare costs [1–3]. Timely intervention and treatment with tocolytics and corticosteroids improves neonatal outcome [4]. However, the diagnostics currently used lack both sensitivity and specificity leading to both under- and overtreatment [5, 6]. A potential new diagnostic tool is the electrohysterogram (EHG), which is a non-invasive abdominal measurement of the electrical activity underlying uterine contractions.

The sequence of contraction and relaxation of the uterus results from a cyclic depolarization and repolarization of its smooth muscle cells in the form of action potentials (APs). APs occur in bursts; they arise in cells that act as pacemakers and propagate from cell to cell through gap junctions [7–9].

Labor and delivery are preceded by two physiological phenomena: increased excitability and increased connectivity among the cells, resulting in increased propagation of APs and more synchronized firing [10]. These changes are reflected in the recorded EHG.

The previous literature demonstrated that the EHG has great potential for monitoring labor, predicting labor time, and discriminating between physiological uterine activity and contractions leading to (preterm) delivery. Therefore, analysis of the EHG can support timely treatment of preterm labor [11–16]. To this end, several studies have focused on analyzing the spectral content of the EHG using either the peak frequency of the power density spectrum [15, 17–19] or the ratio between high and low frequency bands [11]. Another parameter from the EHG that has been proposed for predicting imminent preterm labor is the nonlinear correlation among channels in a multichannel recording [16].

Prior to delivery, the increased connectivity among cells also increases propagation, which can be assessed by estimating the conduction velocity (CV) from the EHG [20–22]. Differently from skeletal muscles, which are striated and present an anatomical direction of propagation parallel to the fiber orientation, the direction of propagation of the uterine APs is a priori unknown [23, 24]. Due to lack of evidence [25], many authors also concluded that no classical linear propagation of single APs could be assumed for the uterus and that only global propagation of the whole burst envelop could be measured [23, 25]. However, more recently, measurements of the electrical activity of the guinea pig uterus using a grid of extracellular electrodes clearly demonstrated that also for the uterus, similarly to the myocardium, a linear propagation of single APs can be measured [26]. However, direction and speed of AP propagation can change even within the same bursts.

Previous research mainly focused on the methods for measuring the CV [27–31]. Recently, the prognostic value of the CV for predicting imminent preterm delivery was investigated by visual inspection of the EHG signal [15]. Despite the very promising results presented in this clinical study, the employed visual approach has the disadvantage of not being reproducible. For use as a clinical tool, it would be desirable to rely on a fully automated CV analysis.

However, automated CV analysis entails a number of scientific challenges, namely, automatic detection of contractions, estimation of amplitude and direction of the CV vector, and exclusion of signals that are not related to propagating APs.

This study investigates the feasibility of a new automated approach for the analysis of the EHG CV for detecting imminent delivery. Our approach integrates previously validated EHG-based methods for contraction detection and automated analysis of the CV in two dimensions using a high-density electrode grid.

2. Materials and Methods

2.1. Study Protocol. A prospective observational cohort study was performed at the Maxima Medical Center Veldhoven, The Netherlands. Approval from the local medical ethical board was obtained and all the included women provided written informed consent for study participation. Patients with singleton pregnancies were enrolled, presenting with at least 3 contractions in 30 minutes, which were either perceived by the patient or visible on the external tocogram. Both term patients (gestational age 37 + 0–41 + 6) and preterm patients (gestational age 24 + 0–36 + 6) were included. Exclusion criteria were oxytocin or prostaglandin administration prior to or during the measurement, induction of labor within 24 hours after the measurement, and known uterine malformation.

Measurements from all enrolled patients were obtained using a measurement setup as shown in Figure 1. A 64-channel high-density (HD) electrode grid with external reference electrode on the hip was used in conjunction with a bipolar electrode pair (1 cm diameter, variable interelectrode

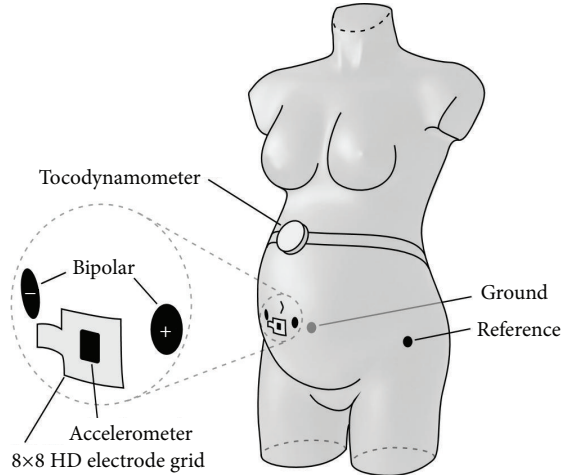


FIGURE 1: Measurement setup showing the position of all abdominal sensors.

distance) to record the EHG. Due to the a priori unknown AP direction of propagation, the bidimensional arrangement of the electrodes on the grid (8 × 8) permits estimating all the possible CV directions along the abdominal plane parallel to the abdominal surface. The bipolar signal initially used to allow recording other signals (such as the fetal ECG) was eventually employed to derive the contraction timing and trigger the CV vector estimation. The HD electrode grid could also be suitable, but the larger surface of the bipolar sensors offered better results for this specific purpose.

The recording of these signals was performed using a Refa multichannel amplifier (TMS International, Enschede, The Netherlands), with a patient ground on the hip. Simultaneously, a tocodynamometer was used as reference for contraction detection. For the same reason, the time instants at which the patient felt a contraction were annotated.

2.2. Signal Analysis. Here, a synthetic overview of the methodology used for the analysis is given. For further details, we refer to [31, 32].

The CV vector was identified during the contraction periods. Differently from previous studies, where contractions were annotated manually, we automatically derived an initial estimation of onset and duration of contractions. To this end, an estimate of the internal uterine pressure (IUP) was derived from the bipolar EHG signal. Based on a validated method [32], indicated by n and f , the discrete time and frequency variables, respectively, the unnormalized first statistical moment $\Psi(n)$ of the bipolar EHG spectrogram, $\rho(n, f)$, was calculated in a selected frequency band, $[f_{\min}, f_{\max}]$; that is,

$$\Psi(n) = \sum_{f=f_{\min}}^{f_{\max}} f \rho(n, f), \quad (1)$$

with $f_{\min} = 0,3$ Hz and $f_{\max} = 0,8$ Hz. An adaptive threshold was then used to detect onset and duration of each

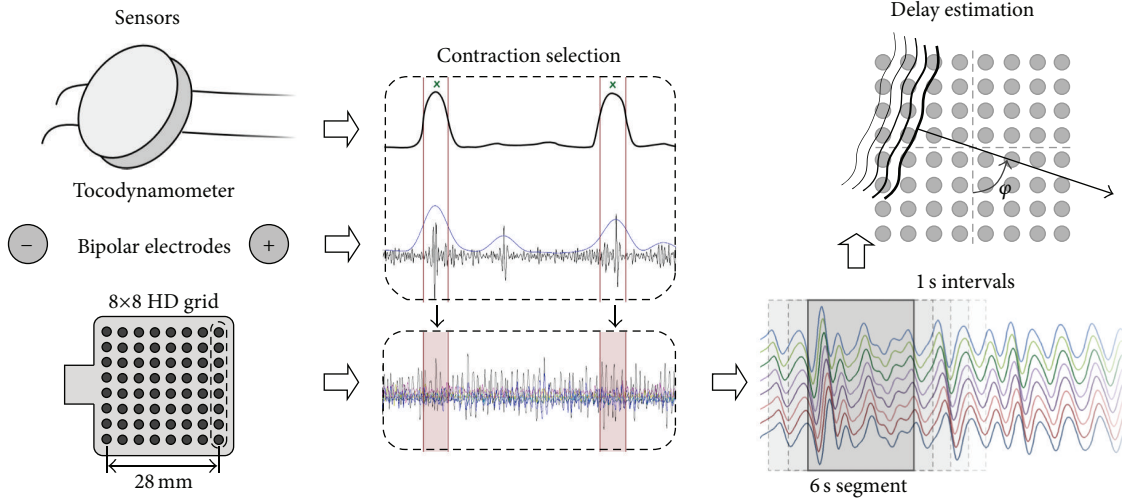


FIGURE 2: The method for analyzing the CV. The EHG is recorded using a 8×8 HD electrode grid plus a bipolar electrode pair. Contractions are selected based on the eIUP, which is derived from the bipolar electrodes, plus the external tocodynamometer and maternal perception. Finally, the delays are estimated in overlapping windows using a maximum likelihood approach.

contraction in 60 s overlapping windows [33]. Differently from our previous work [3], no modeling was used to improve the estimation accuracy of the IUP amplitude. A more accurate estimation of the IUP, which was out of the scope of the present work, would not significantly improve the accuracy of the thresholding procedure used to assess onset and duration of contractions.

Of the contractions selected by EHG signal analysis, only those that were visible on the external tocogram or concurred with annotations of contractions as felt by the patient were eventually selected for further analysis.

In the signal segments selected as contractions, the CV vector was identified in two dimensions from the 8×8 HD electrode grid in overlapping segments (5 s overlap). Following the schematic representation of Figure 2, we describe the EHG propagation by a CV vector v . The vector has an amplitude and an incidence angle θ ($\theta \in [-\pi, \pi]$) with respect to the vertical axis of the electrode grid. The signal is detected by N_r rows and N_c columns of electrodes. Assuming that the same signal shape $s(n)$ is measured at each channel, the signal $x_{r,c}$ measured at the channel (r, c) in the r th row and c th column of the electrode grid can be modeled as

$$x_{r,c}(n) = s(n - (r-1)\tau_r - (c-1)\tau_c) + w_{r,c}(n), \quad (2)$$

where n indicates the time sample ($n = [1, 2, \dots, N]$) and $w_{r,c}(n)$ is the white Gaussian noise which is present at the channel (r, c) . As from (2), we assume the linear propagation of the APs; that is, in each channel (r, c) , the reference signal shape $s(n)$ is delayed by τ_r and τ_c time samples relative to the previous row and column, respectively. Identification of the vector v requires estimation of (τ_r, τ_c) , which we obtain using a maximum likelihood approach, that is, by maximization of the probability density function $p((\tau_r, \tau_c) | x_{r,c}(n), s(n))$ in the frequency domain, where τ_r and τ_c can be estimated without resolution limits. Under the assumption of white Gaussian

noise, the maximum likelihood approach is equivalent to the minimization of the cost function E^2 defined as

$$E^2(\tau_r, \tau_c) = \frac{2}{N} \sum_{r=1}^{N_r} \sum_{c=1}^{N_c} \sum_{f=0}^{(N/2)-1} [X_{r,c}(f) - S(f) e^{-j2\pi f[(r-1)\tau_r - (c-1)\tau_c}]|^2, \quad (3)$$

indicated by f , the discrete frequency; $X_{r,c}(f)$ and $S(f)$ are the Fourier transforms of the signal recorded at the channel (r, c) and of the reference shape, respectively. Following the description in Figure 2, for an interelectrode distance equal to d , it follows that τ_r and τ_c are related to the CV amplitude and to the incidence angle θ by

$$\begin{aligned} \tau_r &= \frac{d \cos \theta}{CV}, \\ \tau_c &= \frac{d \sin \theta}{CV}. \end{aligned} \quad (4)$$

The use of different weighting strategies of the derived cost function was introduced in [31] to deal with poor inter-channel signal similarity due to the presence of noise. The weights are inversely proportional to the estimated channel noise. Of the different weighting strategies proposed in [31], we chose the weighted cost function with the best estimation accuracy.

Segments with a calculated CV value above 30 cm/s, which are significantly higher than the physiological values reported in the literature [23, 26], were considered as outliers and were excluded.

2.3. Statistical Analysis. Patients delivering within 24 hours after the measurement were classified as labor group and those delivering outside this time window were classified as

TABLE 1: Patient characteristics.

	Labor	Nonlabor
Number of patients	9	13
Gestational age (weeks + days) ¹	31 + 1-40 + 4 (37 + 2)	26 + 2-41 + 3 (36 + 1)
Preterm	2	5
Nulliparous	4	8
Age ¹	17-36 (27.9)	16-36 (27.8)
BMI ¹	22-42 (28.2)	24-34 (26.8)
Hours to delivery ¹	1-10 (6)	27-1488 (255)

¹Mean value in parentheses.

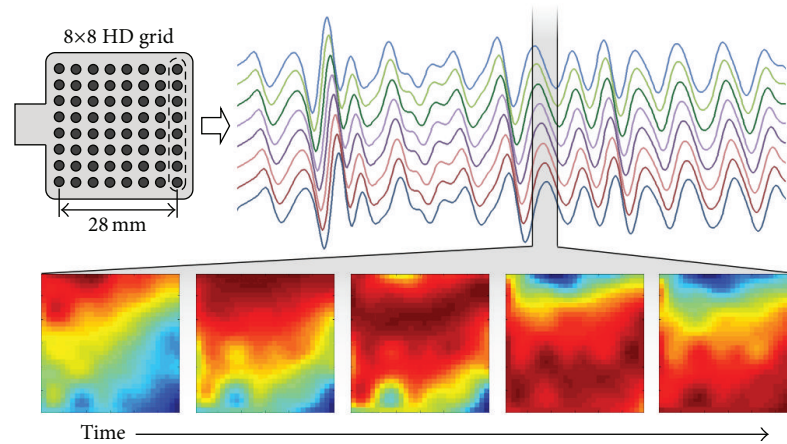


FIGURE 3: Next to the HD electrode grid, the EHG signals of eight electrodes (one column) are shown during a contraction. The five images at the bottom show an interpolated 2D representation of a single EHG pulse propagating from top to bottom.

nonlabor group. CV and propagation path were compared between these groups. In order to be independent of the number of analyzed segments and contractions per patient, an average CV vector was identified for each analyzed contraction and subsequently the average CV vector for each patient was determined. The Shapiro-Wilk test was used to test for a normal distribution of the estimated values of CV vector amplitude. Levene's test was applied to test for equal variances in the labor and nonlabor groups. Finally, an independent samples *t*-test was used to test for a significant difference in amplitude of the CV between both groups. The alpha was set to 0.05 for all statistical tests.

3. Results

Twenty-two patients were included in the study, of which 7 were preterm. Nine patients delivered within 24 hours and were classified as labor group. Table 1 shows the baseline characteristics of the labor and nonlabor groups. An example of a downward propagating wave of uterine activity during a contraction visualized by the adopted high-density grid of 64 electrodes can be seen in Figure 3.

In total, 64 contractions were analyzed. Figure 4 shows the boxplot of the mean CV for the patients in the labor and the nonlabor groups; the median values of the CV of the

groups as a whole are indicated as a horizontal line. The Shapiro-Wilk test was insignificant, supporting the null hypothesis that the data is derived from a normally distributed population. Similarly, Levene's test showed an insignificant result, supporting equal variances in the labor and nonlabor groups. The average amplitude of the CV vector was significantly higher for the labor group, $8.65 \text{ cm/s} \pm 1.90$, compared to the nonlabor group, $5.30 \text{ cm/s} \pm 1.47$ ($P < 0.01$). The angle of propagation showed a high variability among patients in both of the labor and nonlabor groups, even within the same contraction.

4. Discussion

This study investigates the feasibility of a new automated approach for the analysis of the EHG CV for detecting imminent delivery. Our approach integrates validated EHG-based methods for contraction detection and automated analysis of the CV in two dimensions using a high-density electrode grid [31]. The patients in this study presented with uterine contractions and were classified as labor group or nonlabor group based on delivery within or after 24 hours, respectively. The results show a significantly higher amplitude of the CV vector in the labor group.

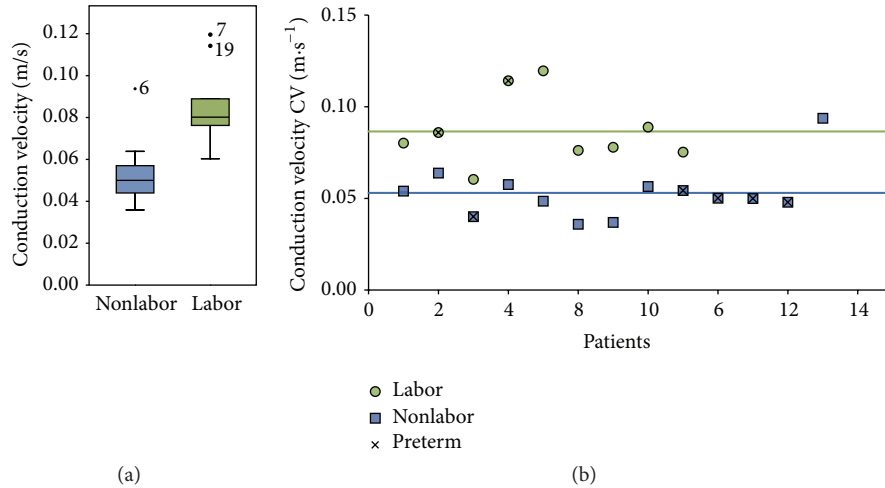


FIGURE 4: On the left, a boxplot shows the average amplitude of the CV vector for the labor and nonlabor groups. The median value is displayed with a horizontal line. On the right, a scatter plot shows the individual average amplitudes of the CV vector for both groups. The horizontal lines represent the average value for the labor and nonlabor groups.

The measurements were performed in a diverse group of patients featuring both term and preterm patients admitted for varying reasons. The common denominator was that all patients had palpable and measurable contractions. The emphasis was placed on investigating the feasibility of automated CV analysis, in order to open the way to future clinical studies and applications based on this parameter as diagnostic tool for imminent (preterm) birth. The assumption here is that comparable changes in conduction properties can be observed in contractions leading to preterm and term delivery. In follow-up studies, it will be important to have a consistent group of patients presenting with premature contractions and who are considered for treatment with tocolytics based on gestational age and clinical parameters.

In this study, additional data other than the EHG signal was used for detecting contractions, namely, an external tocodynamometer and annotations of subjectively perceptible contractions by the patient. This was chosen to achieve a more robust distinction between uterine activity and measurement artifacts. In future work, a fully automated selection of contraction segments and analysis of CV should be pursued. However, while an automated method ensures reproducibility and should therefore be preferred for everyday clinical use, visual inspection might be required in a preliminary phase for discriminating uterine activity from noise and excluding artifacts and signals that do not propagate linearly, from the analysis.

Noteworthy, identification of the EHG CV vector using the present methods implies the assumption that the signal does propagate and that propagation is linear. While it is reasonable to hypothesize that the linearity of the propagation could be a discriminative parameter for predicting imminent delivery in itself, several aspects related to the evolution from pregnancy to labor are not yet fully understood and need further dedicated research [34]. Therefore, we excluded spikes propagating nonlinearly from the analysis as we expected

those cases to be outliers, that is, to have a CV outside the physiological range reported by the previous literature [26, 35]. Only [15] reported values higher than 30 cm/s; these values cannot be considered as a physiological reference due to the specific measurement setup, which allows for information on only a projection of the CV vector [36].

Finally, another novelty of this study is the use of a 64-channel high-density electrode grid for recording the EHG. Due to the a priori unknown AP direction of propagation, the bidimensional arrangement of the electrodes on the grid permits estimating all the possible CV directions along the abdominal plane parallel to the abdominal surface. Furthermore, due to the grid dimensions, planar wave propagation could be assumed and the small interelectrode distance enables following the same spike (action potential) from one electrode to the other [29]. In the present study, we intended to use the conduction velocity as an independent predictor of imminent delivery reflecting the increased propagation of action potentials between myometrial cells. Therefore, we chose a high-density grid with relatively small dimension. However, uterine activity throughout the whole uterus might provide additional information on imminent delivery and for that purpose we would consider a larger grid preferable. Ideally, a combination of local propagation and global synchronicity should be pursued, and this will be possibly considered in our future studies. Moreover, in order to improve user friendliness and simplify signal analysis, a reduced number of electrodes could be used, and depending on the chosen electrode configuration, a different hypothesis (e.g., point source) may be considered for propagation.

5. Conclusion

In agreement with previous studies, our results show that the CV vector amplitude is a promising parameter for predicting imminent (preterm) delivery. Automated estimation of this

parameter from the EHG signal is feasible and should be regarded as an important prerequisite for future clinical studies and applications in this context. Therefore, these results open the way to future studies on the accuracy of EHG parameters, such as the CV, for timely and accurate diagnosis of imminent preterm delivery.

Conflict of Interests

The authors declare that none of them have a conflict of interests.

Acknowledgment

The authors declare that the source of financial support was from ERASysBio European Research Project/Biophysical Modeling of the Uterine Electromyogram for Understanding and Preventing Preterm Labor: <http://www.erasysbio.net/index.php?index=268>.

References

- [1] N. S. Green, K. Damus, J. L. Simpson et al., "Research agenda for preterm birth: recommendations from the March of Dimes," *American Journal of Obstetrics and Gynecology*, vol. 193, no. 3, part 1, pp. 626–635, 2005.
- [2] T. J. Mathews and M. F. MacDorman, "Infant mortality statistics from the 2005 period linked birth/infant death data set," *National Vital Statistics Reports*, vol. 57, no. 2, pp. 1–32, 2008.
- [3] B. J. Stoll, N. I. Hansen, E. F. Bell et al., "Neonatal outcomes of extremely preterm infants from the NICHD Neonatal Research Network," *Pediatrics*, vol. 126, no. 3, pp. 443–456, 2010.
- [4] D. Roberts and S. Dalziel, "Antenatal corticosteroids for accelerating fetal lung maturation for women at risk of preterm birth," *Cochrane Database of Systematic Reviews*, vol. 3, Article ID CD004454, 2006.
- [5] J. F. King, A. Grant, M. J. N. C. Keirse, and I. Chalmers, "Beta-mimetics in preterm labour: an overview of the randomized controlled trials," *British Journal of Obstetrics and Gynaecology*, vol. 95, no. 3, pp. 211–222, 1988.
- [6] R. L. Goldenberg, J. F. Culhane, J. D. Iams, and R. Romero, "Epidemiology and causes of preterm birth," *The Lancet*, vol. 371, no. 9606, pp. 75–84, 2008.
- [7] R. E. Garfield, D. Merrett, and A. K. Grover, "Gap junction formation and regulation in myometrium," *The American journal of physiology*, vol. 239, no. 5, pp. C217–C228, 1980.
- [8] R. E. Garfield, M. G. Blennerhassett, and S. M. Miller, "Control of myometrial contractility: role and regulation of gap junctions," *Oxford Reviews of Reproductive Biology*, vol. 10, pp. 436–490, 1988.
- [9] R. E. Garfield and E. L. Hertzberg, "Cell-to-cell coupling in the myometrium: emil Bozler's prediction," *Progress in Clinical and Biological Research*, vol. 327, pp. 673–681, 1990.
- [10] W. J. Lammers, "The electrical activities of the uterus during pregnancy," *Reproductive Sciences*, vol. 20, no. 2, pp. 182–189, 2013.
- [11] C. Marque, J. M. G. Duchene, S. Leclercq, G. S. Panczer, and J. Chaumont, "Uterine EHG processing for obstetrical monitoring," *IEEE Transactions on Biomedical Engineering*, vol. 33, no. 12, pp. 1182–1187, 1986.
- [12] R. E. Garfield, H. Maul, L. Shi et al., "Methods and devices for the management of term and preterm labor," *Annals of the New York Academy of Sciences*, vol. 943, pp. 203–224, 2001.
- [13] T. Y. Euliano, D. Marossero, M. T. Nguyen, N. R. Euliano, J. Principe, and R. K. Edwards, "Spatiotemporal electrohysterography patterns in normal and arrested labor," *American Journal of Obstetrics and Gynecology*, vol. 200, no. 1, pp. 54.e1–54.e7, 2009.
- [14] M. P. G. C. Vinken, C. Rabotti, M. Mischi, and S. Guid Oei, "Accuracy of frequency-related parameters of the electrohysterogram for predicting preterm delivery: a review of the literature," *Obstetrical and Gynecological Survey*, vol. 64, no. 8, pp. 529–541, 2009.
- [15] M. Lucovnik, W. L. Maner, L. R. Chambliss et al., "Noninvasive uterine electromyography for prediction of preterm delivery," *American Journal of Obstetrics and Gynecology*, vol. 204, no. 3, pp. 228.e1–228.e10, 2011.
- [16] M. Hassan, J. Terrien, C. Muszynski, A. Alexandersson, C. Marque, and B. Karlsson, "Better pregnancy monitoring using nonlinear correlation analysis of external uterine electromyography," *IEEE Transactions on Biomedical Engineering*, vol. 60, no. 4, pp. 1160–1166, 2013.
- [17] C. Buhimschi, M. B. Boyle, and R. E. Garfield, "Electrical activity of the human uterus during pregnancy as recorded from the abdominal surface," *Obstetrics and Gynecology*, vol. 90, no. 1, pp. 102–111, 1997.
- [18] W. L. Maner, R. E. Garfield, H. Maul, G. Olson, and G. Saade, "Predicting term and preterm delivery with transabdominal uterine electromyography," *Obstetrics and Gynecology*, vol. 101, no. 6, pp. 1254–1260, 2003.
- [19] W. L. Maner and R. E. Garfield, "Identification of human term and preterm labor using artificial neural networks on uterine electromyography data," *Annals of Biomedical Engineering*, vol. 35, no. 3, pp. 465–473, 2007.
- [20] S. M. Miller, R. E. Garfield, and E. E. Daniel, "Improved propagation in myometrium associated with gap junctions during parturition," *American Journal of Physiology*, vol. 256, no. 1, part 1, pp. C130–C141, 1989.
- [21] H. Miyoshi, M. B. Boyle, L. B. MacKay, and R. E. Garfield, "Gap junction currents in cultured muscle cells from human myometrium," *American Journal of Obstetrics and Gynecology*, vol. 178, no. 3, pp. 588–593, 1998.
- [22] R. E. Garfield and W. L. Maner, "Physiology and electrical activity of uterine contractions," *Seminars in Cell and Developmental Biology*, vol. 18, no. 3, pp. 289–295, 2007.
- [23] D. Devedeux, C. Marque, S. Mansour, G. Germain, and J. Duchene, "Uterine electromyography: a critical review," *American Journal of Obstetrics and Gynecology*, vol. 169, no. 6, pp. 1636–1653, 1993.
- [24] W. J. Lammers, "The electrical activities of the uterus during pregnancy," *Reproductive Sciences*, vol. 20, no. 2, pp. 182–189.
- [25] J. Duchène CM and S. Planque, "Uterine EMG signal: propagation analysis," in *Proceedings of the 12th Annual International Conference of the IEEE Engineering in Medicine and Biology Society*, pp. 831–832, 1990.
- [26] W. J. E. P. Lammers, H. Mirghani, B. Stephen et al., "Patterns of electrical propagation in the intact pregnant guinea pig uterus," *American Journal of Physiology: Regulatory Integrative and Comparative Physiology*, vol. 294, no. 3, pp. R919–R928, 2008.
- [27] C. Rabotti, M. Mischi, J. van Laar, G. Oei, and J. Bergmans, "On the propagation analysis of electrohysterographic signals,"

- Proceedings of the Annual International Conference of the IEEE Engineering in Medicine and Biology Society*, vol. 2008, pp. 3868–3871, 2008.
- [28] M. Mischi, C. Rabotti, L. P. J. Vosters, S. G. Oei, and J. W. M. Bergmans, “Electrohysterographic conduction velocity estimation,” in *Proceedings of the 31st Annual International Conference of the IEEE Engineering in Medicine and Biology Society: Engineering the Future of Biomedicine (EMBC '09)*, pp. 6934–6937, September 2009.
- [29] C. Rabotti, M. Mischi, J. O. E. H. Van Laar, G. S. Oei, and J. W. M. Bergmans, “Inter-electrode delay estimators for electrohysterographic propagation analysis,” *Physiological Measurement*, vol. 30, no. 8, pp. 745–761, 2009.
- [30] C. Rabotti and M. Mischi, “Two-dimensional estimation of the electrohysterographic conduction velocity,” in *Proceedings of the 32nd Annual International Conference of the IEEE Engineering in Medicine and Biology Society (EMBC '10)*, pp. 4262–4265, September 2010.
- [31] C. Rabotti, M. Mischi, S. G. Oei, and J. W. M. Bergmans, “Non-invasive estimation of the electrohysterographic action-potential conduction velocity,” *IEEE Transactions on Biomedical Engineering*, vol. 57, no. 9, pp. 2178–2187, 2010.
- [32] C. Rabotti, M. Mischi, J. O. E. H. Van Laar, G. S. Oei, and J. W. M. Bergmans, “Estimation of internal uterine pressure by joint amplitude and frequency analysis of electrohysterographic signals,” *Physiological Measurement*, vol. 29, no. 7, pp. 829–841, 2008.
- [33] J. Jezewski, K. Horoba, A. Matonia, and J. Wrobel, “Quantitative analysis of contraction patterns in electrical activity signal of pregnant uterus as an alternative to mechanical approach,” *Physiological Measurement*, vol. 26, no. 5, pp. 753–767, 2005.
- [34] J. Laforet, C. Rabotti, J. Terrien, M. Mischi, and C. Marque, “Toward a multiscale model of the uterine electrical activity,” *IEEE Transactions on Biomedical Engineering*, vol. 58, no. 12, pp. 3487–3490, 2011.
- [35] W. J. E. P. Lammers, B. Stephen, R. Hamid, and D. W. G. Harron, “The effects of oxytocin on the pattern of electrical propagation in the isolated pregnant uterus of the rat,” *Pflugers Archiv European Journal of Physiology*, vol. 437, no. 3, pp. 363–370, 1999.
- [36] C. Rabotti, S. G. Oei, J. Van 'T Hooft, and M. Mischi, “Electrohysterographic propagation velocity for preterm delivery prediction,” *American Journal of Obstetrics and Gynecology*, vol. 205, no. 6, pp. e9–e10, 2011.

Research Article

Comparison of Different EHG Feature Selection Methods for the Detection of Preterm Labor

D. Alamedine,^{1,2} M. Khalil,² and C. Marque¹

¹ CNRS UMR 7338, Biomécanique et Bio-Ingénierie, Université de Technologie de Compiègne, 60200 Compiègne, France

² Azm Platform for Research in Biotechnology and Its Applications, LASTRE Laboratory, Lebanese University, Tripoli, Lebanon

Correspondence should be addressed to D. Alamedine; dima.alamedine@gmail.com

Received 29 June 2013; Revised 11 October 2013; Accepted 4 November 2013

Academic Editor: Brynjar Karlsson

Copyright © 2013 D. Alamedine et al. This is an open access article distributed under the Creative Commons Attribution License, which permits unrestricted use, distribution, and reproduction in any medium, provided the original work is properly cited.

Numerous types of linear and nonlinear features have been extracted from the electrohysterogram (EHG) in order to classify labor and pregnancy contractions. As a result, the number of available features is now very large. The goal of this study is to reduce the number of features by selecting only the relevant ones which are useful for solving the classification problem. This paper presents three methods for feature subset selection that can be applied to choose the best subsets for classifying labor and pregnancy contractions: an algorithm using the Jeffrey divergence (JD) distance, a sequential forward selection (SFS) algorithm, and a binary particle swarm optimization (BPSO) algorithm. The two last methods are based on a classifier and were tested with three types of classifiers. These methods have allowed us to identify common features which are relevant for contraction classification.

1. Introduction

Preterm birth, that is, birth before the 37th week of pregnancy, remains a major problem in obstetrics. Children born before term present a high risk of mortality as well as health and development problems [1]. According to the World Health Organization (WHO), preterm birth rates range between 5% and 12% of births and perinatal mortality occurs in 3% to 47% of these cases in even the most developed parts of the world [2].

Delivery occurs after the onset of regular and effective uterine contractions, which cause dilation of the cervix and expulsion of the fetus. A contraction of the uterine muscle occurs due to the generation of electrical activity in a given uterine cell that spreads to other, neighboring cells. The evolution of uterine contractions, from weak and ineffective during pregnancy to strong and effective during labor, is therefore related to an increase in cellular excitability to an increase in the synchronization of the entire uterus [3].

A primary aim of pregnancy is to maintain the well-being of both mother and fetus and to keep the latter in utero as long as needed for a healthy birth. During pregnancy, the monitoring of uterine contractility is crucial in order to differentiate normal contractions, which are ineffective, from

those effective contractions which might cause early dilation of the cervix and induce preterm birth. Despite increased knowledge and understanding of the phenomena involved in the onset of preterm labor, the methods currently used in obstetrics are not precise enough for an early detection of preterm birth threats. We need a more reliable method for early detection and prevention of preterm birth threats.

One of the most promising methods for monitoring uterine activity began in the 1950s and was developed in the 1980s. It is based on the study of the electrical activity of the uterus as recorded on the mother's abdominal surface [5]. The electrohysterogram (EHG) consists of the summation of the electrical activity generated by the active uterine muscle cells, plus the noise related to corrupting electrical and mechanical activities. EHG, recorded externally, has been demonstrated to be representative of the uterine electrical activity as recorded internally [6].

Many teams have extracted features from the EHG signals in order to find specific information leading to the detection of preterm birth. Firstly, linear methods in both time and frequency domains were used to extract features from the EHG. In order to improve the results obtained by using linear methods and because the EHG, like other biomedical signals, presents some nonlinear characteristics, several measures

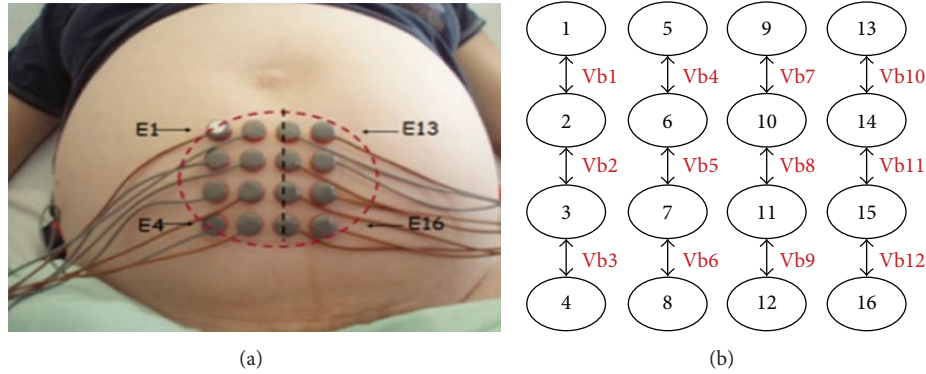


FIGURE 1: (a) Position of the 16 monopolar electrodes [4]. (b) Vb_i ($i = 1-12$) represent the 12 calculated bipolar signals.

have been proposed for detecting nonlinear characteristics in the EHG.

A large number of features have thus far been extracted from the EHG signal by many different researchers using very different population and recording protocols. In general, the complexity of calculations required for diagnostic purposes increases with the number of features in play. The reduction of feature dimensionality through the elimination of irrelevant and noisy features is very important in pattern recognition. The objective of this study is to select the most significant subset, among features extracted from the bibliography, in order to discriminate pregnancy and labor contractions, with these features being computed from the same given population. In this study, we selected from the bibliographic data 20 features (16 linear and 4 nonlinear) extracted from the EHG: mean frequency (MPF) [7], peak frequency (PF) [8–10], and deciles ($D1 \dots D9$) [11] which contain the median frequency [9, 11, 12], parameters extracted from wavelet decomposition ($W1 \dots W5$) [13], Lyapunov exponent (LE) [14, 15], time reversibility (Tr) [15], sample entropy (SE) [12], and variance entropy (VarEn) [16].

In this work, three methods are presented for feature subset selection. The first one, developed in this work, is based on the measurement of the Jeffrey divergence (JD) distance between the parameter histograms computed from the pregnancy and labor EHG classes [17]. The last two methods, developed for data mining, rely on the combination of a classifier and a search procedure: either sequential forward selection (SFS) [18] or binary particle swarm optimization (BPSO) [19]. The goal of these methods is to select, from a given feature set, the features subset that gives the maximum classification accuracy.

This paper is organized as follows. In the first part we will describe the experimental protocol. Then we will present the features extracted from the EHG processing bibliography and the three methods for feature selection. Finally, we will present the results of feature selection.

2. Experimental Protocol

In our study we used signals recorded on 48 women: 32 during pregnancy (33–39 weeks of gestation) and 16 during

labor (39–42 weeks of gestation). The measurements were performed at two hospitals in France and Iceland. In Iceland, the measurements were performed at the Landspítali University Hospital, using a protocol approved by the relevant ethical committee (VSN02-0006-V2). In France, the measurements were performed at the Center for Obstetrics and Gynecology (Amiens), using a protocol approved by the relevant ethical committee (ID-RCB 2011-A00500-41)). After the recording, we followed the pregnant women in order to label the signals as either pregnancy or labor. When the woman gave birth within 24 hours, the signal was labeled “labor”. If the delivery occurred later, the signal was labeled “pregnancy”. In our study not all pregnancies ended by a spontaneous delivery, and in both hospitals different drugs are routinely used for labor induction or progress. In our study, 7 women received oxytocin (79 contractions), 3 women received Prostaglandin (49 contractions), 1 woman received Epidural (3 contractions), and 8 women received no drugs (38 contractions). Our database contains only singleton pregnancies.

The EHG signals were recorded using a multielectrode system composed of 18 electrodes: 16 arranged in a 4×4 matrix positioned on the woman’s abdomen and two reference electrodes placed on each of her hips [20]. The amplifier bandwidth is 0.16–128 Hz. To increase the signal-to-noise ratio, we calculated the vertical bipolar signals (Vb_i). Finally, we obtained 12 bipolar signals as shown in Figure 1. The bandwidth of our signal lies between 0.1 and 3 Hz. The sampling frequency used is 200 Hz, downsampled by a factor of 12 to obtain a new signal of 16.67 Hz.

In this study, we used only one bipolar signal, Vb_7 , because this signal is a reference recording position that has been used for a long time in our research. It is located on the median vertical axis of the uterus. The signal energy in this area remains high throughout the pregnancy as well as during labor. The bursts of uterine electrical activity that correspond to contractions were manually segmented, based on the tocodynamometer signal recorded simultaneously. After this manual segmentation of EHG bursts, we obtained a database containing 133 pregnancy bursts and 133 labor bursts.

3. Materials and Methods

3.1. Parameters Extraction. In our study 20 parameters have been extracted from the EHG. These parameters are divided into two categories: linear and nonlinear.

3.1.1. Linear Parameters

Parameters Related to the Power Spectral Density. Several frequency parameters have been extracted from the power spectral density (PSD), $S_x(f)$. In our work, we use the Welch Periodogram method to calculate the power spectral density of each burst [11]. This Welch Periodogram uses a window of type nfft, with size equal to the length of signal/2, with 50% overlap, for a total of three windows used. Eleven frequency parameters are extracted from this PSD: mean frequency MPF [7], peak frequency (PF) [8–10], and deciles $D1 \dots D9$ [11], which contain the median frequency $D5$ [9, 11, 12]. Deciles correspond to the frequencies $D1 \dots D9$ that divide the power spectral density into parts with each containing 10% of the total energy. Consider the following:

$$\int_{D_{p-1}}^{D_p} S_x(f) df = 0.1 \int_0^{f_{\max}} S_x(f) df. \quad (1)$$

Parameters Extracted from Wavelet Decomposition. Some authors have also used time-frequency methods, such as wavelet decomposition, to characterize the nonstationary characteristics of the EHG. In our work, we used the wavelet symlet 5, a choice based on the study referenced in [21]. This study compared several types of wavelets. The results have shown that the symlet 5 appears to be the most appropriate wavelet for the analysis of EHG signals for detection and classification purposes. After decomposition of each EHG burst into detail coefficients, we calculate the variances on the following detail levels: 2, 3, 4, 5, and 6 (named $W1$, $W2$, $W3$, $W4$, and $W5$) as previously proposed in [13]. These detail coefficients are as follows: $D2$ [2.08–4.17 Hz], $D3$ [1.04–2.08 Hz], $D4$ [0.52–1.04 Hz], $D5$ [0.26–0.52 Hz], and $D6$ [0.13–0.26 Hz] (see Figure 2). The choice of the details depends on the sampling frequency of the signal (sample rate equal to 16.67 Hz after downsampling) in order to correspond to the same frequency bands as the one selected in [13]. These selected details represent more than 96% of the signal energy and cover the frequency band of interest.

3.1.2. Nonlinear Parameters

Time Reversibility (Tr). A time series is reversible if the probabilistic properties are unchanged with respect to time reversal. Time irreversibility is a good indicator of nonlinearity. To calculate the time reversibility (Tr) of the signal x we have used equation described in [15] as follows:

$$\text{Tr}(\tau) = \left(\frac{1}{N - \tau} \right) \sum_{n=\tau+1}^N (x_n - x_{n-\tau})^3, \quad (2)$$

where N is the signal length and τ is the time delay.

Lyapunov Exponent. The Lyapunov exponent (LE) studies the stability and the sensitivity to initial conditions of the system. It measures the rate of trajectory separation between adjacent

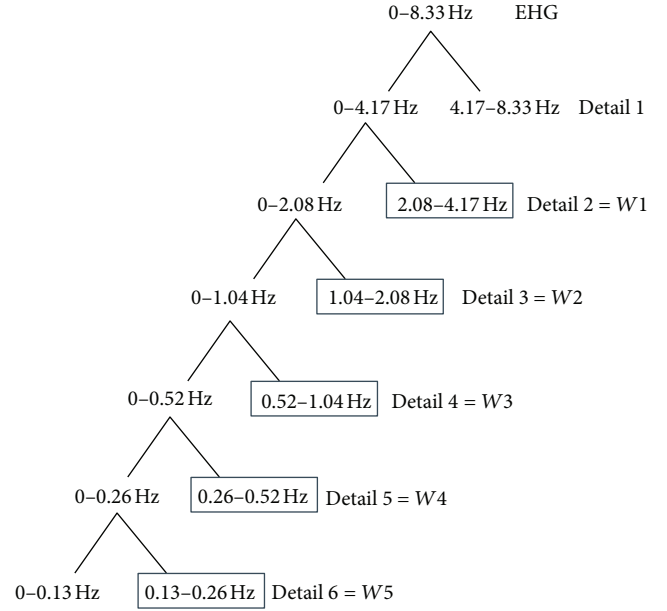


FIGURE 2: Wavelet decomposition.

tracks in the phase space [14, 15]. In our study we used the equation of LE described in [15] and represented by

$$\lambda = \lim_{t \rightarrow \infty} \lim_{\|\Delta_{d_0}\| \rightarrow 0} \left(\frac{1}{t} \right) \log \left(\frac{\|\Delta_{d_t}\|}{\|\Delta_{d_0}\|} \right), \quad (3)$$

where $\|\Delta_{d_0}\|$ represents the Euclidean distance between two states of the system at an arbitrary time t_0 and $\|\Delta_{d_t}\|$ corresponds to the Euclidean distance between the two states of the system at a later time t .

Sample Entropy. We used the sample entropy (SE) to identify the regularity of EHG signals. In our work, we used the sample entropy described in [12]. A less predictable time series presents higher sample entropy. Consider a time series $x(t)$ of length N and patterns $a_j(0, \dots, m-1)$ of length m , with $m < N$, and $a_j(i) = x(i+j)$; $i = 0, \dots, m-1$; $j = 0, \dots, N-m$. The time series $x(t)$ in a time $t = ts$, $x(ts, \dots, ts+m-1)$ is a match for a given pattern a_j , if $|x(ts+i) - a_j(i)| \leq r$, for each $0 \leq i < m$. Sample entropy is then computed as follows:

$$\text{SE}_{m,r}(x) = \begin{cases} -\log \left(\frac{C_m}{C_{m-1}} \right), & C_m \neq 0 \wedge C_{m-1} \neq 0, \\ -\log \left(\frac{(N-m)}{N-m-1} \right), & C_m = 0 \vee C_{m-1} = 0, \end{cases} \quad (4)$$

where the four parameters N , m , r , and C_m represent, respectively, the length of the time series, the length of the sequences to be compared, the tolerance for accepting matches, and the number of pattern matches (within a margin for r) that is constructed for each m .

In our study, the value of m equals 2. This value is determined by the method of the false nearest neighbors (FNN); the value of r equals 0.2 according to the literature [12].

Variance Entropy. Recent studies have used the variance entropy (VarEn) to study biological signals but not for the EHG. We are interested in using variance entropy because this method combines the variance with sample entropy via inverse-variance weighting. For a time series x , variance entropy is defined as

$$\text{VarEn}(x, m, r) = \frac{\sum_{i=1}^p \text{SE}_{m,r}(x_i) \times w_i}{\sum_{i=1}^p w_i}, \quad (5)$$

where x_i is the i th segment of x , w_i is the inverse variance of x_i , and p is the number of sliding windows. p is not fixed because the length of signals in our database depends on EHG burst durations.

The sliding window, of size equal to 50 (window size), slides over time with a step of 45 (step size), leading to an overlap between the sliding windows which is equal to 5. The choices of window size and step size were made empirically after several trials. p therefore depends on window size.

Because variance entropy combines the variance with sample entropy via inverse-variance weighting, the number of windows is very important and can significantly affect the results. p must be neither too high nor too small. A too large p value induces large computing time and does not give a precise result. A too small p value limits detection of variability.

3.2. Feature Selection Techniques

3.2.1. Feature Selection Based on Jeffrey Divergence Distance. This method consists of calculating, for each feature, the Jeffrey divergence (JD) distance between the two histograms obtained from the pregnancy and labor burst classes. This distance between the two histograms allows us to measure the similarity/dissimilarity of their corresponding statistical properties. A smaller distance means a larger similarity while a larger distance implies a lower similarity [22]. The divergence distance is then used to select the discriminating features. Indeed, the greater the distance between the feature histograms of pregnancy and labor classes is, the more discriminating the feature is [17].

This method has two parts. The first part consists of calculating parameters and their histograms. The second part consists of computing the distance between the histograms.

Calculating Parameters and Their Histograms. For each contraction of each group, we apply the following steps.

- (1) Calculate the nonlinear parameters on the whole EHG. These methods are time reversibility (Tr), Lyapunov exponent (LE), sample entropy (SE), and variance entropy (VarEn).
- (2) Calculate the variances on the following details levels after wavelet decomposition 2, 3, 4, 5, and 6 ($W1$, $W2$, $W3$, $W4$, and $W5$).
- (3) For each signal, compute the frequency parameters: deciles ($D1$, $D2$, $D3$, $D4$, $D5$, $D6$, $D7$, $D8$, and $D9$), mean frequency (MPF), and peak frequency (PF), from the PSD of EHG.

- (4) Group these values in a matrix calculated on the whole EHG database. Thus, we obtain, for a given contraction, a vector with dimension 20. The 20 columns of the matrix correspond to the 20 parameter values computed from one EHG. As we have 133 contractions in each class, we obtain 133 vectors of dimension 20 by class (one 133×20 matrix for each class). We then compute from these 133 vectors of each class the histogram for each parameter, giving us 2 sets of 20 histograms, one for each parameter and for each class.

Distance between Histograms. After obtaining, for a given parameter, the two histograms for the labor and pregnancy classes, we measure the distance between the histogram of the two classes. To measure this distance, we use the Jeffrey divergence method presented in [22]:

$$D_{je}(H, G) = \sum_y \left(h_y \log \frac{h_y}{g_y} + g_y \log \frac{g_y}{h_y} \right), \quad (6)$$

where H and G are the two histograms and where N bins ($N = 10$) are defined as $H = \{h_y\}$ and $G = \{g_y\}$, with the bin index $y \in \{1, 2, \dots, N\}$. After calculating the distances between every two corresponding parameter histograms for the 20 parameters, we obtain a distance vector of dimension 20. We compute the distribution of the distances contained in this distance vector. The goal of our study is to select the most discriminating parameters; therefore, we apply a threshold on the vector of distances in order to select the parameters associated with the larger distances. After verification of the Gaussianity of this distribution by using the Lilliefors test, the threshold is chosen to be equal to mean $+1^*$ standard deviation of the distance distribution.

3.2.2. Sequential Forward Selection (SFS). Sequential forward selection (SFS) is a sequential search algorithm for feature selection [23] developed for data mining. SFS begins with an empty subset. The value of the criterion function (J) is calculated for each feature by using a classifier. The feature presenting the best classification performance is selected (Y_k) and then added to the subset. The next step consists of adding sequentially the feature x^+ that has the highest criterion function $J(Y_k + x^+)$ when combined with the features Y_k that have already been selected. This cycle is repeated until no criterion improvement is obtained when extending the current subset. The following steps present the algorithm of SFS [18].

- (1) Start with an empty subset $Y_0 = \{\Phi\}$
- (2) Select the next best feature: $x^+ = \arg \max[J(Y_k + x^+)]$
- (3) If $J(Y_k + x^+) > J(Y_k)$
 - (a) Update $Y_{k+1} = Y_k + x^+, k = k + 1$
 - (b) Go to step 2

End

For our study, three classical classifiers have been used to compute the criterion function J (minimal error). The classifiers are as follows: linear discriminant analysis (LDA) [24], quadratic discriminant analysis (QDA) [25], and K -nearest neighbors (KNN) with $K = 11$ (the choice of K is based on the number of training sets) [24]. The SFS algorithm searches sequentially for the best feature subset. We then chose only the combination of features that presents this minimal error.

The SFS algorithm is applied to synthetic data to test its efficiency. The synthetic data consists of a matrix $400 * 6$ (400 observations corresponding to two classes defined by 6 features). Four features (features 1, 2, 4, and 6) are generated randomly (centered normalized Gaussian). The remaining ones (features 3 and 5) are generated using normalized Gaussian distributions of mean m_1 for class 1 and m_2 for class 2. After verification of its efficiency on synthetic data, we have applied it to our EHG database. We used 70% of the data set for classifier training and the remaining 30% for testing.

3.2.3. Binary Particle Swarm Optimization (BPSO). Particle swarm optimization (PSO) was developed by Eberhart and Kennedy in 1995. It is a population-based stochastic optimization technique that was inspired by the social behavior of bird flocking or fish schooling [26]. PSO uses a number of particles (the swarm) moving around in the search space in order to achieve the best solution. We assume that our search space is n -dimensional and that each particle is a point in this space. The position of the i th particle of the swarm is represented as $X_i = (x_{i1}, \dots, x_{id}, \dots, x_{in})$. Each particle has a best previous position $pbest_i = (p_{i1}, \dots, p_{id}, \dots, p_{in})$, which corresponds to the best fitness value (in our case best classification given by a classifier fed with the selected features). The global best particle among all the particles in the population is represented by $gbest = (p_{g1}, \dots, p_{gd}, \dots, p_{gn})$. The velocity of the i th particle is denoted by $V_i = (v_{i1}, \dots, v_{id}, \dots, v_{in})$. The particles velocity and position are manipulated according to the following two equations:

$$v_{id}^{k+1} = wv_{id}^k + c_1r_1^k(p_{id}^k - x_{id}^k) + c_2r_2^k(p_{gd}^k - x_{id}^k), \quad (7)$$

$$x_{id}^{k+1} = x_{id}^k + v_{id}^{k+1}, \quad (8)$$

where w is the inertia weight, c_1 and c_2 are positive constants, and r_1 and r_2 are two random values in the range $[0, 1]$.

Kennedy and Eberhart also proposed a binary particle swarm optimization (BPSO) in order to solve optimization problems with discrete valued parameters [19]. In BPSO, the position of each particle is represented as binary strings. By comparing PSO and BPSO we found that they have a common velocity equation and a different particle position equation which can be computed as follows:

$$S(v_{id}^{k+1}) = \frac{1}{1 + e^{v_{id}^{k+1}}}, \quad (9)$$

$$x_{id}^{k+1} = \begin{cases} 1 & \text{if } r_3 < S(v_{id}^{k+1}) \\ 0 & \text{otherwise,} \end{cases} \quad (10)$$

where $S(v_{id}^{k+1})$ is the sigmoid function and r_3 is a random number in the range $[0, 1]$.

BPSO has been widely used recently in the literature for feature subset selection [27]. In this case, the length of a binary string of each particle is equal to the length of the total number of features, and each particle presents a candidate for subset selection. If the bit included in the binary strings has a value of "1", the feature is selected; otherwise, the feature is not selected. The following steps present the BPSO algorithm.

- (1) Initialize all particles positions and velocities randomly. Set the number of iterations K and other BPSO parameters.
- (2) Calculate the fitness value $F(X_i)$ of each particle. Fitness represents the percentages of correct classification.
- (3) Compare the fitness of each particle to its best fitness so far ($pbest_i^k$ of last iteration k):

$$\text{if } F(X_i^{k+1}) > F(pbest_i^k) \text{ then } F(pbest_i^{k+1}) = F(X_i^{k+1}) \text{ and } pbest_i^{k+1} = X_i^{k+1}$$

$$\text{Else } F(pbest_i^{k+1}) = F(pbest_i^k) \text{ and } pbest_i^{k+1} = pbest_i^k$$

- (4) Determine the global best position $gbest^{k+1}$ from all $pbest_i^{k+1}$. Then compare $gbest^{k+1}$ with $gbest^k$:

$$\text{if } F(gbest^{k+1}) > F(gbest^k) \text{ then } gbest = gbest^{k+1}$$

$$\text{Else } gbest = gbest^k$$

- (5) Update the position and the velocity of each particle according to (7) and (10).
- (6) Go to step 2, and repeat until the number of iterations is reached.

When the limit number of iterations is reached, we obtain an optimal solution (best subset of feature selection).

The parameters for the BPOS were chosen classically as 30 particles, with the length of each particle being equal to 20 (maximum number of features), $K = 100$ iterations. The acceleration constants c_1 and c_2 were set to 2. We also used a linear descending inertia weight passing from 0.6 to 0.1.

In our paper, for BPSO algorithm, three classical classifiers have been used to compute the fitness: linear discriminant analysis (LDA) [24], quadratic discriminant analysis (QDA) [25], and K -nearest neighbors (KNN) with $K = 11$ (the choice of K is based on the number of training sets) [24]. The best feature subset chosen by the BPSO algorithm is defined as the one giving the maximum percentages of correct classification after 100 iterations (1 run). Then, to evaluate the performances and variability of BPSO, we performed multiple runs (200 runs). This algorithm is applied to the same synthetic and real data as described above.

TABLE 1: Mean \pm standard deviation (STD) of parameters and results of Gaussianity test.

Parameter	Mean \pm STD (pregnancy)	Gaussian	Mean \pm STD (labor)	Gaussian
Tr	0.001 \pm 0.01	N	-0.0001 \pm 0.01	N
LE	5.47 \pm 0.63	Y	5.33 \pm 0.52	Y
SE	1.17 \pm 0.19	Y	1.23 \pm 0.18	Y
VarEn	0.61 \pm 0.30	Y	0.71 \pm 0.29	Y
W1	0.0084 \pm 0.0076	N	0.0118 \pm 0.0114	Y
W2	0.03 \pm 0.02	N	0.04 \pm 0.03	Y
W3	0.07 \pm 0.04	N	0.13 \pm 0.09	Y
W4	0.27 \pm 0.11	N	0.30 \pm 0.10	Y
W5	0.48 \pm 0.11	Y	0.41 \pm 0.13	Y
D1	0.14 \pm 0.02	N	0.15 \pm 0.02	Y
D2	0.16 \pm 0.03	N	0.17 \pm 0.04	N
D3	0.18 \pm 0.03	N	0.20 \pm 0.05	N
D4	0.20 \pm 0.04	N	0.23 \pm 0.07	N
D5	0.22 \pm 0.05	N	0.27 \pm 0.08	N
D6	0.25 \pm 0.06	N	0.32 \pm 0.10	Y
D7	0.29 \pm 0.07	N	0.37 \pm 0.10	Y
D8	0.36 \pm 0.09	N	0.45 \pm 0.12	Y
D9	0.52 \pm 0.18	N	0.64 \pm 0.22	Y
MPF	0.30 \pm 0.06	N	0.35 \pm 0.08	Y
PF	0.18 \pm 0.07	N	0.21 \pm 0.10	N

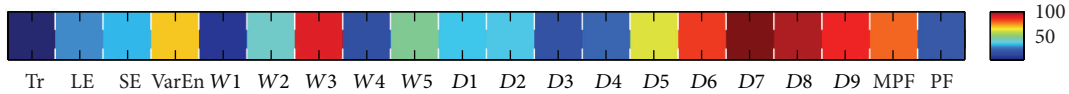


FIGURE 3: Color vector representing the distribution of distances between parameters.

4. Results

4.1. Results of Parameters Extraction. For each contraction of each group, we calculate the 20 parameters (linear and nonlinear parameters) from the EHG. Table 1 presents the mean \pm standard deviation of each of the parameters in each class. Additionally, in this table we present for each parameter the Lilliefors test result concerning its Gaussianity.

4.2. Results of Feature Selection Using JD Distance. We first present the results obtained with the feature selection method based on the Jeffrey divergence. After calculating the distances between every two corresponding feature histograms for the 20 features, we obtain a distance vector of dimension 20, as presented in Figure 3. The red color represents the maximum distance value of the distribution and the blue color its minimum. Each coordinate of this vector represents a different feature.

Figure 4 shows the selection vector obtained after applying the threshold (equal to the mean $+1^*$ standard deviation of the distance distribution) on the distance vector. A white color indicates that the feature has been selected as being discriminating between pregnancy and labor.

With this approach we selected 5 discriminating features: variance on the wavelet decomposition detail level 4 (*W3*), decile 6 (*D6*), decile 7 (*D7*), decile 8 (*D8*), and decile 9 (*D9*).

TABLE 2: Results of BPSO and SFS on synthetic data. The features marked in bold font, correspond to the discriminating features.

Classifiers	BPSO (gbest that have best fitness)	SFS (combination of features with minimal error)
QDA	[3 , 4, 5]	[3 , 5, 6]
LDA	[1, 3 , 4, 5, 6]	[3 , 5, 6]
KNN	[3 , 4, 5, 6]	[2, 3 , 5]

4.3. Results of Feature Selection Using SFS and BPSO

4.3.1. Results on Synthetic Data. The algorithms BPSO and SFS were first applied to the synthetic data described above in order to test their efficiency. Table 2 presents the results obtained after applying SFS and BPSO to these synthetic data. We notice that the two features 3 and 5 marked in bold font in Table 2 are always selected by the two algorithms (BPSO and SFS) whatever the mean $m1$ and $m2$ ($m1 \neq m2$) and whatever the classifier. We can also notice that both methods select larger sets than the minimum set containing the 2 clearly discriminating features, whatever the classifier, with SFS giving smaller sets than BPSO most of the time.

4.3.2. Results on Real Uterine EMG Signals. Table 3 presents the selected feature subset obtained from BPSO and SFS when

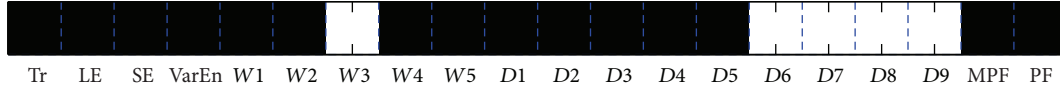


FIGURE 4: Selection vector representing the best parameters for the discrimination between pregnancy and labor.

TABLE 3: Comparison between BPSO and SFS. The common features between the subsets obtained from BPSO and SFS by using the three classifiers are marked in bold font.

Classifier	BPSO (gbest that have best fitness between 200 runs)	SFS (combination of features with minimal error)
QDA	LE, VarEn , W1, W4, D1, D2, D4, D5, D8 , D9	TR, LE, SE, VarEn , W1, W2, W4, D8 , D9
LDA	SE, VarEn , W1, W2, D1, D4, D8 , MPF	SE, VarEn , W2, W3, D1, D3, D7, D8 , D9, MPF
KNN	LE, SE, VarEn , W3, W4, D1, D3, D5, D6, D8	TR, LE, SE, VarEn , W1, W2, W3, W4, W5, D1, D2, D3, D4, D7, D8 , MPF

TABLE 4: Comparison of the percentage of correct classification of the selected features subset by using QDA.

Selection method	Selected feature subset	Correct classification using QDA
JD	W3, D6, D7, D8, D9	79.95%
SFS with QDA	TR, LE, SE, VarEn, W1, W2, W4, D8, D9	87.47%
SFS with LDA	SE, VarEn, W2, W3, D1, D3, D7, D8, D9, MPF	83.71%
SFS with KNN	TR, LE, SE, VarEn, W1, W2, W3, W4, W5, D1, D2, D3, D4, D7, D8, MPF	84.96%
BPSO with QDA	LE, VarEn, W1, W4, D1, D2, D4, D5, D8, D9	88.72%
BPSO with LDA	SE, VarEn, W1, W2, D1, D4, D8, MPF	81.20%
BPSO with KNN	LE, SE, VarEn, W3, W4, D1, D3, D5, D6, D8	86.22%

applied to our EHG database by using the 3 different classifiers. Each selected feature subset corresponds to that giving the maximum percentage of correct classification (93.73% with QDA, 91.23% with LDA, and 89.97% with KNN). Table 3 also presents the best feature subsets as selected by SFS, which corresponds to the minimal error.

From Table 3, we can notice that BPSO always selects 3 features regardless of classifier type. These features are VarEn, D1, and D8. For SFS, the common features between the subsets obtained from the three classifiers are SE, VarEn, W2, and D8. Only VarEn and D8 marked in bold font in Table 3 are systematically selected by both methods.

4.4. Validation. The results presented above give seven subsets of features selected by using JD, SFS with QDA, SFS with LDA, SFS with KNN, BPSO with QDA, BPSO with LDA, and BPSO with KNN. We then evaluated the performances of these seven selected subsets by calculating the percentages of correct classification that they give when used as inputs of a classifier. We used for this validation the same classifiers as used for the selection phase: QDA, LDA, and KNN.

Table 4 presents the percentages of correct classification for each subset by using the QDA classifier. The subset of features selected by BPSO with QDA presents the highest percentage of classification (88.72%) followed by the one selected by SFS with QDA (87.47%). Table 5 presents the percentage of correct classification for each subset by using the LDA classifier. The result indicates that the subset selected by SFS with QDA and SFS with KNN presents the highest percentage (84.96%) followed by the ones selected by SFS with LDA and BPSO with LDA (83.71%). Table 6 presents

the percentage of correct classification for each subset by using the KNN classifier. The result indicates that the subset selected by BPSO with QDA presents the highest percentage of classification (87.47%) followed by the ones selected by BPSO with KNN (84.96%).

5. Discussions and Conclusions

In this paper, we have extracted several features (linear and nonlinear) from the EHG. Then we have applied three selection techniques (Jeffrey divergence distance, SFS, and BPSO) in order to select the most pertinent features allowing discrimination between labor and pregnancy contractions.

It is clear from Table 2 (results obtained for synthetic data) that the algorithms BPSO and SFS have the ability to select discriminating features. In Table 3, which presents the selection results obtained from EHG signals, we notice that BPSO and SFS selected different subsets of features when using the three different classifiers. It is very important to highlight the most repetitive features selected with the different methods. Indeed, these features are expected to be very pertinent. Five features have been selected when applying the JD algorithm (W3, D6, D7, D8, and D9). Three others have been repeatedly selected by BPSO (VarEn, D1, and D8) and three others have been repeatedly selected by SFS (SE, VarEn, W2, and D8), whatever the type of classifier. Only D8 is common to these 3 subsets. D8 corresponds to the decile of mean value 0.36 ± 0.09 for the pregnancy class and 0.45 ± 0.12 for the labor class (Table 1). This increase in D8 value is in agreement with the most accepted observation made by teams that have worked on EHG frequency content,

TABLE 5: Comparison of the percentage of correct classification of the selected features subset by using LDA.

Selection method	Selected feature subset	Correct classification using LDA
JD	$W3, D6, D7, D8, D9$	81.20%
SFS with QDA	TR, LE, SE, VarEn, $W1, W2, W4, D8, D9$	84.96%
SFS with LDA	SE, VarEn, $W2, W3, D1, D3, D7, D8, D9$, MPF	83.71%
SFS with KNN	TR, LE, SE, VarEn, $W1, W2, W3, W4, W5, D1, D2, D3, D4, D7, D8$, MPF	84.96%
BPSO with QDA	LE, VarEn, $W1, W4, D1, D2, D4, D5, D8, D9$	82.46%
BPSO with LDA	SE, VarEn, $W1, W2, D1, D4, D8$, MPF	83.71%
BPSO with KNN	LE, SE, VarEn, $W3, W4, D1, D3, D5, D6, D8$	82.46%

TABLE 6: Comparison of the percentage of correct classification of the selected features subset by using KNN.

Selection method	Selected feature subset	Correct classification using KNN
JD	$W3, D6, D7, D8, D9$	78.70%
SFS with QDA	TR, LE, SE, VarEn, $W1, W2, W4, D8, D9$	83.71%
SFS with LDA	SE, VarEn, $W2, W3, D1, D3, D7, D8, D9$, MPF	81.20%
SFS with KNN	TR, LE, SE, VarEn, $W1, W2, W3, W4, W5, D1, D2, D3, D4, D7, D8$, MPF	83.71%
BPSO with QDA	LE, VarEn, $W1, W4, D1, D2, D4, D5, D8, D9$	87.47%
BPSO with LDA	SE, VarEn, $W1, W2, D1, D4, D8$, MPF	81.20%
BPSO with KNN	LE, SE, VarEn, $W3, W4, D1, D3, D5, D6, D8$	84.96%

whatever the species: a clear shift towards higher frequencies of the EHG frequency content when going from pregnancy to labor [3, 6].

Comparing the 6 subsets of features obtained by BPSO and SFS, we notice that two features, VarEn and D8, are also common. This confirms the observation made by different teams concerning the interest of taking into account the nonlinear characteristics of EHG for diagnostic purposes [12, 14, 15]. VarEn also increases from pregnancy to labor (Table 1), indicating an increase in EHG nonlinearity from pregnancy to labor, which is in agreement with the work done by different teams [12, 14, 15]. VarEn performed better here than the other nonlinear features computed by these teams. This short subset should also be of diagnostic interest.

From the validation study, developed in order to test the performance of the selected subsets, we notice from Table 4 that the feature selected by BPSO with QDA corresponds to the highest percentage of correct classification (88.72%) obtained when using QDA. Table 6 presents the second highest percentage of correct classification (87.47%) obtained with the subset of features selected by BPSO with QDA by using KNN. This allows us to say that BPSO associated with QDA seems to be the most efficient feature selection method in our study.

Two conclusions can be drawn from these results.

- (i) The most discriminating subset should be (or at least should contain) the 2 following features: VarEn and D8. Indeed, they are the most pertinent features selected in the 7 subsets of features defined by using JD, SFS, and BPSO, whatever the classifier.
- (ii) BPSO with QDA gives larger selected sets than the JD method, which might be demanding in time and in training data. But these sets also give much better results for the validation phase when using nonlinear

classifiers. This tends to imply that the classification of EHG should be based on a nonlinear approach, either for feature selection or classification, rather than on linear ones.

As future work, we will classify the EHG by using, as inputs of the classifier, only the selected features in order to compare the obtained results with the ones obtained by using all the features. We will also test the best methods of feature selection on a larger database. Accordingly, we will be able to use more robust and relevant cross-validation techniques than the simple one used in this study. Additionally, we should try other classification methods for the validation phase, such as those based on neural networks, SVM, or KNN. We will also include in this selection process features related to uterine synchronization and activity propagation that have been proven to be of interest for EHG monitoring [4], as soon as they are available from the work currently in progress in our team. With this work we expect to obtain the most pertinent data analysis features for predicting the preterm labor threat as early as possible.

Acknowledgment

The authors are indebted to the French Regional Council of Picardy and FEDER funds for funding this work.

References

- [1] R. L. Goldenberg, J. F. Culhane, J. D. Iams, and R. Romero, "Epidemiology and causes of preterm birth," *The Lancet*, vol. 371, no. 9606, pp. 75–84, 2008.
- [2] "Neonatal and perinatal mortality: country, regional and global estimates, Report WHO," 2006, http://whqlibdoc.who.int/publications/2006/9241563206_eng.pdf.

- [3] R. E. Garfield and W. L. Maner, "Physiology and electrical activity of uterine contractions," *Seminars in Cell and Developmental Biology*, vol. 18, no. 3, pp. 289–295, 2007.
- [4] M. Hassan, J. Terrien, C. Muszynski, A. Alexandersson, C. Marque, and B. Karlsson, "Better pregnancy monitoring using nonlinear correlation analysis of external uterine electromyography," *IEEE Transactions on Biomedical Engineering*, vol. 60, no. 4, pp. 1160–1166, 2013.
- [5] H. Alvarez and R. Caldeyro, "Contractility of the human uterus recorded by new methods," *Surgery, Gynecology & Obstetrics*, vol. 91, no. 1, pp. 1–13, 1950.
- [6] D. Devedeux, C. Marque, S. Mansour, G. Germain, and J. Duchene, "Uterine electromyography: a critical review," *American Journal of Obstetrics and Gynecology*, vol. 169, no. 6, pp. 1636–1653, 1993.
- [7] J. Terrien, T. Steingrimsdottir, C. Marque, and B. Karlsson, "Synchronization between EMG at different uterine locations investigated using time-frequency ridge reconstruction: comparison of pregnancy and labor contractions," *Eurasip Journal on Advances in Signal Processing*, vol. 2010, Article ID 242493, 2010.
- [8] W. L. Maner, R. E. Garfield, H. Maul, G. Olson, and G. Saade, "Predicting term and preterm delivery with transabdominal uterine electromyography," *Obstetrics and Gynecology*, vol. 101, no. 6, pp. 1254–1260, 2003.
- [9] J. Sikora, A. Matonia, R. Czabański, K. Horoba, J. Jezewski, and T. Kupka, "Recognition of premature threatening labour symptoms from bioelectrical uterine activity signals," *Archives of Perinatal Medicine*, vol. 17, no. 2, pp. 97–103, 2011.
- [10] M. Lucovnik, W. L. Maner, L. R. Chambliss et al., "Noninvasive uterine electromyography for prediction of preterm delivery," *American Journal of Obstetrics and Gynecology*, vol. 204, no. 3, pp. 228.e1–228.e10, 2011.
- [11] C. Marque, H. Leman, M. L. Voisine, J. Gondry, and P. Naepels, "Traitement de l'électromyogramme utérin pour la caractérisation des contractions pendant la grossesse," *RBM-News*, vol. 21, no. 9, pp. 200–211, 1999.
- [12] G. Fele-Žorž, G. Kavšek, Ž. Novak-Antolič, and F. Jager, "A comparison of various linear and non-linear signal processing techniques to separate uterine EMG records of term and preterm delivery groups," *Medical and Biological Engineering and Computing*, vol. 46, no. 9, pp. 911–922, 2008.
- [13] M. O. Diab, C. Marque, and M. A. Khalil, "Classification for uterine EMG signals: comparison between AR model and statistical classification method," *International Journal of Computational Cognition*, vol. 5, no. 1, pp. 8–14, 2007.
- [14] T. Ivancevic, L. Jain, J. Pattison, A. Hariz, and others, "Preterm birth analysis using nonlinear methods," *Recent Patents on Biomedical Engineering*, vol. 1, no. 3, pp. 160–170, 2008.
- [15] A. Diab, M. Hassan, C. Marque, and B. Karlsson, "Quantitative performance analysis of four methods of evaluating signal non-linearity: application to uterine EMG signals," in *Proceedings of the 34th Annual International IEEE EMBS Conference*, San Diego, Calif, USA, September 2012.
- [16] M. Hu and H. Liang, "Variance entropy: a method for characterizing perceptual awareness of visual stimulus," *Applied Computational Intelligence and Soft Computing*, vol. 2012, Article ID 525396, 6 pages, 2012.
- [17] D. Alamedine, M. Khalil, and C. Marque, "Parameters extraction and monitoring in uterine EMG signals," in *Detection of Preterm Deliveries, Recherche en Imagerie et Technologies pour la Santé (RITS)*, Bordeaux, France, 2013.
- [18] L. Ladha and T. Deepa, "Feature selection methods and algorithms," *International Journal on Computer Science and Engineering*, vol. 3, no. 5, pp. 1787–1797, 2011.
- [19] J. Kennedy and R. C. Eberhart, "Discrete binary version of the particle swarm algorithm," in *Proceedings of the IEEE International Conference on Systems, Man, and Cybernetics*, pp. 4104–4108, October 1997.
- [20] B. Karlsson, J. Terrien, V. Gudmundsson, T. Steingrimsdottir, and C. Marque, "Abdominal EHG on a 4 by 4 grid: mapping and presenting the propagation of uterine contractions," in *Proceedings of the 11th Mediterranean Conference on Medical and Biological Engineering and Computing*, pp. 139–143, Ljubljana, Slovenia, 2007.
- [21] M. Khalil, *Une approche de la détection et de la classification dans les signaux non stationnaires. Application à l'EMG utérin [Ph.D. thesis]*, Thèse de l'Université de Technologie de Troyes, 1999 French.
- [22] Y. Ma, X. Gu, and Y. Wang, "Histogram similarity measure using variable bin size distance," *Computer Vision and Image Understanding*, vol. 114, no. 8, pp. 981–989, 2010.
- [23] D. W. Aha and R. L. Bankert, "A comparative evaluation of sequential feature selection algorithms," in *Learning from Data*, pp. 199–206, Springer, New York, NY, USA, 1996.
- [24] S. Dudoit, J. Fridlyand, and T. P. Speed, "Comparison of discrimination methods for the classification of tumors using gene expression data," *Journal of the American Statistical Association*, vol. 97, no. 457, pp. 77–87, 2002.
- [25] N. Georgiou-Karistianis, M. A. Gray, D. J. F. Dominguez et al., "Automated differentiation of pre-diagnosis Huntington's disease from healthy control individuals based on quadratic discriminant analysis of the basal ganglia: the IMAGE-HD study," *Neurobiology of Disease*, vol. 51, pp. 82–92, 2013.
- [26] R. Eberhart and J. Kennedy, "New optimizer using particle swarm theory," in *Proceedings of the 6th International Symposium on Micro Machine and Human Science (MHS '95)*, pp. 39–43, October 1995.
- [27] V. Ranaee, A. Ebrahimzadeh, and R. Ghaderi, "Application of the PSOSVM model for recognition of control chart patterns," *ISA Transactions*, vol. 49, no. 4, pp. 577–586, 2010.

Research Article

Coarse-Grained Multifractality Analysis Based on Structure Function Measurements to Discriminate Healthy from Distressed Foetuses

Souad Oudjemia,¹ Amira Zaylaa,² Salah Haddab,¹ and Jean-Marc Girault²

¹ University of Mouloud Mammeri, Tizi-Ouzou, Algeria

² Signal & Imaging Group, University François Rabelais of Tours, UMR INSERM U930, PRES Loire Valley University, 7 Avenue Marcel Dassault, 37200 Tours, Cedex, France

Correspondence should be addressed to Jean-Marc Girault; jean-marc.girault@univ-tours.fr

Received 28 June 2013; Revised 6 November 2013; Accepted 22 November 2013

Academic Editor: Catherine Marque

Copyright © 2013 Souad Oudjemia et al. This is an open access article distributed under the Creative Commons Attribution License, which permits unrestricted use, distribution, and reproduction in any medium, provided the original work is properly cited.

This paper proposes a combined coarse-grained multifractal method to discriminate between distressed and normal foetuses. The coarse-graining operation was performed by means of a coarse-grained procedure and the multifractal operation was based on a structure function. The proposed method was evaluated by one hundred recordings including eighty normal foetuses and twenty distressed foetuses. We found that it was possible to discriminate between distressed and normal foetuses using the Hurst exponent, singularity, and Holder spectra.

1. Introduction

Foetal distress is often the result of reduction in respiratory exchange between the mother and the foetus. In most cases, foetal distress is strongly related to intrauterine growth retardation [1]. Early identification of distressed status from heart rate variability is highly important since it can help the obstetrician to decide on immediate delivery by caesarean section.

The value of analysis of heart rate variability (HRV) to provide a means of diagnosis and prognosis of heart disease is now well established. HRV time series has now become the elementary basis from which most analyses and processes are operated.

Due to the nonstationary and nonlinear nature of HRV time series, many recent studies have tried to take full advantage of the nonlinear nature of heart rate variability by analysing the complexity of time series. This complexity analysis of the foetal heart rate (FHR) that has its roots in adult HRV research can be conceived of in many ways. However, it was probably the scale invariance properties observed through power law spectral density [2] that was the triggering element for several studies based on the multiscale analysis of HRV [3, 4]. Among the overall complexity descriptors, entropy

descriptors [3, 5, 6] with fractal dimension estimators [7–10] were probably the first “nonconventional” tools used to study FHR. Certain studies even used multifractal features of FHR. The research studies by Ivanov et al. were probably the first to demonstrate multifractality in cardiac dynamics as well as in physiologic dynamics in general [11–13]. These seminal studies were then followed by researches such as [14–17], to name but a few.

The starting point of the present study was based on two approaches, the first being that of Wang et al. [15] focusing on the multifractal analysis of adult ECG signals with a coarse-graining approach initially proposed by [18].

The second approach was based on the studies by [19, 20] and more recently those of [16, 21, 22] that themselves used a method based on a structure function [23] of a time series in order to extract multifractal indicators.

In response to these two kinds of research, we investigated a coarse-grained multifractal analysis of the foetal heart rate in order to discriminate healthy from distressed foetuses.

Although the present study has certain similarities to those proposed by Wang et al. [15], our study was different in two ways. First, unlike the study based on a partition function proposed by [15], our study was based on a structure function.

The second difference was that our coarse-graining analysis was performed on the foetal heart rate, whereas that proposed by [15] was evaluated on adult electrocardiograms.

Our study aimed to improve the differentiation between normal and distressed fetuses by investigating the time scale dependency of the multifractal features of the FHR in depth. To do so we investigated the multifractal analysis originating from a structure function from a coarse-graining point of view.

To demonstrate the value of our approach, we tested the proposed method on a dataset derived from normal and distressed fetuses.

2. Materials

Our system comprised a personal computer and a Doppler ultrasound unit. The latter device contained three groups of four transducers and a Doppler acquisition board. The transducers exploring the foetal heart were nonfocused and mono-element. The transducers placed on the mother's abdomen were circular in shape, with a diameter of 13.5 mm and an acoustic power of 1 mW/cm^2 . Each transducer transmitted a sinusoidal pulse at 2.25 MHz with a pulse repetition frequency of 1 kHz. The wave was propagated through the mother's abdomen towards the foetal heart.

The backscattered signal was converted into an electrical signal and amplified to compensate for the attenuation of 1 dB/cm/MHz . The signal was then demodulated in phase (I) and quadrature (Q).

The Doppler signals were acquired at CHRU "Bretonneau" Tours, France. The consent of each patient was obtained and the study was approved by the Ethics Committee of the Clinical Investigation Centre for Innovative Technology of Tours (CIC-IT 806 CHRU of Tours). All patients were over eighteen years of age and pregnancies were single. One hundred examinations (eighty normal fetuses and twenty distressed fetuses) were recorded in this study. Gestational ages of fetuses ranged from 25 to 39 weeks were monitored for 30 minutes. FHR was evaluated as proposed by [24, 25], that is, every 250 ms, yielding 7200 samples for a recording of 30 minutes.

3. Methods

As previously reported, the foetal heart rate was estimated in real time from ultrasound Doppler signals [24, 25] and then recorded. The coarse-graining from HRV recordings procedure was performed offline. Then segmentation was applied. Scaling factors and multifractal spectra were subsequently evaluated using the structure function (see the scheme in Figure 2).

3.1. Coarse-Grained Analysis. Each time series $x(n)$ composed of $M = 7200$ points was analysed from FHR recordings. Multiscale analysis was introduced to capture the fluctuations present in the time series at different scales. This method consisted of evaluating approximate versions of the original time series from a local average of neighbouring

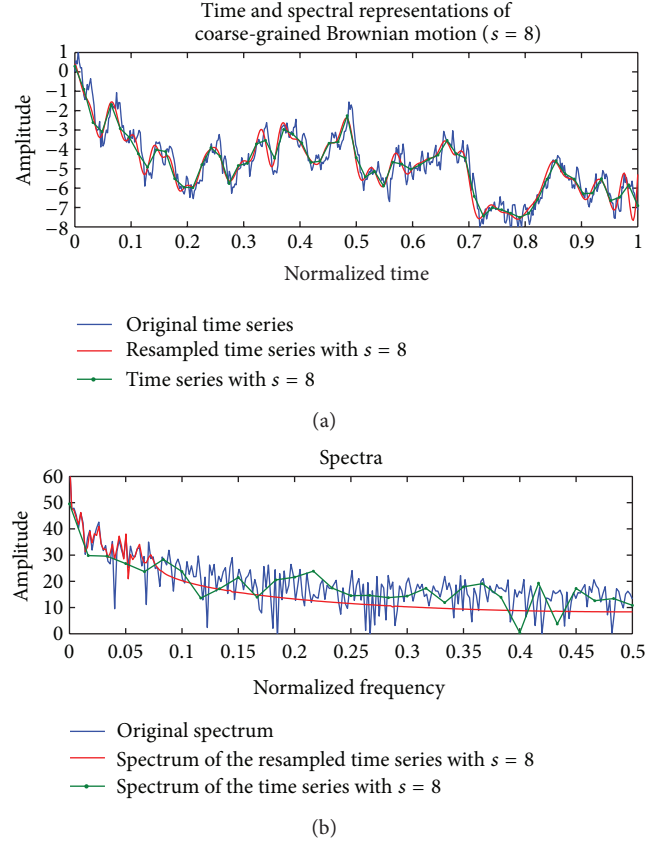


FIGURE 1: Time and spectral representations of a Brownian motion. (a) Original time series superimposed on the coarse-grained time series ($\alpha = 8$) and the resampled coarse-grained time series ($\alpha = 8$). (b) Spectrum of each time series depicted in (a).

points. This procedure is named "coarse-grained" [18]. The new reduced time series composed of M/α samples at scale α was written as

$$y_\alpha(k) = \frac{1}{\alpha} \sum_{i=(k-1)\alpha+1}^{k\alpha} x_i, \quad (1)$$

for $1 \leq k \leq M/\alpha$, $y_1(k) = x(k)$ being the original time series.

Figure 1 sets out the time and the spectral representations of coarse-grained Brownian motion time series used to calculate one of the effects resulting from the coarse-grained procedure. The time and the frequency were normalized. Figure 1(a) shows the original time series superimposed on the coarse-grained time series with $\alpha = 8$ and the resampled coarse-grained time series with $\alpha = 8$. Note that a resampled coarse-grained time series is an interpolated and filtered time series by a factor α . The resampled coarse-grained time series was composed of M samples.

Figures 1(a) and 1(b) show clearly that the coarse-grained time series were filtered time series. It can be claimed from these outcomes that the reducing duration of each coarse-grained time series is a side effect that can be avoided by resampling. In the following the multifractal descriptors were evaluated from resampled coarse-grained time series.

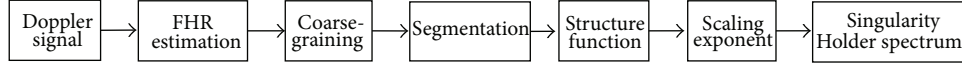


FIGURE 2: Scheme of different processes used to calculate coarse-grained multifractal descriptors.

As previously shown by [26], the more the fBm was filtered, the more the filtered fBm was regular: it can therefore be claimed that the higher the scale factor α , the higher the Hurst exponent H . In the study by [27], it was shown that the coarse-graining affected the anticorrelated time series ($H < 0.5$) in a more pronounced way than the correlated time series ($H > 0.5$). By supposing the coarse-grained effect to be a low pass filtering effect, we suggest that this can be understood in the following way.

- (i) For $H < 0.5$, fBm has several high frequency components that can be removed by the coarse-graining. Time series before and after filtering are quite different, indicating that the coarse-graining has a nonnegligible effect on time series.
- (ii) For $H > 0.5$, fBm has several low frequency components that are slightly removed by the coarse-graining effect. Time series before and after filtering were fairly similar, indicating that the coarse-graining has a negligible effect on time series.

Figure 3 represents different multifractal descriptors for different fBm of Hurst exponents $H = \{0.1, 0.5, 1\}$ with different scale factors $\alpha = \{1, 3, 6\}$. The fBm under consideration was composed of 720 samples. The results derived from Figure 3 showed that the anticorrelated fBm of Hurst exponent $H = 0.1$ was more affected by the coarse-graining effect than the correlated fBm of Hurst exponent $H = 1$. These results were compatible with those reported by [26, 27].

3.2. Multifractal Analysis. Due to the nonstationary nature of the coarse-grained time series analysed, a short-term procedure was performed. This procedure consisted of evaluating multifractal descriptors from subsignals $y_\alpha^{(i)}(k)$ composed of $N = 720$ points (3 min).

Among all the existing methods supplying multifractal descriptors, we used the structure function of order q . Although it has been demonstrated theoretically that for certain types of signals the methods based on structure function of order q have limitations for $q < 0$, we believe that this type of approach is still worth using because of the following.

- (i) The structure function is by far the simplest method to implement compared to DFA, box counting, and wavelet methods.
- (ii) Using $q < 0$ is valuable for analysing very small variations in time series. However, as time series were mostly corrupted by noise, it was impossible to probe small variations in the time series clearly. The practical value of such a negative order q was strongly limited by the presence of noise.

- (iii) The real signals under consideration were not theoretical signals. This means that mathematical demonstrations operating exclusively on theoretical signals are not systematically applicable in practice.
- (iv) Several multifractal analyses showed that it was more possible to discriminate between normal and distressed subjects for $q > 0$ than for $q < 0$. This was particularly the case in (i) [13] where it was shown that the difference between the scaling exponent $\tau(q)$ obtained for healthy and distressed subjects was greater for $q > 0$ than for $q < 0$ and in (ii) [28, 29] where it was clearly shown that for $q > 0$ it was possible to discriminate patients better with atropine than with placebo.

The structure function that we used in this study is defined [23] for $q > 0$ as follows:

$$Q(q, \epsilon) = \left(\int |y_\alpha^{(i)}(t + \epsilon) - y_\alpha^{(i)}(t)|^q dt \right)^{1/q}. \quad (2)$$

This structure function is a length measurement [26] where the term $|y_\alpha^{(i)}(t + \epsilon) - y_\alpha^{(i)}(t)|^q$ reveals a local behaviour while the term $(\int \dots dt)^{1/q}$ reveals a global behaviour.

If $Q(q, \epsilon) = K\epsilon^{\eta(q)}$, then the scaling exponent $\eta(q)$ is expressed (demonstration: $\log Q / \log \epsilon = \eta - (\log K / \log \epsilon)$ and $\lim_{\epsilon \rightarrow 0} (\log Q / \log \epsilon) = \eta$) as

$$\eta(q) = \lim_{\epsilon \rightarrow 0} \frac{\log(Q(q, \epsilon))}{\log(\epsilon)}. \quad (3)$$

Note that for a fractional Brownian motion of Hurst exponent H , the scaling exponent is $\eta(q) = H$. From the previous equation, the singularity spectrum $D(q)$ can be evaluated as follows:

$$D(q) = q^2 \frac{d\eta(q)}{dq} + 1. \quad (4)$$

The Holder spectrum is written as

$$h(q) = q \frac{d\eta(q)}{dq} + \eta(q). \quad (5)$$

Note that this singularity spectrum $D(q)$ can be obtained through a Legendre transform from $\tau(q)$:

$$D(q) = q \frac{d\tau(q)}{dq} - \tau(q), \quad (6)$$

where $\tau(q)$ is another scaling exponent defined by

$$\tau(q) = q\eta(q) - 1. \quad (7)$$

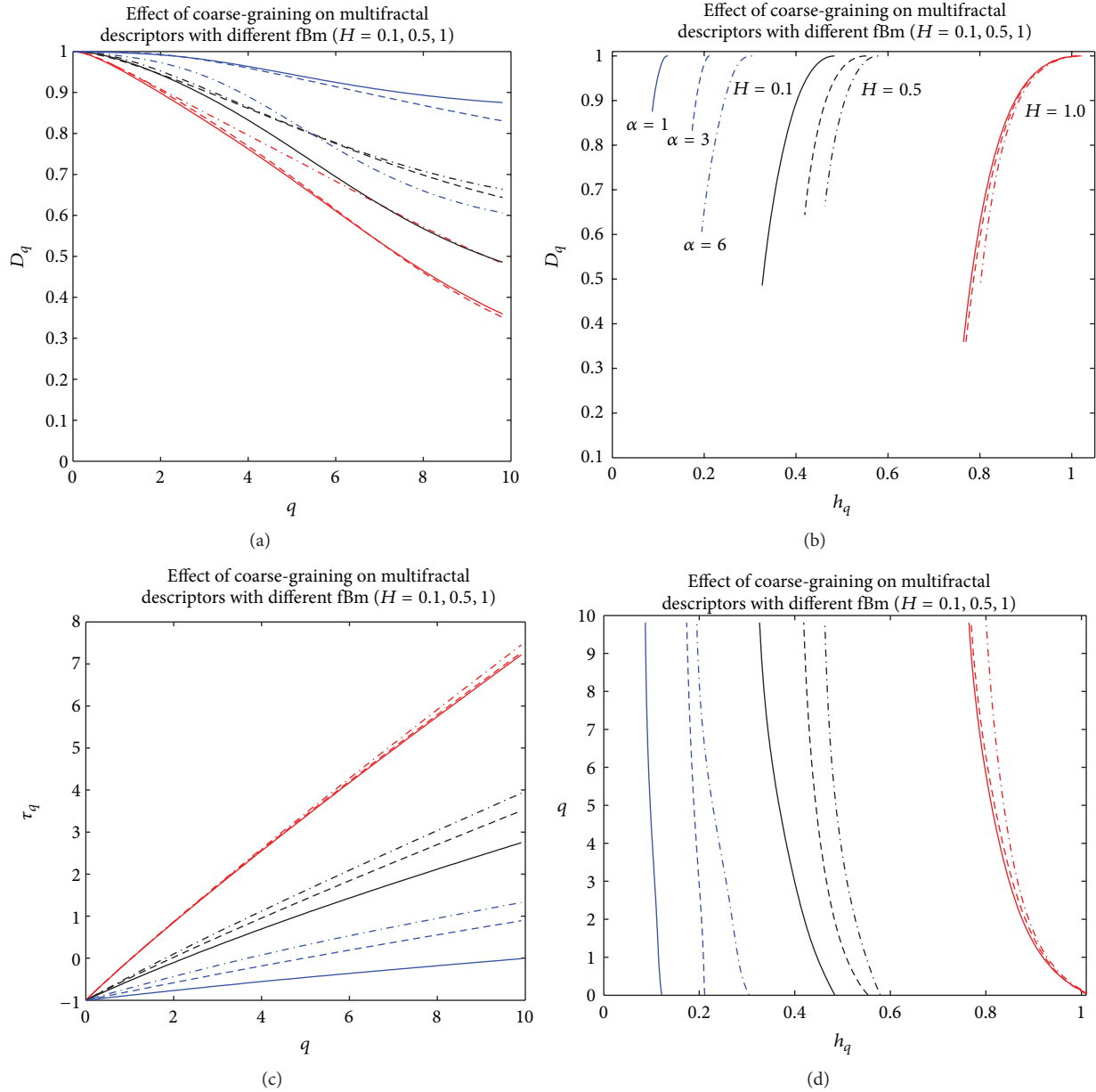


FIGURE 3: Effects of coarse-graining on multifractal descriptors for different fBm of Hurst exponents $H = \{0.1, 0.5, 1\}$ with different scale factors $\alpha = \{1, 3, 6\}$. (a) Singularity spectrum D versus q . (b) Singularity spectrum D versus Holder spectrum h . (c) Scaling exponent τ versus q . (d) Holder spectrum.

In this case, the Holder spectrum is written as

$$h(q) = \frac{d\tau(q)}{dq}. \quad (8)$$

The structure function $Q(q, \epsilon)$ and the scaling exponents $\eta(q)$ and $\tau(q)$ for a normal foetus and a distressed foetus are reported in Figure 4 as an illustration. Figure 4(a) shows that the slopes of the curves obtained for different values of q derived from the structure function $Q(d, \epsilon)$ were similar for the normal foetus. Similar results were derived for a distressed

foetus. Figures 4(b) and 4(c) show that both scaling exponents $\eta(q)$ and $\tau(q)$ were more nonlinear for the healthy foetus than for the distressed foetus.

Other multifractal descriptors such as the singularity spectrum $D(q)$ and the Holder spectrum $h(q)$ are reported in Figure 5. The results set out in Figure 5 were obtained from four different signals: a signal from a distressed foetus of an estimated Hurst exponent $H = 0.07$, a signal from a normal foetus of an estimated Hurst exponent $H = 0.31$, and two fractional Brownian motion (fBm) signals of Hurst exponents $H = 0.07$ and $H = 0.31$. These four signals were each composed of 720 samples. Figure 5 shows that the magnitude of the dynamics of the singularity spectrum $D(q)$ and the

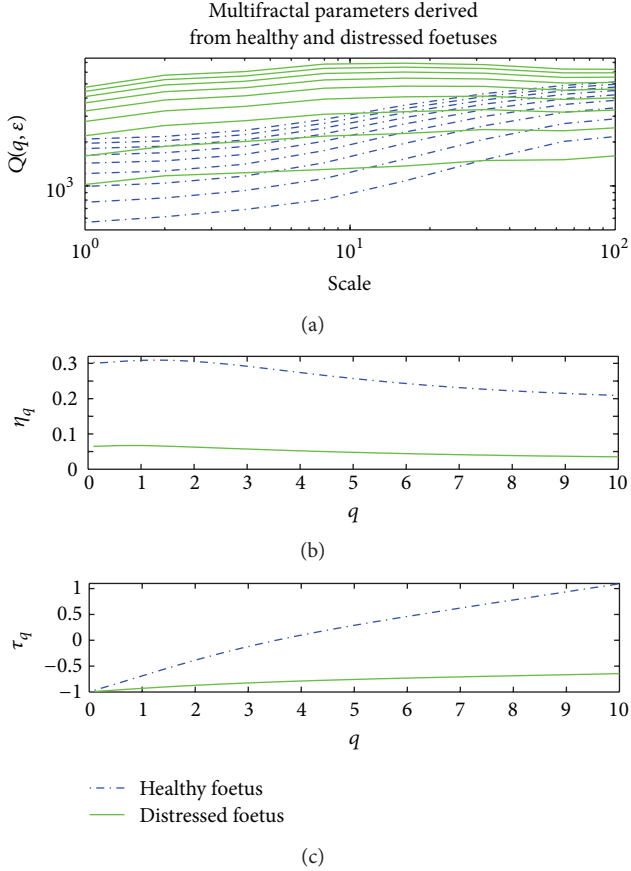


FIGURE 4: Multifractal parameters for a normal foetus (in blue) and a distressed foetus (in green). (a) Structure function $Q(q, \epsilon)$ versus scale. (b) Scaling exponent η versus q . (c) Scaling exponent τ versus q . The two scaling exponents were more nonlinear for a healthy foetus than for a distressed foetus.

Holder spectrum $h(q)$ was higher for the healthy foetus than for the distressed foetus. Similarly, the magnitude of the dynamics of $D(q)$ and $h(q)$ was higher for foetal signals than for the fBm of the Hurst exponent, as for foetal signals. This corroborates most of the studies based on the analysis of multifractal HRV [12] where a more pronounced multifractal feature for healthy subjects was demonstrated than for distressed subjects. The Holder spectrum for healthy and distressed foetuses decreased with increasing values of q , thus supporting the multifractal nature of FHR time series. Such results are consistent with previous similar studies [12, 16]. Note that normal and distressed fetal heart rate time series were reported in Figure 6 as an illustration.

Several measurements were performed in order to quantify the different trends observed in the multifractal indicators $D(q)$ and $h(q)$ for different scales α .

- (i) The relative error RE_1 (in %) of the Hurst exponent is defined as follows:

$$RE_1(\alpha) = \frac{|\overline{H}_n(\alpha) - \overline{H}_d(\alpha)|}{\overline{H}_n(\alpha)}, \quad (9)$$

where $\eta(q) = H$ is the Hurst exponent for all q . Note that $H = \eta(1)$. \overline{H}_n was the mean Hurst exponent corresponding to the average value obtained for all normal foetuses and \overline{H}_d was the mean Hurst exponent corresponding to the average value obtained for all distressed foetuses.

- (ii) The relative error RE_2 (in %) of the dynamics of $h(q)$ is defined as follows:

$$RE_2 = \frac{|\overline{\Delta}_{hn} - \overline{\Delta}_{hd}|}{\overline{\Delta}_{hn}}, \quad (10)$$

where $\Delta_h = \max(h) - \min(h)$ are the dynamics of $h(q)$, $\overline{\Delta}_{hn}$ being the mean dynamics corresponding to the average value obtained for all normal foetuses and $\overline{\Delta}_{hd}$ the mean dynamics corresponding to the average value obtained for all distressed foetuses.

- (iii) The relative error RE_3 (in %) is defined as follows:

$$RE_3 = \frac{|\overline{D}_n - \overline{D}_d|}{\overline{D}_n}, \quad (11)$$

where $\overline{D} = \text{mean}(D(q))$ is the mean value of the singularity spectrum, \overline{D}_n being the mean value corresponding to the average value obtained for all normal foetuses and \overline{D}_d the mean value corresponding to the average value obtained for all distressed foetuses.

- (iv) The relative error RE_4 (in %) is defined as follows:

$$RE_4 = \frac{|\overline{\Delta}_{Dn} - \overline{\Delta}_{Dd}|}{\overline{\Delta}_{Dn}}, \quad (12)$$

where $\Delta_D = \max(D(q)) - \min(D(q))$ is the mean value of the singularity spectrum, $\overline{\Delta}_{Dn}$ being the mean value corresponding to the average value obtained for all normal foetuses and $\overline{\Delta}_{Dd}$ the mean value corresponding to the average value obtained for all distressed foetuses.

4. Results and Discussion

From our own dataset composed of one hundred recordings, each time series of 7200 points was coarse-grained for 6 different scales. From each coarse-grained signal, subsignals composed of 720 points and overlapping by 97% were analysed with multifractal tools.

Figure 7 shows a boxplot representation of the mean Hurst exponent for different scale values ranging from 1 to 6. Red boxplots correspond to distressed foetuses and blue boxplots correspond to normal foetuses. Figure 7 shows that the mean Hurst exponent for normal foetuses was higher than that obtained for distressed foetuses. This meant that the signatures of distressed foetuses were more irregular and complex than those obtained for normal foetuses. Furthermore, Figure 7 shows that there was sufficient deviation between the

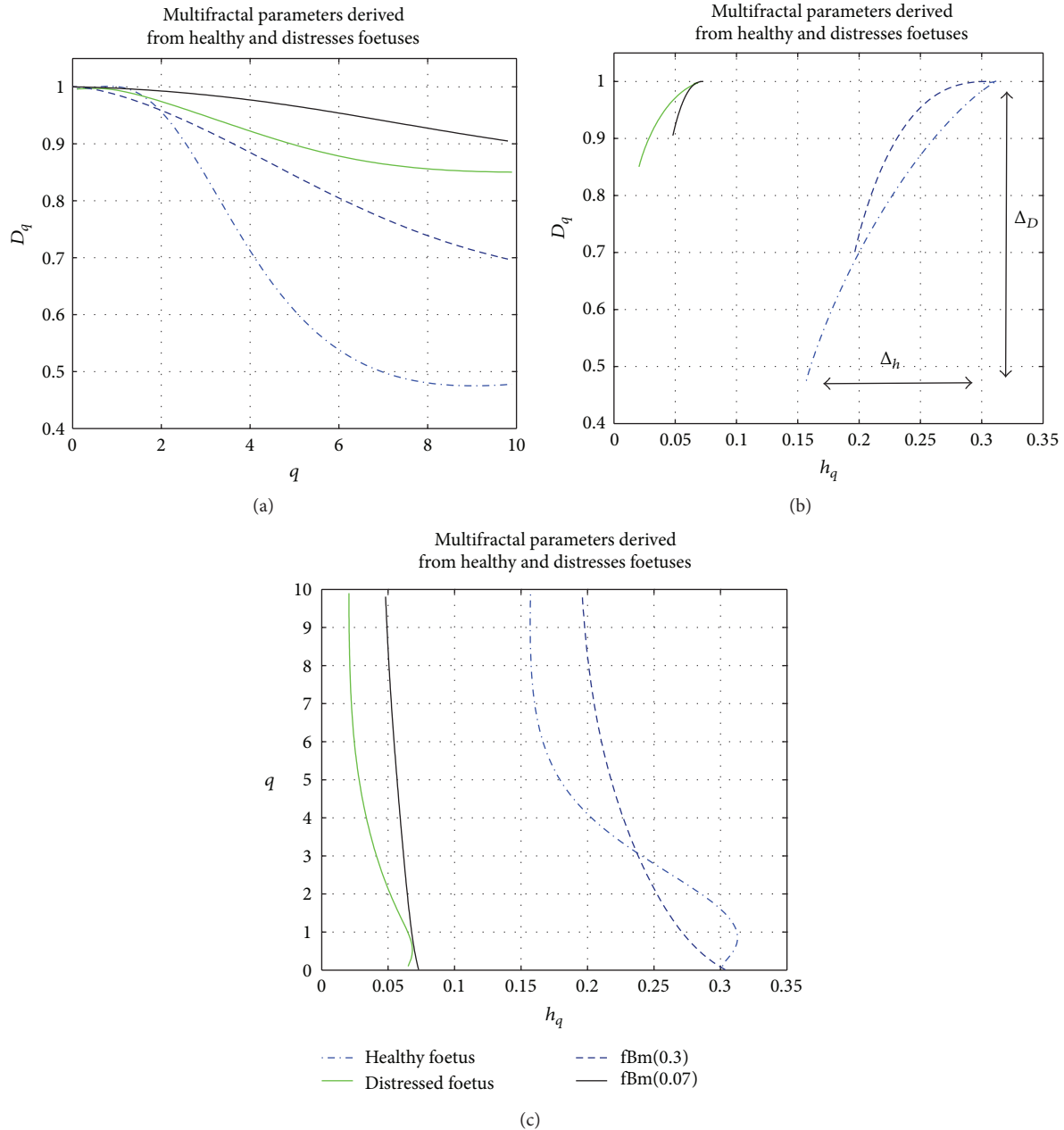


FIGURE 5: Multifractal parameters for a normal foetus (in blue) and a distressed foetus (in green). (a) Singularity spectrum D versus q . (b) Singularity spectrum $D(q)$ versus Holder spectrum $h(q)$. (c) Holder spectrum h versus q .

mean Hurst exponent to discriminate between normal and distressed foetuses. Figure 7 also shows that the higher the scale, the more regular or filtered the signal (as shown in Figure 1). This corroborated the results of [26], showing that the more filtered the time series the higher the Hurst exponent.

Figure 8 shows a boxplot representation of $\Delta_h = \max(h) - \min(h)$. These dynamics are represented for different scale values from 1 to 6. Red boxplots correspond to distressed foetuses and blue boxplots to normal foetuses. Figure 8 shows that the dynamics were higher for normal foetuses than that obtained for distressed foetuses. This meant that the

signatures for normal foetuses were more multifractal than those obtained for distressed foetuses. This has already been reported in recent studies such as [12]. Furthermore, Figure 8 shows that there was sufficient deviation between the dynamics to distinguish normal from distressed foetuses.

Figure 9 shows a boxplot representation of the mean singularity spectrum $\bar{D} = D_{\text{mean}}$. This parameter was represented for different scale values ranging from 1 to 6. Red boxplots correspond to distressed foetuses and blue boxplots to normal foetuses. Figure 9 shows that \bar{D} was higher for distressed foetuses than for normal foetuses. This meant that the signatures of healthy foetuses were more regular than those

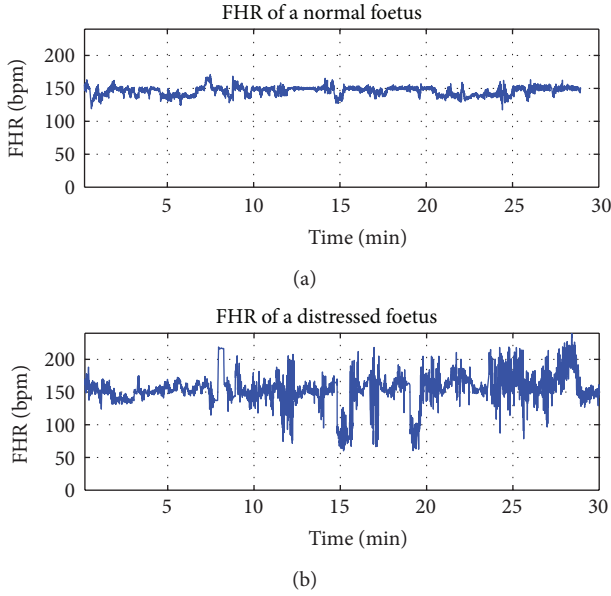


FIGURE 6: FHR of a normal foetus and a distressed foetus.

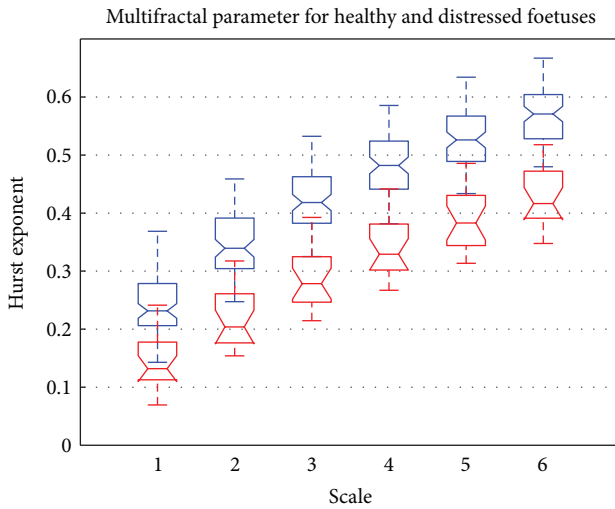


FIGURE 7: Boxplot of Hurst exponents versus scale. Normal foetus (in blue) and distressed foetus (in red).

corresponding to distressed foetuses. Figure 9 also shows that it was more difficult to discriminate between normal and distressed foetuses. This parameter did not seem to be very relevant. Note also that the higher the scale, the lower the relative error.

Figure 10 shows a boxplot representation of Δ_D , that is, the dynamics of D . This dynamics is represented for different scale values from 1 to 6. Red boxplots correspond to distressed foetuses and blue boxplots to normal foetuses. Figure 10 shows that Δ_D was higher for normal foetuses than for distressed foetuses. This meant that the signatures of healthy foetuses were more multifractal than those for distressed foetuses. Figure 10 also shows that there was sufficient deviation between the dynamics to distinguish normal from distressed

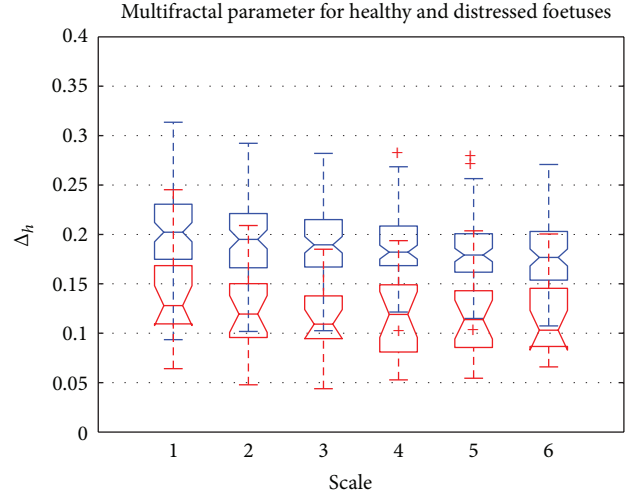


FIGURE 8: Boxplot of $\Delta_h = \max(h) - \min(h)$ versus scale. Normal foetus (in blue) and distressed foetus (in red).

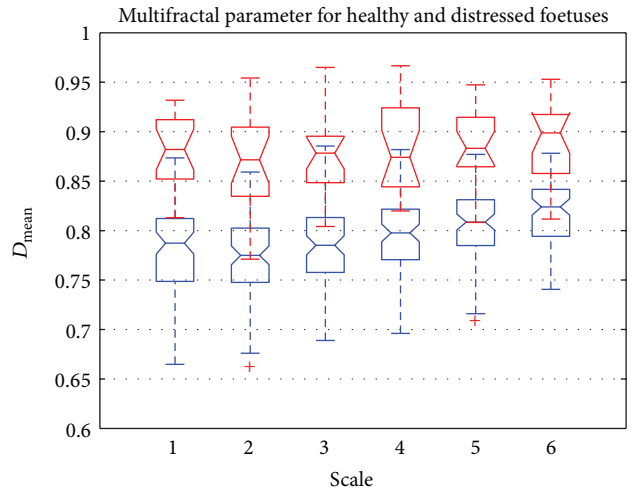


FIGURE 9: Boxplot of D_{mean} versus scale. Normal foetus (in blue) and distressed foetus (in red).

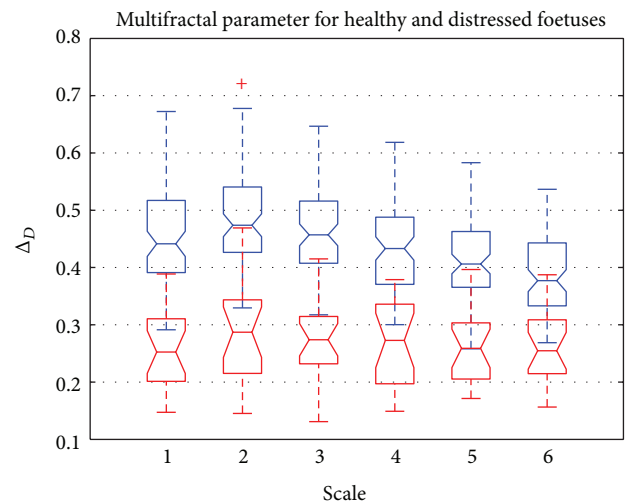


FIGURE 10: Boxplot of Δ_D versus scale. Normal foetus (in blue) and distressed foetus (in red).

TABLE 1: Relative errors of different multifractal parameters between the two groups of fetuses for different scales.

Scale	1	2	3	4	5	6
RE ₁	0.37	0.40	0.33	0.29	0.26	0.24
RE ₂	0.32	0.37	0.38	0.37	0.36	0.35
RE ₃	0.11	0.12	0.11	0.10	0.09	0.08
RE ₄	0.41	0.42	0.41	0.38	0.36	0.33

foetuses. Note also that the higher the scale, the lower the relative error.

To conclude, Table 1 summarizes the relative errors of the four previous parameters. The findings derived from Table 1 showed that the best parameter permitting discrimination between fetuses was RE₄, followed by RE₁ and RE₂. Indeed the best differentiation was obtained for a scale value of 2 for RE₄ and RE₁ and a scale value of 3 for RE₂. This confirms the need to coarse-grain the FHR time series. It is obvious from Table 1 that the higher the scale, the lower the relative error. This requires choosing a maximum scale that is not too high: a value set at 2 seems sufficient whatever the relative error. Furthermore, as the best parameter RE₄ was sensitive to the multifractal features of the time series analyzed for a scale of 2, this finding confirms the need to analyze FHR from a coarse-grained multifractal point of view. However, note also that as the second discriminative parameter was RE₁, sensitive to monofractal features set at a scale of 2, then a coarse-grained monofractal approach is also relevant.

Finally, although the present study was quite similar to that presented in [15], our study was different in several ways. First, our study was dedicated to fetuses, whereas [15] was dedicated to adults. Second, our study was based on a much simpler structure function than the other approach that was based on a partition function.

Furthermore, although a large number of research studies have mainly been based on the use of partition functions (DFA, box-counting and wavelet approaches) on the pretext that structure functions do not operate for negative orders, we have shown here (i) that the use of such structure functions is fully justified due to the simplicity of implementation and (ii) that structure functions completely fulfil their role in distinguishing between healthy and distressed fetuses.

Note that, as our proposed methodology was that of investigating offline, we plan to evaluate multifractal descriptors one line in the near future.

Acknowledgments

This study was supported by the “Agence Nationale de la Recherche” (Project ANR-07-TECSAN-023, Surfoetus). Furthermore, the authors would like to thank the Clinical Investigation Centre for Innovative Technology of Tours (CIC-IT 806 CHRU of Tours) and Professor F. Perrotin’s team in the Obstetric Department for their support in recording the signals.

References

- [1] D. Brodsky and H. Christou, “Current concepts in intrauterine growth restriction,” *Journal of Intensive Care Medicine*, vol. 19, no. 6, pp. 307–319, 2004.
- [2] M. Kobayashi and T. Musha, “1/f fluctuation of heartbeat period,” *IEEE Transactions on Biomedical Engineering*, vol. 29, no. 6, pp. 456–457, 1982.
- [3] M. Ferrario, M. Signorini, G. Magenes, and S. Cerutti, “Comparison of entropy-based regularity estimators: application to the fetal heart rate signal for the identification of fetal distress,” *IEEE Transactions on Biomedical Engineering*, vol. 53, no. 1, pp. 119–125, 2006.
- [4] M. Ferrario, M. Signorini, and G. Magenes, “Complexity analysis of the fetal heart rate variability: early identification of severe intrauterine growth-restricted fetuses,” *Medical and Biological Engineering and Computing*, vol. 47, no. 9, pp. 911–919, 2009.
- [5] S. M. Pincus and R. R. Viscallero, “Approximate entropy: a regularity measure for fetal heart rate analysis,” *Obstetrics and Gynecology*, vol. 79, pp. 249–255, 1992.
- [6] H. Goncalves, J. Bernades, A. P. Rocha, and D. A. de Campos, “Linear and nonlinear analysis of heart rate patterns associated with fetal behavioral states in the antepartum period,” *Early Human Development*, vol. 83, no. 9, pp. 585–591, 2007.
- [7] D. G. Chaffin, C. C. Goldberg, and K. L. Reed, “The dimension of chaos in the fetal heart rate,” *American Journal of Obstetrics and Gynecology*, vol. 165, no. 5, pp. 1425–1429, 1991.
- [8] N. A. J. Gough, “Fractal analysis of fetal heart rate variability,” *Physiological Measurement*, vol. 14, no. 3, pp. 309–315, 1993.
- [9] C. S. Felgueiras, J. P. Marques de Sa, J. Bernardes, and S. Gama, “Classification of foetal heart rate sequences based on fractal features,” *Medical and Biological Engineering and Computing*, vol. 36, no. 2, pp. 197–201, 1998.
- [10] A. Kikuchi, N. Unno, T. Horikoshi, T. Shimizu, S. Kozuma, and Y. Taketani, “Changes in fractal features of fetal heart rate during pregnancy,” *Early Human Development*, vol. 81, no. 8, pp. 655–661, 2005.
- [11] P. C. Ivanov, M. G. Rosenblum, C.-K. Peng et al., “Scaling behaviour of heartbeat intervals obtained by wavelet-based time-series analysis,” *Nature*, vol. 383, no. 6598, pp. 323–327, 1996.
- [12] P. C. Ivanov, L. A. N. Amaral, A. L. Goldberger et al., “Multifractality in human heartbeat dynamics,” *Nature*, vol. 399, pp. 461–465, 1999.
- [13] P. C. Ivanov, L. A. N. Amaral, A. L. Goldberger et al., “From 1/f noise to multifractal cascades in heartbeat dynamics,” *Chaos*, vol. 11, no. 3, pp. 641–652, 2001.
- [14] J. Wang, X. Ning, and Y. Chen, “Modulation of heart disease information to the 12-lead ECG multifractal distribution,” *Physica A*, vol. 325, no. 3–4, pp. 485–491, 2003.
- [15] J. Wang, X. Ning, Q. Ma, C. Bian, Y. Xu, and Y. Chen, “Multiscale multifractality 260 analysis of a 12-lead electrocardiogram,” *Physical Review E*, vol. 71, no. 6, Article ID 062902, 4 pages, 2005.
- [16] R. Sassi, M. Signorini, and S. Cerutti, “Multifractality and heart rate variability,” *Chaos*, vol. 19, no. 2, Article ID 028507, 2009.
- [17] A. Humeau, B. Buard, G. Mahé, F. Chapeau-Blondeau, D. Rousseau, and P. Abraham, “Multifractal analysis of heart rate variability and laser Doppler flowmetry fluctuations: comparison of results from different numerical methods,” *Physics in Medicine and Biology*, vol. 55, no. 20, pp. 6279–6297, 2010.

- [18] Y. C. Zhang, "Complexity and $1/f$ noise: a phase space approach," *Journal de Physique Archives*, vol. 1, no. 7, pp. 971–977, 1991.
- [19] A. L. Barabasi and T. Vicsek, "Multifractality of self-affine fractals," *Physical Review A*, vol. 44, no. 4, pp. 2730–2733, 1991.
- [20] J. F. Muzy, E. Bacry, and A. Arneodo, "Multifractal formalism for fractal signals: the structure-function approach versus the wavelet-transform modulus-maxima method," *Physical Review E*, vol. 47, no. 2, pp. 875–884, 1993.
- [21] D. C. Lin and R. L. Hughson, "Modeling heart rate variability in healthy humans: a turbulence analogy," *Physical Review Letters*, vol. 86, no. 8, pp. 1650–1653, 2001.
- [22] E. S. C. Ching and Y.-K. Tsang, "Multifractality and scale invariance in human heartbeat dynamics," *Physical Review E*, vol. 76, no. 4, Article ID 041910, 2007.
- [23] G. Parisi and U. Frisch, "On the singularity structure of fully developed turbulence (in turbulence and predictability in geophysical fluid dynamics)," in *Proceedings of the International School of Physics Enrico Fermi*, M. Ghil, R. Benzi, and G. Paris, Eds., pp. 84–87, North-Holland .
- [24] I. Voicu, J. M. Girault, and S. Menigot, "Improved estimation of the fetal heart rate using directional Doppler signal and YIN," *IRBM*, vol. 33, no. 4, pp. 262–271, 2012.
- [25] I. Voicu, S. Menigot, D. Kouamé, and J. M. Girault, "New estimators and guidelines for better use of fetal heart 14 rate estimators with Doppler ultrasound devices," *Computational and Mathematical Methods in Medicine*, vol. 2013, Article ID 784862, 2013.
- [26] J.-M. Girault, D. Kouame, and A. Ouahabi, "Analytical formulation of the fractal dimension of filtered stochastic signals," *Signal Processing*, vol. 90, no. 9, pp. 2690–2697, 2010.
- [27] Y. Xu, Q. D. Y. Ma, D. T. Schmitt, P. Bernaola-Galvan, and P. C. Ivanov, "Effects of coarse-graining on the scaling behavior of long-range correlated and anti-correlated signals," *Physica A*, vol. 390, no. 23-24, pp. 4057–4072, 2011.
- [28] H. E. Stanley, L. A. N. Amaral, A. L. Goldberger, S. Havlin, P. C. Ivanov, and C.-K. Peng, "Statistical physics and physiology: monofractal and multifractal approaches," *Physica A*, vol. 270, no. 1, pp. 309–324, 1999.
- [29] L. A. N. Amaral, P. C. Ivanov, N. Aoyagi et al., "Behavioral-independent features of complex heartbeat dynamics," *Physical Review Letters*, vol. 86, no. 26, pp. 6026–6029, 2001.

Research Article

Probabilistic Source Separation for Robust Fetal Electrocardiography

Rik Vullings and Massimo Mischi

Department of Electrical Engineering, Eindhoven University of Technology, P.O. Box 513, 5600 MB Eindhoven, The Netherlands

Correspondence should be addressed to Rik Vullings; r.vullings@tue.nl

Received 18 June 2013; Accepted 11 November 2013

Academic Editor: Maria Gabriella Signorini

Copyright © 2013 R. Vullings and M. Mischi. This is an open access article distributed under the Creative Commons Attribution License, which permits unrestricted use, distribution, and reproduction in any medium, provided the original work is properly cited.

Blind source separation (BSS) techniques are widely used to extract signals of interest from a mixture with other signals, such as extracting fetal electrocardiogram (ECG) signals from noninvasive recordings on the maternal abdomen. These BSS techniques, however, typically lack possibilities to incorporate any prior knowledge on the mixing of the source signals. Particularly for fetal ECG signals, knowledge on the mixing is available based on the origin and propagation properties of these signals. In this paper, a novel source separation method is developed that combines the strengths and accuracy of BSS techniques with the robustness of an underlying physiological model of the fetal ECG. The method is developed within a probabilistic framework and yields an iterative convergence of the separation matrix towards a maximum a posteriori estimation, where in each iteration the latest estimate of the separation matrix is corrected towards a tradeoff between the BSS technique and the physiological model. The method is evaluated by comparing its performance with that of FastICA on both simulated and real multichannel fetal ECG recordings, demonstrating that the developed method outperforms FastICA in extracting the fetal ECG source signals.

1. Introduction

Current fetal monitoring mainly relies on the cardiotocogram (CTG); the simultaneous registration of fetal heart rate; and uterine activity. Unfortunately, in many cases the information provided by the CTG is insufficient. In these cases, obstetricians have to rely on other sources of information or on their intuition and experience to make the optimal treatment plan. A valuable complementary source of information is provided by the fetal electrocardiogram (ECG) [1]. In clinical practice, the fetal ECG is measured during labor using an invasive electrode. The use of this electrode requires the fetal membranes to be ruptured and the cervix to be sufficiently dilated. An alternative method to obtain the fetal ECG makes use of electrodes placed on the abdomen of the mother [2].

Although these abdominal recordings are a promising candidate for use in fetal monitoring, their widespread use is impeded by the quality of the fetal ECG signals which is typically poor. Specifically, each signal recorded from the maternal abdomen consists of a mixture of signals, including the fetal ECG, maternal ECG, activity of abdominal muscles and uterus, and interferences from external sources. Several

methods to extract the fetal ECG from such mixtures have been proposed in the literature [2–5]. Prominent among these methods are the so-called source separation methods such as independent component analysis (ICA) [2, 6]. Despite the successful application of these source separation methods for fetal ECG extraction, their use in clinical practice is limited to virtually none. The key reason for this is the relatively poor robustness in case of significant artifacts and noise [7]. In other words, in case the noninvasive fetal ECG recordings have relatively good quality, the source separation methods perform satisfactory and in case of poor signal quality, their performance breaks down.

One of the reasons for poor robustness with respect to signal quality lies in the fact that ICA assumes no *a priori* knowledge on the origin of the recorded signal mixtures. Hence, ICA-based methods are referred to as blind source separation (BSS) techniques. In case of noninvasive fetal ECG recordings, however, some knowledge on the source signals mixing is available. Exploitation of such knowledge can improve the robustness of the source separation, as demonstrated for audio signals by Knuth [8].

In this paper, we follow the approach by Knuth and develop a probabilistic framework to derive a generic source separation technique. This technique allows for inclusion of a priori knowledge on the mixing of the source signals. In case no *a priori* knowledge is included, this technique reduces to an ICA technique. To include prior knowledge in the source separation, we present a physiology-based probabilistic model that describes how fetal ECG signals mix to the noninvasive abdominal recordings. Our method, consequently, yields a probabilistic, physiology-based source separation technique for fetal ECG extraction.

In Section 2, our method is presented and the methodology for implementation and evaluation is discussed. In Section 3, the performance of our method is illustrated and evaluated by comparing it with the performance of a widely used ICA approach. In Section 4, we draw our conclusions.

2. Materials and Methods

2.1. Probabilistic Description of Source Separation Problem. When we assume a fetal ECG recording of N signals $\mathbf{x}(t)$, each comprising an unknown mixture of M source signals $\mathbf{s}(t)$, the goal of any source separation method is to unmix the recorded signals into the source signals:

$$\mathbf{x}(t) = \mathbf{A}(t) \mathbf{s}(t), \quad (1)$$

where $\mathbf{A}(t)$ is a $[N \times M]$ matrix, referred to as the mixing matrix. In the case of fetal ECG recordings, the time-dependent behavior of \mathbf{A} originates from changes in the volume conductor between fetal heart and abdominal electrodes, for example, due to movement of either mother or fetus.

Using Bayes' rule, the probability that the source model of (1) is correct can be written as [9]

$$p(\mathbf{A}, \mathbf{s} | \mathbf{x}) = \frac{p(\mathbf{x} | \mathbf{A}, \mathbf{s}) p(\mathbf{A}, \mathbf{s})}{p(\mathbf{x})}, \quad (2)$$

where we have omitted the time-dependency for reasons of clarity.

The expression in the denominator of (2) is referred to as the *evidence* and can be regarded as a normalization term, independent of the variables of interest (i.e., \mathbf{A} or \mathbf{s}). Hence, (2) can be simplified to

$$p(\mathbf{A}, \mathbf{s} | \mathbf{x}) \propto p(\mathbf{x} | \mathbf{A}, \mathbf{s}) p(\mathbf{A}, \mathbf{s}). \quad (3)$$

The expression on the left-hand side of (3) is referred to as the *posterior*. The first term on the right-hand side of (3) is referred to as the *likelihood*. The second term is referred to as the *prior*.

As mentioned previously, the goal of the source separation method is to obtain the source signals \mathbf{s} . Considering the source model in (1) with \mathbf{x} known, inference of \mathbf{A} also determines \mathbf{s} . Since \mathbf{A} is typically a smaller matrix than \mathbf{s} , it is often computationally more efficient to estimate \mathbf{A} rather than \mathbf{s} . Hence, the problem of estimating the source signals \mathbf{s} can be translated to the problem of estimating the mixing matrix \mathbf{A} . In this context, the source signals \mathbf{s} can be regarded

as a nuisance parameter and omitted from the posterior by marginalization:

$$p(\mathbf{A} | \mathbf{x}) \propto p(\mathbf{A}) \int p(\mathbf{x} | \mathbf{A}, \mathbf{s}) p(\mathbf{s}) d\mathbf{s}. \quad (4)$$

Here, \mathbf{A} and \mathbf{s} are assumed to be statistically independent, based on the assumption that the properties of signal propagation (i.e., the mixing matrix \mathbf{A}) do not depend on the source signals and their magnitudes (i.e., the source matrix \mathbf{s}).

In the context of this probabilistic description, the challenge of source separation methods is to infer \mathbf{A} by maximizing the posterior probability distribution $p(\mathbf{A} | \mathbf{x})$ with respect to \mathbf{A} . Inference on \mathbf{A} , subsequently, provides an estimate for the source signals $\mathbf{s}(t)$.

2.2. Maximum A Posteriori Solution: Informed Source Separation. Until here, we have followed the descriptions of Knuth [8] and Bell and Sejnowski [10]. As Knuth shows in [8], prior knowledge—in terms of the probability distribution $p(\mathbf{A})$ —can be included in the probabilistic model of (4) to yield a *Maximum A Posteriori* (MAP) solution of the source separation problem. Because of the inclusion of prior knowledge, this method is referred to as an informed source separation (ISS) method (as opposed to the BSS methods that do not allow for inclusion of prior knowledge). For fetal ECG estimation, this prior knowledge entails a mathematical description of the dipole nature of the ECG and of the propagation properties of the abdominal volume conductor [11].

2.2.1. Mixing Model for Fetal ECG. When recorded relatively far away from the heart, the electrical activity of the heart can be approximated by an electrical dipole $\vec{\rho}(t)$ that changes in orientation and amplitude during the course of a cardiac cycle [12]. For a bipolar ECG recording between electrode i and a reference electrode \mathcal{R} , the electrical potential $V_i(t)$ recorded at the skin is accordingly given by

$$V_i(t) = \frac{1}{4\pi\epsilon} \left\{ \frac{\vec{r}_i - \vec{r}_f}{|\vec{r}_i - \vec{r}_f|^3} - \frac{\vec{r}_{\mathcal{R}} - \vec{r}_f}{|\vec{r}_{\mathcal{R}} - \vec{r}_f|^3} \right\} \cdot \vec{\rho}(t), \quad (5)$$

where ϵ describes the conductive properties of the medium between heart and electrode, which in this study are assumed to be the same for all recorded signals (i.e., the conductive properties are uniform), \vec{r}_i describes the position of electrode i , $\vec{r}_{\mathcal{R}}$ describes the position of the reference electrode, and \vec{r}_f describes the position of the fetal heart.

The electrical dipole $\vec{\rho}(t)$ is also known as the vectorcardiogram (VCG) and represents 3 orthogonal ECG sources that, when combined together, can describe any recorded ECG signal. In the context of source separation, $\vec{\rho}$ acts as the source matrix \mathbf{s} in (1). Since the electrical potentials from the skin surface \mathbf{V} correspond to \mathbf{x} , the mixing matrix for fetal ECG can be described as

$$A_{ij} = \frac{1}{c} \left\{ \frac{r_{ij} - r_{fj}}{|\vec{r}_i - \vec{r}_f|^3} - \frac{r_{\mathcal{R}j} - r_{fj}}{|\vec{r}_{\mathcal{R}} - \vec{r}_f|^3} \right\}, \quad (6)$$

where $c = 4\pi\epsilon$.

We can rewrite (6) to

$$A_{ij} = \frac{r_{ij} - r_{\mathcal{R}j}}{c|\vec{r}_i - \vec{r}_f|^3} - \frac{r_{\mathcal{R}j} - r_{fj}}{c} \left\{ \frac{|\vec{r}_i - \vec{r}_f|^3 - |\vec{r}_{\mathcal{R}} - \vec{r}_f|^3}{|\vec{r}_i - \vec{r}_f|^3 |\vec{r}_{\mathcal{R}} - \vec{r}_f|^3} \right\}. \quad (7)$$

In this expression, the first term on the right-hand side involves a (scaled) version of the difference in position between the abdominal electrodes i and \mathcal{R} . When we would assume that the distance between the fetal heart and the various electrodes is approximately the same, or at least that the difference between these heart-electrode distances is much smaller than the heart-electrode distance itself, the term between braces on the right-hand side of (7) tends to zero and, accordingly, we can simplify (7) to

$$A_{ij} = \frac{r_{ij} - r_{\mathcal{R}j}}{c|\vec{r}_i - \vec{r}_f|^3} + \eta_{ij}. \quad (8)$$

Here, η_{ij} is a noise term that expresses our model inaccuracies, such as the assumption to ignore the second term on the right-hand side of (7). Based on the central limit theorem, η_{ij} is taken to be a Gaussian noise term, with variance σ_{ij}^2 and mean μ_{ij} . Based on our geometric assumptions leading to (8), we assume μ_{ij} to be zero.

Finally, to facilitate an analytical solution to the source separation problem, we ignore the dependence of the scaling $\alpha_i = 1/c|\vec{r}_i - \vec{r}_f|^3$ on \vec{r}_i :

$$A_{ij} = \alpha_i (r_{ij} - r_{\mathcal{R}j}) + \eta_{ij}. \quad (9)$$

2.2.2. Prior Probability Distribution. We can express our belief in the mixing model of (9) in terms of the prior probability distribution:

$$p(\mathbf{A} | \sigma) = \int p(\mathbf{A}, \vec{\alpha} | \sigma) p(\vec{\alpha} | \sigma) d\vec{\alpha}. \quad (10)$$

Here, we have assumed the variance σ_{ij}^2 to be known. We will address the estimation of σ_{ij}^2 in Section 2.3.2.

When, for reasons of mathematical simplification, we assume the elements of the mixing matrix to be mutually independent, we can write $p(\mathbf{A}, \vec{\alpha} | \sigma)$ as

$$p(\mathbf{A}, \vec{\alpha} | \sigma) \approx \prod_{ij} p(A_{ij}, \alpha_i | \sigma_{ij}), \quad (11)$$

with, compare (9),

$$\begin{aligned} p(A_{ij}, \alpha_i | \sigma_{ij}) \\ = \frac{1}{\sqrt{2\pi\sigma_{ij}^2}} \exp \left\{ -\frac{1}{2\sigma_{ij}^2} [A_{ij} - \alpha_i (r_{ij} - r_{\mathcal{R}j})]^2 \right\}. \end{aligned} \quad (12)$$

This assumption of mutual independence of the elements of \mathbf{A} is weak and can potentially reduce the performance of the source separation. More specifically, information on the

mixing of ECG signals for one electrode provides information on the mixing for another electrode, since the electrode positions are known.

For the other conditional probability distribution in (10), we know that $\vec{\alpha}$ represents the scaling of ECG signals per electrode. This scaling depends on tissue propagation properties and the distance between fetal heart and electrode. The scaling must be positive and an upper and lower limit a_1 and a_2 , respectively, can be defined based on the possible distances between heart and electrodes as well as on studies on tissue propagation properties [13]. Taking the probability distribution for $\vec{\alpha}$ to be uniformly distributed between these limits and, analogously to considerations above, assuming the elements of $\vec{\alpha}$ to be mutually independent, $p(\alpha_i | \sigma_{ij})$ can be written as

$$p(\alpha_i | \sigma_{ij}) = \begin{cases} \frac{1}{a_2 - a_1} & \text{for } a_1 \leq \alpha_i \leq a_2 \\ 0 & \text{otherwise.} \end{cases} \quad (13)$$

Combining (10)–(13) and solving the integral in (10) give

$$\begin{aligned} p(\mathbf{A} | \sigma) &= \prod_{ij} \int_{a_1}^{a_2} \frac{1}{\sqrt{2\pi\sigma_{ij}^2} (a_2 - a_1)} \\ &\quad \times \exp \left\{ -\frac{1}{2\sigma_{ij}^2} [A_{ij} - \alpha_i (r_{ij} - r_{\mathcal{R}j})]^2 \right\} d\alpha_i \\ &= \prod_{ij} \frac{\text{erf} [f_{ij}(a_1)] - \text{erf} [f_{ij}(a_2)]}{2(a_2 - a_1)(r_{ij} - r_{\mathcal{R}j})}, \end{aligned} \quad (14)$$

where

$$\begin{aligned} \text{erf}(z) &= \frac{2}{\sqrt{\pi}} \int_0^z \exp(-t^2) dt, \\ f_{ij}(a_k) &= \frac{A_{ij} - a_k (r_{ij} - r_{\mathcal{R}j})}{\sqrt{2}\sigma_{ij}}. \end{aligned} \quad (15)$$

2.2.3. Dealing with Multiple Sources. As mentioned in Section 1, noninvasive fetal ECG recordings consist of a mixture of source signals of which the three orthogonal fetal ECG components \mathbf{S} comprise only three source signals. We can estimate the other sources using a standard implementation of ICA. Specifically, we can assume no prior knowledge for these sources and include this lack of knowledge in our probability distribution for \mathbf{A} :

$$p(A_{ij} | \sigma_{ij}) = \begin{cases} \frac{\text{erf} [f_{ij}(a_1)] - \text{erf} [f_{ij}(a_2)]}{2(a_2 - a_1)(r_{ij} - r_{\mathcal{R}j})} & \text{for } i \leq 3 \\ \text{constant} & \text{else.} \end{cases} \quad (16)$$

2.2.4. Towards a Solution. When we consider the posterior probability distribution of (4), we should realize that inference on the mixing matrix \mathbf{A} entails maximization of the

posterior probability with respect to \mathbf{A} . Moreover, due to the fact that the logarithm is a monotonically increasing function, maximization of $p(\mathbf{A} | \mathbf{x})$ yields the same optimal value for \mathbf{A} as would maximization of $\log p(\mathbf{A} | \mathbf{x})$.

As a first step to solve the inference problem, we follow Bell and Sejnowski [10] and assume the source signals \mathbf{s} to be mutually independent. Furthermore, we express our belief in (1) by assigning a delta function to the likelihood $p(\mathbf{x} | \mathbf{A}, \mathbf{s})$. Combining these assumptions with the posterior probability in (4) gives

$$p(\mathbf{A} | \mathbf{x}) \propto p(\mathbf{A}) \int \prod_i^N \delta \left(x_i - \sum_k^M A_{ik} s_k \right) \prod_j^M p_j(s_j) ds, \quad (17)$$

which can be solved to

$$p(\mathbf{A} | \mathbf{x}) \propto \frac{p(\mathbf{A})}{\det \mathbf{A}} \prod_m^M p_m \left(\sum_k W_{mk} x_k \right), \quad (18)$$

with \mathbf{W} being the inverse of \mathbf{A} , referred to as the unmixing matrix.

Taking logarithms on either side gives

$$\begin{aligned} \log p(\mathbf{A} | \mathbf{x}) &= \log p(\mathbf{A}) + \log \det \mathbf{W} \\ &+ \sum_m^M \log p_m \left(\sum_k W_{mk} x_k \right) + C. \end{aligned} \quad (19)$$

Here, C is a constant, independent of \mathbf{A} .

For clarity, we introduce the estimated sources $\hat{\mathbf{s}}$ as $\hat{\mathbf{s}} = \mathbf{W}\mathbf{x}$. Furthermore, instead of maximizing the posterior probability distribution with respect to \mathbf{A} , we maximize it with respect to the separation matrix \mathbf{W} [8]. Accordingly,

$$\begin{aligned} \frac{\partial}{\partial W_{ij}} \log p(\mathbf{A} | \mathbf{x}) &= \frac{\partial}{\partial W_{ij}} \log p(\mathbf{A}) \\ &+ A_{ji} + x_j \left(\frac{(\partial/\partial \hat{s}_i) p_i(\hat{s}_i)}{p_i(\hat{s}_i)} \right), \end{aligned} \quad (20)$$

or in terms of the derivative with respect to the matrix \mathbf{W} :

$$\frac{\partial}{\partial \mathbf{W}} \log p(\mathbf{A} | \mathbf{x}) = -\mathbf{A}^T \mathbf{M} \mathbf{A}^T + \mathbf{A}^T + \left(\frac{(\partial/\partial \hat{s}_i) p_i(\hat{s}_i)}{p_i(\hat{s}_i)} \right) \mathbf{x}^T, \quad (21)$$

where

$$\begin{aligned} M_{ij} &= \frac{\partial}{\partial W_{ij}} \log p(\mathbf{A}) \\ &= \begin{cases} \sqrt{\frac{2}{\pi \sigma_{ij}^2}} \frac{\exp[f_{ij}^2(a_1)] - \exp[f_{ij}^2(a_2)]}{\operatorname{erf}[f_{ij}(a_1)] - \operatorname{erf}[f_{ij}(a_2)]} & \text{for } i \leq 3 \\ 0 & \text{else.} \end{cases} \end{aligned} \quad (22)$$

The optimal unmixing matrix \mathbf{W} can be inferred by implementing a gradient search algorithm. Moreover, by

postmultiplying (21) by $\mathbf{W}^T \mathbf{W}$, the expression can be made invariant to changes in the definition of the coordinate system that defines the various \vec{r} [14]:

$$\Delta \mathbf{W} = -\mathbf{A}^T \mathbf{M} \mathbf{W} + \mathbf{W} + \left(\frac{(\partial/\partial \hat{s}_i) p_i(\hat{s}_i)}{p_i(\hat{s}_i)} \right) \hat{\mathbf{s}}^T \mathbf{W}, \quad (23)$$

where $\Delta \mathbf{W}$ is the update term for the gradient search algorithm:

$$\mathbf{W}_{i+1} = \mathbf{W}_i + \lambda \Delta \mathbf{W}, \quad (24)$$

with λ as the learning rate.

2.3. Implementation Challenges

2.3.1. Numerical Accuracy of Error Function. When implementing the proposed source separation method, singularities can arise due to a finite numerical accuracy in estimating the error functions in the denominator of (22). Specifically, we implemented the source separation in MATLAB (The MathWorks Inc.), which can no longer distinguish between error functions when the arguments have exceeded the value of 6 (or are smaller than -6):

$$\operatorname{erf}(z_1) - \operatorname{erf}(z_2) = 0, \quad \text{if } z_1 \geq 6 \wedge z_2 \geq 6. \quad (25)$$

To avoid such singularities, we can approximate the error function by [15]

$$\operatorname{erf}(z) = \frac{z}{|z|} \left[1 - \frac{1}{\left(\sum_{i=0}^4 b_i |z|^i \right)^4} \right], \quad (26)$$

with $b_0 = 1$, $b_1 \approx 0.28$, $b_2 \approx 0.23$, $b_3 \approx 9.8 \cdot 10^{-4}$, and $b_4 \approx 7.8 \cdot 10^{-2}$.

Implementation of this approximation in MATLAB resolves the issue with finite numerical accuracy of the error function, no longer yielding zero difference when both z_1 and z_2 exceed 6 but are not identical.

2.3.2. Estimating Model Inaccuracies. In Section 2.2.2, we have assumed the variance σ to be known. When analyzing (23), the term $\mathbf{A}^T \mathbf{M} \mathbf{W}$ acts as a physiological component. The other terms together entail a typical BSS solution. In other words, $\mathbf{A}^T \mathbf{M} \mathbf{W}$ is a physiology-based correction to the source separation. According to (22), the degree of correction is controlled by σ . Large values for σ indicate little confidence in the prior, physiology-based model and cause the method to act more or less as a BSS approach. Large confidence in the prior model, represented by small values for σ , results in a larger contribution of the prior model to the source separation.

For fetal ECG recordings, inaccuracies in the prior model arise from noise in the ECG signals or from erroneous assumptions with respect to the uniform propagation properties of the volume conductor or with respect to the sphere-like shape of the pregnant abdomen with the fetal heart in the center. These model inaccuracies can be tested by using the prior model to estimate $\vec{p}(t)$ and, subsequently, inverting

the model to estimate the ECG signals from the estimated $\vec{\rho}(t)$:

$$\begin{aligned}\vec{\rho}(t) &= \mathbf{A}^\dagger \mathbf{V}(t), \\ \widehat{\mathbf{V}}(t) &= \mathbf{A} \vec{\rho}(t).\end{aligned}\quad (27)$$

Here, \mathbf{A}^\dagger indicates the pseudoinverse of \mathbf{A} , and \mathbf{A} is provided by the prior model of (9).

The difference signal $\epsilon(t)$ between the recorded and estimated ECG signals yields an indication for the model accuracy. Specifically, the variance of ϵ can be used as a measure for σ [16]:

$$\sigma_{ij}^2 = \text{var} [\mathbf{V}_i(t) - \widehat{\mathbf{V}}_i(t)]. \quad (28)$$

This expression implicitly assumes that σ_{ij} is independent of j (i.e., $\sigma_{ij} = \sigma_i$).

To account for changes in the circumstances during the fetal ECG recording, for example, when the mother is having uterine contractions, the variance is determined within a sliding window of 2 seconds.

2.4. Evaluation of Source Separation. The developed probabilistic source separation method is evaluated by assessing its performance in extracting fetal ECG source signals from noninvasive recordings. The performance is evaluated by comparing it with that of a widely used ICA method: FastICA [17]. The performance of the source separation techniques is assessed both quantitatively and qualitatively. Quantitative assessment is achieved using simulated recordings and qualitative assessment is done via actual abdominal recordings.

2.4.1. Data

Simulated Fetal ECG Recordings. For simulating fetal ECG recordings, we use three orthogonal ECG signals recorded from an adult. These ECG signals are linearly combined, via a randomly determined mixing matrix, into N ECG signals. To mimic the low quality of fetal ECG signals, these N ECG signals are corrupted by muscular interferences and noise, obtained via a N -channel recording of bipolar measurements on a subject's arm. These measurements contain muscle activity and noise but due to their bipolar nature and position contain virtually no ECG contribution. Finally, also artificial powerline interference is added. An example of a simulated fetal ECG recording is shown in Figure 1.

To evaluate the developed source separation method for various degrees of signal quality, the signal to noise ratio (SNR) is varied between -10 and $+30$ dB. For each SNR, the evaluation is repeated 20 times to suppress the influence of the randomly determined mixing matrix. That is, in each repetition the mixing matrix is determined by picking its coefficients from a Gaussian distribution with unit variance.

Real Noninvasive Fetal ECG Recordings. The noninvasive fetal ECG recordings are performed at the Máxima Medical Center, Veldhoven, The Netherlands, using a NEMO data acquisition system (NEMO Healthcare BV, The Netherlands), after having obtained written informed consent from the mother.

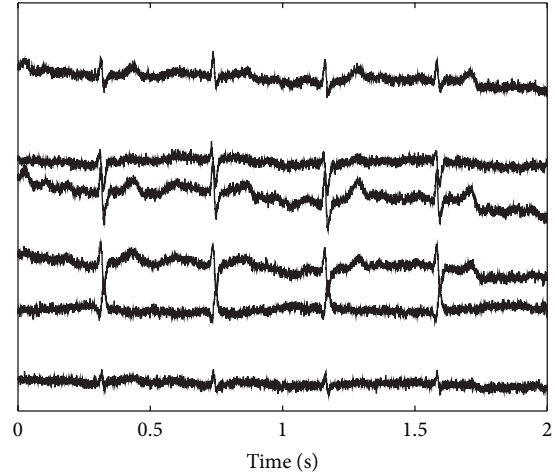


FIGURE 1: Example of a simulated 6-channel fetal ECG recording.

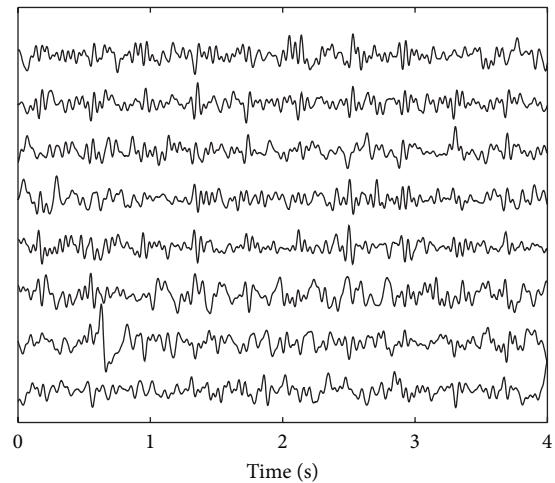


FIGURE 2: Example of real 8-channel fetal ECG recording. In this recording, the maternal ECG has already been removed using an adaptive template subtraction method [5] and high-frequency components of muscular activity have been suppressed by bandpass filtering between 1 and 70 Hz.

At the time of recording, the mother was 28 weeks pregnant. Eight abdominal signals are acquired simultaneously with a 1 kHz sampling rate and are preprocessed to suppress powerline interference, muscle activity, and maternal ECG according to [5]. An example of the abdominal recording after preprocessing is depicted in Figure 2. It should be noted here that the preprocessing, by far, does not yield a good-quality fetal ECG and, hence, the need for additional processing, for example, by source separation. It should be noted as well that many others have applied (blind) source separation techniques without prior removal of the maternal ECG [2, 6]. In that case, the source separation technique, besides fetal ECG, also attempts to estimate the maternal ECG. As a result, fewer sources remain to estimate other interferences as well (i.e., the number of sources that can be extracted is restricted to the number of recorded signals: $M \leq N$) yielding the fetal

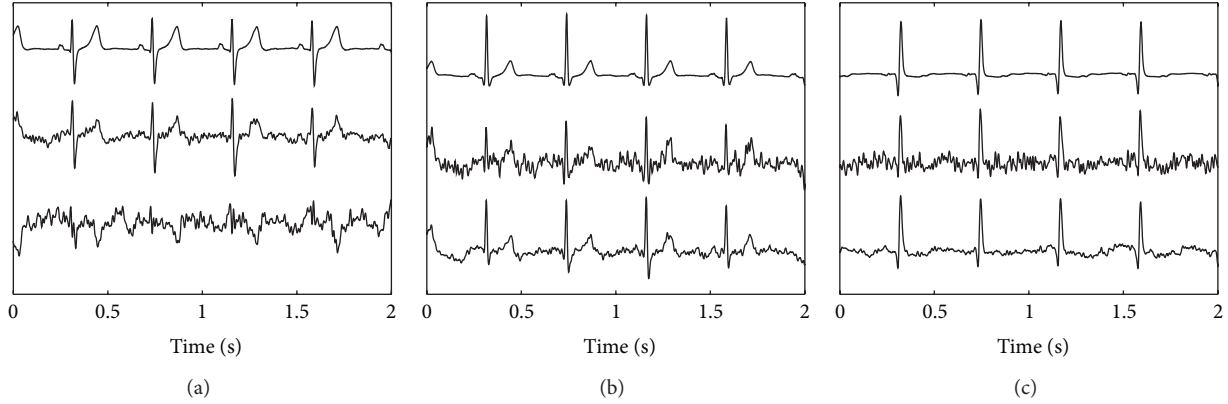


FIGURE 3: Results of source separation by the developed ISS method and FastICA for SNR of 6 dB. Each panel represents one of the three orthogonal ECG sources. In each panel, the top line represents the ECG source used in the simulation, the center line represents the corresponding source extracted by the ISS method, and the bottom line represents the corresponding source extracted by FastICA. The simulated fetal ECG recording used in the source extraction was depicted in Figure 1.

ECG sources to be more likely a mixture of fetal ECG and interferences.

2.4.2. Evaluation Criteria. In our simulations, the performance of the source separation methods is quantified in terms of the normalized mean squared error e between the original sources \mathbf{S} and the estimated sources $\tilde{\mathbf{S}}$:

$$e = \frac{\sum (\tilde{\mathbf{S}} - \mathbf{S})(\tilde{\mathbf{S}} - \mathbf{S})^T}{\sum \mathbf{S}\mathbf{S}^T}. \quad (29)$$

The performance in separating sources in actual fetal ECG recordings is determined by assessing the ability of a peak detection algorithm to determine the fetal heart rate. The employed peak detection algorithm is based on a continuous wavelet transform [18] and the source signal representing the fetal ECG is selected based on visual inspection. The ability to correctly detect fetal ECG peaks is quantified by the sensitivity (Se):

$$\text{Se} = \frac{\text{TP}}{\text{TP} + \text{FN}}, \quad (30)$$

and positive predictive value (PPV):

$$\text{PPV} = \frac{\text{TP}}{\text{TP} + \text{FP}}. \quad (31)$$

Here, TP (true positive) is the number of correctly detected peaks, FP (false positive) the number of detections that were incorrectly labeled as ECG peaks, and FN (false negative) the number of ECG peaks that were missed by the detection algorithm. As a gold standard for assessing whether peaks are detected correctly, visual annotation by a clinical expert, on fetal ECG recordings in which the maternal ECG has been suppressed, is used.

With fetal heart rate detected, further enhancement of the fetal ECG can be achieved by (adaptively) averaging various consecutive ECG complexes, for example, as described in [16].

3. Results and Discussion

3.1. Results on Simulated Data. In Figure 3, an example of the source extraction by both the developed ISS method and FastICA is shown. The sources are extracted from the simulated fetal ECG recording that was depicted in Figure 1 and that has a SNR of 6 dB. As mentioned earlier, three orthogonal ECG sources were used to simulate the $N = 6$ channels of the fetal ECG recording. For each of the orthogonal ECG sources, the extracted source that matches the ECG best, in terms of least squared error, is used for the evaluation.

In Figure 4, the performance of both source separation methods as a function of the SNR of the simulated fetal ECG recordings is depicted. This figure shows that the developed ISS method outperforms FastICA for all SNR.

3.2. Results on Real Data. In Figure 5, the performance of the source separation methods for real fetal ECG recordings is depicted. The upper plot shows one of the recorded fetal ECG signals and the center plot shows the best fetal ECG source determined by ISS. The lower plot shows the best fetal ECG source by FastICA. The best ECG source is hereby defined as the source that yields the highest Se and PPV for ECG peak detection. It has to be noted here that the annotation of the recorded fetal ECG signal was based on visual analysis of all recorded channels at the same time. ECG peaks that are not distinctively discernible in the depicted ECG signal might have been annotated based on a different channel.

In total, 1532 ECG peaks have been annotated by the clinical expert in the 10-minute long abdominal recording. The performance of the employed peak detection algorithm in finding all these peaks in the ISS estimated fetal ECG source signal is $\text{Se} = 0.88$ and $\text{PPV} = 0.84$. In the FastICA estimated source signal, the performance of the peak detection is $\text{Se} = 0.72$ and $\text{PPV} = 0.78$.

3.3. Discussion. As mentioned in Section 2.3.2, when considering the update rule for the developed ISS method in (23), it shows that the last two terms on the right-hand

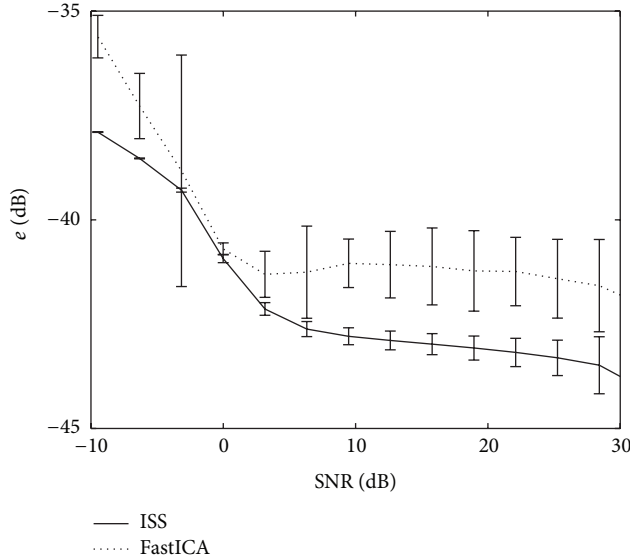


FIGURE 4: Performance of both source separation methods as a function of the SNR of the simulated recordings. Each depicted data point is the mean over 20 simulations with random mixing matrix. The standard deviations over these 20 simulations, although often too small to see in the graph, are also plotted.

side correspond to the ICA method developed by Bell and Sejnowski [10]. The first term on the right-hand side is a correction to the ICA solution and is based on *a priori* knowledge of the electrophysiology of the ECG. Any solution to the source separation problem by ISS, hence, entails a tradeoff between the ICA solution and the solution based on the physiological model of Section 2.2.1. The ratio in which each of these solutions contributes to the ISS solution strongly depends on estimated model inaccuracies: σ , compare (22).

The abovementioned tradeoff between ICA and physiology can also be regarded as a tradeoff between accuracy and robustness. We have illustrated this by applying our method to high-quality, yet realistic, (simulated) fetal ECG recordings and to lower-quality, but commonly more frequently encountered, (real) fetal ECG recordings. The statement of lower quality for the real recordings is based on visual comparison of Figures 1 and 2. The simulated recordings show that the gained robustness (ISS can locate all three fetal ECG sources, while FastICA could only estimate the two sources in Figures 3(b) and 3(c)) comes at the expense of a loss in accuracy; the three sources by ISS contain more noise than the two sources by FastICA. With regard to accuracy, as shown in Figure 4, the lack of accuracy—in terms of more noise in the estimated sources—by the ISS method is limited and is outweighed by the increase in robustness, as evidenced by the better performance of ISS for all SNR. With regard to robustness, as shown in Figure 5, for lower-quality fetal ECG recordings, the lack of robustness in BSS methods causes FastICA to fail in estimating a proper fetal ECG source, while the more robust ISS method can still estimate a fetal ECG source. In terms of detecting the fetal heart rate in the estimated sources, ISS outperforms FastICA by a sensitivity increase of 0.16 and an increase in the positive predictive

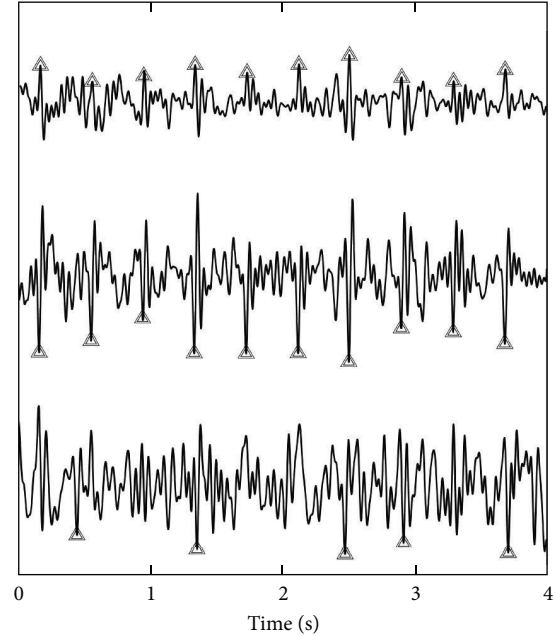


FIGURE 5: The upper plot shows a recorded and annotated fetal ECG signal. This depicted signal was preprocessed as described in Section 2.4.1 and was visually selected out of the $N = 8$ recorded signals as the one with the best fetal ECG. The center plot shows the fetal ECG source signals estimated with the developed ISS method. The lower plot shows the fetal ECG source signal estimated with FastICA. The triangles indicate detected fetal QRS complexes.

value of 0.06. As already indicated, when comparing the sources extracted from the simulated data in Figure 3, it shows that—although ISS can better reproduce the original sources in terms of ECG shape—the ISS sources contain more noise than the FastICA sources. The main reason for this is that FastICA is not capable of estimating, in particular, the first ECG source (Figure 3(a)). As a result, for the 6-channel recording, FastICA has 4 sources remaining that represent noise. The ISS method estimates all three ECG sources and hence has only 3 sources remaining to represent the noise. By increasing the number of recorded signals N and therefore the number of possible sources M that can be estimated, the accuracy of the source separation can be improved. In addition, when the goal of the source separation method is to compute fetal heart rates, the morphology of the extracted sources is more important than the noise in these sources. For example, Figure 3(a) shows that the ISS method can better preserve this morphology than FastICA.

In this paper, the developed ISS method was applied to extract fetal ECG sources from preprocessed abdominal recordings. This preprocessing includes suppression of the maternal ECG and in this paper we used a template-based method to do this. As an alternative approach, others have used BSS techniques to extract fetal ECG sources directly from (unprocessed) abdominal recordings [2, 19]. The developed ISS method can also be applied directly on the unprocessed recordings, but for this approach to perform up to its potential a proper prior model of the maternal ECG has to be

included next to the model for the fetal ECG. This extension of our ISS method is subject for further studies.

4. Conclusions

In this paper, a source separation technique for fetal ECG signals was developed that exploits prior knowledge on the signal mixing. When critically examining the presented solution to the source separation problem, it shows that the developed technique is similar to the Bell and Sejnowski [10] ICA approach, but with a correction that pushes the separation matrix towards a physiological model of the fetal ECG. The confidence in this physiological model determines the degree of correction. Little confidence causes the method to act as BSS technique with little to no pushing towards the physiological model. More confidence, on the other hand, leads to a technique that is more governed by the physiological model.

With respect to FastICA, the developed method performs better in retrieving the ECG sources in simulated and real fetal ECG recordings. More extensive evaluation of the developed method is however required to conclusively state about its performance, for example, in case of poorly determined electrode positions.

Acknowledgment

This work was supported by the Dutch Technology Foundation STW.

References

- [1] I. Amer-Wählin, C. Hellsten, H. Norén et al., "Cardiotocography only versus cardiotocography plus ST analysis of fetal electrocardiogram for intrapartum fetal monitoring: a Swedish randomised controlled trial," *The Lancet*, vol. 358, no. 9281, pp. 534–538, 2001.
- [2] L. De Lathauwer, B. De Moor, and J. Vandewalle, "Fetal electrocardiogram extraction by blind source subspace separation," *IEEE Transactions on Biomedical Engineering*, vol. 47, no. 5, pp. 567–572, 2000.
- [3] P. P. Kanjilal, S. Palit, and G. Saha, "Fetal ECG extraction from single-channel maternal ECG using singular value decomposition," *IEEE Transactions on Biomedical Engineering*, vol. 44, no. 1, pp. 51–59, 1997.
- [4] M. Ungureanu and W. M. Wolf, "Basic aspects concerning the event-synchronous interference canceller," *IEEE Transactions on Biomedical Engineering*, vol. 53, no. 11, pp. 2240–2247, 2006.
- [5] R. Vullings, C. H. L. Peters, R. J. Sluijter, M. Mischi, S. G. Oei, and J. W. M. Bergmans, "Dynamic segmentation and linear prediction for maternal ECG removal in antenatal abdominal recordings," *Physiological Measurement*, vol. 30, no. 3, pp. 291–307, 2009.
- [6] V. Zarzoso, J. Millet-Roig, and A. Nandi, "fetal ecg extraction from maternal skin electrodes using blind source separation and adaptive noise cancellation techniques," in *Computers in Cardiology*, pp. 431–434, 2000.
- [7] S. Harmeling, F. Meinecke, and K.-R. Müller, "Analysing ICA components by injecting noise," in *Proceedings of the 4th International Symposium on Independent Component Analysis and Blind Signal Separation*, pp. 149–154, Nara, Japan, 2003.
- [8] K. H. Knuth, "Bayesian source separation and localization," in *Bayesian Inference for Inverse Problems*, Proceedings of SPIE, pp. 147–158, July 1998.
- [9] E. Jaynes, *Probability Theory: The Logic of Science*, Cambridge University Press, Cambridge, UK, 2003.
- [10] A. J. Bell and T. J. Sejnowski, "An information-maximization approach to blind separation and blind deconvolution," *Neural Computation*, vol. 7, no. 6, pp. 1129–1159, 1995.
- [11] D. B. Geselowitz, "On the theory of the electrocardiogram," *Proceedings of the IEEE*, vol. 77, no. 6, pp. 857–876, 1989.
- [12] E. Frank, "General theory of heat-vector projection," *Circulation Research*, vol. 2, no. 3, pp. 258–270, 1954.
- [13] T. F. Oostendorp, A. Van Oosterom, and H. W. Jongsma, "Electrical properties of tissues involved in the conduction of foetal ECG," *Medical and Biological Engineering and Computing*, vol. 27, no. 3, pp. 322–324, 1989.
- [14] K. Knuth, "Difficulties applying recent blind source separation techniques to EEG and MEG," in *Maximum Entropy and Bayesian Methods*, G. Erickson, J. Rychert, and C. Smith, Eds., Kluwer Academic Publishers, Dordrecht, The Netherlands.
- [15] M. Abramowitz and I. Stegun, *Handbook of Mathematical Functions with Formulas, Graphs, and Mathematical Tables*, Dover, New York, NY, USA, 1972.
- [16] R. Vullings, B. De Vries, and J. W. M. Bergmans, "An adaptive Kalman filter for ECG signal enhancement," *IEEE Transactions on Biomedical Engineering*, vol. 58, no. 4, pp. 1094–1103, 2011.
- [17] A. Hyvärinen, "Fast and robust fixed-point algorithms for independent component analysis," *IEEE Transactions on Neural Networks*, vol. 10, no. 3, pp. 626–634, 1999.
- [18] M. Rooijackers, C. Rabotti, S. Oei, and M. Mischi, "Low-complexity R-peak detection for ambulatory fetal monitoring," *Physiological Measurement*, vol. 33, no. 7, pp. 1135–1150, 2012.
- [19] V. Zarzoso and A. K. Nandi, "Noninvasive fetal electrocardiogram extraction: blind separation versus adaptive noise cancellation," *IEEE Transactions on Biomedical Engineering*, vol. 48, no. 1, pp. 12–18, 2001.

Research Article

Assessment of Parturition with Cervical Light-Induced Fluorescence and Uterine Electromyography

Miha Lucovnik,¹ Ruben J. Kuon,² and Robert E. Garfield³

¹ Department of Perinatology, Division of Obstetrics and Gynecology, University Medical Center Ljubljana, Slajmerjeva 3, 1000 Ljubljana, Slovenia

² Department of Obstetrics and Gynecology, University Hospital Heidelberg, Im Neuenheimer Feld 672, 69120 Heidelberg, Germany

³ Department of Obstetrics and Gynecology, St. Joseph's Hospital and Medical Center, Downtown Campus at TGen, 445 N 5th Street, Phoenix, AZ 85004, USA

Correspondence should be addressed to Robert E. Garfield; robert.garfield@dignityhealth.org

Received 29 May 2013; Revised 15 August 2013; Accepted 20 August 2013

Academic Editor: Brynjar Karlsson

Copyright © 2013 Miha Lucovnik et al. This is an open access article distributed under the Creative Commons Attribution License, which permits unrestricted use, distribution, and reproduction in any medium, provided the original work is properly cited.

Parturition involves increasing compliance (ripening) of the uterine cervix and activation of the myometrium. These processes take place in a different time frame. Softening and shortening of the cervix starts in midpregnancy, while myometrial activation occurs relatively close to delivery. Methods currently available to clinicians to assess cervical and myometrial changes are subjective and inaccurate, which often causes misjudgments with potentially adverse consequences. The inability to reliably diagnose true preterm labor leads to unnecessary treatments, missed opportunities to improve neonatal outcome, and inherently biased research of treatments. At term, the likelihood of cesarean delivery depends on labor management, which in turn depends on accurate assessments of cervical change and myometrial contractility. Studies from our group and others show that noninvasive measurements of light-induced fluorescence (LIF) of cervical collagen and uterine electromyography (EMG) objectively detect changes in the composition of the cervix and myometrial preparedness to labor and are more reliable than clinical observations alone. We present a conceptual model of parturition constructed on cervical LIF and uterine EMG studies. We also explore how these methodologies could be helpful with managing patients experiencing preterm contractions and with optimizing labor management protocols aimed to reduce cesarean section.

1. Introduction

Parturition is a complex process involving increasing compliance of the uterine cervix and activation of the myometrial contractility. Understanding and accurate assessment of these two components are the key to reliable diagnosis and effective management of labor, both at term and preterm. However, methods currently available to evaluate cervical changes and myometrial contractility have several major drawbacks, and evidence shows that misjudgments with important clinical consequences are often made [1–5].

In our previous studies, we documented evidence that cervical collagen content can be monitored noninvasively by measuring light-induced fluorescence (LIF) of collagen [6]. This method allows assessing the change in cervical structure objectively. Myometrial activity, on the other hand, can be monitored by measuring uterine electromyographic (EMG)

activity from the abdominal surface [7–11]. Several studies have demonstrated that uterine EMG detects uterine contractions as reliably as the tocography, and even as the intrauterine pressure catheter (IUP), which is an invasive procedure and cannot be performed anticipating that gestation will be continued (Figure 1) [12–15]. Besides detecting contractions, uterine EMG yields valuable information about changes in the electrical properties of the myometrium which indicate the onset of true labor at term and preterm [7, 9, 16–19].

We present a conceptual model of parturition with a timeline of critical events during labor constructed on data from cervical LIF and uterine EMG studies. We also explore clinical situations, that is, preterm and term contractions, induction of labor, and arrest of labor in the first stage, in which methods to objectively and accurately assess the cervix and the myometrium would be extremely valuable.

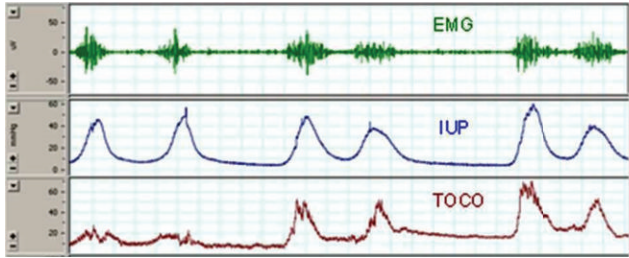


FIGURE 1: Electrical activity of the myometrium (EMG activity—top trace) is responsible for uterine contractions. Note the excellent temporal correspondence between EMG and mechanical contractile events (measured by intrauterine pressure catheter (IUP), middle trace, and tocography (TOCO), bottom trace).

2. Increasing Cervical Compliance

This process, generally referred to as the “cervical ripening,” summarizes many biochemical and functional changes that result in the softening and effacement of the cervix, allowing cervical dilatation and eventually the delivery of the fetus. During this progressive event, the connective tissue in the cervix, consisting predominantly of collagen, is degraded and rearranged [20]. Cervical ripening does not depend on uterine contractions and is similar to an inflammatory reaction. It involves the infiltration of polymorphonuclear cells and a release of degradative enzymes—metalloproteinases, resulting in a decrease of collagen concentration in the tissue [21].

The cervix, its dilation, effacement, consistency, and position are routinely evaluated by digital examination. These are components of the Bishop scoring system, which, although not designed for this purpose, is often used clinically as a predictor of preterm delivery. The clinical exam is, however, a very subjective method to assess the process of cervical ripening [22, 23]. Measuring cervical length by transvaginal ultrasound is more objective and has been shown to have a high negative predictive value for preterm delivery [24–26]. The positive predictive value of cervical length is, however, low, and many patients with a short cervix do not deliver preterm [27].

It has been shown in several studies that changes in collagen content, which are a marker of cervical ripeness, can be assessed non-invasively by measuring LIF of the non-soluble collagen [28]. This methodology allows an objective assessment of the change in cervical structure, and can detect the change in the composition of the cervix, regardless of its length. It is, therefore, a more accurate method to diagnose cervical ripening.

3. Myometrial Contractility

Several events in the myometrium precede labor. Excitability of cells increases due to changes in transduction mechanisms and synthesis of various proteins, including proteins that affect ion channels and receptors for uterotonins [29, 30]. At the same time, systems that inhibit myometrial activity, such as nitric oxide system, are downregulated, leading to withdrawal of uterine relaxation [11]. Electrical coupling

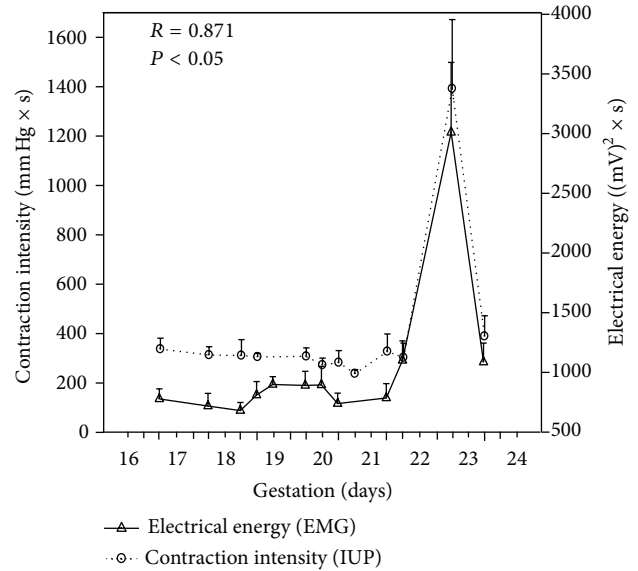


FIGURE 2: Acute changes in myometrial activity preceding delivery in rats (days 22-23 of gestation). Note the excellent correlation between contraction intensity measured by intrauterine pressure catheter (IUP) and energy of uterine EMG signals. Shi S-Q et al., unpublished data.

between myometrial cells also increases due to an increase in gap junctions, and an electrical syncytium allowing the propagation of action potentials from cell to cell is formed [31, 32]. These changes are required for effective contractions that result in the delivery (expulsion) of the fetus.

The most commonly used method to assess uterine contractions is currently the tocography. Unfortunately, this technique became a standard of care without ever undergoing vigorous clinical trials, 40 years ago, when the standards for clinical evidence were not as rigorous as today. Tocography measures the change in shape of the abdominal wall as a function of uterine contractions and, as a result, is a qualitative rather than quantitative method [33]. It has been shown in several studies that monitoring uterine activity with tocography is not helpful in identifying patients in true (active) labor, both at term and preterm [15, 33–35].

The transition from the nonlabor to the labor state of the myometrium can be identified by monitoring the uterine EMG [7, 9, 16–19]. An increase in uterine EMG activity corresponds to the increase of uterine contractility immediately preceding delivery in an animal model (Figure 2). Changes in certain EMG parameters, such as power spectrum (PS) peak frequency and amplitude and propagation velocity of uterine electrical signals, also indicate the onset of true labor at term and preterm in humans [16, 19] (Figure 4(b)).

4. Model of Parturition

Figure 3 presents a conceptual model of parturition constructed on data from cervical LIF and uterine EMG studies. The two components of parturition, that is, increasing cervical compliance and activation of the myometrium, take place

TABLE 1: Predictive measures of uterine EMG (rescaled sum of power spectrum [PS] peak frequency and propagation velocity) compared with current methods to predict preterm delivery within 7 days [19].

Method	AUC	Best cutoff	Sensitivity	Specificity	PPV	NPV
EMG (PV + PS Peak Frequency)	0.96	84.48	70%	100%	100%	90%
Bishop Score	0.72	10	18%	100%	100%	81%
Transvaginal Cervical Length	0.67	0.7 cm	14%	98%	50%	90%
Contractions on tocogram	0.54	N/A	35%	72%	27%	79%

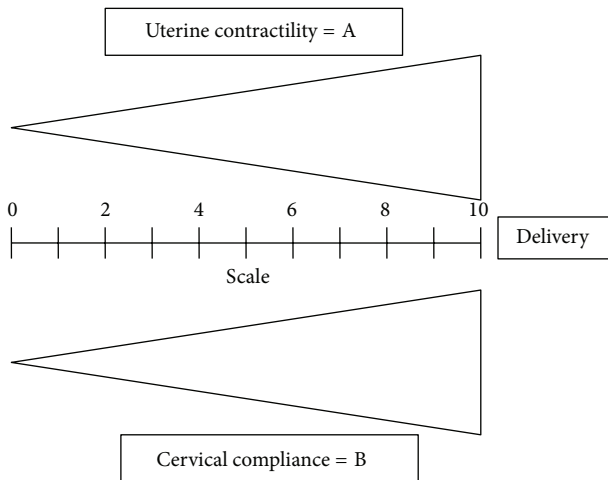


FIGURE 3: Parturition involves increasing compliance of the uterine cervix and activation of the myometrial contractility.

in a different time frame. According to studies of cervical LIF, and also according to studies of changes in cervical length during pregnancy, the process of softening and shortening of the cervix starts in mid-pregnancy, or even sooner [37, 38] (Figure 4(a)). The myometrial activation, in contrast, is a more acute event, occurring relatively close to delivery. In rats, uterine EMG activity increases not more than 24 hours before delivery (Figure 2). Similarly, in humans the increases of EMG PS peak frequency and propagation velocity, which accurately identify myometrial preparedness for labor, do not typically occur more than seven days from delivery preterm and generally even later at term [16, 19] (Figure 4(b)).

5. Diagnosis of Preterm Labor

The inability to reliably diagnose true preterm labor is one of the biggest unsolved problems in obstetrics today. Up to 50% of patients evaluated for preterm labor are not in true labor and will eventually deliver at term [1]. 20% of symptomatic patients, suspected but not confirmed to be in preterm labor, on the other hand, will deliver prematurely [3]. These diagnostic inaccuracies lead to unnecessary treatments, missed opportunities to improve neonatal outcome, and research of potential treatments done on women not chosen on sufficiently objective grounds.

A reliable diagnosis of preterm cervical ripening (increasing compliance) (high B score in Figure 3) and myometrial contractility (high A score in Figure 3) could identify preterm

patients who really benefit from early tocolytic therapy, administration of steroids, and admission or transport to a hospital with facilities for neonatal intensive care. It would also help to avoid side effects and substantial economic costs associated with unnecessary treatments. Moreover, it could be extremely valuable in research of potential treatments for preterm labor because it would allow targeting the treatment only to patients who are really in labor [36, 39]. Cervical LIF and uterine EMG, as studied by our groups and others, may be proved in prospective studies to identify increasing compliance and myometrial activation characteristic of preterm labor much more accurately than the methods currently available to physicians today.

We have reported a study on 88 patients admitted with the diagnosis of preterm labor at less than 34 weeks of gestational age at a single institution (St. Joseph's Hospital and Medical Center, Department of Obstetrics and Gynecology, Phoenix, Arizona) [19]. Propagation velocity (PV) of EMG signals, power spectrum (PS) peak frequency, and the combination (rescaled sum) of these two parameters were significantly higher in patients delivering within 7 days from the EMG measurement compared to those who delivered after 7 days. Both EMG PV and PS peak frequency identified more accurately the true preterm labor than today's clinical methods (Figure 5). By combining the PV and PS peak frequency, we constructed a model for prediction of spontaneous preterm birth. The area under the receiver-operating characteristics curve for this model was 0.96 (Table 1).

6. Lowering Cesarean Delivery Rates

Cesarean section rates have increased significantly worldwide during the last decades but in particular in the middle and high income countries [40–42]. With the growing knowledge of morbidities associated with repeated cesarean sections, many efforts have been made to control this dramatic rise in the rate of cesarean delivery [41, 42]. Given the decline in attempted trials of labor after cesarean, the most effective approach to reducing cesarean section rate is to avoid the first cesarean delivery [43]. Decisions how to induce labor, when to admit patients with contractions, and diagnosis of arrest disorder in the first stage of labor influence significantly the likelihood of cesarean delivery [43]. These management decisions depend heavily on accurate diagnosis of cervical and myometrial changes before and during labor.

A successful vaginal birth is less likely in the absence of a compliant (ripe) cervix. Therefore, accurate assessment of the cervix is crucial in decision-making regarding the method of labor induction. When the cervix is “unfavorable”

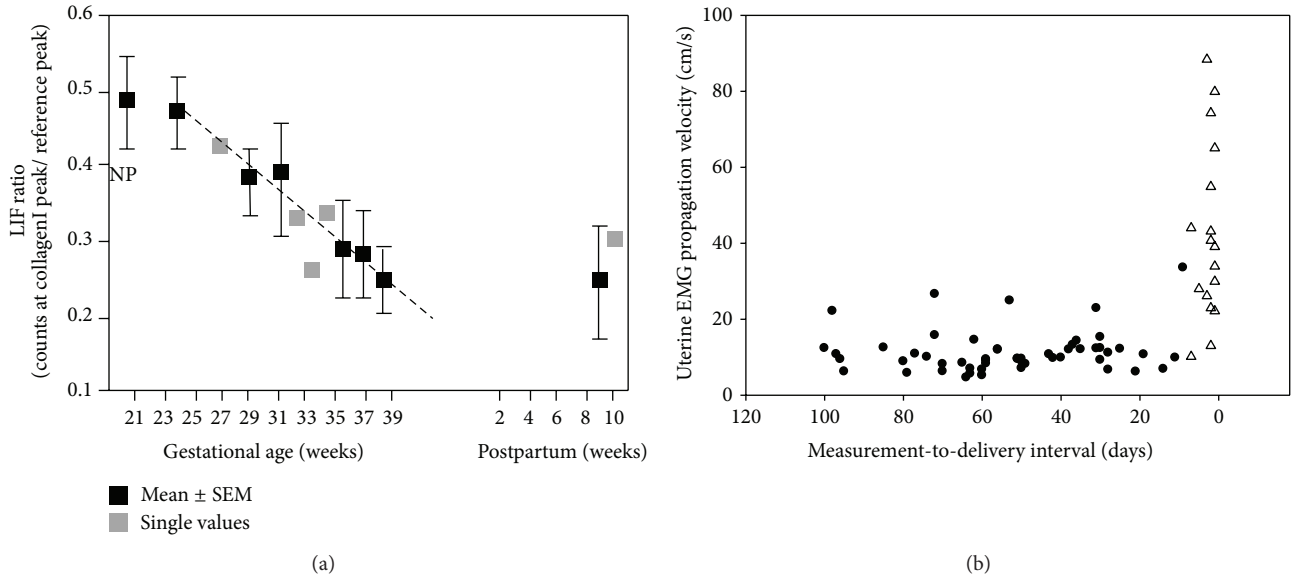


FIGURE 4: (a) Cervical light-induced fluorescence (LIF) ratio throughout human pregnancy and postpartum. NP: nonpregnant; (b) uterine EMG propagation velocity increases immediately prior to delivery. Δ delivery ≤ 7 days from the measurement; \bullet delivery > 7 days from the measurement. Based on data from Schlembach et al. [28] and Lucovnik et al. [19].

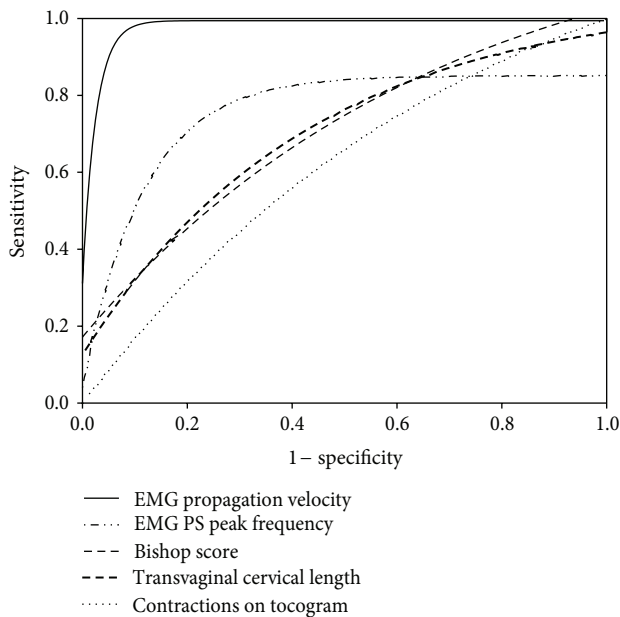


FIGURE 5: Comparison of receiver-operating-characteristics curves for EMG parameters (power spectrum [PS] peak frequency and propagation velocity) versus currently used methods to predict preterm delivery within 7 days [36].

(low B score in Figure 3), cervical ripening agents should be used since this will increase the chance of vaginal delivery [43]. Cervical LIF can objectively assess the cervical structure [28]. Studies evaluating the usefulness of this technology to decide on using cervical ripening methods should, therefore, be performed. Evaluation of cervical change and myometrial contractility is also important when diagnosing a failed

induction, which is defined as failure to generate regular contractions with cervical change [44, 45].

Admission of women in early latent phase of labor has been associated with higher cesarean section rates [46, 47]. Uterine EMG has been shown to identify myometrial activation, characterized by molecular changes leading to an increase in coupling and excitability of cells. This would, therefore, allow clinicians not to admit women in the latent phase or not yet in labor regardless of the presence of contractions on tocogram, since these women are more likely to receive medical intervention such as electronic monitoring, epidural analgesia, oxytocin, and eventually cesarean section [46–48].

Finally, progress in the first stage of labor and/or the diagnosis of arrest in the first stage is based on cervical change and adequacy of contractions. Both of these parameters are difficult to quantify using the currently available subjective methods. On the other hand, cervical LIF can objectively assess change in the cervical structure (score B in Figure 3), and uterine EMG identifies the potential need for additional stimulation of myometrial (score A in Figure 3).

References

- [1] M. L. McPheeters, W. C. Miller, K. E. Hartmann et al., “The epidemiology of threatened preterm labor: a prospective cohort study,” *American Journal of Obstetrics and Gynecology*, vol. 192, no. 4, pp. 1325–1330, 2005.
- [2] P. A. Janssen, C. E. Iker, and E. A. Carty, “Early labour assessment and support at home: a randomized controlled trial,” *Journal of Obstetrics and Gynaecology Canada*, vol. 25, no. 9, pp. 734–741, 2003.
- [3] J. D. Iams and R. Romero, “Preterm birth,” in *Obstetrics: Normal and Problem Pregnancies*, S. G. Gabbe, J. R. Niebyl, and

- J. L. Simpson, Eds., pp. 668–712, Churchill Livingstone Elsevier, Philadelphia, Pa, USA, 5th edition, 2007.
- [4] T. A. Bennett, M. Kotelchuck, C. E. Cox, M. J. Tucker, and D. A. Nadeau, “Pregnancy-associated hospitalizations in the United States in 1991 and 1992: a comprehensive view of maternal morbidity,” *American Journal of Obstetrics and Gynecology*, vol. 178, no. 2, pp. 346–354, 1998.
 - [5] M. Lucovnik, R. L. Chambliss, and R. E. Garfield, “Costs of unnecessary admissions and treatments for threatened preterm labor,” *American Journal of Obstetrics and Gynecology*, vol. 209, no. 3, pp. 1–3, 2013.
 - [6] R. E. Garfield, W. L. Maner, L. Shi, S. Q. Shi, and G. R. Saade, “Uterine EMG and cervical LIF—promising technologies in obstetrics,” *Current Women’s Health Reviews*, vol. 2, no. 3, pp. 207–221, 2006.
 - [7] C. Buhimschi, M. B. Boyle, G. R. Saade, and R. E. Garfield, “Uterine activity during pregnancy and labor assessed by simultaneous recordings from the myometrium and abdominal surface in the rat,” *American Journal of Obstetrics and Gynecology*, vol. 178, no. 4, pp. 811–822, 1998.
 - [8] C. Buhimschi and R. E. Garfield, “Uterine contractility as assessed by abdominal surface recording of electromyographic activity in rats during pregnancy,” *American Journal of Obstetrics and Gynecology*, vol. 174, no. 2, pp. 744–753, 1996.
 - [9] H. Léman, C. Marque, and J. Gondry, “Use of the electrohysterogram signal for characterization of contractions during pregnancy,” *IEEE Transactions on Biomedical Engineering*, vol. 46, no. 10, pp. 1222–1229, 1999.
 - [10] I. Verdenik, M. Pajntar, and B. Leskošek, “Uterine electrical activity as predictor of preterm birth in women with preterm contractions,” *European Journal of Obstetrics Gynecology and Reproductive Biology*, vol. 95, no. 2, pp. 149–153, 2001.
 - [11] R. E. Garfield, G. Saade, C. Buhimschi et al., “Control and assessment of the uterus and cervix during pregnancy and labour,” *Human Reproduction Update*, vol. 4, no. 5, pp. 673–695, 1998.
 - [12] B. C. Jacod, E. M. Graatsma, E. Van Hagen, and G. H. A. Visser, “A validation of electrohysterography for uterine activity monitoring during labour,” *Journal of Maternal-Fetal and Neonatal Medicine*, vol. 23, no. 1, pp. 17–22, 2010.
 - [13] J. Jezewski, K. Horoba, A. Matonia, and J. Wrobel, “Quantitative analysis of contraction patterns in electrical activity signal of pregnant uterus as an alternative to mechanical approach,” *Physiological Measurement*, vol. 26, no. 5, pp. 753–767, 2005.
 - [14] C. Rabotti, M. Mischi, J. O. E. H. van Laar, G. S. Oei, and J. W. M. Bergmans, “Estimation of internal uterine pressure by joint amplitude and frequency analysis of electrohysterographic signals,” *Physiological Measurement*, vol. 29, no. 7, pp. 829–841, 2008.
 - [15] H. Maul, W. L. Maner, G. Olson, G. R. Saade, and R. E. Garfield, “Non-invasive transabdominal uterine electromyography correlates with the strength of intrauterine pressure and is predictive of labor and delivery,” *Journal of Maternal-Fetal and Neonatal Medicine*, vol. 15, no. 5, pp. 297–301, 2004.
 - [16] W. L. Maner, R. E. Garfield, H. Maul, G. Olson, and G. Saade, “Predicting term and preterm delivery with transabdominal uterine electromyography,” *Obstetrics & Gynecology*, vol. 101, no. 6, pp. 1254–1260, 2003.
 - [17] C. Buhimschi, M. B. Boyle, and R. E. Garfield, “Electrical activity of the human uterus during pregnancy as recorded from the abdominal surface,” *Obstetrics & Gynecology*, vol. 90, no. 1, pp. 102–111, 1997.
 - [18] C. K. Marque, J. Terrien, S. Rihana, and G. Germain, “Preterm labour detection by use of a biophysical marker: the uterine electrical activity,” *BMC Pregnancy and Childbirth*, vol. 7, supplement 1, article S5, 2007.
 - [19] M. Lucovnik, W. L. Maner, L. R. Chambliss et al., “Noninvasive uterine electromyography for prediction of preterm delivery,” *American Journal of Obstetrics and Gynecology*, vol. 204, no. 3, pp. 228.e1–228.e10, 2011.
 - [20] P. C. Leppert, “Anatomy and physiology of cervical ripening,” *Clinical Obstetrics and Gynecology*, vol. 38, pp. 267–279, 1998.
 - [21] W. Rath, R. Ismers, B. C. Adelman-Grill, H. W. Stuhlsatz, M. Szevereny, and W. Kuhn, “Biochemical changes in human cervical connective tissue after intracervical application of prostaglandin E₂,” *Prostaglandins*, vol. 45, no. 4, pp. 375–384, 1993.
 - [22] W. L. Holcomb Jr. and J. S. Smeltzer, “Cervical effacement: variation in belief among clinicians,” *Obstetrics & Gynecology*, vol. 78, no. 1, pp. 43–45, 1991.
 - [23] R. Gomez, M. Galasso, R. Romero et al., “Ultrasonographic examination of the uterine cervix is better than cervical digital examination as a predictor of the likelihood of premature delivery in patients with preterm labor and intact membranes,” *American Journal of Obstetrics and Gynecology*, vol. 171, no. 4, pp. 956–964, 1994.
 - [24] J. D. Iams, R. L. Goldenberg, P. J. Meis et al., “The length of the cervix and the risk of spontaneous premature delivery,” *The New England Journal of Medicine*, vol. 334, no. 9, pp. 567–572, 1996.
 - [25] E. Tsoi, I. B. Fuchs, S. Rane, L. Geerts, and K. H. Nicolaides, “Sonographic measurement of cervical length in threatened preterm labor in singleton pregnancies with intact membranes,” *Ultrasound in Obstetrics and Gynecology*, vol. 25, no. 4, pp. 353–356, 2005.
 - [26] I. Fuchs, E. Tsoi, W. Henrich, J. W. Dudenhausen, and K. H. Nicolaides, “Sonographic measurement of cervical length in twin pregnancies in threatened preterm labor,” *Ultrasound in Obstetrics and Gynecology*, vol. 23, no. 1, pp. 42–45, 2004.
 - [27] J. D. Iams, “Prediction and early detection of preterm labor,” *Obstetrics & Gynecology*, vol. 101, no. 2, pp. 402–412, 2003.
 - [28] D. Schlembach, L. Mackay, L. Shi, W. L. Maner, R. E. Garfield, and H. Maul, “Cervical ripening and insufficiency: from biochemical and molecular studies to in vivo clinical examination,” *European Journal of Obstetrics Gynecology and Reproductive Biology*, vol. 144, supplement 1, pp. S70–S76, 2009.
 - [29] N. Tezuka, M. Ali, K. Chwalisz, and R. E. Garfield, “Changes in transcripts encoding calcium channel subunits of rat myometrium during pregnancy,” *American Journal of Physiology—Cell Physiology*, vol. 269, no. 4, pp. C1008–C1017, 1995.
 - [30] A. R. Fuchs, F. Fuchs, P. Husslein, and M. S. Soloff, “Oxytocin receptors in the human uterus during pregnancy and parturition,” *American Journal of Obstetrics and Gynecology*, vol. 150, no. 6, pp. 734–741, 1984.
 - [31] J. Balducci, B. Risek, N. B. Gilula, A. Hand, J. F. X. Egan, and A. M. Vintzileos, “Gap junction formation in human myometrium: a key to preterm labor?” *American Journal of Obstetrics and Gynecology*, vol. 168, no. 5, pp. 1609–1615, 1993.
 - [32] R. E. Garfield, M. G. Blennerhassett, and S. M. Miller, “Control of myometrial contractility: role and regulation of gap junctions,” *Oxford Reviews of Reproductive Biology*, vol. 10, pp. 436–490, 1988.
 - [33] R. K. Freeman, “Problems with intrapartum fetal heart rate monitoring interpretation and patient management,” *Obstetrics & Gynecology*, vol. 100, no. 4, pp. 813–826, 2002.

- [34] A. M. Peaceman, W. W. Andrews, J. M. Thorp et al., "Fetal fibronectin as a predictor of preterm birth in patients with symptoms: a multicenter trial," *American Journal of Obstetrics and Gynecology*, vol. 177, no. 1, pp. 13–18, 1997.
- [35] J. D. Iams, R. B. Newman, E. A. Thom et al., "Frequency of uterine contractions and the risk of spontaneous preterm delivery," *The New England Journal of Medicine*, vol. 346, no. 4, pp. 250–255, 2002.
- [36] M. Lucovnik, R. J. Kuon, L. R. Chambliss et al., "Use of uterine electromyography to diagnose term and preterm labor," *Acta Obstetrica et Gynecologica Scandinavica*, vol. 90, no. 2, pp. 150–157, 2011.
- [37] L. Shi, S.-Q. Shi, G. R. Saade, K. Chwalisz, and R. E. Garfield, "Changes in cervical resistance and collagen fluorescence during gestation in rats," *Journal of Perinatal Medicine*, vol. 27, no. 3, pp. 188–194, 1999.
- [38] C. P. Durnwald, C. D. Lynch, H. Walker, and J. D. Iams, "The effect of treatment with 17 alpha-hydroxyprogesterone caproate on changes in cervical length over time," *American Journal of Obstetrics and Gynecology*, vol. 201, no. 4, pp. 410.e1–410.e5, 2009.
- [39] M. Lucovnik, Z. Novak-Antolic, and R. E. Garfield, "Use of non-invasive uterine electromyography in the diagnosis of preterm labour," *Facts, Views & Vision in Obgyn*, vol. 4, pp. 66–72, 2012.
- [40] J. A. Martin, B. E. Hamilton, S. J. Ventura et al., "Final data for 2010, National vital statistics reports, National Center for Health Statistics, Hyattsville, Md, USA, 2012," <http://www.cdc.gov/nchs/data/nvsr/nvsr61/nvsr61.01.pdf>.
- [41] EURO-PERISTAT Project, European Perinatal Health Report, 2010, <http://www.europeristat.com/>.
- [42] J. M. Belizán, F. Althabe, and M. L. Cafferata, "Health consequences of the increasing caesarean section rates," *Epidemiology*, vol. 18, no. 4, pp. 485–486, 2007.
- [43] C. Y. Spong, V. Berghella, K. D. Wenstrom, B. M. Mercer, and G. R. Saade, "Preventing the first cesarean delivery," *Obstetrics & Gynecology*, vol. 120, pp. 1181–1193, 2012.
- [44] L. M. Harper, A. B. Caughey, A. O. Obido, K. A. Roehl, and Q. Zhao, "Normal progress of induced labor," *Obstetrics & Gynecology*, vol. 119, pp. 1113–1118, 2012.
- [45] D. J. Rouse, S. J. Weiner, S. L. Bloom et al., "Failed labor induction: toward an objective diagnosis," *Obstetrics & Gynecology*, vol. 117, no. 2, pp. 267–272, 2011.
- [46] M. C. Klein, A. Kelly, J. Kaczorowski, and S. Grzybowski, "The effect of family physician timing of maternal admission on procedures in labour and maternal and infant morbidity," *Journal of Obstetrics and Gynaecology Canada*, vol. 26, no. 7, pp. 641–645, 2004.
- [47] E. Hemminki and R. Simukka, "The timing of hospital admission and progress of labour," *European Journal of Obstetrics Gynecology and Reproductive Biology*, vol. 22, no. 1-2, pp. 85–94, 1986.
- [48] P. Holmes, L. W. Oppenheimer, and S. Wu Wen, "The relationship between cervical dilatation at initial presentation in labour and subsequent intervention," *British Journal of Obstetrics and Gynaecology*, vol. 108, no. 11, pp. 1120–1124, 2001.

Research Article

Automatic Evaluation of Progression Angle and Fetal Head Station through Intrapartum Echographic Monitoring

**Sergio Casciaro,¹ Francesco Conversano,¹ Ernesto Casciaro,¹ Giulia Soloperto,¹
Emanuele Perrone,² Gian Carlo Di Renzo,² and Antonio Perrone³**

¹ National Research Council, Institute of Clinical Physiology, University Campus Ecotekne, Via Monteroni, 73100 Lecce, Italy

² Department of Obstetrics and Gynecology, University of Perugia, Santa Maria della Misericordia University Hospital, San Sisto, 06132 Perugia, Italy

³ Obstetrics and Gynecology Department, "Vito Fazzi" Hospital, Piazza Filippo Muratore, 73100 Lecce, Italy

Correspondence should be addressed to Sergio Casciaro; sergio.casciaro@cnr.it

Received 31 May 2013; Accepted 2 August 2013

Academic Editor: Massimo Mischi

Copyright © 2013 Sergio Casciaro et al. This is an open access article distributed under the Creative Commons Attribution License, which permits unrestricted use, distribution, and reproduction in any medium, provided the original work is properly cited.

Labor progression is routinely assessed through transvaginal digital inspections, meaning that the clinical decisions taken during the most delicate phase of pregnancy are subjective and scarcely supported by technological devices. In response to such inadequacies, we combined intrapartum echographic acquisitions with advanced tracking algorithms in a new method for noninvasive, quantitative, and automatic monitoring of labor. Aim of this work is the preliminary clinical validation and accuracy evaluation of our automatic algorithm in assessing progression angle (PA) and fetal head station (FHS). A cohort of 10 parturients underwent conventional labor management, with additional translabial echographic examinations after each uterine contraction. PA and FHS were evaluated by our automatic algorithm on the acquired images. Additionally, an experienced clinical sonographer, blinded regarding the algorithm results, quantified on the same acquisitions of the two parameters through manual contouring, which were considered as the standard reference in the evaluation of automatic algorithm and routine method accuracies. The automatic algorithm (mean error \pm 2SD) provided a global accuracy of 0.9 ± 4.0 mm for FHS and $4^\circ \pm 9^\circ$ for PA, which is far above the diagnostic ability shown by the routine method, and therefore it resulted in a reliable method for earlier identification of abnormal labor patterns in support of clinical decisions.

1. Introduction

The monitoring of pregnancy demands for safe and accurate methods, tailored upon the specific gestational stage, is aiming to obtain a baseline evaluation of the anatomy and prenatal health of the fetus, ultimately trying to provide specific indications towards the best possible delivery management. Diagnostic imaging and a number of clinical tests (i.e., amniocentesis and cordocentesis) are often used for the early pregnancy monitoring [1]. By this stage, clinical considerations can lead to the indication towards a Caesarian Section (CS) based upon fetal health and the physiology of the pregnant patient (e.g., previous CS, pelvis conformation, etc.).

Successively, throughout the course of gestation, obstetrics and gynecologists are supported by few biomedical

devices introduced in the last decades, such as intrapartum Electronic Fetal heart rate Monitoring (EFM) [2–4], external tocodynamometer, or internal intrauterine amniotic pressure sensor for uterine contraction monitoring [5, 6]. Furthermore, quantitative processing of electrohysterogram (EHG) data has experimentally proven its advantages over current practice in monitoring uterine contractile activity [7–11]; labor and nonlabor contraction classifications could enable the prediction of preterm delivery and, in case, the proper planning of an operative delivery [12, 13].

Therefore, the currently available methodologies allow the clinicians to formulate in advance clinical recommendations towards CS or operative childbirth in the minority of cases; for the remaining patients, no indicators to date have been found to identify the correct timing and modality of

interventional childbirth. These parturients reach the final stage of pregnancy in jeopardy when entering the delivery room, since an incorrect management of childbirth labor may have a crucial impact on the neonatal health regardless of the cares taken during the course of the gestation. In fact, intrapartum assessment of progression indicators (cervical dilatation, fetal head station (FHS) and rotation, progression angle (PA), etc.), essential for deciding for a surgical (i.e., CS) or an operative intervention (i.e., application of forceps or vacuum extractor), is currently performed by highly subjective transvaginal manual inspections, although relevant literature extensively reported evidence of their unreliability with errors up to 88% in FHS [14] and up to 50% in cervix dilatation [15, 16] assessment. Using ultrasound (US) assessment as the standard reference, a high rate of error (65%) in transvaginal digital determination of fetal head position during the second stage of labor was also demonstrated, almost independently of the operator's experience [17–21]. The occurrence of these wrong assessments combined with the uncertain correlation between fetal distress and EFM [5] may cause uncontrollable fatal complications. The most concerning consequence of such lack of objective evidence in support of clinical choices, coupled with the inherently poor sensitivity and reliability problems of EFM [22], is the currently unacceptable rate of CS, largely above the 15% recommended by the World Health Organization [23].

Recently, various attempts have been made to design instruments for improving accuracy of cervical dilatation and fetal head station measurements [24–27], but none of them introduced significant advancement in the labor management. Being US the best suited method for safe and real-time childbirth-related diagnostic purposes, as it uses non-ionizing radiation and offers intraoperative guidance features [28–32], recently proposed diagnostic techniques for intrapartum monitoring involve transperineal US measurements of fetal head engagement [33], transvaginal sonographic assessment of the cervix [34], or positioning echographic receivers and electrodes pinned on the fetal head scalp [24]. These methodology are characterized by invasiveness and discomfort for the parturient as well as an increased infection risks for the fetus [35]. On the other hand, intrapartum translabial echographic acquisitions demonstrated their efficacy in imaging fetal head underneath the pubic bone [36]. Thus, we combined the latter modality with a pattern tracking algorithm, in order to automatically measure several labor progression parameters [37], realizing a new method for noninvasive, quantitative, and automatic monitoring of childbirth labor. Whereas a preliminary evaluation of the feasibility of the method in the clinical practice has already been conducted [38], this study represents the first quantitative comparative analysis of the outcomes of our algorithm with other methods. In particular, aim of this work is to perform a preliminary clinical validation of this new technique, quantifying its actual accuracy with respect to manual methods, representing the currently adopted “routine method,” and to a reference standard, represented by the echographic manual contouring performed by an experienced operator.

2. Materials and Methods

A US system was combined with a real-time tracking algorithm in order to automatically measure labor progression parameters, like fetal head station (FHS), head position, and progression angle (PA), based on patient specific anatomical references (Patent no. PCT/EP2009/008321) [37]. The algorithm was in-house developed (MatLab R2011b; The MathWorks Inc.) and employs a combination of morphological filters and pattern recognition methods [39] to perform the automatic segmentation and tracking of the fetal head outline and the pubic symphysis axis.

A clinical digital echograph (MyLab70 XVG, Esaote Spa, Florence, Italy), employing a 2D convex ultrasound transducer (CA631, Esaote Spa, Florence, Italy), connected to a PC for real-time image processing was employed to measure FHS and PA (see description of the algorithm in Section 2.1). First, a validation study was carried out on a birth simulator (details of the experimental setup are provided in Section 2.2); then, a preliminary clinical validation (Section 2.3) was conducted on patients in labor using the developed method and the corresponding algorithm. Obtained results were compared with the current clinical routine method (i.e., transvaginal digital inspection) and the reference standard (i.e., image-based measurement of considered parameters by an experienced sonographer).

2.1. Description of the Algorithm. The method is used for automatic labor monitoring processes B-mode echographic image frames by means of the new algorithm, based on pattern tracking, for the calculation of FHS and PA along the typical trajectory of fetal head within the birth canal (Figure 1(a)).

In particular, FHS is defined as the horizontal distance between the line perpendicular to the symphysis longitudinal axis and a parallel line, passing by the fetal head outermost point (Figure 1(b)), whereas the PA is the angle comprised between the symphysis longitudinal axis and the line connecting the distal end of the symphysis with the fetal head outermost point (Figure 1(c)).

The algorithm's working principle is schematically illustrated in Figure 2 and could be described as follows:

- (a) each B-mode image is processed by the algorithm applying, separately, two dedicated sets of filters in order to selectively enhance the regions containing the fetal head outline and the symphysis medial axis;
- (b) on the initial B-mode image analyzed, the two substructures are automatically segmented and identified as the two patterns to be searched within the subsequent images by means of maximization of either similarity or crosscorrelation coefficients [39];
- (c) pubic symphysis axis and distal end are segmented on subsequent images and displacements from previous position are also calculated. Specifically, at the point corresponding to the distal end of the symphysis, a line perpendicular to the axis is defined;

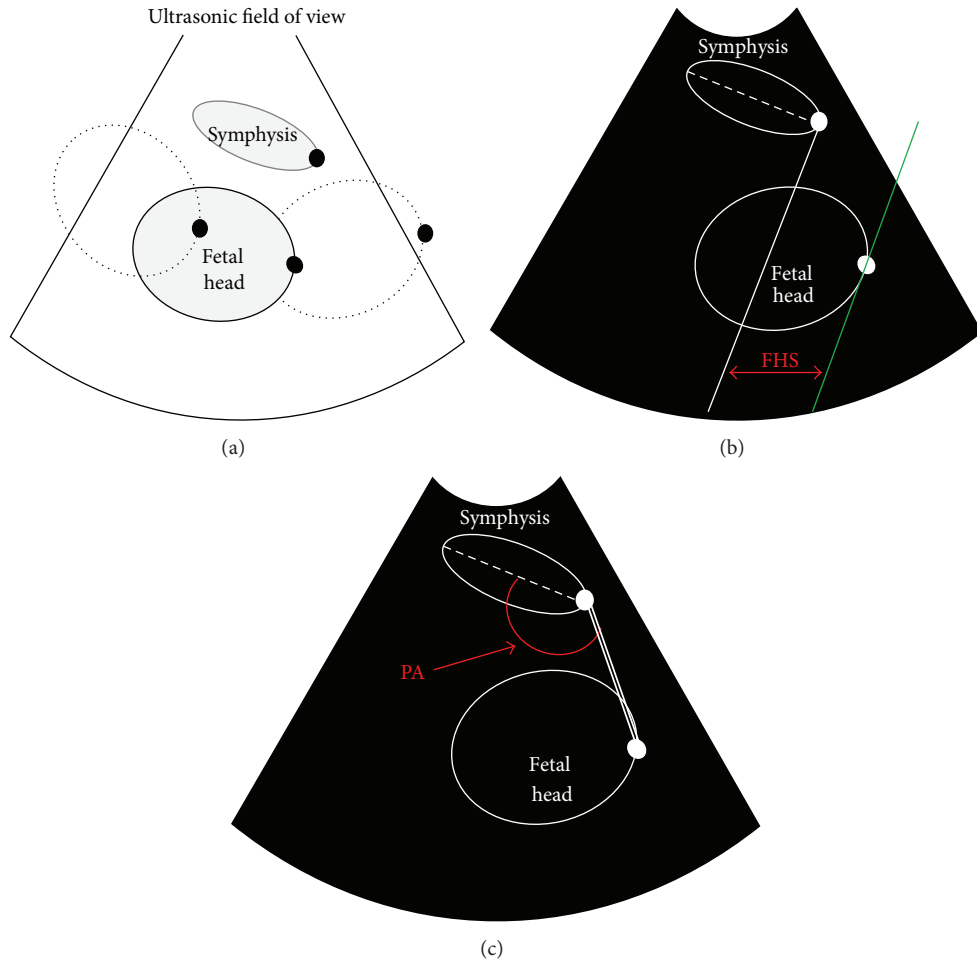


FIGURE 1: (a) Schematic diagram of the experimental setup adopted for assessment of tracking accuracy. (b) Scheme of the conventions is adopted to define fetal head station (FHS) indicated in red, where the solid white line is the line perpendicular to the symphysis longitudinal axis (dashed white line); the green line is the line passing by the fetal head outermost point; (c) scheme of the conventions adopted to define progression angle (PA) indicated in red, where the double white line is the connection between the symphysis distal end and the fetal head outermost point. By positioning the fetal head at different locations in the space comprised within the maternal pubic bone (birth canal), different stages of labor were simulated and relative position of the fetal head outermost point and distal end of the symphysis (both indicated by a solid black dot) were evaluated in terms of FHS and PA.

- (d) pattern location of fetal head is employed to initialize the automatic edge outlining from subsequent images and to calculate the displacement of fetal head right-most point (i.e., the outermost point, when assuming the fetal descent progresses from left to right) from previous position. A line is defined, passing by the fetal head outermost point and parallel to the line perpendicular to the symphysis axis;
- (e) for each frame, coordinates and displacements of the fetal head are registered with respect to the reference system associated to the pubic symphysis distal end in order to calculate FHS and PA.

Obtained values were compared with the respective reference; furthermore, FHS measurements were also converted in one of the 11 possible stations (−5 cm to +5 cm distance from the plane of the ischial spines, which are slightly above the distal level of the symphysis), according to the definitions

of the American College of Obstetricians and Gynaecologists (ACOG) [40].

2.2. Birth Simulator Experiments. An experimental setup was developed to reproduce the expected working conditions of a US probe adherent to the pubic area of the body of a parturient.

The birth simulator was a mechanical device consisting of a maternal mannequin and a fetal head, reproducing anatomical features of pubic bone and fetal head in tissue-mimicking materials taking into account recently reported findings available in the literature [41–44]. The birth simulator was immersed in a water bath, in order to eliminate air within the different simulator components. The fetal head was moved along its typical trajectory within the birth canal, and the position of its outermost point was identified with respect to the distal end of the symphysis. Once the probe was fixed on

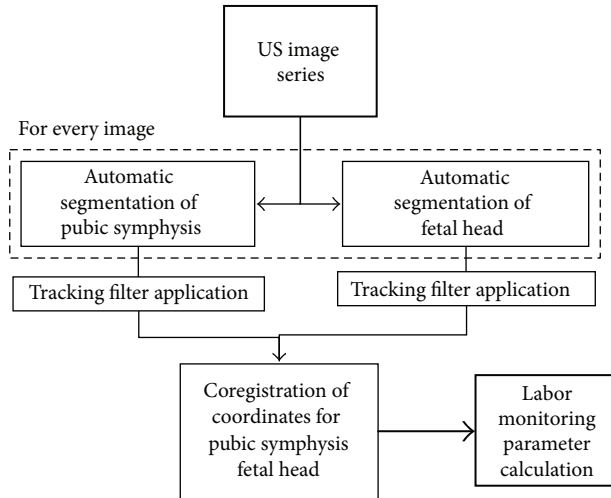


FIGURE 2: Schematic illustration of algorithm's working principle. The dashed line represents the iterative processing occurring on each image frame of the echographic acquisition.

the model of the symphysis, anatomical reference points were chosen by an operator on the initial echographic image; then, the fetal mannequin was moved following a pre-established sequence of locations, including all possible values of FHS (according to the corresponding definitions provided by the ACOG), PA, and several combinations of possible occiput presentations (anterior-posterior, left-right, etc.).

B-mode echographic image frames were acquired during the described experiments and were real time processed by the algorithm for the calculation of labor monitoring parameters.

2.3. Clinical Validation Study. A total of 10 parturients were recruited for this study employing the following criteria: singleton cephalic-presenting fetus, body mass index (BMI) $<30 \text{ kg/m}^2$, gestation age >38 weeks, absence of documented fetal malformations, active labor stage with cervical dilatation $<2 \text{ cm}$, and informed consent. These selection criteria allow to evaluate the algorithm's performance in monitoring childbirth progression throughout all labor phases in nonobese women without biases of parameter calculation deriving from fetal malformations or severe dystocia.

All the enrolled patients underwent the conventional labor management (continuous EFM and tocodynamometer, obstetric examinations, etc.) and an additional translabial echographic examinations, with prior application of ultrasonic coupling gel (Aquasonic 100, Parker Laboratories, Fairfield, NJ, USA) on the probe contact surface in order to eliminate air within the probe and the patient. The echographic acquisition was regularly performed, employing the same echographic system adopted for the birth simulator experiments, within 1 minute after the peak intensity of every contraction, as identified in the chart of the tocodynamometer connected to the parturient.

Acquired B-mode US images were analyzed offline, in order to avoid interference with the normal clinical activity of

the obstetrics unit, by our fully automatic custom-developed algorithm for image processing and pattern tracking, which provided the temporal evolution of PA and FHS.

The same parameters were also calculated upon manual contouring of the same images by an experienced operator (standard reference), that was blinded regarding the automatic algorithm results. The accuracy of algorithm results was quantified with respect to standard measurements for both FHS and PA. Obtained values were compared with the corresponding routine transvaginal measurements performed by experienced gynecologists at the same time instants during childbirth labor (routine method).

3. Results

In the birth simulator, the automatic identification of symphysis distal end and fetal head outermost point was correct in 98% of the computed images providing high visual reliability for the operator and the average errors (expressed as mean error $\pm 2\text{SD}$) were $0.8 \pm 1.8 \text{ mm}$ for FHS and $3^\circ \pm 4^\circ$ for the PA. Our results were achieved through maximization of the similarity coefficient at a frame rate that guarantee real-time monitoring of labor progression. However, accuracies of pattern tracking could be improved by about 30% through the maximization of the correlation coefficient, despite determining higher computational costs and a consequently lower frame-rate to be processed, that is, from 1 fps to 0.2 fps, which is still suitable for the purpose.

The methodology has been successfully translated in a preliminary intrapartum echographic study, during which the outcome of the routine method for FHS evaluation through digital inspection was conducted according to existing clinical protocols and recorded for our analyses.

Echographic imaging was performed immediately after contraction; pubic symphysis appeared always recognizable in the acquired US images whereas fetal head outline appeared sometimes discontinuous because portions of the US were attenuated by the pubic bone. In these cases the ultrasonic probe was not entirely positioned in correspondence with the cartilaginous pubic symphysis which would have, otherwise, allowed US transmission without attenuation. Nonetheless, the expert operator was able to manually detect on screen the references of the fetal head outermost point and the longitudinal axis of the symphysis (Figure 3) in order to elaborate their coordinates and calculate the PA and FHS values used as standard reference measurements.

In all the examined images, the tracking algorithm easily identified the symphysis, successfully interpolated fetal head outline and derived outermost point coordinates as well as the location of the distal end of the symphysis, as demonstrated by the results obtained on a 32-year-old woman at the 38th week of gestation of a 3.45 kg weighting baby boy, belonging to our cohort of patients (Figure 4). Results regarding this patient, taken as a typical case, will be further discussed in detail in this section to compare the accuracies of manual inspections versus the automatic calculations.

FHS values obtained with the routine method and with the automatic algorithm (i.e., the FHS values calculated by the algorithm from those US images acquired approximately



FIGURE 3: Example of manual contouring performed by an experienced sonographer (standard reference). “A” represents the fetal head outermost point; “B” and “C” are, respectively, the distal and proximal ends of the pubic symphysis.

at the same time of digital inspection) were evaluated against the standard reference measurements. Specifically, due to its invasiveness, the routine method was executed on average more than 3 times less often than the translabial echographic acquisition. In addition to that, intrapartum measurements based on the routine method failed in addressing timely the different phases of labor progression identifying the correct ACOG station only in 20% of cases. The clinical consequence of a wrong assessment of the stage of labor in terms of ACOG station is potentially dangerous when a “nonengaged” head was misdiagnosed as “engaged”, since the possibly required maneuvers could be erroneously directed and, for instance, the inappropriate modality of forceps or vacuum application could be applied. The comparison between the routine method and the automatic algorithm measurements is presented in detail for the case chosen from the cohort of patients. We compared the measurements obtained after manual inspection of the birth canal with values of FHS calculated from echographic images acquired after the same contraction. Due to the invasiveness of the procedure, the number of manual inspections was in all cases smaller than the number of acquired echographic image sequences; for the considered patients, the clinical staff performed 5 vaginal inspections whereas the echographic image series acquired were 20. Therefore, only a portion of the automatic algorithm measurements was plotted in Figure 5. Within the limited number of values available for comparison, the FHS assessment performed through the automatic algorithm showed a high rate of agreement with the standard reference ($R^2 = 0.98$, $P < 0.01$), and in one case the measured value overlapped the line of equality, whereas employment of the routine method achieved a good yet lower agreement with the standard reference ($R^2 = 0.85$, $P < 0.05$) and led to missing the identification of the FHS value equal to “0” (Figure 5).

Moreover, referring to the same parturient, the 20 automatic measurement values of FHS performed throughout labor duration maintained high correlation ($R^2 = 0.97$,

$P < 0.001$) with the standard reference, and this two techniques simultaneously identified the FHS value equal to “0” (Figure 6). Whereas PA is not currently assessed by manual inspection, its value throughout labor was measured by means of the standard reference methodology and the examined automatic algorithm. When compared, the two techniques demonstrated a good agreement ($R^2 = 0.86$, $P < 0.001$) although a minor overestimation of the parameter was shown by the automatic algorithm (Figure 7) over the 20 values examined.

The evaluation of the two labor progression parameters measured by the different assessment methodologies was performed on the entire cohort of patients, returning global accuracy of automatic parameter measurement, compared to standard reference, of 0.9 ± 4.0 mm for FHS and $4^\circ \pm 9^\circ$ for PA (mean error $\pm 2SD$); thus automatically measured FHS values always are coincided to the correct ACOG station.

4. Discussion

Our methodology, tested for labor monitoring on a number of volunteers, resulted well tolerated by the patients and allowed objective quantification of labor progression with a level of accuracy and time effectiveness higher than that achievable applying vaginal inspections (routine method). Similar to the performance assessed on the birth simulator, the algorithm successfully and timely identified, in the studied parturients, the correct ACOG stations also thanks to a number of measurements higher than those made with the routine method. Specifically, the FHS position “0” was correctly identified on US images, shown in Figure 4(a), by both automatic algorithm and standard reference method; conversely the manual inspection of the birth canal assessed such FHS level only 25 minutes later, simultaneously with the acquisition of the frame presented in Figure 4(b), when the FHS was already nearly level “+2”. Therefore, evaluation of labor progression made with the routine method was confirmed qualitative and subjective, implying, in some cases, that the fetus would stay in the same position within the birth canal for long time without knowledge of the event by the operators, enhancing the risk of fetal distress. In fact, the routine method presented potentially dangerous errors in 15% of measurements over the cohort of patients; defining dangerous errors of all those cases in which a “nonengaged” head misdiagnosed as “engaged” (i.e., $FHS > -2$ [40]) could lead to unnecessary operative interventions. Furthermore, the presented method provided high correlation with the reference gold standard in assessing both FHS and PA ($R^2 = 0.97$ and $R^2 = 0.86$, resp., both with $P < 0.001$), successfully monitoring the fetal head descent.

Future studies will include the repetition of experiments, similar to those reported in this work, employing a 3D ultrasound probe, whose field of view will allow the simultaneous measurement of FHS, PA, and, possibly, of other labor parameters, that were not considered in this study, that is, fetal head rotation; increased number of variable parameters measured by the algorithm would significantly

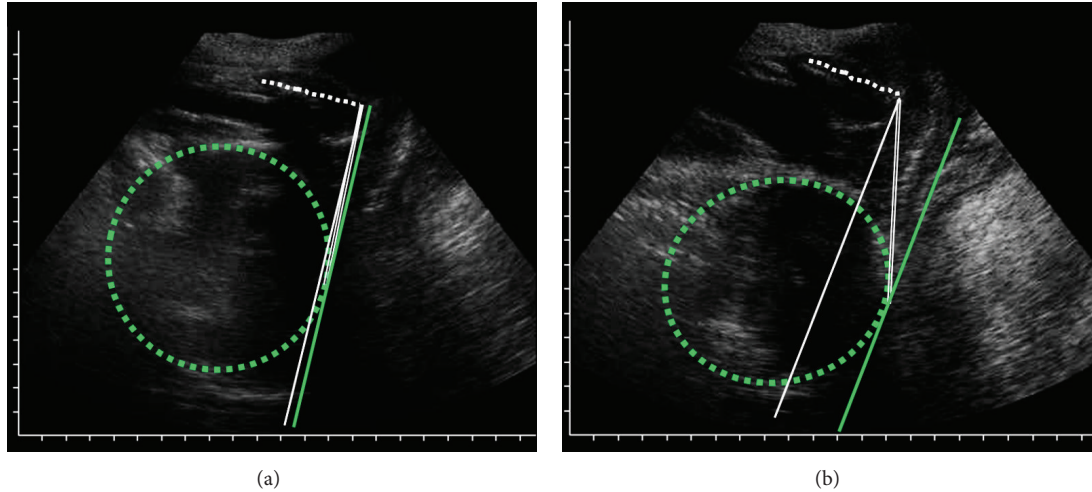


FIGURE 4: Example of algorithm output. The dashed green outline represents the fetal head; the white dashed line represents the symphysis longitudinal axis; the solid white line is the line perpendicular to the symphysis longitudinal axis; the solid green line is the line passing by the fetal head outermost point; the solid white double line is the connection between the symphysis distal end and the fetal head outermost point. (a) Image representing FHS = 0 cm and PA = 90°; (b) image representing FHS = 1.8 cm and PA = 103°.

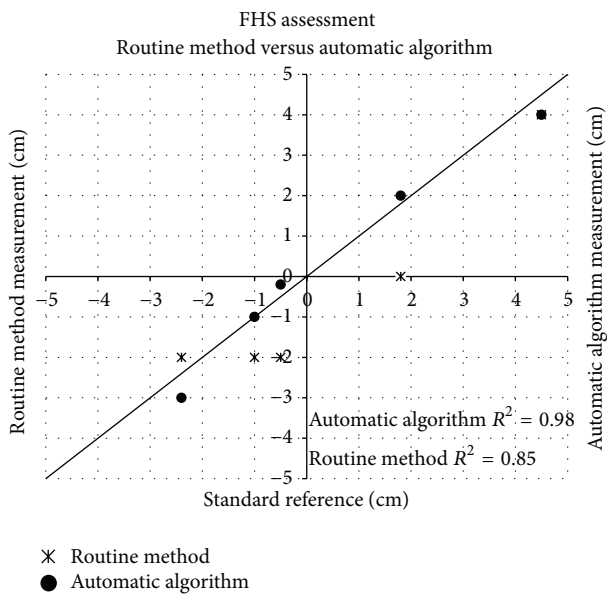


FIGURE 5: Scatter plot showing the fetal head station (FHS) measurements and corresponding automatic algorithm values, performed on a 32-year-old parturient at the 38th week of gestation, obtained through transvaginal manual inspection against the measurements obtained from the expert operator (standard reference), provided with the respective R^2 . The line of equality is also shown.

improve operator’s capability of assessing childbirth labor progression.

Therefore, our approach can address the needs of evidence to support medical decision with quantitative, objective, and storable indicators in all those cases of unpredicted dystocic labor and in those cases in which indicator of dystocia predictors, obtained during pregnancy monitoring,

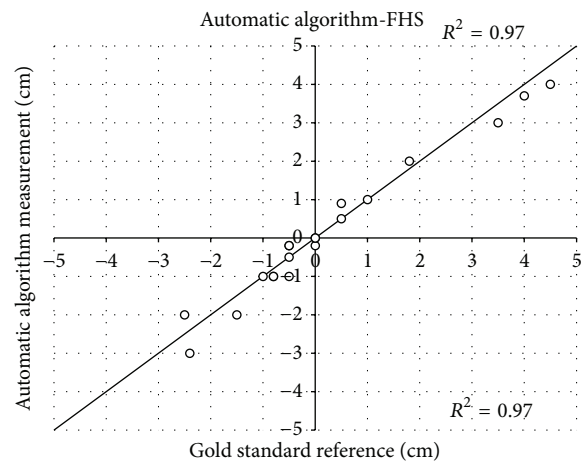


FIGURE 6: Scatter plot showing the fetal head station (FHS) measurements, performed on a 32-year-old parturient at the 38th week of gestation, obtained through the automatic algorithm against the measurements obtained from the expert operator (standard reference), provided with the respective R^2 . The line of equality is also shown. In the stage of labor between stations “-1” and “0”, 3 points out of 20 are overlapped due to the lack of progression in consecutive FHS measurements.

failed to describe the actual scenario in the delivery room. The proposed methodology showed the ability to overcome the limits of current labor-monitoring methods, providing a possible effective tool for earlier identification of abnormal labor patterns and accurate decision-taking support.

5. Conclusions

The study demonstrated the effectiveness of using ultrasound methods and automatic tracking algorithms for monitoring

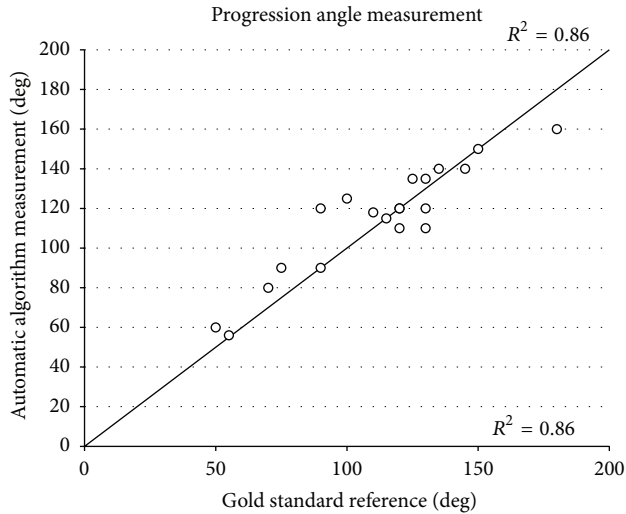


FIGURE 7: Scatter plot showing the progression angle (PA) measurements, performed on a 32-year-old parturient at the 38th week of gestation, obtained through the automatic algorithm against the measurements obtained from the expert operator (standard reference), provided with the respective R^2 . The line of equality is also shown. At the stage of labor corresponding station “-1” and “0”, 1 point out of 20 is overlapped due to the lack of progression in consecutive PA measurements.

of labor progress. Specifically, the experiments conducted on the birth simulator were useful to quantify the accuracy of the newly developed method. Moreover, the clinical translation of the methodology was confirmed to be feasible through clinical validation on ten parturients, who did not manifest any kind of discomfort during the echographic examination. The implementation of the method allowed measuring labor progression indicators, such as FHS and PA, during all phases of labor with satisfactory accuracy compared to standard reference (0.9 ± 4.0 mm for FHS and $4^\circ \pm 9^\circ$ for PA).

Therefore, this new technique is qualified as an objective approach to childbirth labor monitoring and could provide additional and quantitative information throughout all phases of labor, potentially advancing the current clinical practice which merely relies on transvaginal digital inspections. In particular, compared to other quantitative experimental methods, our approach minimizes invasiveness for mother and babies. Furthermore, the automatic algorithms evaluated in this work could address the needs of new standardized quantitative monitoring approaches and new guidelines to possibly reduce the high rate of CS, and also providing documentation records of objective parameters to avoid legal litigations in case of damages to patients and/or to babies that occurred during delivery.

References

- [1] A. Malvasi Tinelli, C. Cavallotti et al., “Imaging managing in obstetrics and gynecology: current trend and future perspectives,” in *Novel Technologies for Minimally Invasive Therapies*, S. Casciaro and E. Samset, Eds., Lecce Lupiensis Biomedical Publications, 2007.
- [2] E. H. Hon, “The electronic evaluation of the fetal heart rate. Preliminary report,” *American Journal of Obstetrics and Gynecology*, vol. 75, no. 6, pp. 1215–1230, 1958.
- [3] E. H. Hon and O. W. Hess, “The clinical value of fetal electrocardiography,” *American Journal of Obstetrics and Gynecology*, vol. 79, no. 5, pp. 1012–1023, 1960.
- [4] C. V. Ananth, S. P. Chauhan, H. Y. Chen et al., “Electronic fetal monitoring in the United States: temporal trends and adverse perinatal outcomes,” *Obstetrics & Gynecology*, vol. 121, no. 5, pp. 927–933, 2013.
- [5] R. E. Garfield, H. Maul, L. Shi et al., “Methods and devices for the management of term and preterm labor,” *Annals of the New York Academy of Sciences*, vol. 943, pp. 203–224, 2001.
- [6] C. Rabotti, M. Mischi, S. G. Oei, and J. W. M. Bergmans, “Noninvasive estimation of the electrohysterographic action-potential conduction velocity,” *IEEE Transactions on Biomedical Engineering*, vol. 57, no. 9, pp. 2178–2187, 2010.
- [7] M. Hassan, J. Terrien, C. Muszynski et al., “Better pregnancy monitoring using nonlinear correlation analysis of external uterine electromyography,” *IEEE Transaction on Biomedical Engineering*, vol. 60, no. 4, pp. 1160–1166, 2013.
- [8] C. Marque and J. Duchene, “Human abdominal EHG processing for uterine contraction monitoring,” *Biotechnology*, vol. 11, pp. 187–226, 1989.
- [9] C. Rabotti, M. Mischi, J. O. E. H. Van Laar, G. S. Oei, and J. W. M. Bergmans, “Estimation of internal uterine pressure by joint amplitude and frequency analysis of electrohysterographic signals,” *Physiological Measurement*, vol. 29, no. 7, pp. 829–841, 2008.
- [10] C. Rabotti, M. Mischi, S. G. Oei, and J. W. M. Bergmans, “Noninvasive estimation of the electrohysterographic action-potential conduction velocity,” *IEEE Transactions on Biomedical Engineering*, vol. 57, no. 9, pp. 2178–2187, 2010.
- [11] J. Laforet, C. Rabotti, J. Terrien, M. Mischi, and C. Marque, “Toward a multiscale model of the uterine electrical activity,” *IEEE Transactions on Biomedical Engineering*, vol. 58, no. 12, pp. 3487–3490, 2011.
- [12] W. L. Maner, R. E. Garfield, H. Maul, G. Olson, and G. Saade, “Predicting term and preterm delivery with transabdominal uterine electromyography,” *Obstetrics and Gynecology*, vol. 101, no. 6, pp. 1254–1260, 2003.
- [13] D. Devedeux, C. Marque, S. Mansour, G. Germain, and J. Duchene, “Uterine electromyography: a critical review,” *American Journal of Obstetrics and Gynecology*, vol. 169, no. 6, pp. 1636–1653, 1993.
- [14] O. Dupuis, R. Silveira, A. Zentner et al., “Birth simulator: Reliability of transvaginal assessment of fetal head station as defined by the American College of Obstetricians and Gynecologists classification,” *American Journal of Obstetrics and Gynecology*, vol. 192, no. 3, pp. 868–874, 2005.
- [15] J. Y. Phelps, K. Higby, M. H. Smyth, J. A. Ward, F. Arredondo, and A. R. Mayer, “Accuracy and intraobserver variability of simulated cervical dilatation measurements,” *American Journal of Obstetrics and Gynecology*, vol. 173, no. 3 I, pp. 942–945, 1995.
- [16] D. J. Tuffnell, F. Bryce, N. Johnson, and R. J. Lilford, “Simulation of cervical changes in labour: reproducibility of expert assessment,” *The Lancet*, vol. 2, no. 8671, pp. 1089–1090, 1989.
- [17] D. M. Sherer, M. Miodovnik, K. S. Bradley, and O. Langer, “Intrapartum fetal head position I: comparison between transvaginal digital examination and transabdominal ultrasound assessment during the active stage of labor,” *Ultrasound in Obstetrics and Gynecology*, vol. 19, no. 3, pp. 258–263, 2002.

- [18] A. Ugwumadu, "The role of ultrasound scanning on the labor ward," *Ultrasound in Obstetrics and Gynecology*, vol. 19, no. 3, pp. 222–224, 2002.
- [19] S. Akmal, E. Tsoi, R. Howard, E. Osei, and K. H. Nicolaides, "Investigation of occiput posterior delivery by intrapartum sonography," *Ultrasound in Obstetrics and Gynecology*, vol. 24, no. 4, pp. 425–428, 2004.
- [20] M. R. Chou, D. Kreiser, M. M. Taslimi, M. L. Druzin, and Y. Y. El-Sayed, "Vaginal versus ultrasound examination of fetal occiput position during the second stage of labor," *American Journal of Obstetrics and Gynecology*, vol. 191, no. 2, pp. 521–524, 2004.
- [21] S. M. Rane, R. R. Guirgis, B. Higgins, and K. H. Nicolaides, "The value of ultrasound in the prediction of successful induction of labor," *Ultrasound in Obstetrics and Gynecology*, vol. 24, no. 5, pp. 538–549, 2004.
- [22] M. M. Constantine and G. R. Sade, "The first cesarean: role of "Fetal Distress" diagnosis," *Seminars in Perinatology*, vol. 36, pp. 379–383, 2012.
- [23] J. A. Lauer, A. P. Betrán, M. Merialdi et al., "Determinants of caesarean section rates in developed countries: supply, demand and opportunities for control," World Health Report, Background Paper, no. 29, 2010.
- [24] O. Barnea, O. Luria, A. Jaffa, M. Stark, H. E. Fox, and D. Farine, "Relations between fetal head descent and cervical dilatation during individual uterine contractions in the active stage of labor," *Journal of Obstetrics and Gynaecology Research*, vol. 35, no. 4, pp. 654–659, 2009.
- [25] M. Letić, "Inaccuracy in cervical dilatation assessment and the progress of labour monitoring," *Medical Hypotheses*, vol. 60, no. 2, pp. 199–201, 2003.
- [26] R. S. Lucidi, L. A. Blumenfeld, and R. A. Chez, "Cervimetry: a review of methods for measuring cervical dilatation during labor," *Obstetrical and Gynecological Survey*, vol. 55, no. 5, pp. 312–320, 2000.
- [27] M. C. Antonucci, M. C. Pitman, T. Eid, P. J. Steer, and E. S. Genevier, "Simultaneous monitoring of head-to-cervix forces, intrauterine pressure and cervical dilatation during labour," *Medical Engineering and Physics*, vol. 19, no. 4, pp. 317–326, 1997.
- [28] M. A. Malvindi, A. Greco, F. Conversano et al., "Magnetic/silica nanocomposites as dual-mode contrast agents for combined magnetic resonance imaging and ultrasonography," *Advanced Functional Materials*, vol. 21, no. 13, pp. 2548–2555, 2011.
- [29] F. Conversano, A. Greco, E. Casciaro, A. Ragusa, A. Lay-Ekuakille, and S. Casciaro, "Harmonic ultrasound imaging of nano-sized contrast agents for multimodal molecular diagnoses," *IEEE Transactions on Instrumentation and Measurement*, vol. 61, no. 7, pp. 1848–1856, 2012.
- [30] F. Conversano, G. Soloperto, A. Greco et al., "Ecographic detectability of optoacoustic signals from low-concentration PEG-coated gold nanorods," *International Journal of Nanomedicine*, vol. 7, pp. 4373–4389, 2012.
- [31] P. A. Tinelli, A. Malvasi, A. J. Schneider et al., "First abdominal access in gynecological laparoscopy: which method to utilize?" *Minerva Ginecologica*, vol. 58, no. 5, pp. 429–440, 2006.
- [32] P. Lamata, F. Lamata, V. Sojar et al., "Use of the resection map system as guidance during hepatectomy," *Surgical Endoscopy and Other Interventional Techniques*, vol. 24, no. 9, pp. 2327–2337, 2010.
- [33] T. M. Eggebo, L. K. Gjessing, C. Heien et al., "Prediction of labor and delivery by transperineal ultrasound in pregnancies with prelabor rupture of membranes at term," *Ultrasound in Obstetrics and Gynecology*, vol. 27, no. 4, pp. 387–391, 2006.
- [34] M. Saito, S. Kozuma, A. Kikuchi et al., "Sonographic assessment of the cervix before, during and after a uterine contraction is effective in predicting the course of labor," *Ultrasound in Obstetrics and Gynecology*, vol. 22, no. 6, pp. 604–608, 2003.
- [35] C. O. Onyeama, H. Srinivasan, M. Lotke, and D. L. Vickers, "Subgaleal abscess and E. coli septicemia following scalp electrode in a preterm newborn: a case report," *Journal of Maternal-Fetal and Neonatal Medicine*, vol. 22, no. 12, pp. 1201–1203, 2009.
- [36] W. Henrich, J. Dudenhausen, I. Fuchs, A. Kämena, and B. Tutschek, "Intrapartum translabial ultrasound (ITU): sonographic landmarks and correlation with successful vacuum extraction," *Ultrasound in Obstetrics and Gynecology*, vol. 28, no. 6, pp. 753–760, 2006.
- [37] S. Casciaro, F. Conversano, and E. Casciaro, "Ultrasonic apparatus for measuring a labor progress parameter," Patent Application PCT/EP2009/008321.
- [38] S. Casciaro, F. Conversano, E. Casciaro et al., "Quantitative and automatic echographic monitoring of LABor progression-AMOLAB," in *Proceedings of the IEEE International Ultrasonics Symposium*, Dresden, Germany, October 2012.
- [39] F. Conversano, E. Casciaro, R. Franchini, A. Lay-Ekuakille, and S. Casciaro, "A quantitative and automatic echographic method for real-time localization of endovascular devices," *IEEE Transactions on Ultrasonics, Ferroelectrics, and Frequency Control*, vol. 58, no. 10, pp. 2107–2117, 2011.
- [40] P. A. Robertson, R. K. Laros Jr., and R.-L. Zhao, "Neonatal and maternal outcome in low-pelvic and midpelvic operative deliveries," *American Journal of Obstetrics and Gynecology*, vol. 162, no. 6, pp. 1436–1444, 1990.
- [41] S. Cox, C. Werner, B. Hoffman et al., *Williams Obstetrics*, McGraw-Hill, 22nd edition, 2005.
- [42] S. Casciaro, F. Conversano, S. Musio, E. Casciaro, C. Demitri, and A. Sannino, "Full experimental modelling of a liver tissue mimicking phantom for medical ultrasound studies employing different hydrogels," *Journal of Materials Science*, vol. 20, no. 4, pp. 983–989, 2009.
- [43] S. Casciaro, C. Demitri, F. Conversano, E. Casciaro, and A. Distanti, "Experimental investigation and theoretical modelling of the nonlinear acoustical behaviour of a liver tissue and comparison with a tissue mimicking hydrogel," *Journal of Materials Science*, vol. 19, no. 2, pp. 899–906, 2008.
- [44] C. Demitri, A. Sannino, F. Conversano, S. Casciaro, A. Distanti, and A. Maffezzoli, "Hydrogel based tissue mimicking phantom for in-vitro ultrasound contrast agents studies," *Journal of Biomedical Materials Research B*, vol. 87, no. 2, pp. 338–345, 2008.